High temperature oxidation behavior of γ-Ni+γ'-Ni_3Al alloys and coatings modified with Pt and reactive elements

by

Nan Mu

A dissertation submitted to the graduate faculty
In partial fulfillment of the requirements for the degree of
DOCTOR OF PHILOSOPHY

Major: Materials Science and Engineering

Program of Study Committee:
Brian Gleeson, Major Professor
Daniel Sordelet
Xiaoli Tan
Kurt Hebert
Pranav Shrotriya

Iowa State University
Ames, Iowa
2007

Table of Contents

LIST OF FIGURES v
LIST OF TABLES x
ACKNOWLEDGEMENTS xi
ABSTRACT xiii
CHAPTER 1 INTRODUCTION 1
CHAPTER 2 LITERATURE REVIEW 5
2.1 High Temperature Oxidation of Metals 5
2.1.1 Thermodynamics of Metal Oxidation 5
2.1.2 Kinetics of Metal Oxidation 9
2.1.3 Stress Generation in Oxide Scales 14
2.1.3.1 The Origin of Stresses in Growing Oxide Scales 14
2.1.3.2 Scale Stresses Induced by Temperature Change 16
2.2 Fundamental Aspects of Alloy Oxidation 16
2.2.1 Classifications of Alloy Oxidation 17
2.2.2 Limiting Cases of Alloy Oxidation 20
2.3 Al_2O_3-Scale Forming Alloys 22
2.3.1 β-NiAl 23
2.3.2 Pt-Modified γ-Ni + γ'-Ni_3Al 24
2.4 Effect of Reactive Element Additions on High Temperature Oxidation Resistance 26
2.4.1 Basic Properties of Reactive Elements 27
2.4.2 Reactive Element Doping Methods 29
2.4.3 Reactive Element Effects and Mechanisms 30
2.5 Protective Coatings for Turbine Blades 32
2.5.1 Phase Composition and Structure of Diffusion Coatings 33
2.5.2 High Temperature Degradation of Coatings 34
2.6 Purpose of Current Study 35
CHAPTER 3 EXPERIMENTAL PROCEDURES 37
3.1 Sample Preparation 37
3.2 High-Temperature Oxidation Tests 38

3.2.1 Early-Stage Oxidation 38
3.2.2 4-Day Isothermal Oxidation 40
3.2.3 Cyclic Oxidation 40
3.2.4 Thermal Gravimetric Analysis 40
3.3 Characterization 40
CHAPTER 4 RESULTS 43
4.1 Single-Phase γ-Ni and γ'-Ni_3Al Alloys 43
4.1.1 Early-Stage Oxidation Behavior 45
4.1.1.1 Pt Effects in γ-Ni Alloys 45
4.1.1.2 Pt Effects in γ'-Ni_3Al Alloys 54
4.1.1.3 Hf Effects in γ'-Ni_3Al Alloys 82
4.1.2 4-Day Isothermal Oxidation Results 85
4.1.2.1 Effects of Platinum in γ-Ni Allloys 87
4.1.2.2 Effects of Platinum in γ'-Ni_3Al Allloys 89
4.1.2.3 Effects of Hafnium in γ'-Ni_3Al Alloys 90
4.2 Two-Phase γ-Ni+γ'-Ni_3Al Alloys 92
4.2.1 TGA Results 93
4.2.2 Cyclic Oxidation Results 99
4.2.3 Partitioning Behavior of Hf 102
4.2.4 Thermally Grown Oxide Characterizations 105
4.2.4.1 Confocal Photo-Stimulated Microspectroscopy Results 105
4.2.4.2 In-Lens SEM Examination of Al_2O_3 Scale 109
4.2.4.3 TEM Examination of Al_2O_3 Grain Boundaries 110
4.3 Development of Pt+Hf-Modified γ-Ni+γ'-Ni_3Al Coatings 118
4.3.1 Advantages of Pt+Hf-modified γ-Ni+γ'-Ni_3Al Coatings 118
4.3.2 Coating Composition Dependence on Temperature and Time 121
4.3.3 Coating Short-Term Oxidation Performance 124
4.3.4 Coating Cyclic Oxidation Performance 126
4.3.5 Comparison between Coatings and Alloys 128
CHAPTER 5 DISCUSSION 131

5.1 Pt Effects on Al_2O_3 Formation 131
5.2 Hf Effects on NiO Growth 133
5.3 Cooperation of Pt and Hf 134
5.4 Pt and Hf effects on Scale Spallation Behavior 137
5.5 Al_2O_3 Microstructures Affected by Hf Additions 144
5.6 Hf Effects of θ-α-Al_2O_3 Transformation 147
5.7 Hf Effects on Scale Stress Evolution 150
5.8 Determination of Al_2O_3 Scale Growth Rate 151
5.9 Surface Segregation of Indigenous Sulfur 153
5.10 Pt+Hf-Modified γ-Ni+γ'-Ni_3Al Coatings 155
CHAPTER 6 SUMMARY 158
6.1 Single-Phase γ-Ni and γ'-Ni_3Al Alloys 158
6.2 Two-Phase γ-Ni+γ'-Ni_3Al Alloys 159
6.3 Development of Pt+Hf-Modified γ-Ni+γ'-Ni_3Al Coatings 160
REFERENCES 162

LIST OF FIGURES

Figure 1. Ellingham diagram showing the standard free energy as a function of temperature for selected oxides [40]. 8

Figure 2. Logarithmic and inverse logarithmic oxidation [43]. 10

Figure 3. Schematic representation of scale formation according with Wagner's model [41]. 12

Figure 4. A schematic representation of oxidation modes of alloy AB of variable composition, where B is the less noble metal. 18

Figure 5. A schematic showing the early stages of simultaneous formation of immiscible oxides AO and BO [54] 20

Figure 6. Dependence of the mechanism of oxidation for Ni-Al alloys on temperature and alloy composition according to Pettit [59]. 23

Figure 7. A schematic showing the $L1_2$ crystal structure of γ'-Ni_3Al. 24

Figure 8. Isothermal phase equilibria on Ni-Pt-Al alloys at 1150°C [38]. 25

Figure 9. The weight change of Ni22Al30Pt and Ni22Al30Pt0.8Hf (in at.%) alloys at 1150°C after 500 cycles. 27

Figure 10. Stability relationships of oxides arranged in periodic table [69]. 29

Figure 11. Cyclic oxidation results for the René N5 superalloy with different treatments at 1149°C in air [74] 32

Figure 12. Cross section of an as-deposited nickel aluminide coatings on CMSX-4. 33

Figure 13. Cross-sectional SEM image showing the surface rumpling of Pt-modified β-NiAl coating after 1000 cycles at 1150°C. 35

Figure 14. SEM image showing the formation of secondary reaction zone. 36

Figure 15. Schematic showing the automated furnace used for the early-stage oxidation tests. 39

Figure 16. A representative measured heating profile of the test sample. 39

Figure 17. A section of the equilibrium Ni-Al-Pt ternary phase diagram at 1150°C with the alloy compositions superimposed. 44

Figure 18. The early-stage anisothermal oxidation kinetics of the γ-Ni alloys affected by Pt additions 46

Figure 19. SEM images showing the surface morphology of scales formed on Ni-12.5Al-xPt (x=0, 10 and 20) alloys 47

Figure 20. GD-OES composition profiles from the surface of oxidized Ni-12.5Al after 90, 180 and 1800 seconds. 49

Figure 21. GD-OES composition profiles from the surface of oxidized Ni-12.5Al-10Pt after 90, 180 and 1800 seconds. 51

Figure 22. GD-OES composition profiles from the surface of oxidized Ni-12.5Al-20Pt after 90, 180 and 1800 seconds. 53

Figure 23. The early-stage anisothermal oxidation kinetics of the γ'-Ni_3Al alloys affected by Pt additions (a) Ni-25Al-xPt, (b) Ni-25Al-0.2Hf-xPt and (c) Ni-25Al-0.5Hf-xPt. 55

Figure 24. The relationship between the weight change and Pt contents of Hf-modified Ni-25Al alloys. 56

Figure 25. SEM images showing the surface morphology of scales formed on Ni-25Al-xPt (x=0, 10 and 20) alloys 58

Figure 26. SEM images showing the surface morphology of scales formed on Ni-25Al-0.2Hf-xPt (x=0, 10 and 20) alloys. 60

Figure 27. SEM images showing the surface morphology of scales formed on Ni-25Al-0.5Hf-xPt (x=0, 10 and 20) alloys. 62

Figure 28. GD-OES composition profiles from the surface of oxidized Ni-25Al after 90, 180 and 1800 seconds. 64

Figure 29. GD-OES composition profiles from the surface of oxidized Ni-25Al-10Pt after 90, 180 and 1800 seconds. 66

Figure 30. GD-OES composition profiles from the surface of oxidized Ni-25Al-20Pt after 90, 180 and 1800 seconds. 68

Figure 31. GD-OES composition profiles from the surface of oxidized Ni-25Al-0.2Hf after 90, 180 and 1800 seconds. 70

Figure 32. GD-OES composition profiles from the surface of oxidized Ni-25Al-10Pt-0.2Hf after 90, 180 and 1800 seconds 72

Figure 33. GD-OES composition profiles from the surface of oxidized Ni-25Al-20Pt-0.2Hf after 90, 180 and 1800 seconds 74

Figure 34. GD-OES composition profiles from the surface of oxidized Ni-25Al-0.5Hf after 90, 180 and 1800 seconds. 76

Figure 35. GD-OES composition profiles from the surface of oxidized Ni-25Al-10Pt-0.5Hf after 90, 180 and 1800 seconds 78

Figure 36. GD-OES composition profiles from the surface of oxidized Ni-25Al-20Pt-0.5Hf after 90, 180 and 1800 seconds 80

Figure 37. The early-stage anisothermal oxidation kinetics of the γ'-Ni_3Al alloys affected by Hf additions (a) Ni-25Al-xHf, (b) Ni-25Al-10Pt-xHf and (c) Ni-25Al-20Pt-xHf. 83

Figure 38. Digital optical micrographs showing the surface morphologies of disk-shaped oxidized coupons. 86

Figure 39. Cross-sectional SEM images showing alloys oxidized at 1150°C for 4 days: a) Ni-12.5Al; b) Ni-12.5Al-10Pt and c) Ni-12.5Al-20Pt. 87

Figure 40. Measured scale thickness of each oxide-scale layer formed on γ-Ni alloys at 1150°C for 4 days: a) Ni-12.5Al; b) Ni-12.5Al-10Pt and c) Ni-12.5Al-20Pt. 88

Figure 41. Cross-sectional SEM images showing alloys oxidized at 1150°C for 4 days: a) Ni-25Al; b) Ni-25Al-0.2Hf; c) Ni-25Al-0.5Hf; d) Ni-25Al-10Pt; e) Ni-25Al-10Pt-0.2Hf; f) Ni-25Al-10Pt-0.5Hf; g) Ni-25Al-20Pt; h) Ni-25Al-20Pt-0.2Hf and i) Ni-25Al-20Pt-0.5Hf..... 88

Figure 42. Measured thickness of constituent layers in the oxide scales formed on γ'-Ni_3Al alloys at 1150°C for 4 days: a) Ni-25Al; b) Ni-25Al-10Pt; c) Ni-25Al-20Pt; d) Ni-25Al-0.2Hf; e) Ni-25Al-10Pt-0.2Hf; f) Ni-25Al-20Pt-0.2Hf; g) Ni-25Al-0.5Hf; h) Ni-25Al-10Pt-0.5Hf and i) Ni-25Al-20Pt-0.5Hf. 90

Figure 43. Measured thickness of constituent layers in the oxide scales formed on γ'-Ni_3Al alloys at 1150°C for 4 days: a) Ni-25Al; b) Ni-25Al-0.2Hf; c) Ni-25Al-0.5Hf; d) Ni-25Al-10Pt; e) Ni-25Al-10Pt-0.2Hf; f) Ni-25Al-10Pt-0.5Hf; g) Ni-25Al-20Pt; h) Ni-25Al-20Pt-0.2Hf and i) Ni-25Al-20Pt-0.5Hf. 92

Figure 44. Isothermal mass change of Ni-20Al-20Pt-xHf at 1150°C for 100 hours..... 94

Figure 45. Instantaneous rate constant kp' as a function of time for Ni-20Al-20Pt-xHf alloys at 1150°C after 100 hours..... 95

Figure 46. SEM images showing the surface morphology of scales formed on Ni-20Al-20Pt-xHf alloys at 1150C after 100 hours: a) 0Hf; b) 0.05Hf; c) 0.13Hf; d) 0.23Hf; e) 0.31Hf; f) 0.48Hf and g) 0.91Hf..... 97

Figure 47. Cross-sectional SEM images showing the scale formed on Ni-20Al-20Pt-xHf alloys at 1150C after 100 hours: a) 0Hf; b) 0.05Hf; c) 0.13Hf; d) 0.23Hf; e) 0.31Hf; f) 0.48Hf and g) 0.91Hf..... 98

Figure 48. The weight change of Ni-20Al-20Pt-xHf alloys at 1150C after a) 500 cycles and b) 10 cycles. 100

Figure 49. SEM images showing the surface morphology of scales formed on Ni-20Al-20Pt-xHf alloys at 1150°C after 500 cycles: a) 0Hf; b) 0.05Hf; c) 0.13Hf; d) 0.23Hf; e) 0.31Hf; f) 0.48Hf and g) 0.91Hf..... 101

Figure 50. Cross-sectional SEM images showing the scale formed on Ni-20Al-20Pt-xHf alloys at 1150°C after 500 cycles: a) 0Hf; b) 0.05Hf; c) 0.13Hf; d) 0.23Hf; e) 0.31Hf; f) 0.48Hf and g) 0.91Hf..... 102

Figure 51. SEM images showing the high temperature phases presented in Ni-20Al-20Pt-xHf alloys at 1150°C: a) 0Hf; b) 0.05Hf; c) 0.13Hf; d) 0.23Hf; e) 0.31Hf; f) 0.48Hf and g) 0.91Hf..... 103

Figure 52. Alloys phase percentage as a function of Hf content..... 104

Figure 53. Partitioning behavior of Hf in Ni-20Al-20Pt-xHf alloys..... 105

Figure 54. Evolution of compressive residual stress on Ni-20Al-20Pt and Ni-20Al-20Pt-0.48Hf as a function of oxidation time at 1100°C..... 106

Figure 55. Alumina phase map showing the evolution of oxide phases with increasing oxidation time on both Ni-20Al-20Pt and Ni-20Al-20Pt-0.48Hf at 1100°C..... 108

Figure 56. SEM in-lens images showing the grain structure of oxide formed on a) Ni-20Al-20Pt and b) Ni-20Al-20Pt-0.48Hf at 1150°C after 100 hours..... 110

Figure 57. A bright field TEM micrograph showing the scale formed on Ni-20Al-20Pt-0.48Hf at 1150C after 50 hours..... 111

Figure 58. Elemental spectroscopy imaging (ESI) showing the elemental composition of the scale formed on the isothermally oxidized Ni-20Al-20Pt-0.48Hf at 1150°C after 50 hours..... 112

Figure 59. Hf segregation into Al_2O_3 grain boundaries: a) a bright field image showing the Al_2O_3 grain boundary with marked position for b) XEDS line scanning..... 113

Figure 60. Isothermally oxidized Ni-20Al-20Pt-0.48Hf at 1150°C after 100 hours a) SEM image showing the surface morphology; b) CPSM determined room temperature residual stress..... 115

Figure 61. Site-specific examination of the scale formed on isothermally oxidized Ni-20Al-20Pt-0.48Hf at 1150°C after 100 hours a) SEM surface image; b) bright field TEM cross sections; c) CPSM resolved residual stress..... 116

Figure 62. Microstructural analysis on selected oxide scale at a) region 1; b) region 2 and c) region 3..... 117

Figure 63. Cross-sectional SEM images showing the comparison between a) γ-Ni + γ'-Ni_3Al coating and b) commercial Pt-modified β-NiAl coating on René-N5 superalloy at 1150°C for 1000 cycles..... 119

Figure 64. EPMA results showing composition profiles of a) as-coated and b) 1000 cycles at 1150°C oxidized γ-Ni + γ'-Ni_3Al coating..... 120

Figure 65. Optical image illustrating the as-coated airfoil span with test schemes..... 122

Figure 66. Selected coatings composition of a) Al, b) Hf and c) Pt..... 123

Figure 67. SEM images showing the oxide scale formed at 1080°C fro 30 minutes on the suction side of coatings prepared by pack cementation process a) at temperature T4 after t1 hours; b) at temperature T5 after t2 hours..... 125

Figure 68. Cross-sectional SEM images showing the oxide scale formed at 1150°C for 100 cycles on the suction side of coatings prepared by pack

cementation process a) at temperature T4 after t1 hours; b) at temperature T5 after t2 hours. 127

Figure 69. Weight change of selected alloys and coatings at 1150°C for 100 cycles. 129

Figure 70. Cross-sectional SEM images showing the scale formed on selected alloys and coatings at 1150°C after 100 cycles. 130

Figure 71. A schematic Ellingham diagram showing the standard free energy of formation vs. temperature for Al_2O_3 and HfO_2. 136

Figure 72. SEM images showing the surface of 4-day isothermally oxidized Ni-25Al: a) intact oxide; b) spalled area; c) higher mag. of spalled area; and Ni-25Al-10Pt: d) intact oxide; e) spalled area; f) higher mag. of spalled area; at 1150°C. 139

Figure 73. Interfacial voids formation detected by CPSM on alloys Ni-25Al, Ni-25Al-10Pt and Ni-25Al-20Pt isothermally oxidized at 1100°C for 50 hours. 140

Figure 74. CPSM resolved 3D projections showing the voids formed at scale/alloy interface on isothermally oxidized a) Ni-25Al and b) Ni-25Al-10Pt at 1100°C for 50 hours. 141

Figure 75. SEM images showing the surface morphology of scales formed on Ni-25Al-xPt (x=0, 10 and 20) alloys with 15keV beam accelerating voltage. 142

Figure 76. Arrhenius plot of the parabolic rate constants kp of NiAl oxidation [140]. 148

Figure 77. A schematic showing the $\theta \rightarrow \alpha$-$Al_2O_3$ transformation area in a) Hf-free alloy and b) Hf-modified alloy. 149

Figure 78. A schematic showing the relationship between interface fracture strength and interfacial sulfur content affected by Pt, Hf and Cr. 155

LIST OF TABLES

Table 1. Selected oxide-metal volume ratios for some common metals [49]. 15

Table 2. Basic properties of some major alloying and reactive elements and their compounds [67, 68]. 28

Table 3. Nominal single-phase alloy compositions (in at.%) investigated. 44

Table 4. Nominal composition (in at.%) of bulk Ni-20Al-20Pt-xHf alloys. 93

Table 5. Parabolic rate constants at steady state from TGA for Ni-20Al-20Pt-xHf at 1150°C after 100 hours. 96

Table 6. Calculated average compressive stresses on Ni-20Al-20Pt and Ni-20Al-20Pt-0.48Hf. 106

Table 7. Coating samples coding scheme. 121

Table 8. Oxide products formed on the suction side of airfoil spans at 1150°C after 100 cycles 128

Table 9. Sulfur segregation vs. interface strength 155

ACKNOWLEDGEMENTS

I would like to express my earnest acknowledgements to my major advisor, Dr. Brian Gleeson, who is now the Harry S. Tack Chair in the Department of Mechanical Engineering and Materials Science at University of Pittsburgh, for his continued support, guidance, inspiration and suggestion throughout my studies in Iowa. It is my honor and privilege to conduct my Ph.D. research with such a wise and philosophical friend. His patience and encouragement during my hard times are gratefully acknowledged.

I would also like to thank my other committee members, Dr. Daniel Sordelet, Dr. Xiaoli Tan, Dr. Kurt Hebert and Dr. Pranav Shrotriya for their assistance and guidance in this research, which is primarily supported by the Office of Naval Research with Dr. David Shifler being the program manager.

I am indebted to numerous colleagues in academia, national laboratories and industry, foreign and domestic, for their generous contribution. This work could not have been accomplished without their close collaboration. I am grateful to Dr. Shigenari Hayashi and his graduate student Yuri Kitajima at Hokkaido University for their dedicated GD-OES analysis. I am also grateful to Prof. Arthur H. Heuer, Dr. David Hovis and graduate student Lin Hu at Case Western Reserve University for their keen CPSM and TEM analysis. I have also benefited from Dr. Peggy Hou at Lawrence Berkeley National Laboratory with the attentive measurement of the sulfur content and precious discussion. I would like to thank Dr. W. Joe Quadakkers, Dr. Dmitry Naumenko, and graduate student Peng Song at Forschungszentrum Jülich for their help with in-lens SEM examination. It is a pleasure to acknowledge Dr. Ann Bolcavage at Rolls Royce Corporation, USA, Dr. Ram Darolia at GE Aircraft Engines, Dr. Kenneth S. Murphy at Alcoa Howmet Research Corporation, Dr. Yannick Cadoret at Snecma, France for providing coating samples. Valuable discussion with Dr. David R. Clarke at University of California, Santa Barbara, Dr. Daniel E. Monceau at Cirimat Laboratory, France, and Dr. Boyd Veal at Argonne National Laboratory is greatly appreciated.

I am grateful to my officemates, Dr. Bingtao Li, Dr. Liming Zhang and Dr. Takeshi Izumi for their continued advice and assistance. I also thank Matthew Besser and Lawrence L. Jones at Ames laboratory for their generous technical support.

Finally, I would like to dedicate this work to my parents for their remote everlasting love and understanding throughout my academic Long March. Special thanks go to my beloved wife, Xiaocui, for giving me endless support and countless strength.

ABSTRACT

Materials for high-pressure turbine blades must be able to operate in the high-temperature gases (above 1000°C) emerging from the combustion chamber. Accordingly, the development of nickel-based superalloys has been constantly motivated by the need to have improved engine efficiency, reliability and service lifetime under the harsh conditions imposed by the turbine environment. However, the melting point of nickel (1455°C) provides a natural ceiling for the temperature capability of nickel-based superalloys. Thus, surface-engineered turbine components with modified diffusion coatings and overlay coatings are used. Theses coatings are capable of forming a compact and adherent oxide scale, which greatly impedes the further transport of reactants between the high-temperature gases and the underlying metal and thus reducing attack by the atmosphere. Typically, these coatings contain β-NiAl as a principal constituent phase in order to have sufficient aluminum content to form an Al_2O_3 scale at elevated temperatures. The drawbacks to the currently-used β-based coatings, such as phase instabilities, associated stresses induced by such phase instabilities, and extensive coating/substrate interdiffusion, are major motivations in this study to seek next-generation coatings.

The high-temperature oxidation resistance of novel Pt+Hf-modified γ-Ni+γ′-Ni_3Al-based alloys and coatings were investigated in this study. Both early-stage and 4-days isothermal oxidation behavior of single-phase γ-Ni and γ′-Ni_3Al alloys were assessed by examining the weight changes, oxide-scale structures, and elemental concentration profiles through the scales and subsurface alloy regions. It was found that Pt promotes Al_2O_3 formation by suppressing the NiO growth on both γ-Ni and γ′-Ni_3Al single-phase alloys. This effect increases with increasing Pt content. Moreover, Pt exhibits this effect even at lower temperatures (~970°C) in the very early stage of oxidation. It was also inferred that Pt enhances the diffusive flux of aluminum from the substrate to the scale/alloy interface. Relatively low levels of hafnium addition to Pt-free γ′-Ni_3Al increased the extent of external NiO formation due to non-protective HfO_2 formation. Accordingly, this effect intensified with increasing Hf content from 0.2 to 0.5at.%.

The synergistic effect of Pt and Hf co-addition was realized by examining Pt+Hf-modified γ'-Ni_3Al alloys. It was inferred that Pt decreases the chemical activity of Hf so that HfO_2 formation could be suppressed with increasing Pt content. Thus, the early-stage Al_2O_3 formation facilitated by Pt additions and NiO development assisted by Hf additions are the competing scale growth processes that are influenced by the relative contents of Pt and Hf. Large interfacial voids were observed on the γ'-Ni_3Al alloy after 4-days isothermal oxidation at 1150°C, which could be attributed to the Kirkendall effect. Platinum addition was also found to improve Al_2O_3-scale adhesion.

Pt and Hf effects on two-phase γ-Ni+γ'-Ni_3Al alloys of compositions Ni-20Al-20Pt-xHf (x ranges from 0 to 0.91) were examined by both thermal gravimetric analyses and cyclic oxidation tests. Scale microstructures were characterized by confocal photo-stimulated microspectroscopy (CPSM), in-lens SEM, and FIB-TEM. Hafnium additions up to about 0.48at.% markedly decreased the weight change of isothermally oxidized Pt-modified γ+γ' alloys by forming thinner oxide scales than that on the Hf-free Ni-20Al-20Pt base alloy. This could be attributed to an Al_2O_3 grain boundary blocking effect imparted by the segregated Hf. However, an over-doped alloy with 0.91at.% Hf exhibited detrimental effect by forming internal HfO_2.

It was observed that Hf additions altered the Al_2O_3 scale microstructure. The most remarkable difference was that the columnar width of the Al_2O_3 scale grains formed on Ni-20Al-20Pt was much larger than it was on Ni-20Al-20Pt-0.48Hf. Even so, the Hf-doped alloys exhibited much slower scaling kinetics with a correspondingly thinner scale. This behavior could be ascribed to the Hf blocking diffusing paths as it segregated into Al_2O_3 grain boundaries. Therefore, the Hf-doped scale grew at a lower rate even though it contained more grain boundaries. Accompanied with this scale microstructure modification, Hf additions led to the following two additional effects: 1) Hf delayed the $\theta \rightarrow \alpha$ structural transformation of Al_2O_3; and 2) compressive residual stress in the scale formed on Hf-doped alloys was lower than that on the Hf-free Ni-20Al-20Pt alloy.

Guided by the results from the bulk-alloy studies, a feasible method to deposit Pt+Hf-modified γ+γ' coatings having overall compositions closely approaching Ni-$Al_{15\text{-}20}$-$Pt_{15\text{-}20}$-Hf was subsequently developed. A key improvement of the application of Pt+Hf-modified γ-

Ni+γ'-Ni_3Al coatings is the relief of TCP phases generated from coating/substrate interdiffusion. This could be simply attributed to the inherited phase compatibility between $\gamma+\gamma'$ coatings with Ni-based superalloys. Another important advantage of $\gamma+\gamma'$ coatings is the exclusion of phase transformations during thermal cycling.

The Pt+Hf-modified γ-Ni+γ'-Ni_3Al coating compositions had a strong dependence on the temperature and time in both pack cementation and post-heat-treatment processes. Meanwhile, coating performance was apparently more sensitive to the Hf content than what was observed with the alloys. Coating performance was also considerable affected by the surface finish and the composition of the superalloy substrate.

CHAPTER 1 INTRODUCTION

Surface engineering is now a key materials technology in the design of future advanced gas-turbine engines. The drive to improve engine combustion efficiency while reducing emissions has meant that the operating temperatures within the turbine section of gas-turbine engines, whether aero, industrial, or marine, have increased significantly during the last 40 years [1]. In future years, it is desired for turbine engines to reach new heights of efficiency and service life. But to keep pace in meeting new challenges with further demanding conditions, coating engineers will have to design improved coating materials concurrently with the development of next-generation superalloys [2]. Possible materials can be separated into distinct classes: evolutionary and revolutionary materials. The former represent incrementally improved materials, mostly metals. The latter represent intermetallic compounds, and metal, polymer and ceramic composites [3]. Despite the promising potentials exhibited by revolutionary materials, there are still many limitations to their application such as high cost and low-temperature brittleness. Therefore, traditional metallic materials with inherited excellent high-temperature resistance remain as prospective candidates as core engine materials and will be studied in this research.

Materials for high-pressure turbine blades must be able to operate in the high-temperature gases (above 1000°C) emerging from the combustion chamber. They experience a combination of high temperatures and centrifugal stresses. Accordingly, the development of nickel-based superalloys has, almost entirely, been motivated by the requirement to improve the efficiency, reliability and operating life of gas turbines since the 1940s. Over the last 60 years or so, very significant improvement of Ni-based superalloys has progressed from wrought alloys to cast and single-crystal alloys. The most advanced single-crystal superalloy turbine blades are now operating at a temperature greater than 85% of their absolute melting temperature (T_m) [4]. Ni-based superalloys enjoy high strengths at elevated temperatures through the disposition of a high volume fraction of the coherently dispersed γ' precipitate (up to 70% by volume) in the γ-Ni matrix. In addition, these alloys are strengthened by incoherent phases (carbides) and solid solutions (W, Ta, Mo, and Re). However, the melting point of nickel (1455°C=1728K) provides a natural ceiling for the

temperature capability of nickel-based superalloys [5, 6]. Thus, uncooled blades have been surpassed by cooled blades that, in turn, have been replaced by coated, cooled blades. Advances in cooling technology involve sophisticated convection, impingement, and film-cooling designs [7, 8, 9].

Since the development of most advanced superalloys is inevitably in pursuit of attractive mechanical properties, the need for coating systems to impart adequate resistance to high-temperature oxidation and corrosion became essential since the early 1960s. Early coatings involved surface modification of a component by diffusion. Later in the early to mid-1970s, in response to the demand for higher performance, surface-engineered turbine components with modified diffusion coatings and overlay coatings were introduced. Since the late 1980s, thermal barrier coating (TBCs) technologies were applied to reduce underlying metal surface temperature by up to 150°C. The most successful and widely-applied TBC material is 7wt.% yttria partially stabilized zirconia (7PYSZ) by virtue of its low thermal conductivity and good thermal stability at temperatures of up to 1500°C [10]. However, TBCs offer their greatest benefit at higher working temperatures, and under these conditions meanwhile, bond coat oxidation is at its most severe [1, 11, 12].

At high temperatures, coatings form a compact, adherent oxide scale which provides a diffusion barrier to the transport of reactants between the high-temperature gases and the underlying metal, thus greatly reducing further attack by the atmosphere. This thermally grown oxide (TGO) also acts as a bonding layer, connecting the top ceramic coat and bond coat in a TBC system. The onset of coating spallation is mostly triggered by oxide microstructural instabilities, such as microcracks, rumpling and spallation. Maintaining the oxide integrity, therefore, is of key importance in determining coatings lifetime [13]. In most circumstances, an adequate lifetime requires the transportation of diffusing species, both cation and anion, through the oxide to be slow. This requires the oxide to be compact, continuous and highly adherent. α-Al_2O_3 is the greatly preferred oxide due to its highly thermal stability and slow growth rate at temperatures above 1000°C. Although the development and growth of protective α-Al_2O_3 scales on alloys have been widely studied [14, 15, 16, 17,18, 19], further understanding of its growth mechanisms and properties with advancing analytical techniques is always in progress.

As the potential of a higher performance thermal barrier can only be exploited if it remains adhered to the substrate, improving bond coats which are capable of forming a more protective alumina scale continues to be regarded as the highest priority in current and emerging thermal barrier systems [8]. Major challenges in enhancing the bond coat temperature capability are:

(i) to reduce the TGO growth rate and the concomitant buildup in strain energy [7];

(ii) to increase the yield/creep strength and suppress cyclic plasticity effects [20];

(iii) to minimize interdiffusion with the substrate that leads to Al depletion and upward migration of deleterious elements [1].

One way to promote high-temperature oxidation resistance is to incorporate Pt into aluminide coatings to produce so-called Pt-modified aluminide coatings. The addition of Pt to an Al_2O_3-scale forming alloy has been known to improve scale adhesion since the 1970s [21, 22]. Despite numerous studies of Pt-modified aluminides [23, 24, 25], the exact mechanism by which Pt improves the coating performance is still not well understood. It has been proposed that Pt may interact with indigenous sulfur [25, 26], reduce the growth rate of interfacial voids [27, 28] and limit the outward diffusion of minor alloying elements (e.g., Ti, Ta, etc.) from the superalloy [29], all of which would improve scale adhesion. The other well-established way of improving the oxidation resistance of high-temperature alloys and coatings is by additions of so-called reactive elements (e.g., Y, Zr and Hf, etc.) and/or their oxide dispersions [30, 31]. A number of mechanisms [32, 33] have been proposed to explain the reactive element effects. These effects most importantly include: (1) the adhesion between scale and alloy is markedly improved and this increases the alloy's resistance to thermal cycling exposure; and (2) in some but not all cases the actual growth rate of the oxide is reduced [32]. The effects may generally be interpreted on the basis of the following mechanistic model: (i) scale growth mainly takes place through grain boundary diffusion; and (ii) the reactive elements exert their effects through enrichment/segregation at grain boundaries and thereby on the diffusional transport through the scales, grain growth, high temperature creep, etc. of the scales [31].

Considerable past research has focused on understanding and developing metallic coatings based on the ordered intermetallic compound β-NiAl for high-temperature

applications in advanced aerospace structures and propulsion systems [34]. However, there are limitations associated with β coatings owing to surface instabilities (e.g., rumpling) and interdiffusion with the Ni-based superalloy substrate. The latter can lead to unwanted topologically close-packed (TCP) phase formation [35, 36].

Next-generation superalloys containing higher levels of refractory metals are even more susceptible to the formation of TCP phases underneath β-NiAl coatings [37]. Thus, there is an increasing need for alternative coating compositions. Gleeson *et al.* [38] recently reported that the addition of platinum to γ-Ni+γ'-Ni_3Al alloys is highly beneficial to promoting exclusive α-Al_2O_3 scale growth. It was shown by Gleeson *et al.* that the γ+γ' phase constitution could be retained for up to ~35at.% Pt and an Al range of ~12-22at.%. Moreover, oxidation resistance could be substantially improved by Hf addition [39].

The principal goal of this dissertation is to determine the effects of chemical and microstructural factors on the oxidation behavior of γ+γ' alloys and coatings. Both single- and two-phase bulk alloys were examined in order to comprehend the Pt and reactive element effects and, hence, obtaining the composition range possessing the best high-temperature oxidation performance. The results will be used as target compositions for coatings prepared by a pack cementation process. A Pt-modified β-NiAl coating will be studied as a comparison with Pt+Hf-modified γ+γ'-based coatings. The specific aims of this study were as follows:

(1) Determine the chemical and structural factors affecting the development of a compact, adherent and slow-growing α-Al_2O_3 scale on γ+γ'-based bulk alloys modified with Pt and reactive elements. Emphasis will be placed on (a) the establishment of a RE-modified α-Al_2O_3 scale; (b) the scaling kinetics; (c) the optimum level of Pt and reactive elements in growing the protective oxide; and (d) the mechanisms exerted by Pt and reactive elements.

(2) Further develop γ+γ'-based coatings, having better performance than the current β-NiAl coatings. The primary goals here were to: (a) achieve a preferred composition range for the γ+γ'-based coatings; (b) better understand the factors affecting the performance of coatings; and (c) understand the temperature and time dependence of a given γ+γ' composition on cyclic oxidation resistance.

CHAPTER 2 LITERATURE REVIEW

2.1 High Temperature Oxidation of Metals

Most metals have a strong tendency to react with oxygen. The overall driving force of this metal-oxygen reaction is the Gibbs free-energy change associated with the formation of the oxide from the reactants. Thermodynamics consideration allows the prediction of the final equilibrium state for the oxidation process; however, it does not provide any information on the time it takes to reach that final state. Accordingly, a complete understanding of the oxidation process requires both thermodynamics and kinetics analyses. Studies of reaction rates and kinetics provide valuable information about the reaction mechanism and the rate-limiting step of the total reaction.

2.1.1 Thermodynamics of Metal Oxidation

The study of metal oxidation has been a subject of considerable basic and applied research due in large part to its technological importance. In its simplest form, an oxidation reaction is represented by the interaction of metal with oxygen to form an oxide. However, the oxidation behavior and the reaction mechanism of a metal depend upon many variables that can prove to be quite complicated. Therefore, a sound understanding of equilibrium thermodynamics is invaluable for an interpretation of oxidation mechanisms.

The equation for the reaction between gaseous oxygen and a metal M to form a metal oxide may be written as:

$$\frac{2a}{b}M(s)+O_2(g)=\frac{2}{b}M_aO_b(s) \tag{1}$$

The standard Gibbs free-energy change for this formation reaction is given by:

$$\Delta G_f^o=\frac{2}{b}G^o_{M_aO_b(s)}-G^o_{O_2(g)}-\frac{2a}{b}G^o_{M(s)} \tag{2}$$

where $\Delta G_f^o=-RT\ln K$, with K being the temperature-dependant equilibrium constant that is given by the quotient:

$$K=\frac{a^{2/b}_{M_aO_b}}{a^{2a/b}_{M}p_{O_2}} \tag{3}$$

which is in accordance with the stoichiometry of reaction (1). In the above equation, $a_{M_aO_b}$ and a_M are the chemical activities of the oxide and the metal, respectively, and p_{O_2} is the partial pressure of the oxygen gas. As the oxide and the metal are pure, i.e., in their standard states, then by definition $a_{M_aO_b} = a_M = 1$, thus:

$$\Delta G_f^o = -RT \ln \frac{1}{p_{O_2}} \tag{4}$$

Thus, at any fixed temperature, the establishment of reaction equilibrium occurs at a unique p_{O_2} value, which is defined as the equilibrium dissociation pressure of the oxide, $p_{O_2}^{diss}$, i.e.,

$$p_{O_2}^{diss} = \exp(\Delta G_f^o / RT) \tag{5}$$

If the actual p_{O_2} is greater than the $p_{O_2}^{diss}$ at a given temperature, spontaneous oxidation of the metal can occur. When the actual oxygen pressure has been decreased to the dissociation pressure, provided that both metal and metal oxide phases are still present, the oxidation and oxide dissociation occur at equal rates. If the oxygen pressure is less than the dissociation pressure, spontaneous dissociation of the oxide phase will take place [40, 41, 42].

The standard Gibbs free energy change of a reaction can also be expressed in terms of its enthalpy and entropy as:

$$\Delta G_f^o = \Delta H_f^o - T\Delta S_f^o \tag{6}$$

where ΔH_f^o is the temperature-independent standard enthalpy change of the formation reaction and ΔS_f^o is the temperature-independent standard entropy change for that reaction. The enthalpy is a measure of the actual energy that is liberated when the reaction occurs. If it is negative, then the reaction gives off energy (i.e., heat), while if it is positive the reaction absorbs energy. The entropy is a measure of the change in the possibilities for disorder in the products compared to the reactants. There is normally a large negative change in the entropy for the reaction from a disordered state to an ordered state.

The Ellingham diagram [40], as shown in Figure 1, plots the standard Gibbs free energy of the reaction versus temperature for the formation of such compounds as oxides, sulphides, and carbides. The standard Gibbs free energy change of an oxidation reaction is negative for most metals, and so the diagram is drawn such that only negative ΔG_f^o values

are considered. The standard state oxygen partial pressure is taken as one atmosphere and all of the reactions are normalized to consume one mole of O_2 (i.e., similar to reaction (1)). According with Equation (6), the length of the intercept of a given metal/oxide line with the T = 0°C axis gives ΔH_f^o, and $-\Delta S_f^o$ is given by the slope of that line. The majority of the lines slope upwards because both the metal and the oxide are present as condensed phases such that $\Delta S_f^o \approx -\Delta S_{O_2}$. The reactions are therefore reacting from a disordered state to an ordered state, which reduces the entropy. The change in the slope of the lines at certain points indicates a phase change in the metal, which could be melting, boiling or a change in structure.

The position of the line for a given oxidation reaction on the Ellingham diagram is indicative of the stability of the oxide as a function of the temperature. The most stable oxide has the largest negative value of ΔG_f^o and is represented by the lowest line in the diagram. As a counterpart, reactions closer to the top of the diagram are the most noble metals and their oxides are most easily reduced. The nomographic scale on the right-hand side of the diagram labeled as P_{O_2} is used to determine the dissociation partial pressure of oxygen at a given temperature. This is obtained by starting from the point O on the line on the left of the diagram and intersecting the reaction line at a point corresponding to the reaction temperature of interest and extending it to the nomographic scale at the right or bottom edge, which will give the corresponding $p_{O_2}^{diss}$.

In practice, a low partial pressure of oxygen in ambient gases is achieved from a mixture of gases in which oxygen is one of the components. The oxidation potential is controlled by either the pCO/pCO_2 or pH_2/pH_2O ratio and determined by the following respective reactions:

$$2CO(g) + O_2 = 2CO_2(g) \tag{7}$$

$$2H_2(g) + O_2(g) = 2H_2O(g) \tag{8}$$

Metals oxidize by these species as shown by the following reactions:

$$aM(s) + bCO_2(g) = M_aO_b(s) + bCO(g) \tag{9}$$

$$aM(s) + bH_2O(g) = M_aO_b(s) + bH_2(g) \tag{10}$$

To determine the pCO/pCO_2 or pH_2/pH_2O to oxidize a metal at a particular temperature, use the same procedure as for determining the equilibrium pressure of oxygen, except line-up the straightedge with the point C or H on the line on the left of the diagram, and read the ratio from the nomographic scale marked pCO/pCO_2 or pH_2/pH_2O.

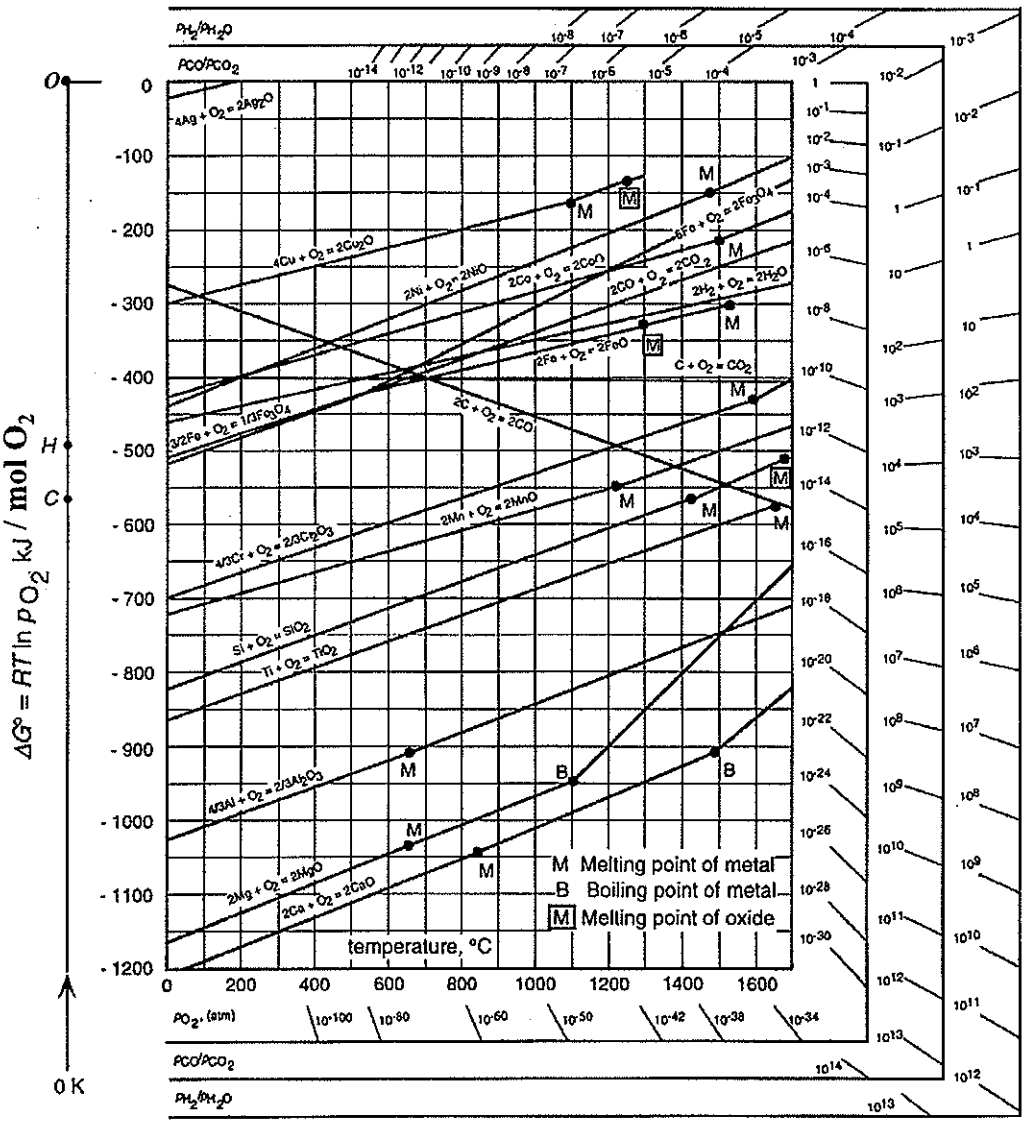

Figure 1. Ellingham diagram showing the standard free energy as a function of temperature for selected oxides [40].

2.1.2 Kinetics of Metal Oxidation

Knowledge of reaction rates is an important basis for elucidation of reaction mechanism. Reaction rates and the corresponding rate equations for the oxidation of a metal depend upon a number of factors, such as temperature, oxygen pressure, elapsed time of reaction, surface preparation and pre-treatment of the metal. Methods of examining the growth of oxidation layers include determinations of the changes in the scale thickness, metal-sample weight, or pressure of the surrounding gas. Most quantitative data are recorded as changes in sample weight per unit surface area. Such data should preferably be obtained in a continuous manner by means of thermogravimetry. The thickness of the surface layer can be obtained from the increase in weight by means of the relation:

$$x = \frac{M_{M_aO_b} \times \Delta m}{b \times M_o \times \rho} \tag{11}$$

where x is the oxide scale thickness; $M_{M_aO_b}$ and ρ are the molecular weight (g/mol) and density (g/cm^3) of the scale, respectively; b is the stoichiometric coefficient of oxygen in M_aO_b; M_o is the atomic weight of oxygen (g/mol); and Δm is the increase in weight per unit surface area (mg/cm^2).

The rate equations that are most commonly encountered may be classified as logarithmic, linear and parabolic. They represent only limiting and ideal cases. Deviations from theses rate equations and intermediate rate equations are also encountered frequently. Combinations of two or more of these relationships in a single oxidation-time curve are also quite common [43].

(a) Logarithmic Rate Laws

When metals are oxidized under certain conditions, typically at low temperatures of up to about 400°C, the initial oxide formation, up to the 1000Å range, is characterized by an initial rapid reaction that quickly reduces to a very low rate. This behavior can often be described by the logarithmic rate equations, which include the direct logarithmic and the inverse logarithmic rate equations:

Direct Logarithmic: $$x = k_{\log} \cdot \log(t + t_0) + A \tag{12}$$

Inverse Logarithmic: $$\frac{1}{x} = B - k_{il} \cdot \log t \tag{13}$$

where x may alternatively represent the amount of oxygen consumed per unit surface, the amount of metal transformed to oxide, or the thickness of the oxide film provided the film is uniform and plane-parallel with the metal surface; t denotes time, k_{log} and k_{il} represent the rate constants, and A and B are constants. A graphical representation of the two rate equations is shown in Figure 2.

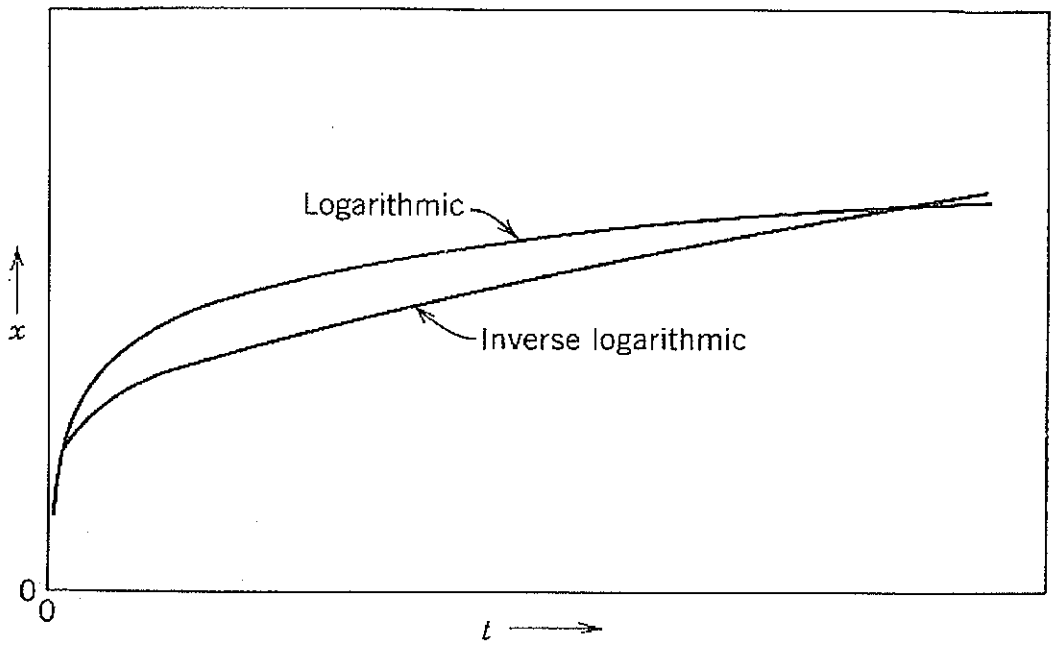

Figure 2. Logarithmic and inverse logarithmic oxidation [43].

(b) Linear Rate Law

There are certain metals where the rate of oxidation remains constant with time and is independent of the amount of gas or metal previously consumed in the reaction. In such cases, the rate of reaction is directly proportional to the time as:

$$x = k_l t + C \tag{14}$$

where k_l is the linear rate constant and C is the integration constant. Linear reactions usually take place by surface or phase-boundary controlled process, which may involve a reaction

limited by the supply of reactant at the surface, a reaction governed by the formation of oxide at the metal/oxide interface, or diffusion through a layer of constant thickness.

(c) Parabolic Rate Law

Under most conditions high temperature oxidation of metals results in the formation of an oxide film or scale on the metal surface. A compact scale acts as a barrier that separates the metal and the oxygen gas. If sufficient oxygen is available at the oxide surface, the rate of oxidation at high temperatures will be limited by solid-state diffusion through the compact scale. As the diffusion distance increases as the oxide grows in thickness, the rate of reaction will decrease with time. The reaction rate is therefore inversely proportional to the scale thickness or the weight of oxide formed, which can be represented as:

$$\frac{dx}{dt} = \frac{k_p'}{x} \tag{15}$$

where k_p' is a proportionality constant. Integration of Equation (15) becomes:

$$x^2 = k_p t + D \tag{16}$$

where k_p denotes the parabolic rate constant in cm^2s^{-1} and is equal to $2k_p'$, D is the integration constant.

After the formation of the initial oxide layer, further scale growth requires transport of metal ions from the substrate, oxygen ions from the gas or some combination of these. If sufficient oxygen is available at the oxide surface, the rate of oxidation at high temperatures will be limited by a solid-state diffusion including lattice, grain boundary, or short-circuit diffusion through the scale. In accordance with a diffusion-controlled process, most oxidation reactions have shown that the temperature dependence of the oxidation rate constant at constant ambient oxygen pressure obeys the empirical Arrhenius equation as:

$$k = k_0 \exp(-Q/RT) \tag{17}$$

where k is the rate constant for the oxidation at temperature T; the pre-exponential factor, k_0, is a constant with dimensions the same as those of k and assumed to be independent of temperature; Q is the activation energy commonly given in J/mole; R is the gas constant and T is the absolute temperature.

Wagner [44] assumed that transport of reactants through an oxide reaction-product layer under conditions for interfacial equilibria proceeded by independent migration of ions

and electrons under the influence of the electrochemical potential gradient. Consequently, metal ions and oxygen ions will tend to migrate across the scale in opposite directions, as seen in Figure 3.

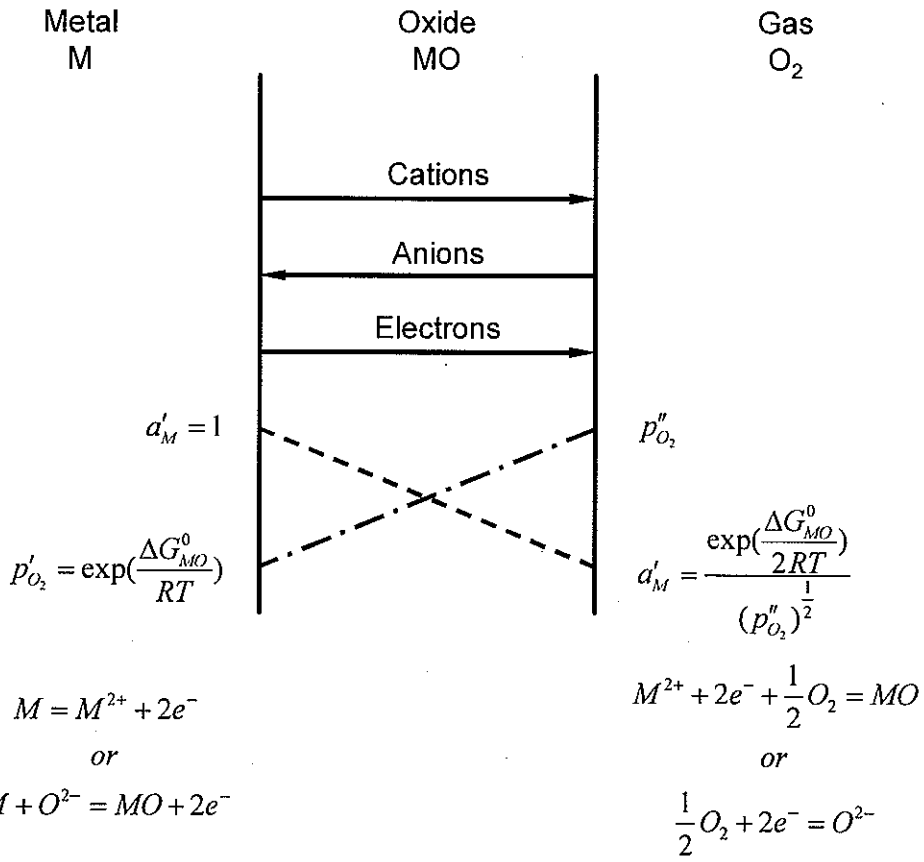

Figure 3. Schematic representation of scale formation according with Wagner's model [41].

The mobility or diffusion coefficients for the cations, anions, and electrons are not equal, and because of this difference a separation of charges takes place in a growing oxide scale. But the resulting space charge also creates an electric field which opposes a further separation of charges, and a stationary state is reached for which no net electric current flows through the scale. Being charged particles, ions will respond to both chemical and electrical potential gradients, which together provide the net driving force for ionic migration. On this basis the number of reacting components passing through $1\,cm^2$ of a plane per second is given by:

$$j_i = c_i u_i = -c_i B_i \left(\frac{d\mu_i}{dx} + z_i e \frac{d\phi}{dx} \right) \tag{18}$$

where $d\mu_i/dx$ is the chemical potential gradient of component i, $d\phi/dx$ is the electric field strength, e is electronic charge, z_i is the valence of the component, c_i is the component concentration. Moving through an ionic lattice under a constant force, an ion rapidly assumes a constant velocity known as the terminal drift velocity as u_i. The value of the terminal drift velocity when the ion is acted on by unit force is known as the mobility, B_i, of the species.

Wagner [45] has also derived an expression relating the parabolic rate constant and the diffusion coefficients of the anions and cations in the oxide M_aX_b forming the ions M^{m+} and X^{r-} as:

$$k_t = \frac{c_X}{bkT} \int_{\mu_X^i}^{\mu_X^o} \left(\frac{m}{r} D_M + D_X \right) d\mu_X \tag{19}$$

or

$$k_t = \frac{c_M}{akT} \int_{\mu_M^i}^{\mu_M^o} \left(\frac{r}{m} D_X + D_M \right) d\mu_M \tag{20}$$

where μ_i^o and μ_i^i represent the chemical potential of the components at the gas/oxide interface and metal/oxide interface, respectively. D_M and D_X represent the diffusion coefficients of components M and X, respectively.

Thus, in order to be able to calculate values of the parabolic rate constant, the relevant diffusion coefficients must be known as a function of the chemical potential of the mobile species. Such data are frequently not available or are incomplete. Furthermore, it is usually easier to measure the parabolic rate constant directly than to carry out experiments to measure the diffusion data. Notwithstanding, the real value of Wagner's analysis lies in providing a complete mechanistic understanding of the high-temperature oxidation process under a set of steady-state conditions.

Deviation from Wagner's theory may be observed in many cases due to the disagreement between reality and the assumptions used in the theory [43, 46]. For instance, an oxide scale is not always compact and adherent in actual cases. Complete stoichiometry and thermodynamic equilibria are seldom established. Grain-boundary and short-circuit

diffusion in growing oxide scales may be expected to be particularly significant at intermediate and low temperatures.

2.1.3 Stress Generation in Oxide Scales

Metals and alloys rely on the establishment of a slow-growing oxide scale for oxidation resistance at high temperatures. However, as the scale thickens, internal or intrinsic stresses develop as a result of the oxidation process and the geometry of the component. In addition, most high temperature processes involve the application of external or extrinsic stresses. These include the stresses induced by temperature changes and the resulting differences in thermal contraction (or expansion) between the scale and metal substrate. The effects of these thermal cycling stresses can be particularly significant since they can develop rapidly and two of the possible mechanisms for relief of oxidation stresses, namely time-dependent creep deformation of the oxide or the metal substrate, become difficult. Hence, detachment of the scale from the metal, fracture, and even spallation may occur. Indeed, such loss of scale by spallation is a major problem for high temperature alloys [47].

2.1.3.1 The Origin of Stresses in Growing Oxide Scales

The first to consider in detail stresses in oxide scales were Pilling and Bedworth [48]. Then simple treatment assumed that only the oxygen ion was mobile in the scale and that consequently the transition of the metal lattice to the cation lattice in the oxide was produced by a homogeneous dilation. If one further assumes that the dilation is isotropic then the sign and magnitude of the stress are related to the so-called Pilling-Bedworth ratio (PBR), which is given by:

$$PBR = \frac{V_{ox}}{V_m} \tag{21}$$

where V_{ox} and V_m correspond to volume per metal ion in the oxide and volume per metal atom in the metal, respectively. Typical PBR values, taken from Kubaschewski and Hopkins [49], are shown in Table 1.

The oxide is expected to be in compression if the PBR is greater than unity, which is the case for most metals, and in tension if the PBR is less than unity. Strictly speaking, the PBR is not applicable to scales that grow primarily by cation diffusion (i.e., $D_m >> D_o$). Thus,

while the volume ratio is a cause of growth stresses in some cases, additional mechanisms must also be operative in many systems [42, 50].

Table 1. Selected oxide-metal volume ratios for some common metals [49].

Metal-Oxide	PBR
Al-Al_2O_3	1.28
Ni-NiO	1.65
Zr-ZrO_2	1.56
Cr-Cr_2O_3	2.07
Si-SiO_2	1.88
Y-Y_2O_3	1.39
Ca-CaO	0.64
Ce-Ce_2O_3	1.16
Ta-Ta_2O_5	2.50
Fe-Fe_2O_3	2.14
Fe-Fe_3O_4	2.10
Fe-FeO	1.68
V-V_2O_5	3.19

Other proposed mechanisms, which will not be discussed in detail here, include: (a) epitaxial stresses; (b) recrystallization stresses; (c) composition changes; (d) point defect stress; (e) oxide growth within the oxide layer and (f) specimen geometry. Direct measurement of growth stresses by high temperature X-ray peak shift measurements indicate that these stresses range from zero for Ni-base alloys to about 1 GPa for FeCrAl alloys [51].

2.1.3.2 Scale Stresses Induced by Temperature Change

The stress generated during cooling or thermal cycling is more severe for a scale-metal system since they are usually rapidly induced and thus, are unlikely to be relieved by time dependent creep processes. Ambient temperature measurements by laser piezo-spectroscopic techniques indicate that thermal expansion misfit between the metal and the scale results in compressions that, on the average, range between 3 and 6 GPa [52]. Indeed, spallation of Cr_2O_3, Al_2O_3, or SiO_2 scales is observed commonly during cooling of high temperature alloys. Such stresses arise because of differential thermal expansion/contraction coefficients between the scale and metal and, on cooling from temperature T_H to temperature T_L are given by the expression:

$$\sigma_{ox} = \frac{-E_{ox}(\alpha_{ox} - \alpha_m)\Delta T}{(1-\nu)(1+\frac{d_{ox}}{d_m}\frac{E_{ox}}{E_m})} \tag{22}$$

where E, α, ν and d are elastic modulus, thermal expansion coefficient, Poisson's ratio and thickness, respectively. Subscripts ox and m correspond to oxide and metal. Assuming $\Delta T = T_L - T_H$, which is negative and α_{ox} is typically less than α_m, the stress in the oxide is typically compressive.

2.2 Fundamental Aspects of Alloy Oxidation

Many of the factors described for the oxidation of pure metals also apply to the oxidation of alloys. However, it must be realized that in practical terms it is far more difficult to develop a comprehensive understanding of the mechanisms involved in alloy oxidation compared to metal oxidation. Such an understanding is important in order to predict reaction rates or to design alloys that are more oxidation resistant. According to Wagner [53], the oxidation of alloys differs from that of pure metals in the following respects:

(a) The metal constituent in alloys will have different affinities for oxygen.

(b) Ternary and higher oxides may be formed.

(c) A degree of solid solubility between the oxides may exist.

(d) The various metal ions will have different mobilities in the oxide phases.

(e) The various metal constituents will have different diffusivities in the alloy.

(f) Dissolution of oxygen into the alloy may result in sub-surface precipitation of oxides of one or more alloying elements (internal oxidation).

2.2.1 Classifications of Alloy Oxidation

When an alloy is oxidized, the oxides of the components may be completely miscible, producing an oxide solid solution, or they may be completely or partially immiscible, producing multiphase scales. In the case of completely or partially immiscible oxides, a simple categorization for a range of alloys AB, in which A is the more noble metal and B the less noble metal, may be made as follows:

1. A relatively narrow composition range near pure A where AO is produced almost exclusively, at least in the external scale.

2. A relatively wide composition range near pure B where BO is produced exclusively.

3. An intermediate composition range where both AO and BO are produced.

In composition ranges 1 and 3, it is often possible to get doping of the major oxides. For example, if AO is produced almost exclusively, small concentrations of B may dissolve in the oxide. If B is of a different valency to A, the AO host may compensate by creating or eliminating ionic defects which, in turn, changes the scale growth rate. Furthermore, in the intermediate composition range, AO and BO may combine to give partial or complete layers of a more complex oxide compound.

This classification has been elaborated by Wood [14] and summarized as follows in Figure 4:

Class I: Only one of the following elements oxidizes under the prevailing conditions, giving BO.

(a) As a minor elements B oxidizes in the following manner:

(1) Internally, giving BO particles in a matrix of A as seen in Figure 4(a), e.g., Ag-Si alloys dilute in silicon producing SiO_2 particles in a silver matrix. The oxygen pressure in the atmosphere is less than the equilibrium dissociation pressure of AO.

(2) Exclusively externally, giving a single layer of BO above an alloy matrix depleted in B as seen in Figure 4(b), e.g., Ag-Si alloys richer in silicon, producing an external SiO_2

layer. The oxygen pressure in the atmosphere is again generally less than the dissociation pressure of AO. A special case of this situation exists, however, where both alloying elements can oxidize but the kinetic and geometrical conditions permit B to be selectively oxidized, e.g., Fe-Cr and Ni-Cr alloys reasonably rich in chromium produce essentially Cr_2O_3 scales, especially when oxidized at low partial pressures of oxygen. In practice, small amounts of iron or nickel do enter the Cr_2O_3 scales, producing solid solutions or doping effects.

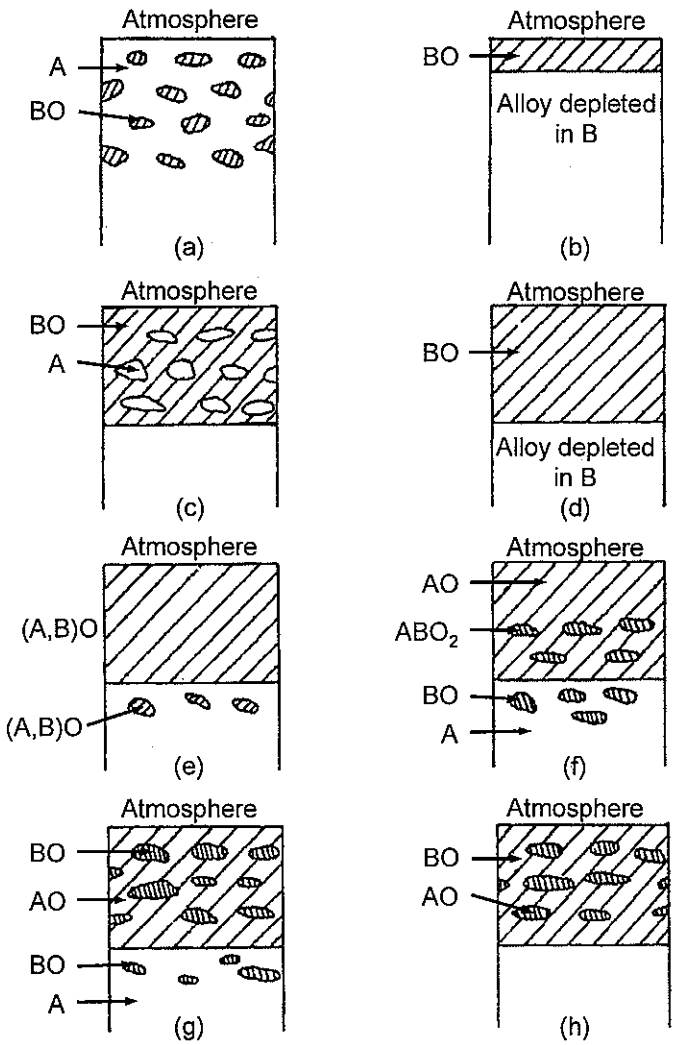

Figure 4. A schematic representation of oxidation modes of alloy AB of variable composition, where B is the less noble metal.

The formation of BO internally or externally depends on the balance between the outward flux of B and the inward flux of oxygen in the alloy. The conditions necessary to sustain the growth of a complete surface layer of less noble metal oxide, BO, have been discussed in detail by Wagner [44]. Assuming the formation of a compact, pore-free oxide, the critical concentration of B in the alloy for sustained parabolic growth of BO scale is given by:

$$N_B = \frac{V}{z_B M_O} \cdot (\pi k_p / D)^{\frac{1}{2}} \tag{23}$$

where V is the molar volume of the alloy; z_B is the valency of B atoms; M_O is the atomic weight of oxygen; D is the diffusion coefficient of B in the alloy; and k_p is the parabolic rate constant for oxidation.

(b) The element B now is the major element and oxidizes exclusively:

(1) Leaving the nonoxidizable metal A dispersed in BO as seen in Figure 4(c), e.g., Cu-Au alloys rich in copper.

(2) Leaving the nonoxidizable metal A in an A-enriched zone beneath the BO scale as seen in Figure 4(d), e.g., Ni-Pt alloys. Fe-Cr alloys richer in chromium than those in Class I(a)(2) come in this category.

Class II: Both alloying elements oxidize simultaneously to give AO and BO, the oxygen pressure in the atmosphere being greater than the equilibrium dissociation pressures of both oxides.

(a) AO and BO react to give a compound:

(1) AO and BO give a single solid solution (A,B)O as seen in Figure 4(e), e.g., Ni-Co alloy. In practice, some internal (A,B)O richer in B than the surface scale is found in the alloy.

(2) A double oxide is formed, often as a spinel, which may give a complete surface layer of variable composition as seen in Figure 4(e), with certain Fe-Cr alloys providing actual examples, or particles incorporated into a matrix of AO if the reaction is incomplete, as seen in Figure 4(f), with certain Ni-Cr alloys providing examples.

(b) AO and BO are virtually insoluble in each other:

(1) The less noble metal B is the minor component. An internal oxide of BO lies beneath a mixed layer of AO and BO, as seen in Figure 4(g), e.g., certain Cu-Ni, Cu-Zn and Cu-Al alloys.

(2) The less noble metal is the major component so that no internal oxidation is observed, as seen in Figure 4(h). In practice, the second phase may not be present in the outer regions of the scale because AO may grow rapidly to produce outer regions exclusively of this oxide. The outer regions may be oxidized to higher oxides, e.g., a CuO layer is found outside Cu_2O on Cu-Si alloys. Conditions may develop so that the internal oxide particles link up to give a complete healing layer of BO at the scale base. This can apply to alloys which begin scaling as in Figure 4(g).

2.2.2 Limiting Cases of Alloy Oxidation

Wagner [53] examined the limiting case in which BO has a lower dissociation pressure than AO, but AO grows faster on pure A than BO grows on pure B. That is, $P_{O_2}^{diss}(BO) < P_{O_2}^{diss}(AO)$, $k_p(BO) < k_p(AO)$. A hypothetical ternary equilibrium diagram for the case considered is shown in Figure 5a.

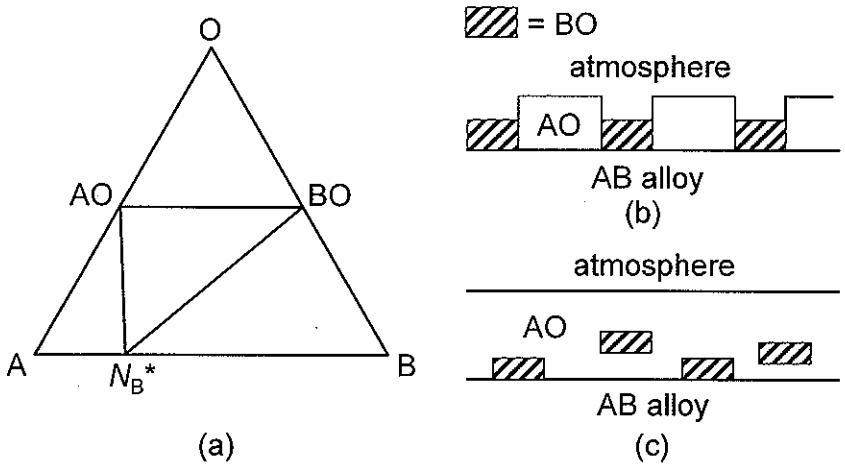

Figure 5. A schematic showing the early stages of simultaneous formation of immiscible oxides AO and BO [54].

Two limiting cases were investigated:

Case 1

If diffusion in the alloy is much faster than in the oxide BO, the stable BO must eventually come to occupy the alloy/oxide interface region unless the B concentration is too low and interdiffusion too fast for BO to become stable at all, for faster initial growth AO can only deplete A in the alloy. It is important to determine whether fast-growing AO predominates initially and whether A is depleted initially in the alloy layer as a consequence. But for long-term protection of the alloy, the central issue is whether or not BO consolidates to form a continuous layer. As seen in Figure 5b, BO and AO may nucleate simultaneously at the early stage of oxidation in alloys containing nearly equal A and B concentrations. With increasing time, BO becomes surrounded by the fast-growing AO as seen in Figure 5c. Further formation of BO particles could be via the chemical displacement reaction:

$$AO + B(alloy) = BO + A(alloy) \tag{24}$$

Case 2

If diffusion is slow in both the alloy and BO, alloy depletion effects are more important than in the preceding case because in some circumstances B can be depleted instead of A.

(a) If the initial bulk alloy concentration N_B^0 is low enough, only AO forms. Although component B is enriched at the interface, if $N_B^0 < N_B$, the interface concentration never reaches the critical value N_B^* corresponding to the ternary phase diagram as shown in Figure 5a.

(b) If $N_B^0 > N_B$, B is subsequently enriched at the interface up to or beyond N_B^*, BO begins to form along with AO, although some overshoot or delay for nucleation of BO would be expected. With AO growing more rapidly than BO particles, any excess B in the interfacial region diffuses back into the alloy at the same time that it is being oxidized. The A to B ratio averaged over the whole oxide thickness is likely to remain less than the bulk ratio in the alloy.

(c) If $N_B^0 \approx N_B^*$, AO and BO should form together yielding little composition change near the alloy interface because local depletion of one element favors nucleation of particles of the other oxide.

(d) If $N_B^0 > N_B^*$, slow-growing BO may cause little depletion of the alloy. But when depletion does occur N_B may reach N_B^* and AO may appear. If BO fails to cover the reaction area it may still restrict the diffusional area for A through the continuous AO layer and decrease the overall rate of growth.

(e) If N_B^0 exceeds some lower limit N_B, BO may form a continuous protective layer, and N_B may not drop to N_B^*. Hence AO may be effectively blocked off. N_B could be relatively low if interdiffusion in the alloy is fast compared with diffusion in BO, as in case 1.

2.3 Al_2O_3-Scale Forming Alloys

There has been much research into the development of protective α-Al_2O_3 scales [16, 18, 55, 56, 57] on Al-containing alloys. The systems investigated range from simple binary alloys to complex commercial alloys, with or without additions of reactive elements. One of the most crucial factors in the oxidation of alumina-formers is the temperature, which must be high enough to promote the formation of α-Al_2O_3 in preference to the less protective transition aluminas. Another critical factor is the aluminum content, which must be sufficiently high to develop and maintain an alumina layer and prevent subsequent breakaway oxidation [58].

Pettit [59] interpreted the oxidation behavior of nickel-aluminum alloys over the temperature range 900-1300°C in terms of the three regions identified in Figure 6. Group I corresponds to internal oxidation of the aluminum, with external formation of NiO doped with aluminum. Group II consists of alloys which contain enough aluminum to form an external α-Al_2O_3 layer, but this depletes the surface to the point at which, if the scale fractures, NiO and $NiAl_2O_4$ may be formed. A protective Al_2O_3 layer may reform in time, but layered scale develops as these processes repeat. With still a higher aluminum content, however, the Al_2O_3 layer is maintained and this is group III.

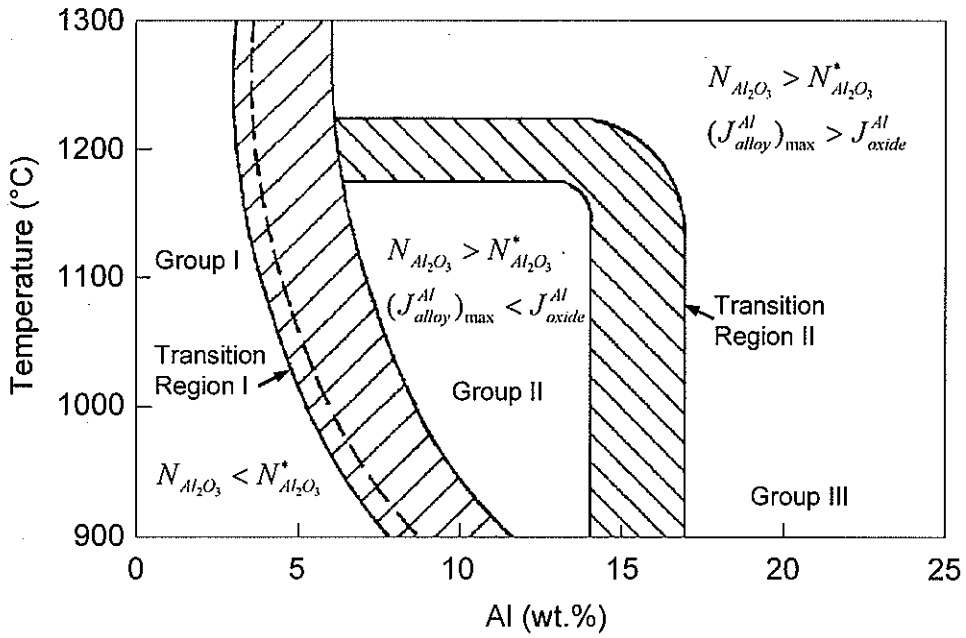

Figure 6. Dependence of the mechanism of oxidation for Ni-Al alloys on temperature and alloy composition according to Pettit [59].

2.3.1 β-NiAl

Nickel aluminides with Al levels of 40 to 50 at.% as β-NiAl have received considerable attention due to their combination of desirable properties, such as high melting temperature and good thermal conductivity [60, 61]. One of the attractive characteristics of NiAl is its excellent oxidation resistance due to the formation of a protective Al_2O_3 scale. The adherence of aluminum oxide scales on coating alloys can be improved by the addition of platinum. However, the role of Pt in improving the scaling behavior of alumina-forming coatings remains unclear. A number of Pt-related mechanisms have been proposed as: mechanical keying of the scale [55], rapid self-healing of Al_2O_3 [62], modification of aluminide Al content [63], inhibition of refractory element diffusion [64],and suppression of void formation along the oxide-metal interface [24].

However, owing to its inferior high-temperature creep strength compared to most Ni-based γ+γ' superalloys, the utilization of β-NiAl is compromised by the occurrence of progressive rumpling accompanied with the martensitic transformation and eventual β-to-γ'

transformation [65]. Therefore, pursuing an alternative high-temperature coating material with better oxidation resistance and phase compatibility with superalloy substrates is highly necessary [10].

2.3.2 Pt-Modified γ-Ni + γ'-Ni_3Al

γ′ precipitation-hardened Ni-base superalloys, which have superior mechanical properties at elevated temperatures, have been used as gas turbine blades and vanes for power plants and aeroengines for many years. It is remarkable that these alloys can be utilized to $0.85T_M$ (absolute melting point) and for times of up to 100,000 hours at somewhat lower temperatures. A majority of these alloys have microstructures consisting of an austenitic face-centered cubic (FCC) γ-Ni matrix that is strengthened by precipitates of the γ′-Ni_3Al with $L1_2$ structure. The γ phase consists of a great amount of solid-solution-strengthening elements, such as Mo, Cr, and Re. This phase possesses good inherent ductility and is amenable to alloying without phase instability, but to a limit. The $L1_2$ intermetallic structure of the γ′ precipitate phase can be considered as ordered FCC with Al atoms at the corner positions and Ni atoms at the face centers, as shown schematically in Figure 7. The γ′ forms coherently or semi-coherently within the austenitic γ matrix owing to a low lattice constant mismatch of less than 1% [5]. The γ′ phase is often highly alloyed with Co, Pt, and Cu substituting for the nickel positions, and Nb, Ta, V, and Mo substituting for the Al positions. All of these elements provide some degree of solid-solution strengthening to the γ′.

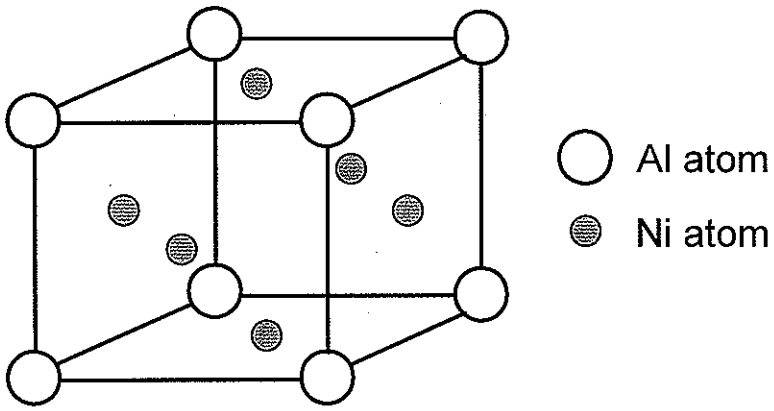

Figure 7. A schematic showing the $L1_2$ crystal structure of γ'-Ni_3Al.

A recent examination of the γ/γ′ Ni-Pt-Al system by Gleeson *et al.* [38] showed that compositions with only 22at.% Al are excellent alumina formers and, hence, have good oxidation resistance. This study by Glesson *et al.* corrected heretofore the only Ni-Pt-Al phase diagram available in the open literature, which was a speculated isothermal section at 1060°C published by Jackson and Raiden [64]. This latter study was based on experimental work on aluminized platinum coatings deposited onto the industrial Ni-superalloy IN-738. So that work was not specific to the ternary Ni-Al-Pt system.

Dedicated phase equilibria determinations conducted by Gleeson et at. [38] showed that there are significant differences between the experimentally determined Ni-Pt-Al phase diagram at 1100°C/1150°C and the phase equilibria speculated at 1060°C. As seen in Figure 8, a phase equilibria in ternary space associated with α-NiPt was found with an $L1_0$ ordered face centered tetragonal (FCT) crystal structure. The α phase was reported to be stable up to 1250°C [38]. On cooling a martensitic transformation from β-NiAl also gives an $L1_0$ type structure. The current diagram also shows a very high Pt solubility in γ′ (~35at.%) and β (~35at.%).

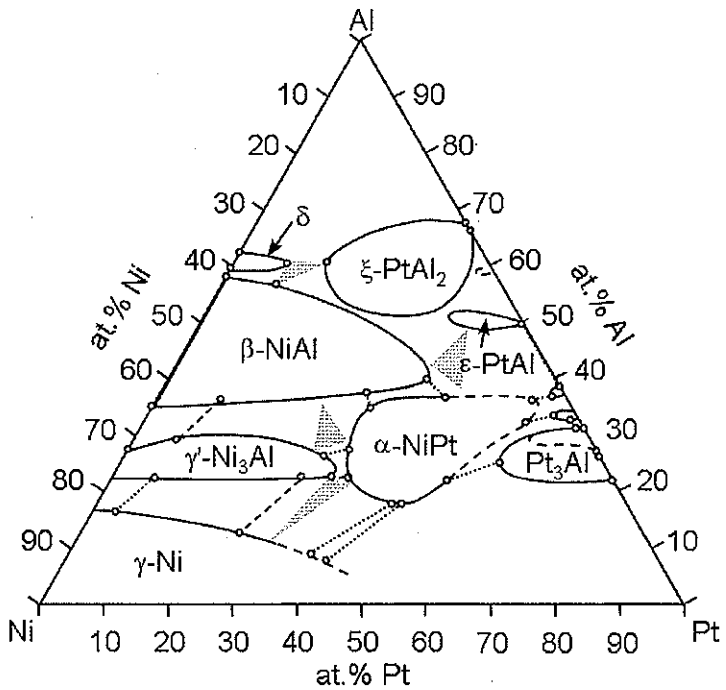

Figure 8. Isothermal phase equilibria on Ni-Pt-Al alloys at 1150°C [38].

2.4 Effect of Reactive Element Additions on High Temperature Oxidation Resistance

The so-called reactive element (RE) effect was first patented in 1937 by Pfeil [30]. Since then, a vast amount of research has been conducted on this phenomenon. In 1980, a literature review by Whittle and Stringer [32] summarized a wide range of experimental results and proposed hypotheses regarding the reactive element effect that has been widely studied and cited for the past years.

Experimentally, Pfeil [30] discovered that the heat-resisting properties, and particularly the resistance to oxidation of alloys consisting of 80wt.% Ni and 20wt.% Cr are significantly improved by the inclusion of small quantities of calcium, cerium, or calcium+thorium. In 1945, a subsequent patent from Pfeil [66] indicated that surface coatings of reactive elements, of oxides or hydroxides, or of other salts that would decompose to oxides at high temperature could provide an alternative to alloy additions in improving the lifetimes to failure in cyclic heating and cooling tests. According to Pfeil [66] the beneficial effect was observed for different levels of doping with chemical elements belonging to the groups II, III, IV and V of the Periodic Table, whereby the efficiency decreases from group II to V but increases with the atomic weight in a given group.

An example showing the beneficial RE effect of Hf additions in reducing the oxide growth kinetics was illustrated, as seen in Figure 9. It is clearly seen that 0.8at.% Hf effectively reduced the oxidation kinetics of the Pt-modified γ-Ni+γ'-Ni_3Al alloy. The weight change of the Hf-modified Ni22Al30Pt (0.37mg/cm^2) after 500 thermal cycles between 1150°C and ~80°C was about three times lower than that of the Hf-free Ni22Al30Pt alloy (1.45mg/cm^2). Moreover, the oxide formed on both alloys was quite protective with no indication of the scale spallation.

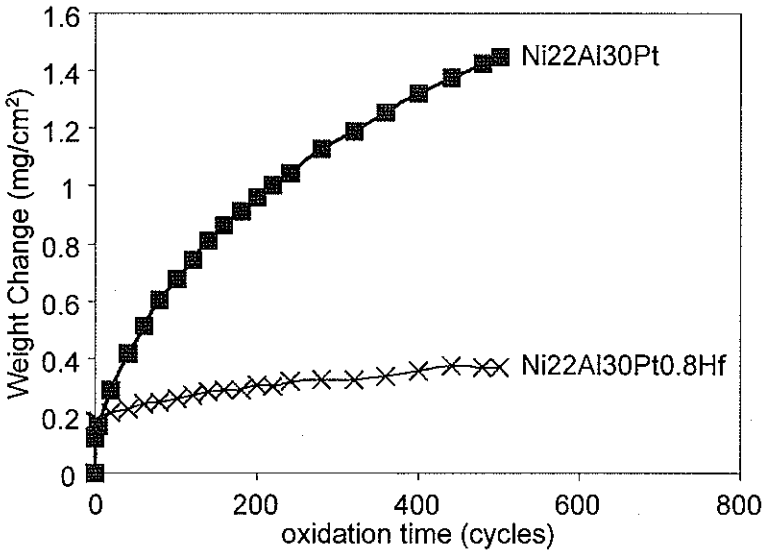

Figure 9. The weight change of Ni22Al30Pt and Ni22Al30Pt0.8Hf (in at.%) alloys at 1150°C after 500 cycles.

2.4.1 Basic Properties of Reactive Elements

All reactive elements that are known to improve the high-temperature oxidation resistance of alloys have a similar electronic structure for their cations when associated to oxygen in their main oxides. After ionization, the surrounding electrons of the reactive element's nuclei possess a similar configuration with eight electrons in their outer shell, like the corresponding noble gas of the preceding period as shown below:

Y : $1s^2\ 2s^2\ 2p^6\ 3s^2\ 3p^6\ 3d^{10}\ 4s^2\ 4p^6\ 4d^1\ 5s^2$

Y^{3+} (Y_2O_3) : $1s^2\ 2s^2\ 2p^6\ 3s^2\ 3p^6\ 3d^{10}\ 4s^2\ 4p^6$

Zr : $1s^2\ 2s^2\ 2p^6\ 3s^2\ 3p^6\ 3d^{10}\ 4s^2\ 4p^6\ 4d^2\ 5s^2$

Zr^{4+} (ZrO_2) : $1s^2\ 2s^2\ 2p^6\ 3s^2\ 3p^6\ 3d^{10}\ 4s^2\ 4p^6$

Kr : $1s^2\ 2s^2\ 2p^6\ 3s^2\ 3p^6\ 3d^{10}\ 4s^2\ 4p^6$

Ce : $1s^2\ 2s^2\ 2p^6\ 3s^2\ 3p^6\ 3d^{10}\ 4s^2\ 4p^6\ 4d^{10}\ 4f^1\ 5s^2\ 5p^6\ 5d^1\ 6s^2$

Ce^{3+} (Ce_2O_3) : $1s^2\ 2s^2\ 2p^6\ 3s^2\ 3p^6\ 3d^{10}\ 4s^2\ 4p^6\ 4d^{10}\ 4f^1\ 5s^2\ 5p^6$

Hf : $1s^2\ 2s^2\ 2p^6\ 3s^2\ 3p^6\ 3d^{10}\ 4s^2\ 4p^6\ 4d^{10}\ 4f^{14}\ 5s^2\ 5p^6\ 5d^2\ 6s^2$

Hf^{4+} (HfO_2) : $1s^2\ 2s^2\ 2p^6\ 3s^2\ 3p^6\ 3d^{10}\ 4s^2\ 4p^6\ 4d^{10}\ 4f^{14}\ 5s^2\ 5p^6$

Xe : $1s^2\ 2s^2\ 2p^6\ 3s^2\ 3p^6\ 3d^{10}\ 4s^2\ 4p^6\ 4d^{10}\ 5s^2\ 5p^6$

From a thermodynamic point of view, as seen in Table 2, the main oxides of reactive elements have both a high melting temperature (T_m > 2000°C) and a high formation enthalpy ($-\Delta H_{298K}$ > 1000kJ/mol) which implies that these oxides are very stable. Moreover, the reactive elements do tend to form very stable sulfides.

As high-temperature oxidation resistance is always due to the presence of a protective oxide film, a knowledge of the stability and thermodynamic properties of oxides serves as a basis for any assessment of potential metal materials used at high temperatures. Figure 10 shows the stability relationships of the oxides of Group I to V metals. In this figure, the solid lines represent constant free energy of formation per oxygen atom and the darkest area corresponds to the region of maximum stability.

Table 2. Basic properties of some major alloying and reactive elements and their compounds [67, 68].

	T_m (°C)	-ΔH (kJ/mol)	P.B. ratio	R_{ion} (Å)
Al	660	0		
Al_2O_3	2050	1675.7	1.28	0.50
Al_2S_3	208			
Hf	2227	0		
HfO_2	2758	1112	1.62	0.78
Ce	799	0		
CeO_2	2600	1088	1.17	0.90
Ce_2O_3	1687	1254	1.15	1.20
Ce_2O_2S		1003		
Y	1522	0		
Y_2O_3	2410	1267	1.13	0.89
YS		836		
Y_2S_3		836		
Y_2O_2S		1526		1.06
Zr	1852	0		
ZrO_2	2700	1087	1.57	0.80
ZrS_2		577		
Zr_2S_3		669		

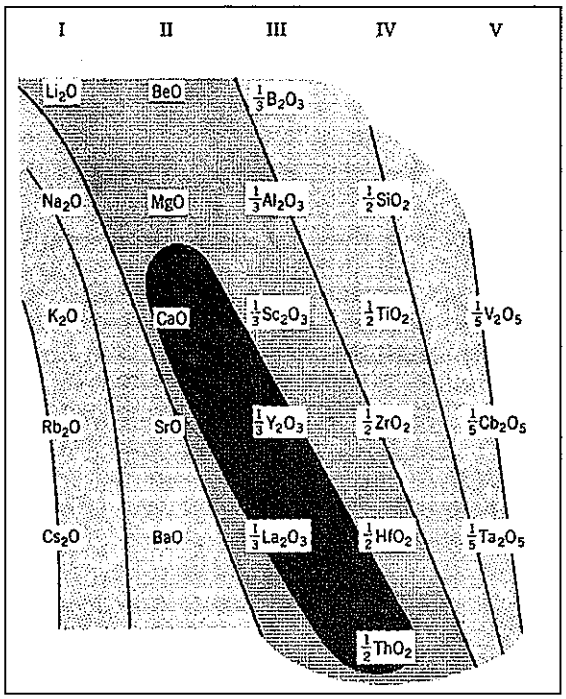

Figure 10. Stability relationships of oxides arranged in periodic table [69].

2.4.2 Reactive Element Doping Methods

In practice, RE additions can be incorporated into the bulk alloy in elemental form or as an oxide dispersoid component [32]. Alternatively, surface enrichment of RE may be done by such processes as ion implantation, pack cementation, sol-gel dipping, and hot dipping.

Scientifically, the surface modification route is attractive because it is well-suited to fundamental investigations due to the flexibility in testing a wide range of elements at various concentrations. In practical engineering studies, surface modification offers commercial advantages of low cost in terms of RE quantities and processing equipments, and of relative ease of applications, especially for components of complex geometry or large size. In addition, it avoids problems associated with adding metallic or oxide dispersoid induced mechanical properties or processing difficulties [33, 70] However, it is often difficult to achieve the low RE levels that are needed by this method, which affects production yield.

2.4.3 Reactive Element Effects and Mechanisms

Extensive research and a large number of papers have concentrated on the RE effects since the first patent by Pfeil in 1937 [30]. Numerous mechanisms have been proposed to explain the RE effects, in part aided by the continual development of examination techniques. In general, these advances in instrumentation and analytical techniques have led to better understanding of RE effects on growth mechanisms and reaction rates, and to examining the scale microstructure and the RE location(s) within the scale and substrate.

Important advancements range from better analytical techniques for measuring reaction kinetics, to field emission gun scanning transmission electron microscopes (FEG-STEM), which produce high-quality images of scales at higher magnifications, to high resolution electron microscopes (HREM), which have allowed for the detection and observation to the atomic level of RE ions segregated at scale grain boundaries and the scale-substrate interfaces. Advances also include secondary ion mass spectrometry (SIMS) for detecting ^{18}O tracers, scanning Auger microscopy (SAM) for detecting impurity segregants, and atomic forces microscopy (AFM) for quantifying microstructural features. A latest exploited characterization technique is the focused ion beam (FIB) instrument, which has been used for the preparation of site-specific TEM samples for characterization [71].

Based on the extensive research and progress made in understanding the mechanisms of the RE effects over the past 60 years, there now seems to be the view that a single theory for all the manifestations of the RE effect in the various alloys is unlikely [72]. A standard list of the most frequently mentioned RE effects would be classified as follows, some of which are clearly interrelated [32, 33, 67, 70, 73]:

(1) RE oxides act as heterogeneous nucleation sites to promote the selective oxidation of the protective scale-forming elements such as aluminum or chromium and consequently reduce their content necessary to form the continuous protective scale than addition-free alloys. Therefore, the transient oxidation stage is curtailed and less base-metal oxidation occurs.

(2) RE additions modify the scale-growth mechanism, due to their larger ion sizes, by physically blocking the grain boundaries which are generally accepted to be the short-

circuit pathways for both anionic and cationic diffusing species. Thus a significant reduction in parabolic scaling rates results.

(3) RE additions modify the morphology and microstructure of the scale. Generally, the oxide grains are small and zones of both equiaxed and columnar grains are often observed.

(4) RE additions influence the scale plasticity by a smaller gain size which could reduce spallation by assisting relaxation of growth stress. Reductions in scale growth rate result in thinner scales, which generate lower thermal mismatch stresses on cooling.

(5) RE additions act by creating a mechanical keying effect. The oxides of reactive elements formed by internal oxidation promote the growth of oxide pegs or stringers, leading to the enhanced adherence.

(6) RE additions, their oxide particles or RE oxides may act as vacancy sinks, minimizing the development of voids and porosity at the scale-alloy interface due to the Kirkendall effect hereby enhancing the scale adherence.

(7) RE additions appear to prevent the segregation of indigenous impurities, such as sulphur, phosphorus and chlorine, at the scale-alloy interface.

Among all of the proposed mechanisms mentioned above, number 7 is the most generally accepted. Sulfur is an example of the impurity element (at very low bulk concentrations) that segregates to the scale/alloy interface and damages the adhesion of the alumina scale. Schaeffer et al. [74] examined the cyclic oxidation behavior of René N5 superalloy at 1149°C in air with different treatments to enhance the scale/alloy adhesion. They found that the yttrium addition improved the scale/alloy adhesion when it was added to Y-free René N5, as shown in Figure 11. It could be attributed to the RE effect that Y tied up the S as stable RE sulfides, which has high stability. Therefore, little "free" sulfur remains to segregate to the scale/alloy interface. Moreover, they also observed that the desulfurization by H_2 annealing on Y-free René N5 was the most effective with respect to the scale adhesion. One of the methods used to reduce bulk S levels is the high-temperature anneal in hydrogen. The H_2 reacts with S, which segregates to the gas/metal interface and forms a hydrogen-sulfide species (e.g., H_2S) that is removed from the system.

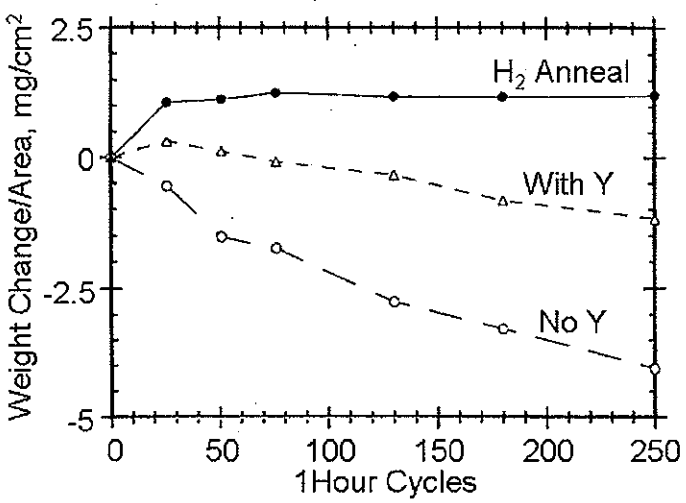

Figure 11. Cyclic oxidation results for the René N5 superalloy with different treatments at 1149°C in air [74].

2.5 Protective Coatings for Turbine Blades

After a costly process which required the development of numerous generations of new superalloys for the past 40 years, aerospace gas turbine engines are now designed such that the nickel superalloy components operate at temperatures very close to their melting point. Required by the increasing firing temperatures and severe environments encountered in gas turbines, however, the need for coatings to protect structural materials has become increasingly important. The most current strategies for performance improvements are centered on state-of-the-art thermal barrier coatings (TBCs), which typically comprise a thermally grown oxide (TGO), that forms between a (partially) Y_2O_3-stabilized ZrO_2 (YSZ) ceramic top layer and a metallic bond coat.

The current study focuses on high-temperature oxidation resistant coatings. As indicated above, the primary roles of coatings are (1) to enable high-temperature structural components to operate at even higher temperatures, (2) to improve component durability and (3) to allow use of a broader variety of fuels. There are essentially two types of high temperature coatings. One is a diffusion coating in which the deposited mass is diffused

and/or reacted with the substrate to form a continuous gradation in composition. The other type is an overlay coating in which material is directly deposited onto the substrate surface.

2.5.1 Phase Composition and Structure of Diffusion Coatings

Pack cementation is a very common chemical vapor deposition (CVD) process to produce the diffusion nickel-aluminide coating, which is one of the most-widely used high-temperature metallic coating systems. While the details of the coating deposition processes used by commercial vendors are usually held proprietary, two general types of aluminide pack cementation coatings are applied. The "high activity" pack coatings are applied at low temperatures and grow primarily inward, while the "low activity" pack coatings are applied at higher temperatures and grow outward [2, 75, 76].

Figure 12 shows a secondary electron micrograph of an as-deposited β-NiAl coating on the substrate superalloy CMSX-4. The coating in the surface layer consists primarily of the Al-rich β-phase, which has an ordered B2 (BCC) crystal structure. Since most superalloys contain many refractory elements, such as W, Ta, Re, Mo and Cr, these elements usually precipitate out as carbides, metals and topological close packed (TCP) phases due to their low solubility in the β-NiAl phase formed in the interdiffusion zone.

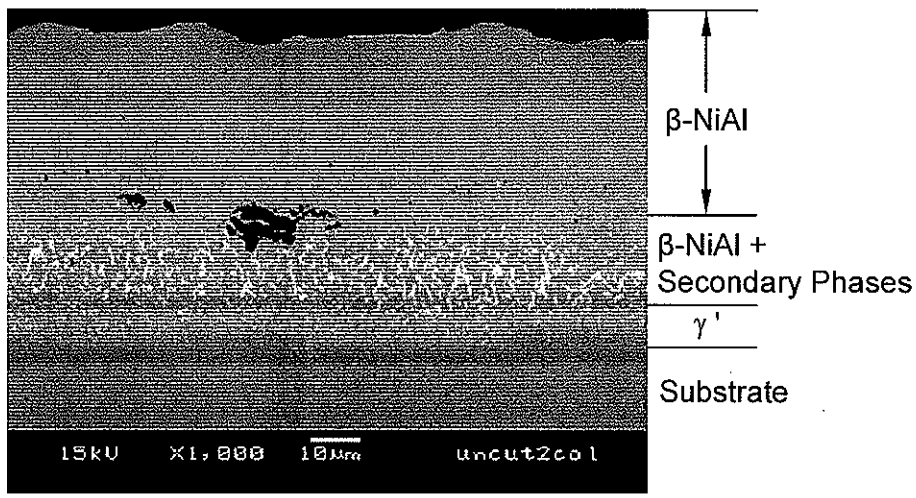

Figure 12. Cross section of an as-deposited nickel aluminide coatings on CMSX-4.

2.5.2 High Temperature Degradation of Coatings

At high temperatures, coatings that protect against oxidation form a compact and adherent Al_2O_3 oxide scale that provides a barrier between the high temperature gases and the underlying material. However, formation of this protective oxide scale by the selective oxidation of Al results in loss of aluminum from the coating. Moreover, there is significant decrease in the Al content of the coating from coating/substrate interdiffusion.

The time- and temperature-dependent decrease in the Al content of the coating has a number of important consequences. One is that the β phase will undergo a martensitic transformation on cooling if the Al content dropped to approximately 38at.%. The martensitic transformation that occurs on cooling shrinks the volume of the coating and enhances the strain at the oxide coating interface to disturb the oxide adherence [77].

Another consequence is that loss of Al eventually results in formation of γ′-Ni_3Al. It has been shown that a protective Al_2O_3 scale cannot be sustained over an unmodified γ′ phase during thermal cycling, and instead a less-protective $NiAl_2O_4$ spinel forms and grows. The rapid growth of this spinel phase results in the consumption of both Al and Ni producing a higher rate of surface recession and consequent loss of the load carrying capabilities [78].

Figure 13 shows that the surface of a Pt-modified β-NiAl coating undergoes extensive rumpling after 1000 thermal cycles between 1150°C and ~80°C. EDS analysis of the coating composition showed that the β had completely transformed into γ-Ni. When applied onto such metallic coating surface, it is inevitable that the relative rigid ceramic top layer in a TBC system will be subjected to spallation induced failure.

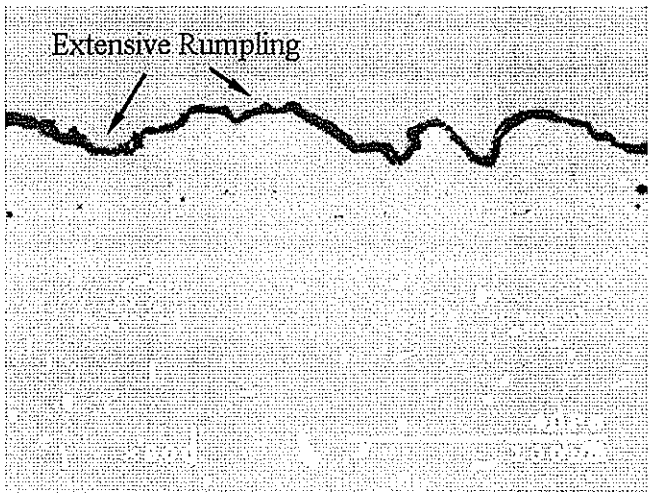

Figure 13. Cross-sectional SEM image showing the surface rumpling of Pt-modified β-NiAl coating after 1000 cycles at 1150°C.

2.6 Purpose of Current Study

A common method for improving the oxidation resistance of aluminide coatings is to incorporate Pt, the beneficial effects of which have been a topic of study for at least 30 years [22, 79]. However, there is no widely agreed upon mechanism for the beneficial role of Pt. One possible mechanism is that the presence of Pt has a catalytic effect on the reaction between O and Al and in this way promotes the nucleation of α-Al_2O_3, possibly by increasing the dissociation rate of O_2, thus decreasing the time for a continuous α-Al_2O_3 scale to form without taking part in the reaction itself [80, 81]. Other studies suggest that the diffusion of aluminum is enhanced by the presence of the platinum due to a consequential increase in the Al activity [22, 82]. However, very recent work on the effects of Pt on the Ni-Al system showed the opposite effect, with Pt decreasing both the oxygen solubility in γ-γ' alloys and the chemical activity of Al [38].

In the case of less-stable third generation superalloys and higher, interdiffusion with a β-containing coating leads to the formation of TCP phases within a secondary reaction zone (SRZ) that forms in the alloy, as shown in Figure 14. Excessive quantities of TCP formation decreases the mechanical properties of the superalloy [83]. The inferior performance of traditional Pt-modified β-NiAl coatings on higher-generation superalloys, which have higher

amount of refractory elements for strengthening purposes, is a major incentive for developing the substitute coatings with improved high-temperature performance. γ-γ′-based coatings provide an attractive alternative to β-containing coatings, since the former are very compatible with the superalloy substrate in terms of phase constitution and, hence, minimizing coating/substrate interdiffusion.

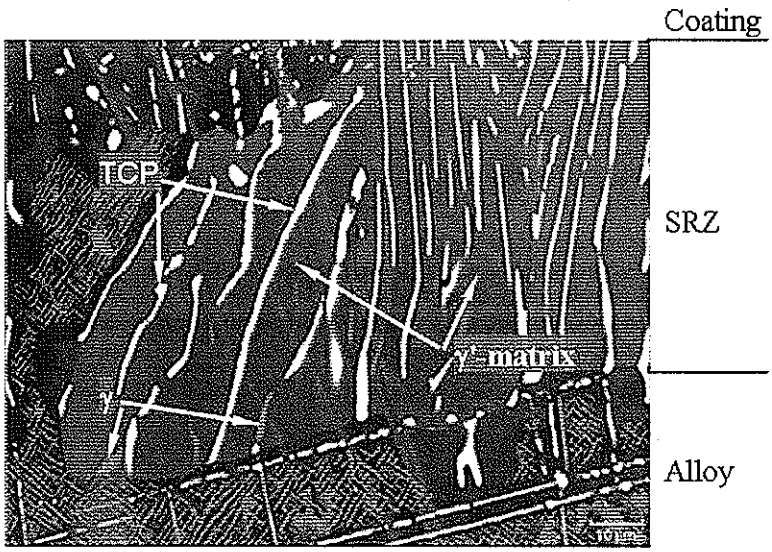

Figure 14. SEM image showing the formation of secondary reaction zone.

CHAPTER 3 EXPERIMENTAL PROCEDURES

High-temperature isothermal and cyclic oxidation tests of selected alloys and coatings were conducted at 1150°C in air. Thermal gravimetric analyses (TGA) were performed at 1150°C in ambient air to investigate the mass-gain kinetics. Single-phase γ-Ni and γ'-Ni_3Al alloys modified with Pt and/or Hf were examined to manifest their alloying effects independently and synergistically. Pt+Hf-modified two-phase alloys were studied to elucidate the reactive element effects on the growth of alumina scale affected by hafnium contents quantitatively. Bare superalloy with/without stand-alone Pt- and Pt+Hf-modified γ+γ'-based coatings were inspected to appraise their high-temperature performance comparing with traditional Pt-modified β-NiAl coatings. All samples were weighed using an analytical balance with 0.01mg resolution both before and after oxidation testing. The sample dimensions (diameter and thickness) were measured by using a caliper with ±0.1mm accuracy and the surface area was then calculated. The weight change Δm, with the typical units of mg/cm^2, was calculated for each sample tested as:

$$\Delta m = \frac{w_f - w_0}{A_0} \tag{25}$$

where w_f and w_0 are the measured weight after and before oxidation, respectively, and A_0 is the original sample surface area.

3.1 Sample Preparation

Alloy samples were prepared by the Materials Preparation Center (MPC) at the U.S. Department of Energy's (DOE) Ames Laboratory. The specific alloy compositions studied will be detailed in the following Results section in the order that they were examined and analyzed. All alloys were Ar-arc melted followed by drop casting into a chilled rod mold having an internal diameter of 10mm. As-cast alloys were homogenized at 1200°C for 6 hours in flowing argon followed by a non-oxidizing stabilization treatment at 1150°C for 2 days under flowing argon gas. Disk-shaped test samples ~1mm thick were cut from the heat-treated rods, ground to a 1200-grit surface finish using SiC abrasives, ultrasonically cleaned in acetone to remove grease, and then rinsed in alcohol and dried prior to oxidation testing.

To examine the phase composition presented in the two-phase alloys at 1150°C, all samples were heated to 1150°C for 1 hour followed with water quenching to withhold the high-temperature phases, then cross-sectioned and etched with chromic acid to enhance the phase contrast for SEM examination.

Pt- and Pt+Hf-modified γ-Ni + γ′-Ni_3Al coatings with compositions close to Ni-20Al-20Pt were deposited onto Ni-based superalloys by Pt electroplating followed by — in the case of the Pt+Hf-modified coatings — a proprietary pack cementation process [64, 84, 85]. Commercial bare superalloys and Pt-modified β-NiAl coatings obtained from commercial vendors were also tested in order to provide a baseline for comparison. All weight and dimension measurements of the coating samples were made in the same way as those for alloy samples.

3.2 High-Temperature Oxidation Tests

3.2.1 Early-Stage Oxidation

Early-stage oxidation testing was performed on certain single-phase γ-Ni and γ'-Ni_3Al alloys since the characteristics of the early-stage oxides have an important impact on their later steady-stage growth. Oxidation testing was performed using an open vertical furnace equipped with a timer-controlled sample elevation system, as shown schematically in Figure 15. For a given test, the sample was initially placed into a ceramic tube holder hooked at the end of a quartz rod, then lifted into the furnace hot zone which was kept constant at 1150°C. After completion of a preset oxidation time, the sample was automatically lowered out of the furnace to the initial position where it air-cooled.

Oxidation times were chosen as 90, 180 and 1800 seconds, with initiation being when the sample entered the furnace hot zone. To measure the corresponding sample temperature at each time, an R-type thermocouple was placed near the sample surface and the heating curve was recorded, as shown in Figure 16. It is seen that it took nearly 300 seconds for the sample to reach 1150°C. The sample surface temperature was 970, 1110 and 1150°C at the times of 90, 180 and 1800 seconds, respectively.

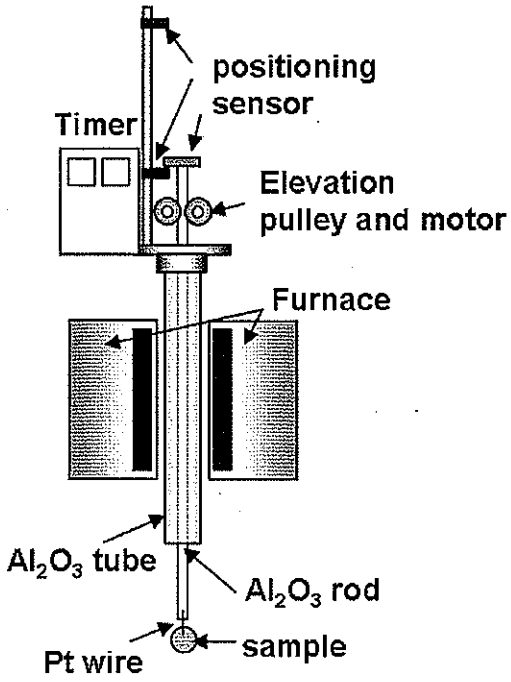

Figure 15. Schematic showing the automated furnace used for the early-stage oxidation tests.

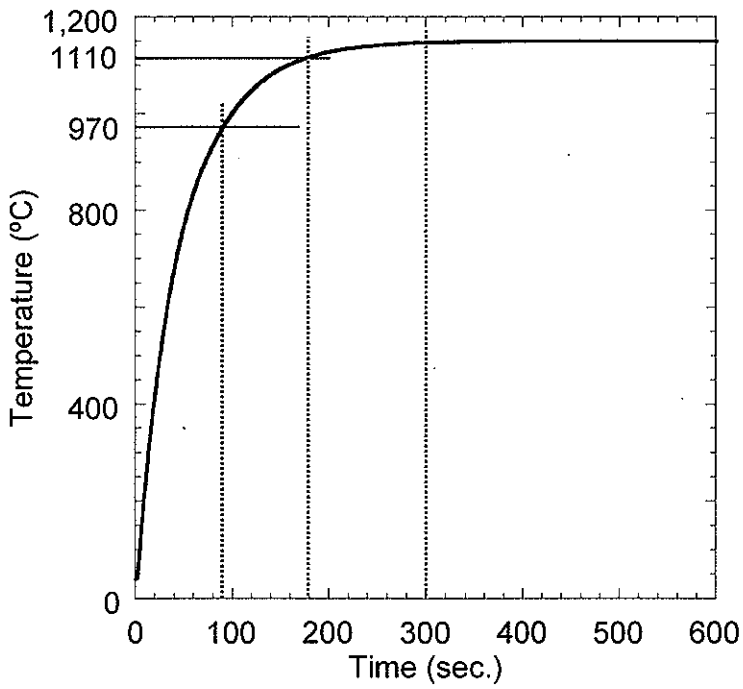

Figure 16. A representative measured heating profile of the test sample.

3.2.2 4-Day Isothermal Oxidation

To evaluate longer-term isothermal oxidation behavior, four-day exposures were conducted at 1150°C within a horizontal tube furnace in still lab air. Test samples were placed in an alumina tray in a manner that allowed both sides to be exposed to the high-temperature atmosphere. The tray was then slid into the preheated hot-zone of the furnace and oxidized for 4 days. The samples were air-cooled at the completion of testing.

3.2.3 Cyclic Oxidation

To assess the long-term performance of alloys and coatings under thermal cycling conditions, cyclic oxidation testing of samples was conducted at 1150°C in ambient air within a vertical furnace having timer-controlled sample-extraction system as described in Chapter 3.2.1. Each cycle consisted of one hour at 1150°C followed by 30 minutes at ~75°C. Heating and cooling rates were approximately 200°C/minute. Weight-change measurements were made intermittently. No effort was made to retain any spalled scale. As a consequence, weight losses were sometimes recorded. This testing scheme is being employed by most engine companies as a standard procedure.

3.2.4 Thermal Gravimetric Analysis

Standard thermal gravimetric analyses (TGA) of alloy samples were performed at 1150°C to examine the mass-gain kinetics during high temperature exposure. To have heating rates similar to what were obtained with the previously-described oxidation tests, all TGA tests commenced by quickly immersing the sample into the furnace which was preheated to 1150°C. After a 100-hour exposure in air at a flow rate of 70cm^3/minute, all samples were then furnace-cooled to room temperature. Experimental details are reported in Chapter 4.2.

3.3 Characterization

Surface products of the oxidized samples were studied using Cu-K_α X-ray diffraction to identify the oxide structures formed, then carbon coated and inspected using a Hitachi S-2460N secondary electron microscope (SEM) equipped with the energy dispersive spectrometer (EDS) to assess the oxide surface morphology. To measure the oxide thickness

and survey the scale/metal interface and subsurface, cross sections of the oxidized samples were prepared by standard metallographic procedures. All oxidized samples were firstly electroplated with Cu in order to separate the oxide scale from expoxy mountings for SEM observations. Samples and Cu plates were connected to the cathode and anode, respectively, through a PGS151 potentialstat manufactured by Intertech Systems Inc. They were then immerged into a beaker with the electrolyte comprised of $CuSO_4$ (200~250g/l), H_2SO_4 (45~90g/l) and distilled water. The beaker was placed on a PC-410 single position stirrer manufactured by Corning Inc. with the stirring speed of 100rpm to equalize the solution. The deposition current density was selected as $10mg/cm^2$ and the whole plating process lasts for about 24 hours to gain sufficient Cu-layer thickness. Cu-plated samples were then cold-mounted using LECO long-cure epoxy kits, which is consisted of the resin and the hardener. Mounted samples were placed in a vacuum chamber to remove entrapped air and fill voids, following with cure in air for about 10 hours. Cross-sectioned samples were then polished for SEM examination. Elemental concentration profiles were measured using a JEOL JXA-8200 electron microprobe analyzer (EPMA) with pure metals (at least 99.9% in purity) being the elemental standards.

To examine the thin films formed during the early-stage oxidation, glow-discharge-optical emission spectrometry (GD-OES) was employed for determination of the oxide chemical composition. This thin-film analysis technique is based on a controlled surface erosion as a result of energetic particle bombardment, with matter being removed continuously as a function of bombardment time. The analysis of the sputtered matter as a function of the sputtering time allows for the determination of the compositional distribution of a thin film versus the depth of the layer. GD-OES used in this study allows for the measurement of concentration profiles several nm to tens of μm from the surface with sensitivity of about 10ppm for each element [86, 87]. This analysis was conducted at Hokkaido University with assistance from Dr. Shigenari Hayashi.

To specially identify the individual crystallographic phases presented in the oxide scales, chromium luminescence spectroscopy was utilized with the assistance from Prof. Arthur Heuer at Case Western Reserve University. The R-line photoluminescence in corundum is identical to the well-known phenomenon of ruby fluorescence. It arises in

response to electronic transitions in trace Cr^{3+} impurities incorporated into the alumina scale during oxidation [88, 89]. The presence of the α-alumina phase is characterized by a strong *R*-line doublet at nominal frequencies of 14,432 and 14,402 cm^{-1}. The θ-alumina phase exhibits its own characteristic photoluminescence with a similar but weaker doublet at frequencies of approximately 14,530 and 14,610 cm^{-1}.

To analyze oxide grain structures with higher resolution and their crystallographic orientations, selected oxidized samples were investigated with an FEG-SEM equipped with in-lens and electron backscatter diffraction (EBSD) detectors. It was collaborated with Dr. Joe W. Quadakkers and Dr. Dmitry Naumenko at Forschungszentrum Jülich, Germany. The in-lens detector is located within the electron optical column and collects mainly the secondary electrons (SE) leaving the sample normal to the surface. The in-lens imaging provides an excellent grain boundary contrast and allows quantitative oxide grain size measurements on mirror-polished cross-sections.

Selected samples were examined by confocal photo-stimulated microspectroscopy (CPSM) to accurately measure the residual stresses in aluminum oxide [90]. The CPSM is a refinement of the photo-stimulated luminescence spectroscopy (PSLS) using confocal laser scanning microscopy (CLSM). Focused ion beam (FIB) milling was employed for the preparation of samples for transmission electron microscopy (TEM) analysis to associate the scale microstructure with stress analysis.

CHAPTER 4 RESULTS

4.1 Single-Phase γ-Ni and γ'-Ni_3Al Alloys

As discussed in Chapter 2 of this thesis, there have been many studies focused on Pt effects on the performance of β-NiAl coatings, with numerous proposed mechanisms attempting to explain the experimental results. The mechanisms inferred from the experimental observations, either in agreement or not, were influenced by many factors such as coating composition, superalloy substrate and oxidation temperature and time. The current study focuses on gaining an understanding of the effects of Pt and Hf on the oxidation behavior of γ-Ni and γ'-Ni_3Al alloys. Single-phase model alloys have been selected to more clearly elucidate the effectiveness of Pt and Hf.

To examine the Pt and Hf effects on the high-temperature oxidation performance of γ-Ni and γ'-Ni_3Al alloys, twelve single-phase model alloys were investigated. The alloy compositions are indicated in the partial 1150°C Ni-Al-Pt phase diagram in Figure 17 and listed in Table 3. These γ-Ni and γ'-Ni_3Al alloys were of fixed aluminum contents of 12.5at.% and 25at.%, respectively. Thus, in the case of the Pt-containing alloys, 10 or 20at.% Pt was added at the expense of Ni. Due to the limited solubility of Hf in γ-Ni, only the γ'-Ni_3Al alloys were given additions of 0.2at.% or 0.5at.% Hf. The investigation of such alloy design serves to understand the beneficial and/or detrimental role(s) performed by platinum and hafnium both independently and together. Results gained from these single-phase alloys will aid in directing the paths for tailoring the compositions of γ-Ni + γ'-Ni_3Al two-phase coatings with desired high-temperature oxidation resistance.

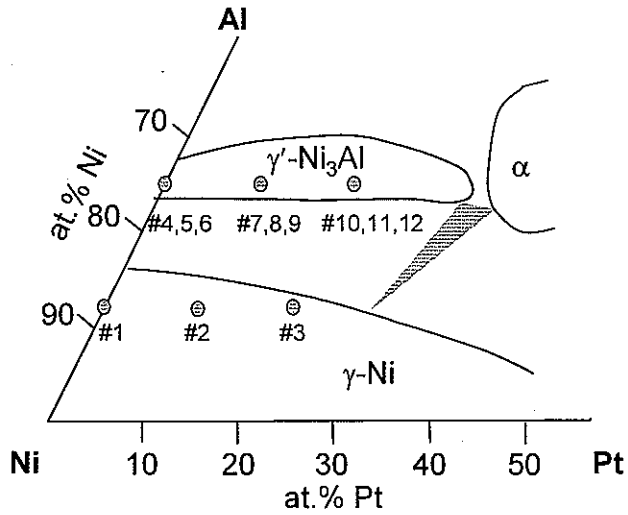

Figure 17. A section of the equilibrium Ni-Al-Pt ternary phase diagram at 1150°C with the alloy compositions superimposed.

Table 3. Nominal single-phase alloy compositions (in at.%) investigated.

	Alloy	Ni	Al	Pt	Hf	Phase Constituents
#1	Ni-12.5Al	bal.	12.5	0	0	
#2	Ni-12.5Al-10Pt	bal.	12.5	10	0	γ
#3	Ni-12.5Al-20Pt	bal.	12.5	20	0	
#4	Ni-25Al	bal.	25	0	0	
#5	Ni-25Al-0.2Hf	bal.	25	0	0.2	
#6	Ni-25Al-0.5Hf	bal.	25	0	0.5	
#7	Ni-25Al-10Pt	bal.	25	10	0	
#8	Ni-25Al-10Pt-0.2Hf	bal.	25	10	0.2	γ'
#9	Ni-25Al-10Pt-0.5Hf	bal.	25	10	0.5	
#10	Ni-25Al-20Pt	bal.	25	20	0	
#11	Ni-25Al-20Pt-0.2Hf	bal.	25	20	0.2	
#12	Ni-25Al-20Pt-0.5Hf	bal.	25	20	0.5	

4.1.1 Early-Stage Oxidation Behavior

4.1.1.1 Pt Effects in γ-Ni Alloys

The early-stage oxidation kinetics of single γ-phase Ni-12.5Al-xPt (x = 0, 10 and 20) during heating to 1150°C is shown in Figure 18. It is recalled that the surface temperature of the sample was at 970 and 1110°C at 90 and 180 seconds, respectively, and 1150°C was attained after 300 seconds of heating. It is seen that the establishment of scales was slower during the initial 90 seconds of heating than it was in the latter period from 90 to 180 seconds. This suggests that the temperature was too low for the oxide growth being kinetically favorable. The instantaneous oxide growth rate declined after 180 seconds, suggesting that the oxide film was continuous over the metal surface and that surface reaction was not controlling the scale growth process. The binary Ni-12.5Al alloy exhibited the highest scale growth rate from the very beginning stage and acquired 1.33mg/cm^2 after 1800 seconds. Although not showing a significant difference until 180 seconds, 10at.% Pt addition to Ni-12.5Al effectively reduced the scale growth rate, with a weight change of 1.01mg/cm^2 at 1800 seconds. 20at.% Pt addition in Ni-12.5Al had an extremely remarkable effect in reducing the scale growth rate from the initial heating through relatively lower temperatures all the way to 1800 seconds, at which the weight change was 0.05mg/cm^2. This is two orders of magnitude lower than that of the Pt-free Ni-12.5Al base alloy. It is seen that the kinetics reducing effect imparted by Pt addition is not in proportion to its content in the alloy. Rather than the slight decrease in weight change when going from 0 to 10at.% Pt, 20at.% Pt to the binary base alloy significantly reduced scale growth kinetics. As will be shown, this can be attributed to the effect that the oxidation mechanism is altered by the Pt addition.

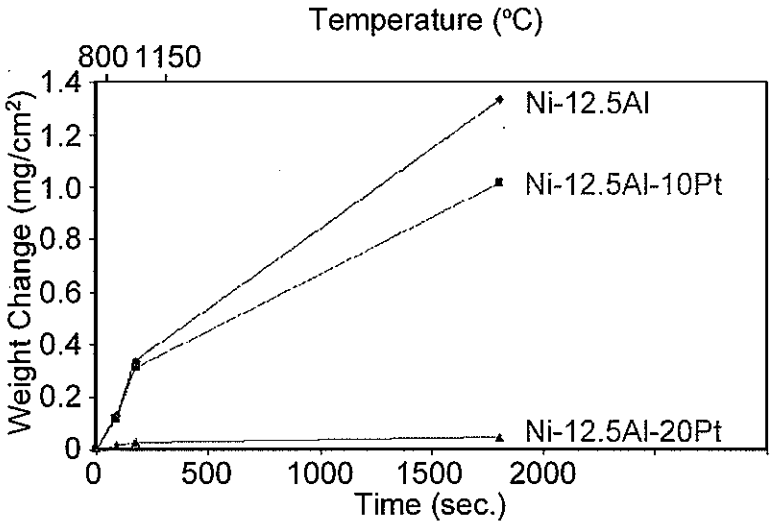

Figure 18. The early-stage anisothermal oxidation kinetics of the γ-Ni alloys affected by Pt additions.

Figure 19 shows the scale surface morphology of Ni-12.5Al-xPt (x=0, 10 and 20) alloys over the span of early-stage oxidation times from 90 to 1800 seconds. Figure 19a shows a characteristic morphology of an NiO scale, which formed on Ni-12.5Al after 90 seconds of heating. The NiO grains are seen to be highly faceted, as is commonly observed for outward growing scales [91, 92]. These faceted grains evolved from a smaller size (~170nm at 90 seconds, 970°C) to a larger size (~300nm at 180 seconds, 1110°C; ~2.5μm at 1800 seconds, 1150°C) with increasing oxidation time and temperature, as seen in Figures 19b and c. There was no indication that the scale grain size was affected by the substrate alloy orientation.

As seen in Figure 19d, the surface of Ni-12.5Al-10Pt after 90 seconds heating was comprised of faceted NiO grains that were similar in size as what formed on Ni-12.5Al after the same time. With increasing temperature to 1110°C (180 seconds), the grains grew to about 280nm, which is again similar to the NiO grain size on the Pt-free Ni-12.5Al after the same exposure. Shown in Figure 19f, however, the NiO grain size on Ni-12.5Al-10Pt after 1800 seconds of exposure was about 1.1μm, which is less than half of what was on Ni-12.5Al after the same exposure.

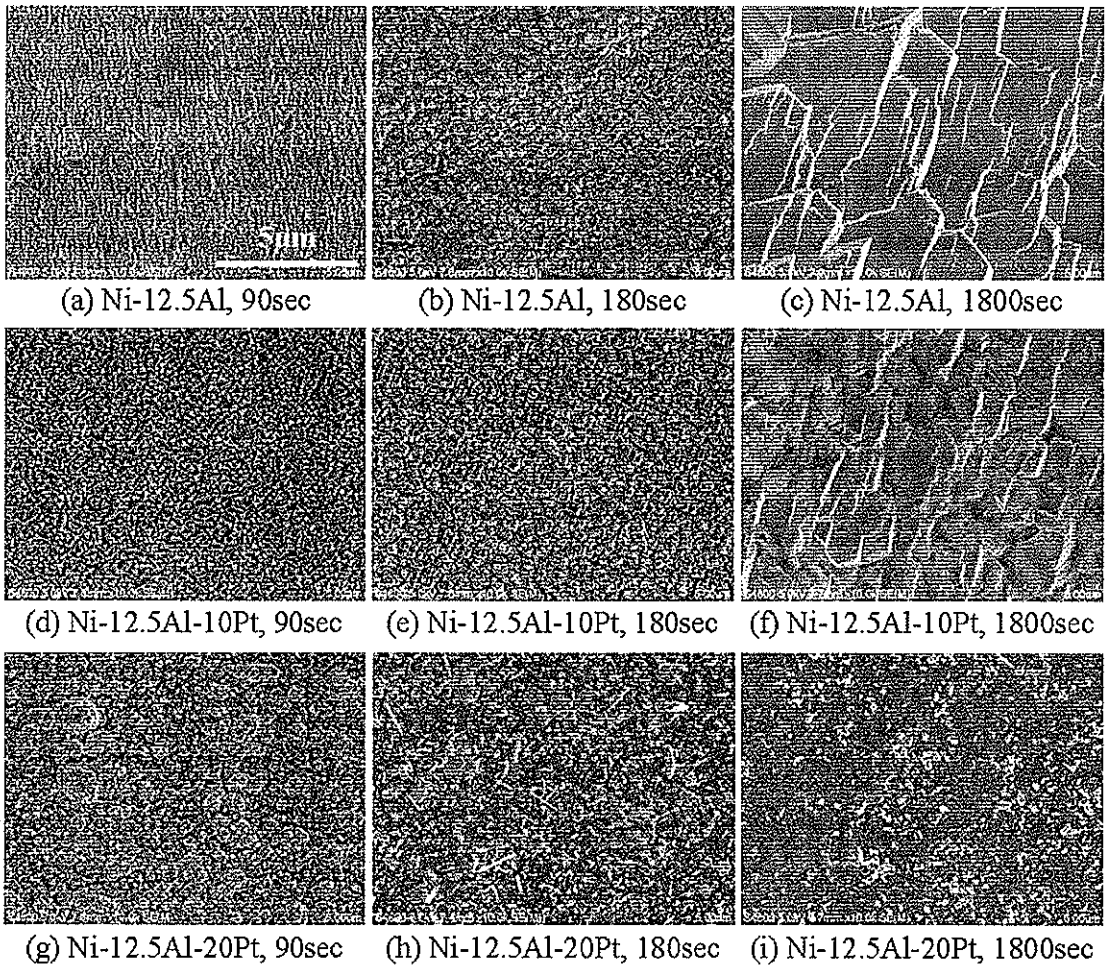

Figure 19. SEM images showing the surface morphology of scales formed on Ni-12.5Al-xPt (x=0, 10 and 20) alloys.

As shown in Figure 19g, 20at.% Pt modified the scale morphology to a cluster of fine particles around 140nm in size. With increasing heating time to 180 seconds (1110°C), a mixed scale morphology of both particles and whiskers had developed, as shown in Figure 19h. It is worth noting that oxide whiskers are usually regarded as corresponding to metastable alumina phases such as γ- and/or θ-Al_2O_3 [58, 93]. It is seen in Figure 19i that the remarkable change with Ni-12.5Al-20Pt was the disappearance of large faceted NiO grains after 1800 seconds (1150°C). Instead, network ridges with randomly-distributed larger particles started to develop. Considering the remarkably low weight change of Ni-12.5Al-

20Pt after 1800 seconds, it is inferred from the surface morphology that 20at.% Pt assisted in the formation of more protective Al_2O_3 scale.

It is clear that the 12.5at.% of Al in the Pt-free binary alloy was well below the critical level need to form a protective Al_2O_3 scale. 10at.% Pt addition decreased the faceted NiO grain size to less than half the size formed on Ni-12.5Al after the same exposure. This may be due to Pt affecting the outward flux of nickel through the scale. It is clearly shown that 20at.% Pt addition is sufficient to significantly alter the oxidation behavior of a Ni-12.5Al alloy by promoting Al_2O_3-rich scale formation.

Figure 20 shows GD-OES resolved elemental concentration profiles as a function of distance from the scale surface into the Ni-12.5Al substrate alloy after each oxidation time. With no indication of Al near the surface, the oxide layers formed throughout the early-stage oxidation are seen to be mainly comprised of Ni-rich oxide. This oxide is surmised to be NiO. It is seen that the measured Ni:O atomic ratio in the oxide layer was not unity. This is believed to be an error due to uncertainty in the quantitative analysis of oxygen [87, 94]. It is clear that the formation of fast-growing NiO on Ni-12.5Al was kinetically favorable at temperature as low as 970°C. The oxide thickened to 1.2μm after only 90-seconds heating. This rapid establishment and growth of NiO caused a slight Ni depletion in the alloy subsurface about 5μm in thickness after 90 seconds. As a counterpart, there was aluminum enrichment within the same area. During further heating from 90 seconds to 180 seconds with the temperature increasing to 1110°C, the oxide scale has thickened to about 2.5μm. The reason of Ni enrichment at the scale/alloy interface is not clear. Since this GD-OES analysis was a one-time examination, results obtained here are not assured to be repeatable and accurate. After 1800 seconds of heating with the formation of a 15μm NiO, there was a steep Ni depletion accompanied with 10μm aluminum enrichment inside the alloy subsurface. These results, together with kinetics shown in Figure 18 and scale morphology shown in Figure 19, clearly demonstrated that Ni-12.5Al alloy is not a protective alumina former.

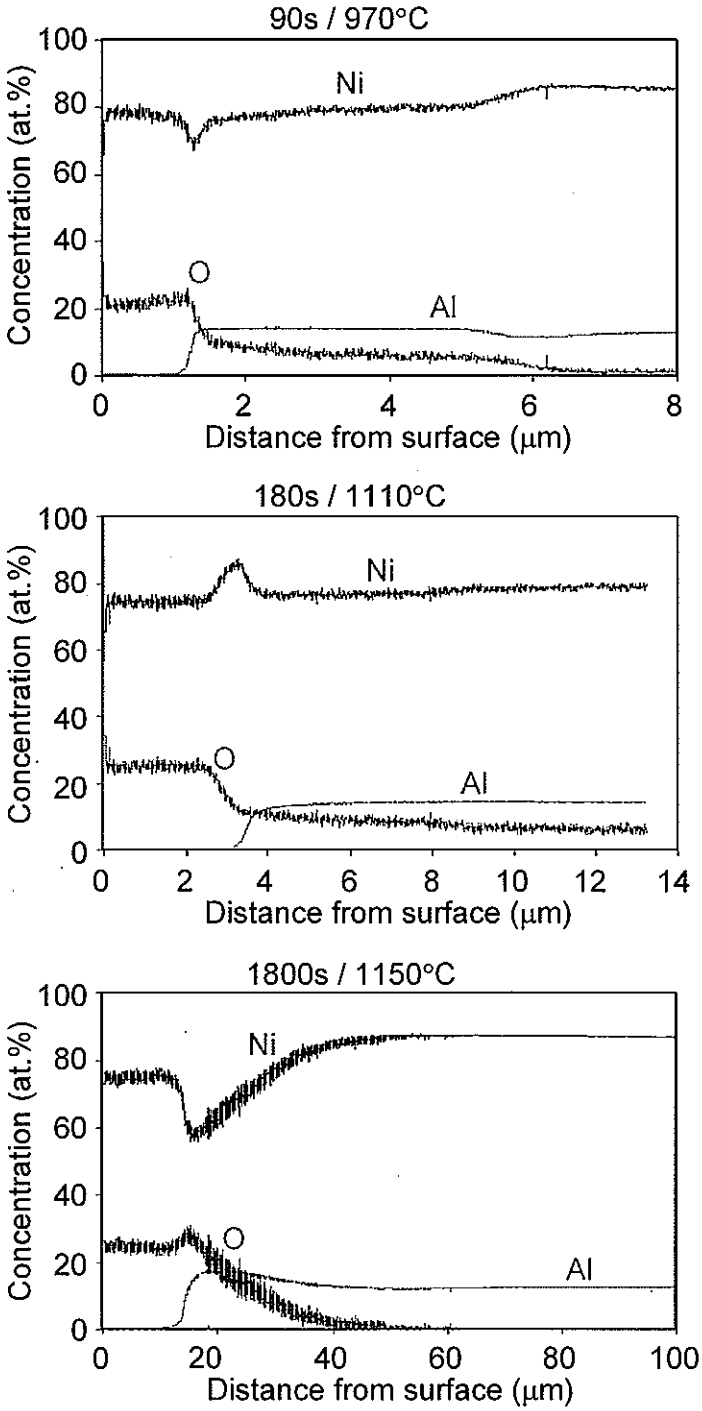

Figure 20. GD-OES composition profiles from the surface of oxidized Ni-12.5Al after 90, 180 and 1800 seconds.

GD-OES resolved elemental concentration profiles as a function of distance penetrating from the scale surface into the substrate Ni-12.5Al-10Pt alloy after each oxidation time are shown in Figure 21. Similar to the binary alloy, a 1.2μm NiO layer formed after 90 seconds. However, with the addition of 10at.% Pt, a more noticeable Al enrichment within the subsurface region was found together with a certain Pt enrichment. Meanwhile, a steep Ni concentration gradient was present in the same region of around 3μm in thickness. Subsequent heating to 1110°C led the NiO growing to about 3.6μm, which is similar as what was on the Pt-free binary alloy after the same exposure. This is evidenced as well by the kinetics plot shown in Figure 18 that the weight change after 180 seconds was similar for both Ni-12.5Al and Ni-12.5Al-10Pt. What changed was that the subsurface aluminum enrichment persisted and even further expanded to about 8μm, rather than diminishing as it did in the binary alloy. NiO was the major oxide at the surface when Ni-12.5Al-10Pt was heated up to 1150°C after 1800 seconds. The scatter in measured data was quite high near the surface for the concentration profile at 1800 seconds. Even so, the oxide scale thickness is inferred be a little thinner at this stage compared to that on the Pt-free Ni-12.5Al. Indeed, the final weight change of Ni-12.5Al-10Pt was slightly lower than the binary alloy, as seen in Figure 18. Enrichment of both Al and Pt was furthermore enhanced to about 14μm in thickness in the 10Pt alloy. Results collected suggest that the 10at.% Pt addition was unable to change the early-stage oxidation behavior when added into single-phase Ni-12.5Al alloy. However, this alloy started showing the Pt beneficial effect by decreasing the weight change and reducing the NiO grain size. It should note that Pt was not present in the oxide scale. Therefore, the reduced NiO grain size must be a result from the Pt affected outward flux of Ni.

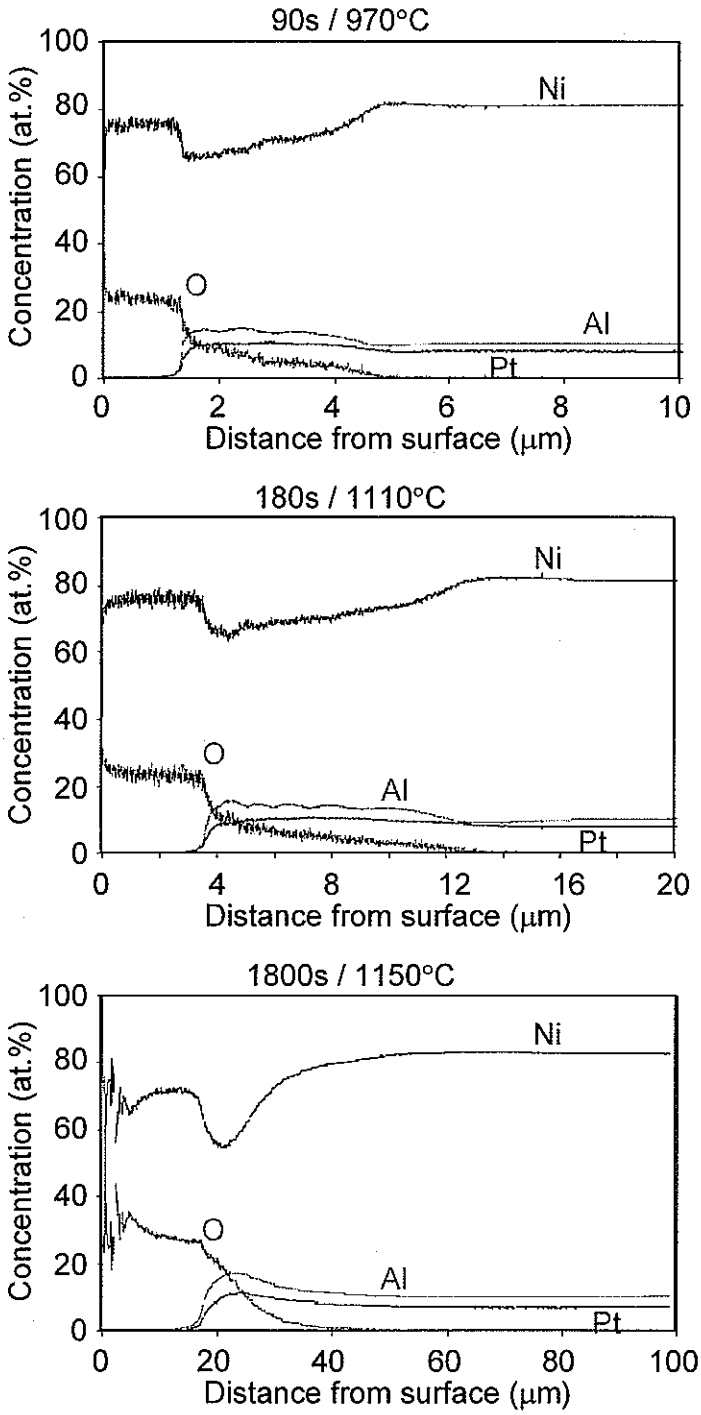

Figure 21. GD-OES composition profiles from the surface of oxidized Ni-12.5Al-10Pt after 90, 180 and 1800 seconds.

Figure 22 shows GD-OES determined elemental concentration profiles as a function of distance starting from the scale surface into the substrate of Ni-12.5Al-20Pt alloy after each oxidation time. It is noteworthy that the profile depth at 90 seconds was only about 0.1μm. Ni-12.5Al-20Pt formed a ~0.1μm NiO after heating to 970°C. An enrichment of 40at.% aluminum around 0.1μm at the scale/metal interface is assumed to be the formation of Al_2O_3-rich scale. It is distinct that the 20at.% Pt assisted the formation of more-protective alumina even at such early stage and the weight change was an order of magnitude lower than on Ni-12.5Al and Ni-12.5Al-10Pt, which is also shown in Figure 18. A trivial Pt enrichment was also observed at the subsurface area with certain Al depletion, resulted from its outward diffusion. The overall scale thickness was less than 0.6μm after 180 seconds heating. This alloy continued to form Al-rich oxide at the scale/metal interface throughout the heating process to 1800 seconds and the total scale thickness was about 1.5μm. Despite the formation of Ni-rich oxide at the outer surface, it is seen that more-protective Al_2O_3 scale started developing from the initial oxidation stage and continued growing on 20at.% Pt-modified Ni-12.5Al.

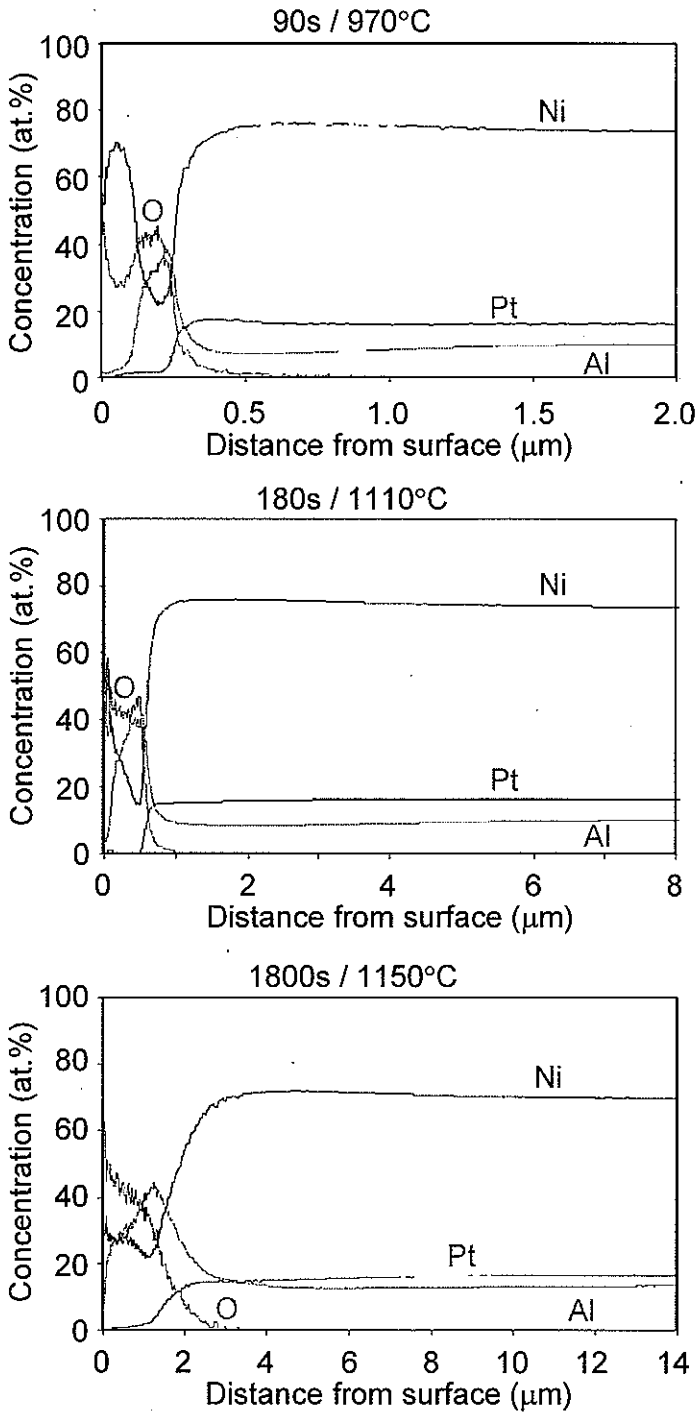

Figure 22. GD-OES composition profiles from the surface of oxidized Ni-12.5Al-20Pt after 90, 180 and 1800 seconds.

Selected to investigate Pt effects, Ni-12.5Al alloy is indeed not an Al_2O_3-former due to its low aluminum content. Regardless of that, Pt beneficial effects were plainly manifested when it was added from 10 up to 20at.% into the single-phase γ-Ni alloy. In one word, Pt promotes Al_2O_3 formation. Due to its inert properties to react with oxygen, 10at.% Pt started showing the enrichment within the subsurface area together with Al enrichment. This provides the possibility for low Al-containing alloys to form Al_2O_3 if the Al concentration could reach a critical value. Clearly, 10at.% Pt was not high enough to cause such a transition. However, when a sufficient amount like 20at.% Pt is added, the principal reaction product becomes Al-rich oxide. Thus, the oxidation kinetics was lowered significantly with the formation of a slow-growing Al_2O_3 scale and the suppression of NiO growth. Pt exhibits this effect even at lower temperatures in the very early stage of oxidation. It is seen that the formation of Al_2O_3 on Ni-12.5Al-20Pt started below 1000°C in Figures 19h and 22, which resulted in the much lower scale growth kinetics during the overall oxidation times, as shown in Figure 18.

4.1.1.2 Pt Effects in γ'-Ni_3Al Alloys

The early-stage oxidation kinetics of single γ'-phase Ni-25Al-xPt, Ni-25Al-0.2Hf-xPt and Ni-25Al-0.5Hf-xPt (x = 0, 10 and 20) during heating to 1150°C are shown in Figure 23. It is seen that Pt consistently contributes to decreasing the weight change for all γ'-Ni_3Al alloys throughout the overall oxidation times. The Ni-25Al base alloy exhibited quite fast scale growth rate during the first 180 seconds and gained 0.18mg/cm^2 after 1800 seconds. Both Ni-25Al-10Pt and Ni-25Al-20Pt behaved similarly during the first 180 seconds and their final weight change after 1800 seconds was 0.09 and 0.08mg/cm^2, respectively. Thus, the effect of Pt in decreasing the weight change is more prominent from 0 to 10at.% than it is from 10 to 20at.% for Ni-25Al base alloy. However, this is not true for Hf-modified Ni-25Al alloys. Ni-25Al-0.2Hf showed fast initial scaling kinetics for the first 180 seconds of heating and the weight gain was 0.25mg/cm^2 after 1800 seconds. In comparison, the weight change for Ni-25Al-10Pt-0.2Hf (0.15mg/cm^2) and Ni-25Al-20Pt-0.2Hf (0.07mg/cm^2) after 1800 seconds was 0.6 and 0.28 times the weight change of Ni-25Al-0.2Hf, respectively.

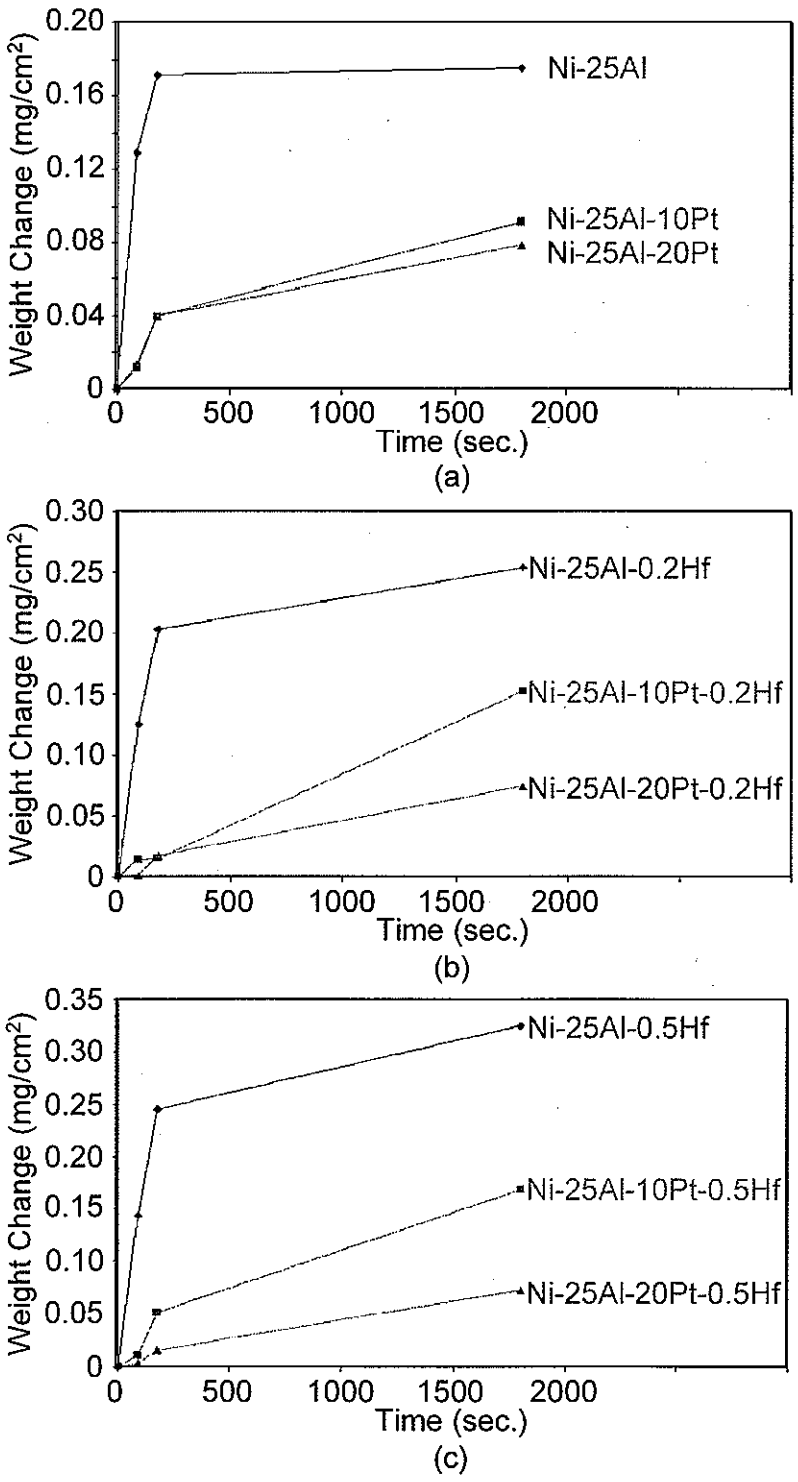

Figure 23. The early-stage anisothermal oxidation kinetics of the γ'-Ni_3Al alloys affected by Pt additions (a) Ni-25Al-xPt, (b) Ni-25Al-0.2Hf-xPt and (c) Ni-25Al-0.5Hf-xPt.

Similarly, the weight change for Ni-25Al-10Pt-0.5Hf (0.17mg/cm^2) and Ni-25Al-20Pt-0.5Hf (0.07mg/cm^2) after 1800 seconds was 0.5 and 0.22 times the weight change of Ni-25Al-0.5Hf (0.32mg/cm^2), respectively. Thus, the decreasing in weight change is roughly linear with the Pt concentration when added to the Hf-modified Ni-25Al alloy, as shown in Figure 24. Comparing the results of Pt effects on weight change obtained from Hf-free Ni-25Al and Hf-modified Ni-25Al, it is found that Pt has a strong chemical impact on Hf in γ'-Ni_3Al alloys, which will be further investigated in the sections that follow.

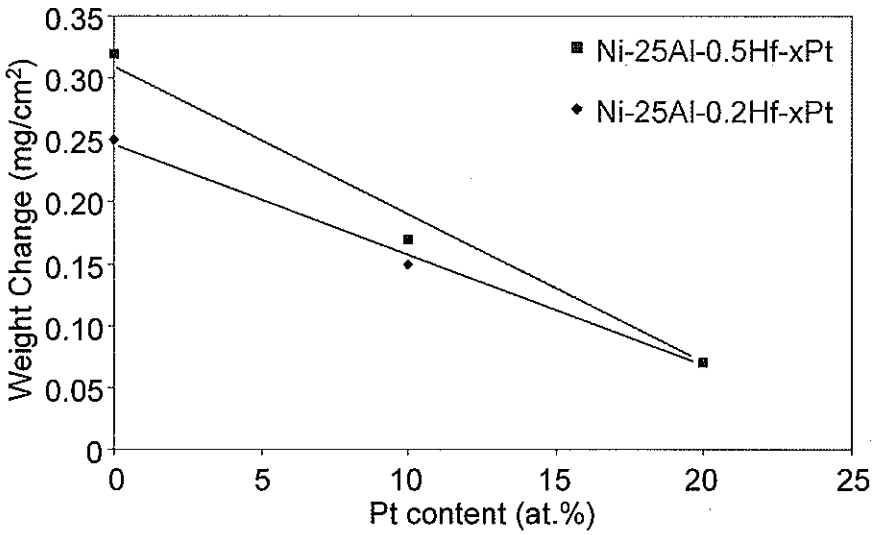

Figure 24. The relationship between the weight change and Pt contents of Hf-modified Ni-25Al alloys.

Figure 25 shows the scale surface morphology of Ni-25Al-xPt (x=0, 10, and 20) alloys with increasing early-stage oxidation time from 90 to 1800 seconds. Figure 25a shows a typical surface morphology of faceted NiO grains on Ni-25Al after 90 seconds. These faceted grains developed from a smaller size (~260nm at 90seconds, 970°C) to a larger size (~550nm at 180 seconds, 1110°C; ~700nm at 1800 seconds, 1150°C) with increasing oxidation time and temperature, as seen in Figures 25b and c. There was no indication of the scale grain size affected by the substrate alloy orientation when examining the lower magnification SEM images on all samples.

As seen in Figure 25d, the surface of Ni-25Al-10Pt after heating for 90 seconds was characterized by fine, directionally-oriented, cuboid-shaped grains. The orientation of the grains is along the polishing marks on the alloy surface. The polishing marks clearly served as primary oxide nucleation sites. The area between the polishing marks was even and smooth. With heating to 1110°C (180 seconds), the grains grew to a larger size and covered the entire alloy surface, diminishing polishing mark features, as seen in Figure 25e. It is worth noting that the surface was decorated by some sporadically distributed oxide whiskers which were usually regarded as metastable alumina structures, such as γ- and/or θ-Al_2O_3 [58, 93]. Oxide ridges of α-Al_2O_3 developed with further oxidation to 1800 seconds (1150°C), as seen in Figure 25f. Oxide whiskers disappeared at this higher oxidation temperature and longer time.

It is seen in Figure 25g that Ni-25Al-20Pt performed in a similar way as Ni-25Al-10Pt after 90 seconds heating (970°C), though the oxide on the former had finer grains along polishing marks with larger spacing. Oxide whiskers were observed on Ni-25Al-20Pt after 90 seconds heating which is earlier than those formed on Ni-25Al-10Pt after 180 seconds. With increasing time and temperature to 180 seconds (1110°C), oxide whiskers retreated with the surface becoming covered with cuboidal grains occupying the entire alloy surface completely, as seen in Figure 25h. Noticeable oxide network ridges can be discerned in Figure 25i, which is the alloy after 1800 seconds of exposure (1150°C). Ridges-enclosed area was featured by smooth oxide grains.

The aluminum content in the Ni-25Al single-phase γ′-Ni_3Al alloy was insufficient to form a protective Al_2O_3-rich scale during anisothermal early-stage oxidation. Faceted NiO established from the initial stage and developed to a larger grain size with continued exposure up to the maximum time of 1800 seconds. Pt addition into Ni-25Al modified surface products from faceted NiO to fine-grained Al_2O_3 being decorated with ridge-type network. Oxide whiskers were observed on Pt-modified Ni-25Al alloys during the heating stages as 180 seconds for Ni-25Al-10Pt and 90 seconds for Ni-25Al-20Pt, respectively. Results summarized above suggest that Pt addition in γ′-Ni_3Al alloys contributes to promote the Al_2O_3 formation during the heating period by suffocating the establishment of NiO, which is similar as it did to γ-Ni alloys as stated in Chapter 4.1.1.1.

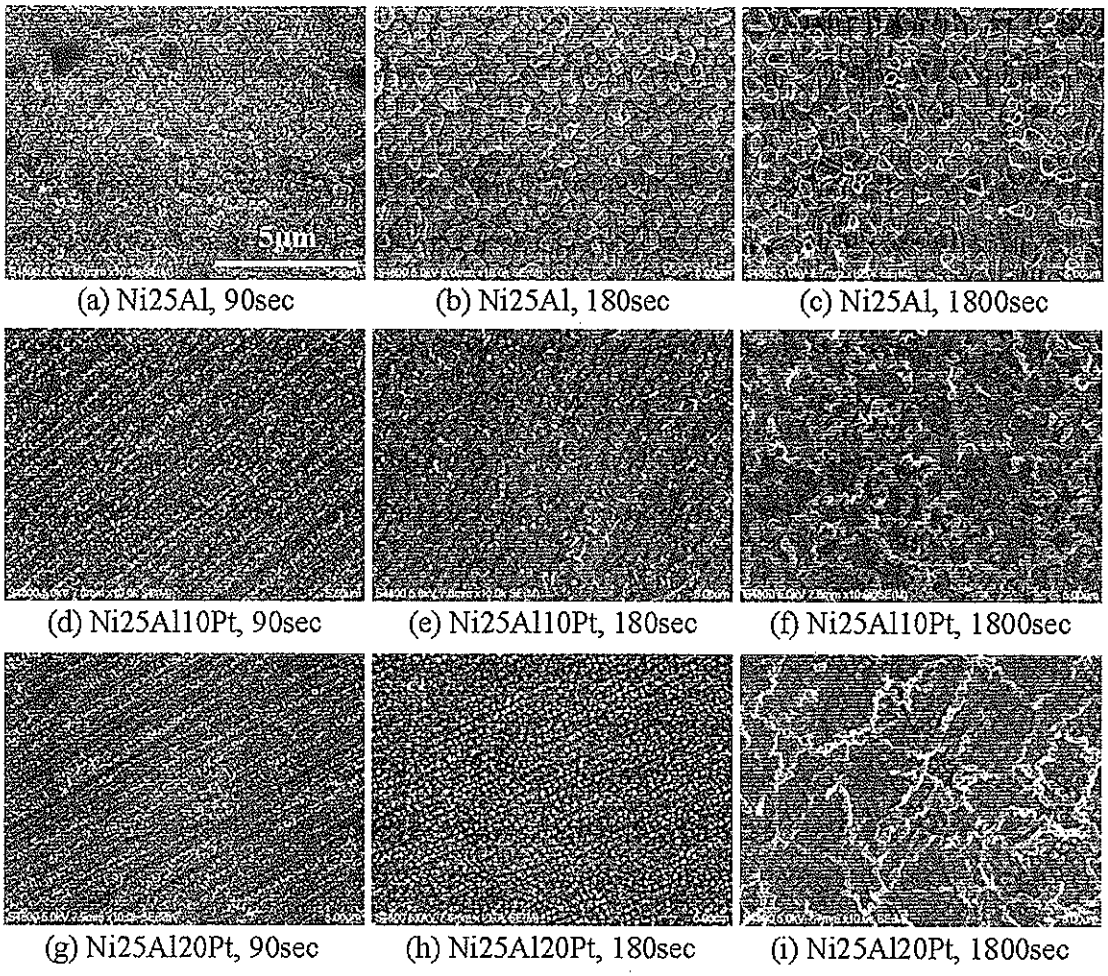

Figure 25. SEM images showing the surface morphology of scales formed on Ni-25Al-xPt (x=0, 10 and 20) alloys.

The scale surface morphology of Ni-25Al-0.2Hf-xPt (x=0, 10, and 20) alloys developed with increasing early-stage oxidation time from 90 to 1800 seconds is shown in Figure 26. Ni-25Al-0.2Hf formed faceted grain structure about 270nm in diameter after 90 seconds (970°C), shown in Figure 26a. These NiO grains grew to about 540nm after further heating to 180seconds (1110°C), as seen in Figure 26b. The grain size on Ni-25Al-0.2Hf was nearly same as it on Ni-25Al after both 90 and 180 seconds, respectively. As shown in Figure 26c, however, NiO grains size enlarged to about 1.3μm after 1800 seconds heating (1150°C), which was approximately two times of it on Ni-25Al after the same exposure.

The surface of Ni-25Al-10Pt-0.2Hf was characterized with fine-grained particles orientated along polishing marks after 90 seconds heating, as shown in Figure 26d. With increasing oxidation time and temperature, oxide particles became larger and denser with few scarcely-dispersed whiskers after 180 seconds exposure, as seen in Figure 26e. Entire sample surface was covered by close-packed oxide after 1800 seconds (1150°C) without the trace of oxide whiskers as seen in Figure 26f.

Figure 26g shows fine particles on Ni-25Al-20Pt-0.2Hf after 90 seconds heating with noticeable polishing mark features. The interlined spacing was wider than on Ni-25Al-10Pt-0.2Hf after the same exposure time. These oxide particles became bigger and condenser with the increasing time and temperature from 180 to 1800 seconds, as shown in Figure 26h and i.

It is seen that 0.2at.% Hf addition in Ni-25Al enlarged the size of faceted NiO particles about one time than on Hf-free Ni-25Al alloy after 1800 seconds. Pt additions to Ni-25Al-0.2Hf changed oxidation products from faceted NiO to fine Al_2O_3-rich particles. Comparing Figures 25d, e, g and h with Figures 26d, e, g and h, the interlined spacing of both Ni-25Al-10Pt-0.2Hf and Ni-25Al-20Pt-0.2Hf were larger than on their counterpart Hf-free version alloys as Ni-25Al-10Pt and Ni-25Al-20Pt. This suggests that Pt additions decelerated the oxide nucleation and growth rate during the heating process from 90 to 180 seconds, which is also validated by the kinetics plot seen in Figure 23b. Moreover, lace-like networks were diminished when 0.2at.% Hf added to Pt-modified Ni-25Al alloys. This Hf effect will be discussed later in Chapter 4.1.1.3.

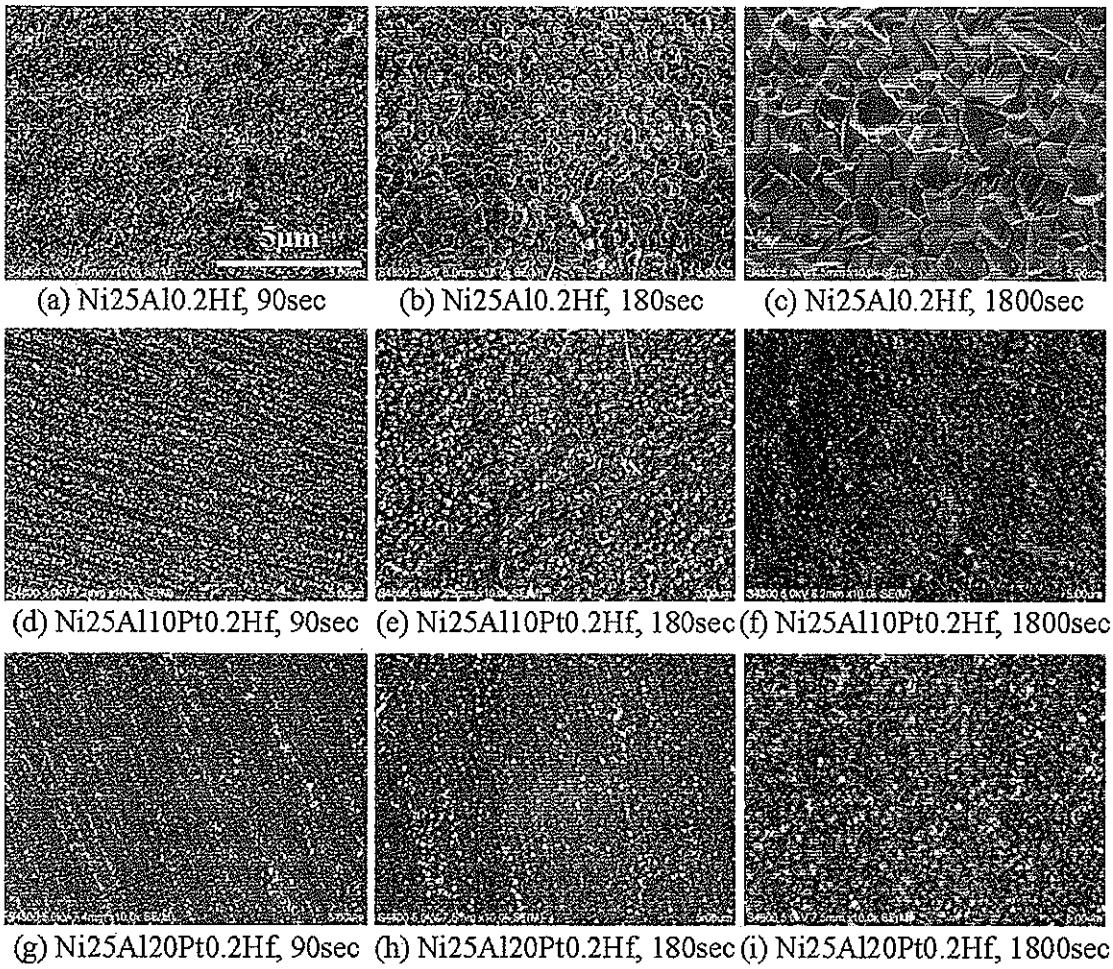

(a) Ni25Al0.2Hf, 90sec (b) Ni25Al0.2Hf, 180sec (c) Ni25Al0.2Hf, 1800sec

(d) Ni25Al10Pt0.2Hf, 90sec (e) Ni25Al10Pt0.2Hf, 180sec (f) Ni25Al10Pt0.2Hf, 1800sec

(g) Ni25Al20Pt0.2Hf, 90sec (h) Ni25Al20Pt0.2Hf, 180sec (i) Ni25Al20Pt0.2Hf, 1800sec

Figure 26. SEM images showing the surface morphology of scales formed on Ni-25Al-0.2Hf-xPt (x=0, 10 and 20) alloys.

Figure 27 presents the scale surface morphology of Ni-25Al-0.5Hf-xPt (x=0, 10, and 20) alloys with increasing early-stage oxidation time from 90 to 1800 seconds. It seen in Figure 27a that large faceted NiO grains rapidly nucleated after 90 seconds heating on Ni-25Al-0.5Hf, although the scale was not compact with localized depressed areas. The oxide scale became more compact when the alloy heated to 1110°C as seen in Figure 27b, and finally developed into large faceted grains about 2μm after 1800 seconds exposure, shown in Figure 27c. The NiO grain size enlarged from about 1.3μm to 2μm when Hf content in Ni-25Al increased from 0.2 to 0.5at.%.

Figure 27d shows mixed oxide morphology as both platelets and particles on Ni-25Al-10Pt-0.5Hf after 90 seconds heating (970°C). With increasing oxidation time and temperature to 180 seconds (1110°C), the scale became more compact with many blade-like whiskers, as seen in Figure 27e. After 1800 seconds exposure shown in Figure 27f, the surface was characterized as smooth oxide grains without distinct features.

Fine-grained oxide scale formed on Ni-25Al-20Pt-0.5Hf after 90 seconds heating with preferential orientation along polishing marks, as seen in Figure 27g. These grains grew larger with increasing oxidation time and temperature as shown in Figures 27h and i. There was no apparent oxide whiskers observed on Ni-25Al-20Pt-0.5Hf throughout the entire heating period.

Early-stage oxidation results obtained from Ni-25Al-0.5Hf-xPt (x=0, 10 and 20) alloys again suggested that Pt additions in γ'-Ni_3Al alloys assisted the formation and growth of more-protective Al_2O_3 scale by limiting the establishment of more kinetically-favored NiO during the heating progress. Chemically, it could be inferred that Pt acts by the gettering effect in a similar way as Cr promoting Al_2O_3 formation in Ni-Cr-Al ternary alloy system, which is usually referred as the third-element effect [95]. With Pt additions, Ni-25Al-xHf (x=0, 0.2 and 0.5) alloys changed from NiO formers to more-protective alumina formers.

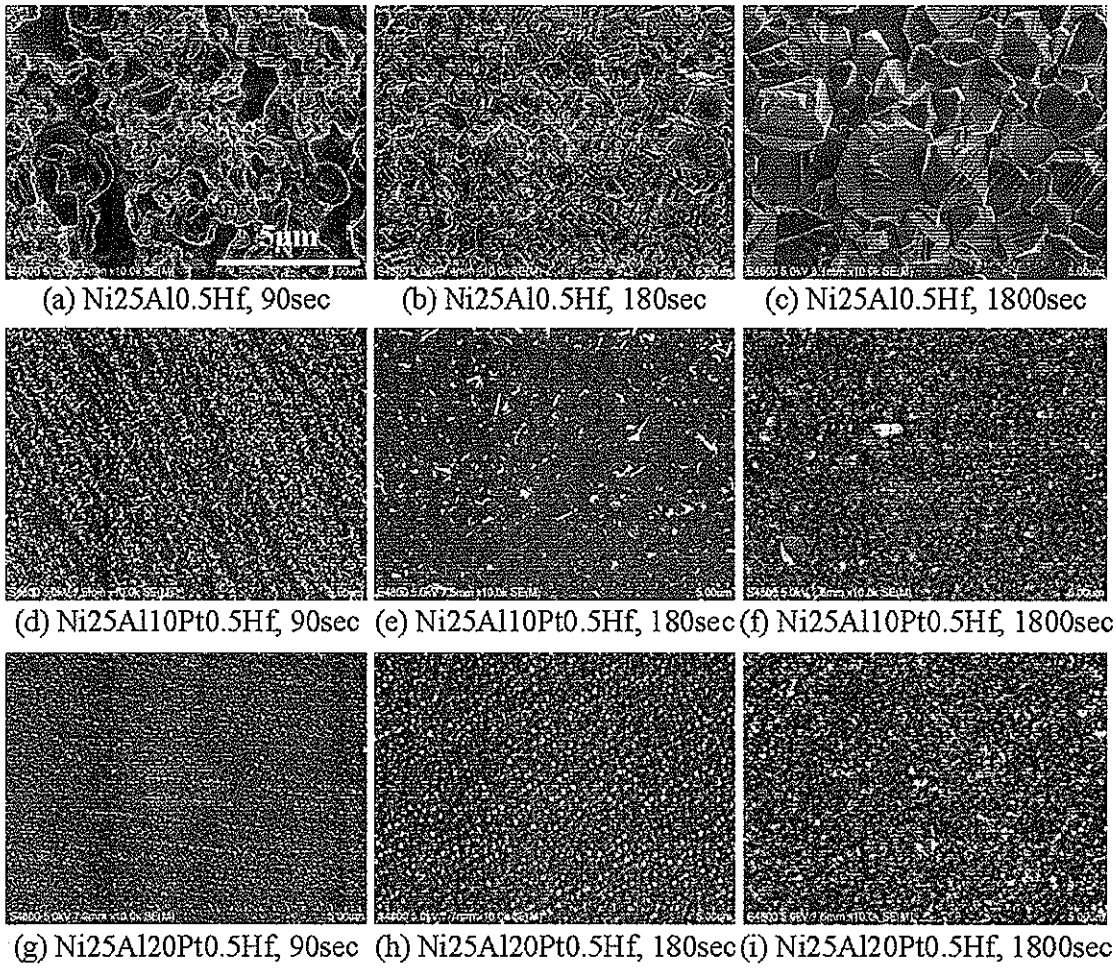

(a) Ni25Al0.5Hf, 90sec (b) Ni25Al0.5Hf, 180sec (c) Ni25Al0.5Hf, 1800sec

(d) Ni25Al10Pt0.5Hf, 90sec (e) Ni25Al10Pt0.5Hf, 180sec (f) Ni25Al10Pt0.5Hf, 1800sec

(g) Ni25Al20Pt0.5Hf, 90sec (h) Ni25Al20Pt0.5Hf, 180sec (i) Ni25Al20Pt0.5Hf, 1800sec

Figure 27. SEM images showing the surface morphology of scales formed on Ni-25Al-0.5Hf-xPt (x=0, 10 and 20) alloys.

Figure 28 shows GD-OES determined elemental concentration profiles as a function of distance starting from the scale surface into the substrate of Ni-25Al alloy after each early-stage oxidation time. It is seen that Ni-rich oxide formed on the surface throughout the entire early-stage oxidation, which is evidenced by the scale surface morphology as shown in Figures 25a, b and c. A ~1.5μm NiO formed after 90 seconds heating with the formation of a 4μm subsurface depletion of Ni and enrichment of Al. This NiO further thickened to ~1.7μm after 180 seconds heating (1110°C) with more enrichment of Al near the scale/alloy interface. Al-rich oxide started forming below outer NiO and the overall scale thickness was about 2.3μm after 1800 seconds exposure, which is only 1/10 of it on Ni-12.5Al alloy after the

same oxidation time, as shown in Figure 20. Therefore, Ni-25Al alloy has a greater potential to form more-protective Al_2O_3-rich scale than Ni-12.5Al alloy. Although the fast nucleation and growth of NiO was inevitable even with 25at.% Al during the early-stage oxidation, Ni-25Al was able to develop Al-rich oxide near the scale/alloy interface which may undercut the pathway for subsequent outward diffusion of Ni. This could be simply attributed to the original high Al content in Ni-25Al so that the critical concentration to form Al_2O_3 was easier to achieve. Spikes presented around 8.2μm (1800 seconds) could be ascribed as error data points. Results obtained from Ni-25Al basically confirmed that higher Al content in Ni-Al binary alloys assists the formation of more-protective Al-rich oxide.

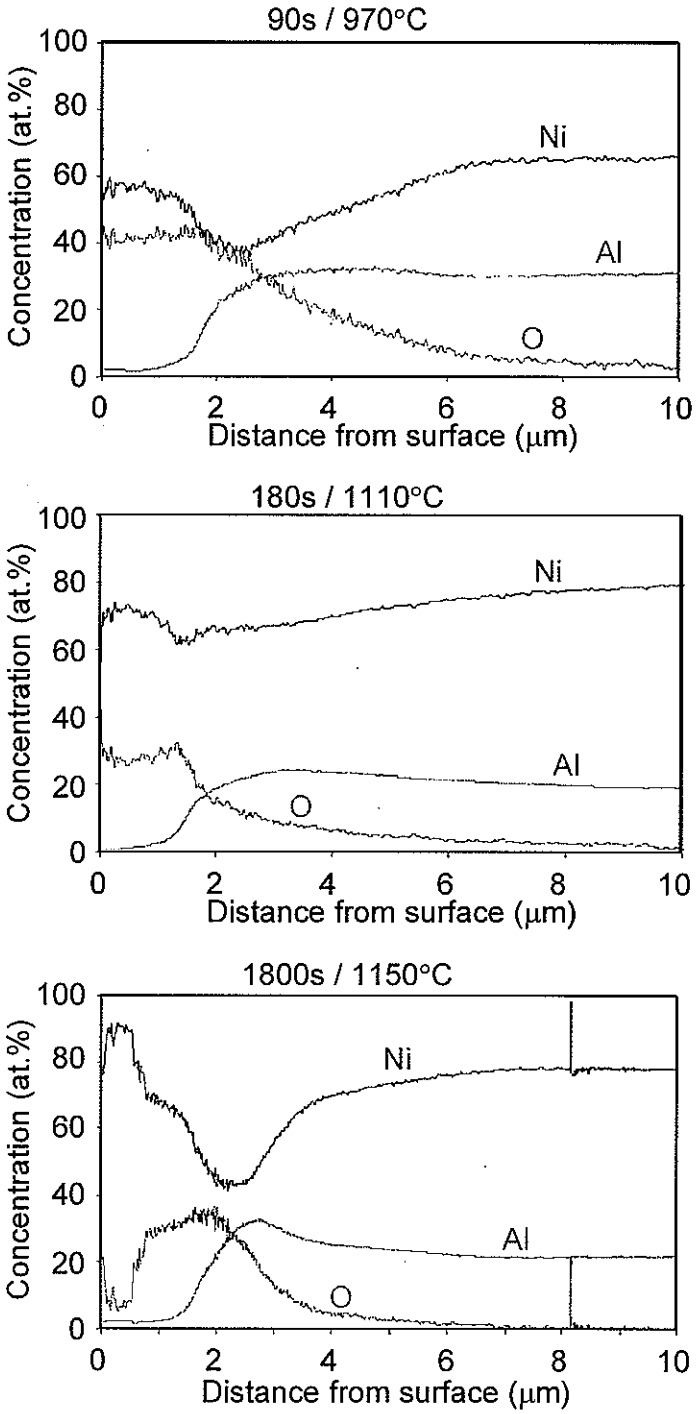

Figure 28. GD-OES composition profiles from the surface of oxidized Ni-25Al after 90, 180 and 1800 seconds.

GD-OES resolved elemental concentration profiles as a function of distance starting from the scale surface into the substrate of Ni-25Al-10Pt alloy after each early-stage oxidation time are shown in Figure 29. Rather than the formation of NiO, Al-rich oxide ~0.13μm developed after 90 seconds heating to 970°C. There was a slight Al depletion (~0.3μm) in the subsurface accompanied with enrichment of Ni. Al_2O_3 scale thickened to about 0.4μm with increasing oxidation time after 180 seconds heating to 1110°C. Subsurface depletion zone of Al further enlarged to ~1.6μm. Accordingly, the Ni concentration gradient from subsurface down to the alloy substrate was build up in response to the formation of Al_2O_3. During the following heating to 1800 seconds, the concentration gradient of Ni was reduced by backward diffusion from the subsurface area to the substrate and the final scale thickness was about 0.9μm. It is also seen that the Al concentration gradient was reduced from 180 seconds to 1800 seconds. This reduction could be achieved by the outward diffusion of Al from the substrate to the scale/alloy interface. There was no apparent Pt concentration gradient observed during the early-stage oxidation period. Results summarized above suggest that Pt increases the outward diffusion of Al to form Al-rich surface oxide in early-stage oxidation, even at relatively lower temperatures.

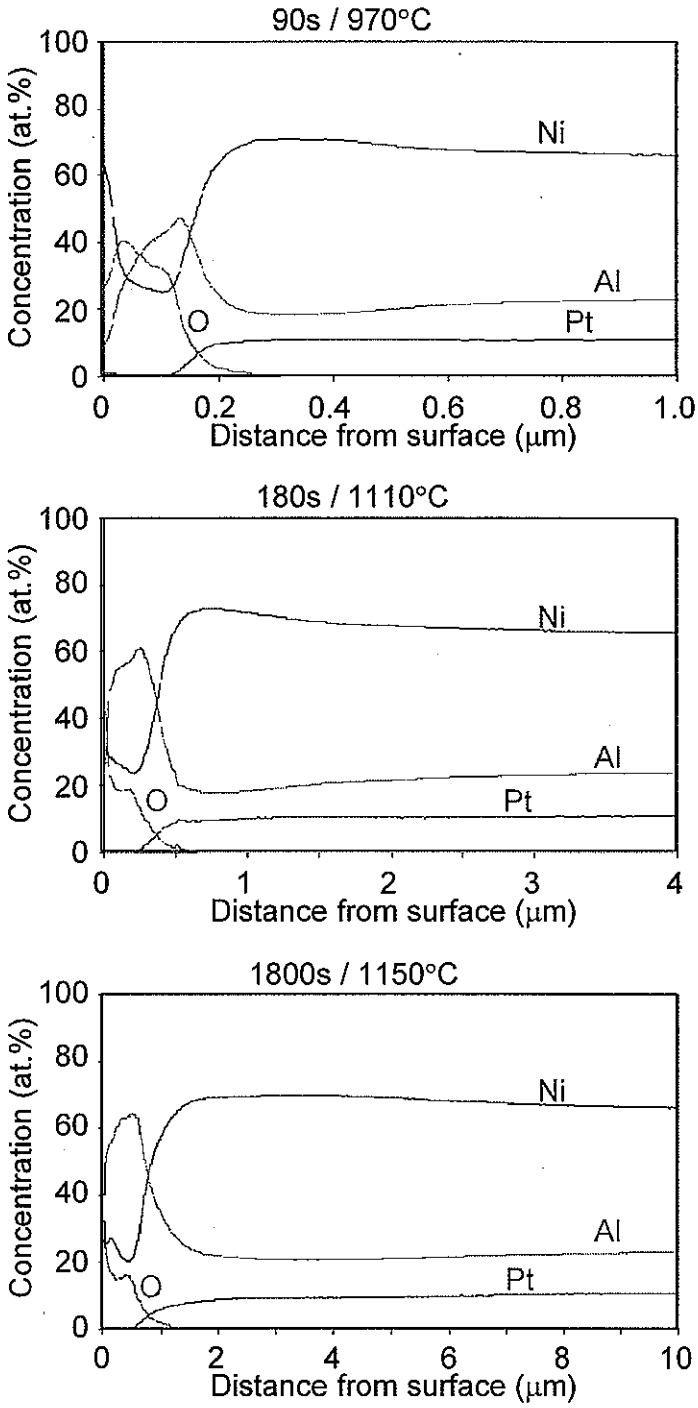

Figure 29. GD-OES composition profiles from the surface of oxidized Ni-25Al-10Pt after 90, 180 and 1800 seconds.

Figure 30 shows GD-OES resolved elemental concentration profiles as a function of distance penetrating from the scale into the substrate Ni-25Al-20Pt alloy after each oxidation time. Al-rich oxide about 0.2μm was formed after 90 seconds heating, which was nearly same as on Ni-25Al-10Pt after the same exposure. This is confirmed by their similar weight change after 90 seconds, as shown in Figure 23a. Careful examination discloses that Pt slightly enriched near the subsurface zone around 0.4μm at 970°C. Following heating to 1110°C after 180 seconds resulted in the growth of Al_2O_3 to about 0.4μm, which is quite similar as on Ni-25Al-10Pt after the same oxidation time. The scale thickness was around 0.8μm after 1800 seconds heating (1150°C). Reduced Ni content with Pt addition to Ni-25Al made the alloy easier to form more-protective Al_2O_3 scale since the Al:Ni ratio was relatively increased. However, the weight changes of Ni-25Al-10Pt and Ni-25Al-20Pt were almost same after 1800 seconds exposure. This could be ascribed to the nature of slow-growing Al_2O_3. Diffusion-controlled growth mechanism dictates the thickening process of alumina. This explains why the Pt content, added with enough amounts to promote Al_2O_3 formation, had insignificant impacts on the early-stage alloy weight changes. Nevertheless, it is clearly seen that the Al depletion zone near the subsurface area continued to decrease so that the consumption of Al to form Al_2O_3 was quickly compensated by the outward diffusion of Al from the substrate. These results implied that Pt and Al are chemically favorable with each other.

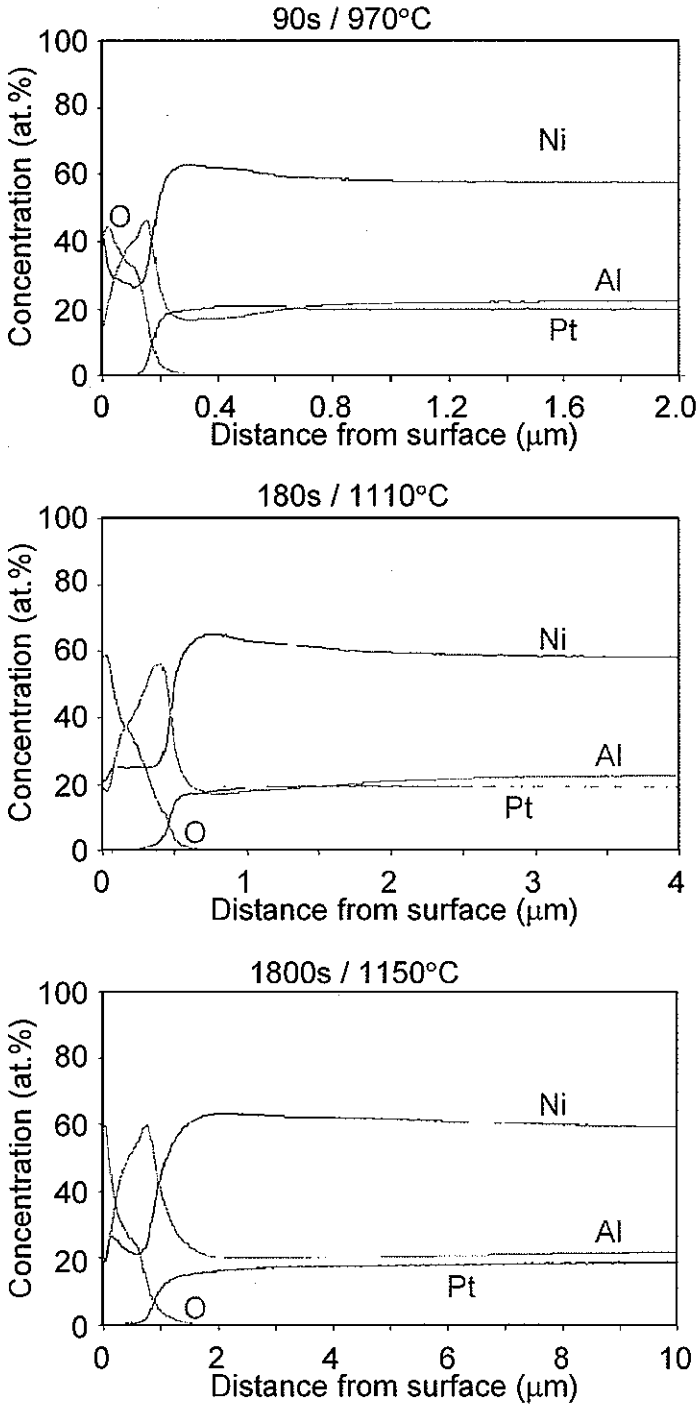

Figure 30. GD-OES composition profiles from the surface of oxidized Ni-25Al-20Pt after 90, 180 and 1800 seconds.

GD-OES resolved elemental concentration profiles as a function of distance starting from the scale surface into the substrate of Ni-25Al-0.2Hf alloy after each early-stage oxidation time are shown in Figure 31. NiO about 1.2μm formed on the surface of Ni-25Al-0.2Hf after 90 seconds heating (970°C). This resulted in the development of a subsurface zone around 2.3μm with the depletion Ni and enrichment of Al. With further increasing oxidation temperature to 1110°C, NiO thickened to about 2.1μm with enlarged subsurface area about 3μm. There was no observable concentration gradient of Hf at this stage. Al-rich oxide started forming near the scale inner surface and the total scale thickness was around 3.2μm after 1800 seconds exposure (1150°C). It is worth noting that the enrichment of Hf at the scale/alloy interface initiated at this time. Comparing with the GD-OES results from Hf-free Ni-25Al shown in Figure 28, it is seen that NiO was growing faster with 0.2at.% Hf addition, as the scale thickness was larger on Ni-25Al-0.2Hf after 1800 seconds exposure. Previous results showed that the NiO grain size on Ni-25Al-0.2Hf was about 2 times of it on Ni-25Al after 1800 seconds heating, as shown in Figures 25c and 26c. These results all together suggest that Hf may increase the lattice diffusion coefficient of Ni in NiO, which led to the faster growth rate and larger grain size of NiO at higher temperatures above 1000°C.

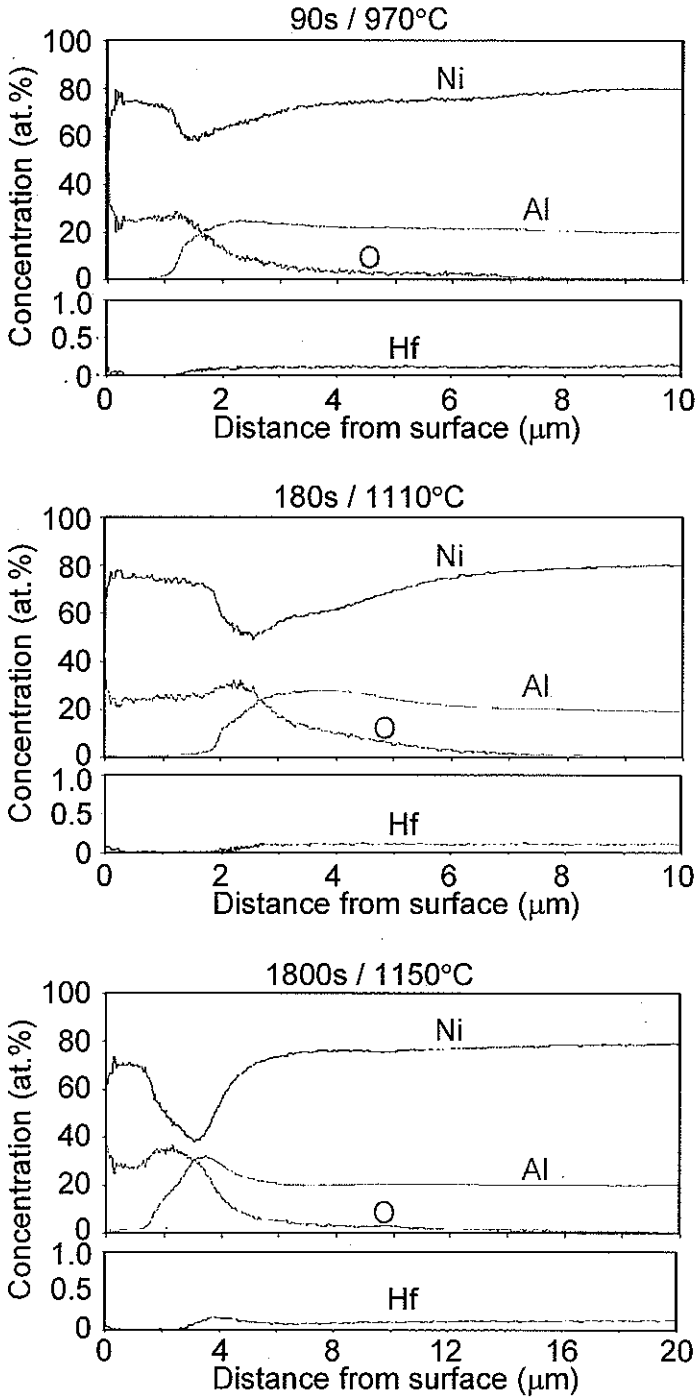

Figure 31. GD-OES composition profiles from the surface of oxidized Ni-25Al-0.2Hf after 90, 180 and 1800 seconds.

Figure 32 shows GD-OES resolved elemental concentration profiles as a function of distance penetrating from the scale surface into the substrate alloy Ni-25Al-10Pt-0.2Hf after each oxidation time. It is notably seen that the thin film formed after 90 seconds heating was less than 0.2μm, which was 5 times thinner than the oxide formed on the Pt-free Ni-25Al-0.2Hf alloy. This corresponds well with their different weight change after 90 seconds exposure, as shown in Figure 23b. Despite the non-reacting Pt, all other elements including Ni, Al and Hf were enriched in this thin scale. The surface enrichment of Hf was assumed to be the formation of HfO_2 due to its high thermal stability and fast growing kinetics. With further heating after 180 seconds (1110°C), scale thickness enlarged to about 0.5μm and the major oxide was Al_2O_3. Therefore, the major improvement of 10at.% Pt addition to Ni-25Al-0.2Hf was to promote the formation of more-protective Al_2O_3 during the early-stage oxidation at relatively lower temperatures. The scale thickness was about 1μm after 1800 seconds heating without indication of further enrichment of Ni in the scale. However, Hf enriched at the scale/alloy interface and its behavior will be discussed later in Chapter 4.1.1.3.

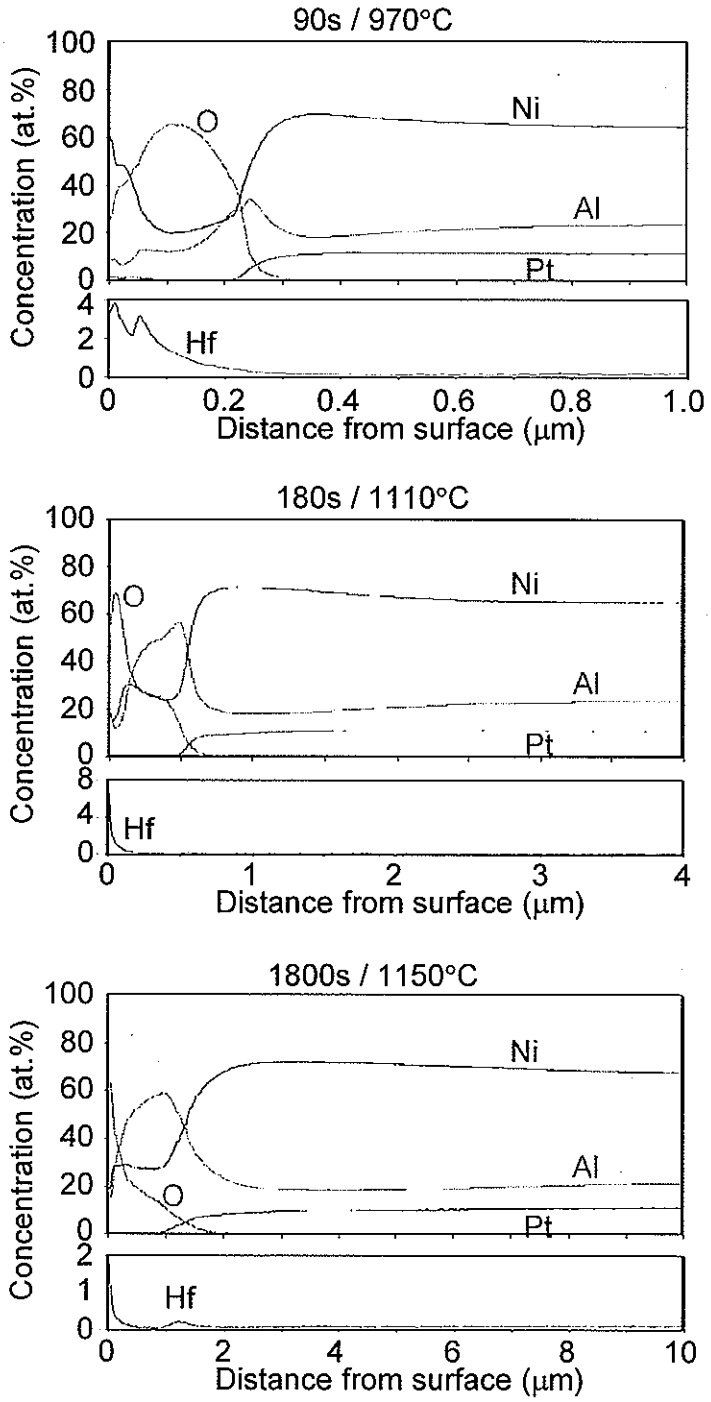

Figure 32. GD-OES composition profiles from the surface of oxidized Ni-25Al-10Pt-0.2Hf after 90, 180 and 1800 seconds.

GD-OES resolved elemental concentration profiles as a function of distance penetrating from the scale surface into the substrate of Ni-25Al-20Pt-0.2Hf alloy after each oxidation time are shown in Figure 33. The thin film formed after 90 seconds was about 0.2μm, which is similar as it formed on Ni-25Al-10Pt-0.2Hf after the same time. Besides the formation of both Al- and Ni-rich oxide, however, the enrichment of Hf at the scale outer surface was not observed with 20at.% Pt addition. With further increasing oxidation time after 180 seconds (1110°C), scale thickened to about 0.7μm. Meanwhile, it is also observed that the profile near the scale/alloy interface was anomalously divergent. This could be attributed to many factors such as nonuniform scale thickness and/or tilted sample surfaces. In addition, segregation of Hf at the scale/alloy interface was observed. This alloy continued to form Al-rich oxide to about 1.2μm after 1800 seconds heating (1150°C), which was less than half of on Ni-25Al-10Pt-0.2Hf after the same exposure time. Interestingly, enrichment of Hf at the scale/alloy interface formed after 180 seconds disappeared during the further heating to 1800 seconds. It is further seen that 20at.% Pt addition not only promotes the formation of Al_2O_3, but also inhibits the initial enrichment of HfO_2 at the scale outer surface.

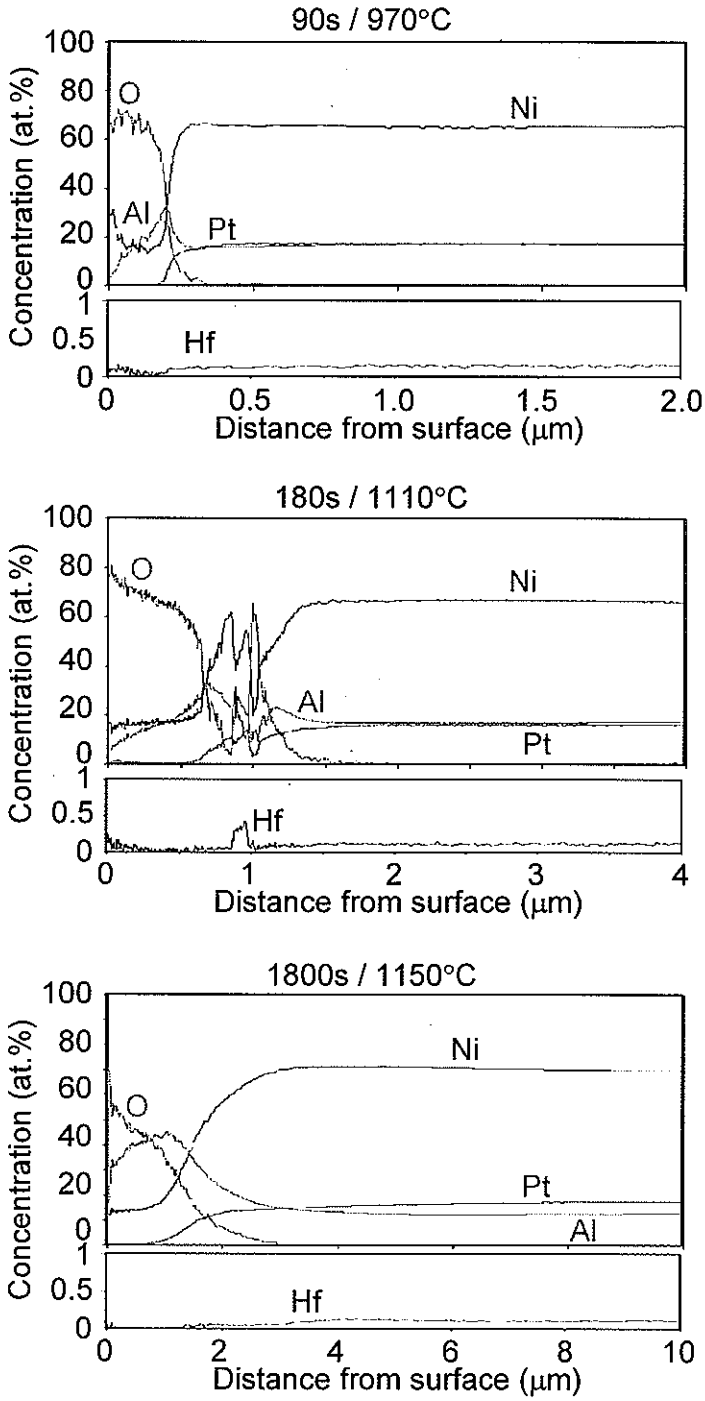

Figure 33. GD-OES composition profiles from the surface of oxidized Ni-25Al-20Pt-0.2Hf after 90, 180 and 1800 seconds.

Figure 34 shows GD-OES determined elemental concentration profiles as a function of distance starting from the scale surface into the substrate of Ni-25Al-0.5Hf alloy after each oxidation time. Without Pt addition, a 0.6μm NiO formed on Ni-25Al-0.5Hf after 90 seconds heating (970°C). With further increasing oxidation time after 180 seconds (1110°C), NiO thickened to ~2.3μm with the formation of a 5μm subsurface zone of the depletion of Ni and enrichment of Al. Moreover, Al enriched at the scale inner surface indicating the formation of more Al-rich oxide. There was a slight enrichment of Hf in the subsurface area at this stage. Due to its fast growing behavior, the thickness of NiO scale continued to increase to about 3.3μm after 1800 seconds exposure (1150°C). It is also seen that the Al concentration was higher than Ni in the oxide inner layer, which could provide the opportunity to the formation of more-protective Al_2O_3 scale. The scale thickness of outer NiO increased with increasing oxidation up to 1800 seconds, which suggests that the inner Al-rich oxide was not an exclusive Al_2O_3 scale so that the outward diffusion of Ni was continued. The enrichment of Hf within the subsurface area was prominent after 1800 seconds exposure. Results summarized above indicate that Hf-doped binary γ'-Ni_3Al alloys, without Pt additions, are certainly not protective Al_2O_3 formers.

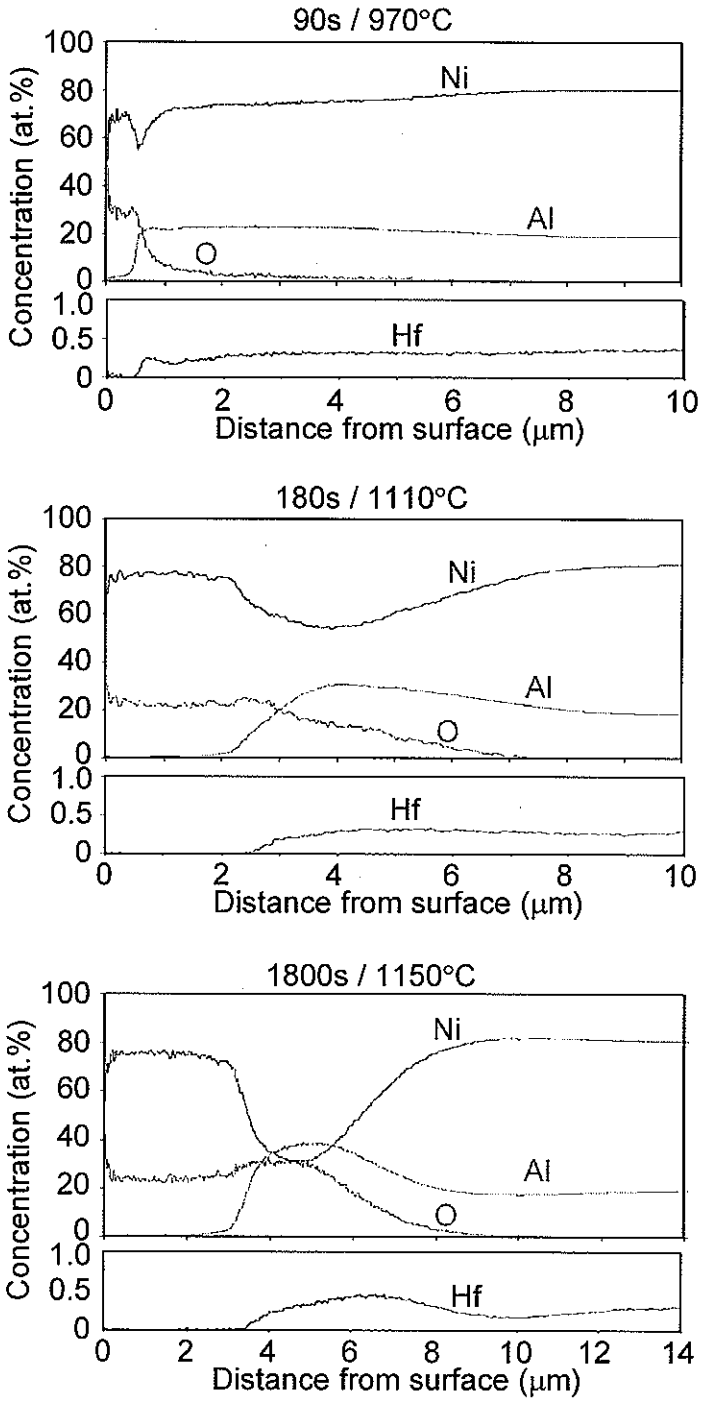

Figure 34. GD-OES composition profiles from the surface of oxidized Ni-25Al-0.5Hf after 90, 180 and 1800 seconds.

GD-OES resolved elemental concentration profiles as a function of distance penetrating from the scale surface into the subsurface Ni-25Al-10Pt-0.5Hf alloy after each oxidation time are shown in Figure 35. It is seen that 10at.% Pt to Ni-25Al-0.5Hf promote the formation of Al-containing oxide after 90 seconds heating (970°C). The scale thickness was about 0.3μm with increasing Al concentration towards the scale/alloy interface. Hf enriched at the scale outer surface. Meanwhile, a small peak of Hf was observed at the scale/alloy interface. The oxide became enriched with Al_2O_3 near the scale/alloy interface with further heating after 180 seconds (1110°C). Segregation of Hf at the scale/alloy interface was more prominent at this stage. With further heating after 1800 seconds exposure (1150°C), the scale was mostly comprised of Al_2O_3 without further increase of Ni content. The total scale thickness was about 1.2μm. Hf continued to segregate into the scale/alloy interface, where it could rather form very thermal stable HfO_2. This dynamic segregation process also resulted in the Hf concentration gradient from the alloy substrate down to the scale/alloy interface. It is verified that 10at.% Pt addition changed Ni-25Al-0.5Hf alloy from a NiO former to the protective Al_2O_3 former during the early-stage oxidation. This is also evidenced by that the weight change of Ni-25Al-10Pt-0.5Hf was less than half of on Pt-free Ni-25Al-0.5Hf after 1800 seconds exposure, as shown in Figure 23.

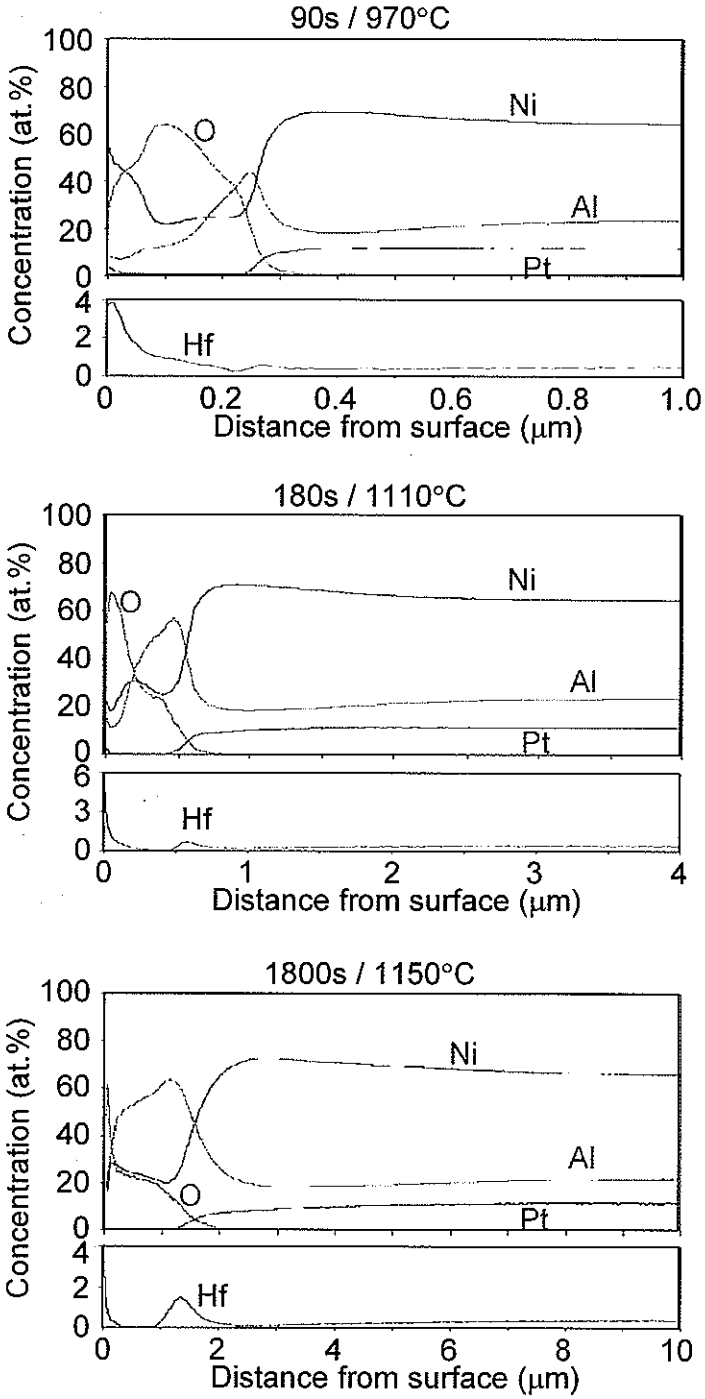

Figure 35. GD-OES composition profiles from the surface of oxidized Ni-25Al-10Pt-0.5Hf after 90, 180 and 1800 seconds.

Figure 36 shows GD-OES resolved elemental concentration profiles as a function of distance starting from the scale surface into the substrate of Ni-25Al-20Pt-0.5Hf alloy after each oxidation time. A thin scale less than 0.3μm formed after 90 seconds heating (970°C) with increasing Al content towards the scale/alloy interface. Contrary to Ni-25Al-10Pt-0.5Hf, there was not obvious enrichment of Hf at the scale outer surface on the alloy with 20at.% Pt addition. The thickness of Al-rich oxide further increased to about 0.5μm with increasing oxidation time after 180 seconds heating (1110°C). It is seen that there was less segregation of Hf at the scale/alloy interface after 180 seconds heating when 20at.% Pt was added to Ni-25Al-0.5Hf alloy. Al-rich oxide further thickened to about 1.6μm after 1800 seconds heating (1150°C). Meanwhile, segregation of Hf at the scale/alloy interface was much lowered than on Ni-25Al-10Pt-0.5Hf. Another important difference was the Ni content present in the scale. It is seen that the scale formed on Pt-modified Ni-25Al-0.5Hf alloys was the Ni-containing Al_2O_3 rather than exclusive alumina. The Ni content in the oxide layer was always lower on Ni-25Al-20Pt-0.5Hf alloy than on Ni-25Al-10Pt-0.5Hf alloy. These results suggest that higher Pt content facilitates the development and growth of more-exclusive Al_2O_3 scale in Hf-modified γ'-Ni_3Al alloys.

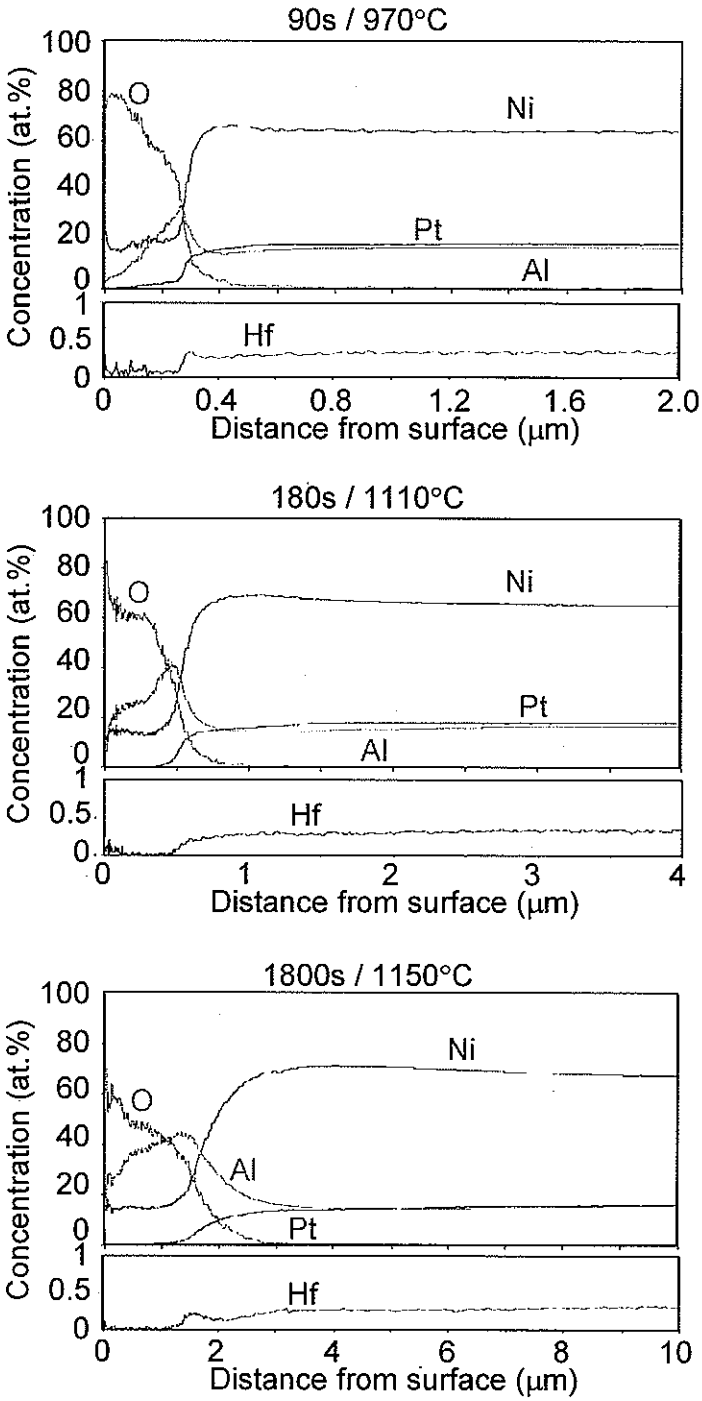

Figure 36. GD-OES composition profiles from the surface of oxidized Ni-25Al-20Pt-0.5Hf after 90, 180 and 1800 seconds.

So far the effects of Pt on the early-stage oxidation behavior of single-phase γ-Ni and γ′-Ni_3Al alloys have been assessed by examining the weight change, oxide surface morphology and GD-OES resolved elemental concentration profiles of each alloy after designated exposure time. The methodology used was to systematically increase Pt content from 0, 10 to 20at.% in each base model alloy, such as Ni-25Al, Ni-25Al-0.2Hf and Ni-25Al-0.5Hf.

When added into Hf-free γ′-Ni_3Al alloy Ni-25Al, Pt promotes the formation of Al_2O_3 by suppressing the development of fast-growing NiO. This was confirmed by the GD-OES results shown in Figures 29 and 30, which suggests that Pt and Al are chemically favorable with each other. Although Pt itself is relatively non-reacting at high temperatures, its presence may enhance the availability of Al at the scale/alloy interface so that the formation of more protective Al_2O_3 is possible in alloys with a relatively low Al content such as Ni-25Al. More appealing effect is that an adequate amount of Pt is able to promote the Al_2O_3-rich scale formation at lower temperatures (less than 1000°C), such as it does to Ni-12.5Al and Ni-25Al. The earlier a protective scale forms, the more resistant the alloy is to high-temperature oxidation. Once the protective Al_2O_3 forms, however, its growth rate is diffusion controlled and not much related to the Pt content in this early-stage oxidation. Figure 23a shows that Ni-25Al-10Pt and Ni-25Al-20Pt have similar weight changes after 1800 seconds of oxidation. This is also confirmed by their comparable scale thicknesses, as indicated by the GD-OES results in Figures 29 and 30.

When added to Hf-doped γ′-Ni_3Al alloys Ni-25Al-0.2Hf and Ni-25Al-0.5Hf, Pt additions not only affect Al_2O_3 growth, but also have an impact on the Hf behavior. Pt helps to enhance Al-rich oxide formation from the initial oxidation stage. It was shown in Figure 24 that the weight change of Ni-25Al-0.2Hf-xPt and Ni-25Al-0.5Hf-xPt (x=0, 10 and 20) alloys was proportionately decreased with increasing Pt content after 1800 seconds exposure. From the Al_2O_3-forming point of view, this corresponds well with the Pt effects exhibited on single-phase γ-Ni alloys and Hf-free γ′-Ni_3Al alloys. Comparing Figures 32 and 33, Figures 35 and 36 separately, it was also shown that higher Pt content helps to form a more exclusive Al_2O_3 scale as the Ni content detected by GD-OES was always lower in 20at.% Pt alloys than it in 10at.%Pt alloys. Meanwhile, the Hf enrichment at gas/scale interface, which is

believed to be the HfO_2 formation, was also lower on 20at.% Pt alloys than it on 10at.% Pt alloys. Besides, Pt additions change Ni-25Al-0.2Hf and Ni-25Al-0.5Hf alloys from NiO formers to Al_2O_3 formers. This suggests that the Pt addition may reduce the Hf activity so that there are less HfO_2 formation in alloys with higher Pt contents.

4.1.1.3 Hf Effects in γ'-Ni_3Al Alloys

Pt effects have been investigated and summarized above. For simplicity and clarity, Hf effects will be explored in this section. Hf was originally added to single-phase γ'-Ni_3Al alloys to confer the well-known reactive element effect on Al_2O_3 growth. Since Pt-free Ni-25Al is not an alumina former, however, Hf effects on the establishment and growth of NiO could be studied as a subsidiary topic. Therefore, all γ'-Ni_3Al alloys were grouped with fixed Al and Pt contents and their weight changes were plotted in Figure 37. This treatment leaves the Hf content as the only variable in each alloy group so that further illustration of Hf effects on scale growth rates could be more clearly seen. By going through the following results, it will be shown that Hf effects are inseparable with Pt effects when both elements were added into γ'-Ni_3Al alloys.

Figure 37a shows the weight change of Ni-25Al-xHf (x=0, 0.2 and 0.5) alloys after each early-stage oxidation time with increasing temperature. It is seen that all three alloys have similar weight change after 90 seconds (970°C), which could be attributed to the early establishment of NiO. With increasing temperature to 1110°C (180 seconds), the weight change of each alloy increased proportionally with its Hf content. The final weight change after 1800 seconds exposure for Ni-25Al, Ni-25Al-0.2Hf and Ni-25Al-0.5Hf was 0.18, 0.25 and 0.32 respectively. It is clearly seen that Hf accelerates the scale growth rates on Pt-free γ'-Ni_3Al alloys. This is also confirmed by the increasing NiO grain size with higher Hf content, as shown in Figures 25c, 26c and 27c. Although not forming oxide due to the competing NiO growth process, Hf tended to enrich at scale/alloy interface where HfO_2 growth could eventually take place. This is seen in Figures 31 and 34, with more Hf segregated at the scale/alloy interface with increasing oxidation exposure.

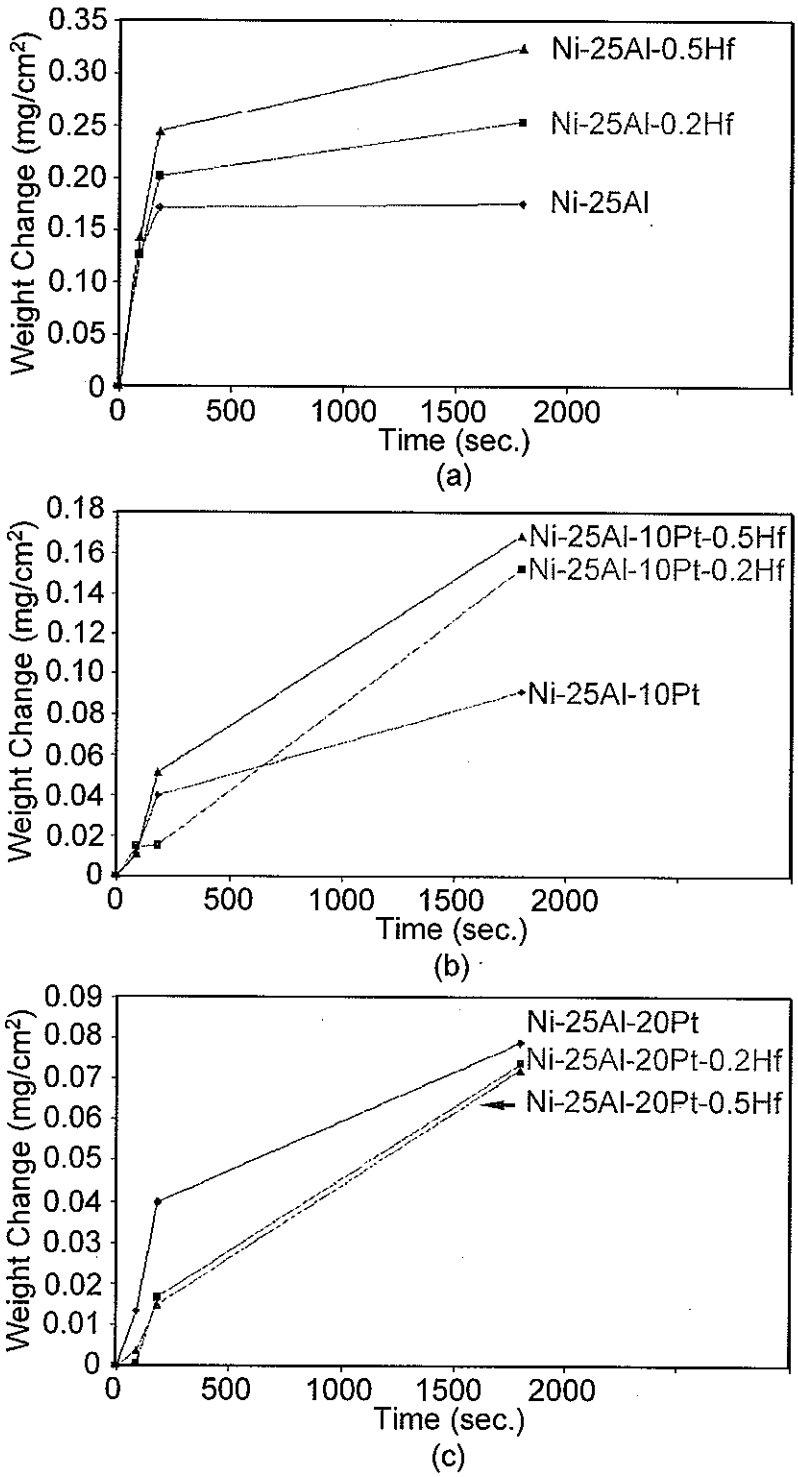

Figure 37. The early-stage anisothermal oxidation kinetics of the γ'-Ni_3Al alloys affected by Hf additions (a) Ni-25Al-xHf, (b) Ni-25Al-10Pt-xHf and (c) Ni-25Al-20Pt-xHf.

With 10at.% Pt added to Ni-25Al alloy, the single-phase γ'-Ni_3Al alloys became alumina-rich oxide formers in which Hf addition could act to decrease Al_2O_3-scale growth kinetics. It is shown in Figure 37b that the weight change of Ni-25Al-10Pt-xHf (x=0, 0.2 and 0.5) alloys increased with increasing Hf content after 1800 seconds at 1150°C. The final weight change of Ni-25Al-10Pt, Ni-25Al-10Pt-0.2Hf and Ni-25Al-10Pt-0.5Hf was 0.09, 0.15 and 0.17mg/cm^2, respectively. Therefore, Hf additions are likely to increase the early-stage oxidation kinetics, which is contrary to the desired beneficial RE effects as reducing the oxide growth rate. Figures 25f, 26f and 27f clearly showed that the scale surface morphology changed from typical Al_2O_3 network ridges to fine and compact particles, which are all notably differentiated from the large faceted NiO grains. This suggests that Hf additions in Ni-25Al-10Pt altered the early-stage scale growth mode and corresponding products. Indeed, GD-OES determined elemental concentration profiles provided some insights on the scale growth evolution affected by Hf additions.

It is seen in Figure 29 that Al content quickly surpassed Ni content and increased rapidly from the scale surface towards the scale/alloy interface; although the thin film was only about 0.13μm after 90 seconds of heating. During the following exposure to 1800 seconds, Al content remained continuously as the highest among all other elements present in the oxide scale. This result validates that Pt promotes Al_2O_3-scale formation. With Hf promoting NiO formation, there would thus be a competing process between Al_2O_3 and NiO formation when both Pt and Hf are co-doped into γ'-Ni_3Al alloys. Besides, Hf itself would take part in the oxidation process due to its high stability and fast oxygen conducting nature. It is shown in Figure 32 that Hf content was quite high near scale outer surface and Al content was lower than Ni after 90 seconds of heating. This implies that the thin film formed at the beginning was not as protective as a continuous and stoichiometric Al_2O_3 scale. This was reflected by the higher weight change with Ni-25Al-10Pt-0.2Hf alloy after 1800 seconds of exposure. The same deduction can be applied to Ni-25Al-10Pt-0.5Hf, except only that the higher Hf content may promote more NiO formation at the scale surface. As soon as the more protective Al-rich oxide formed, the scale growth kinetics significantly slowed. As shown in Figure 37b, Ni-25Al-10Pt-0.2Hf and Ni-25Al-10Pt-0.5Hf had similar scale growth rates after 180 seconds up to 1800 seconds. It is also worth noting that the Hf started

segregating to the scale/alloy interface with increasing oxidation time, as seen in Figures 32 and 35. More Hf enriched at the scale/alloy interface on Ni-25Al-10Pt-0.5Hf after 1800 seconds of heating than it did on Ni-25Al-10Pt-0.2Hf after the same exposure.

Figure 37c shows the progressive weight change of Ni-25Al-20Pt-xHf (x=0, 0.2 and 0.5) alloys after each early-stage oxidation time. The final weight change of each alloy after 1800 seconds of heating decreased with increasing Hf content: 0.078mg/cm^2 for Ni-25Al-20Pt, 0.074mg/cm^2 for Ni-25Al-20Pt-0.2Hf and 0.072mg/cm^2 for Ni-25Al-20Pt-0.5Hf. It is seen that Hf-free Ni-25Al-20Pt formed Al-rich oxide from the initial stage through to 1800 seconds, which is rather similar to the Ni-25Al-10Pt alloy shown in Figure 29. The difference in Hf-doped alloys is that there was only trivial Hf enrichment at the outer scale surface when 20at.% Pt was added. As shown in Figures 33 and 36, there was no noticeable surface enrichment of Hf, regardless of its content. Meanwhile, it is seen that the Hf enrichment at scale/alloy interface was suppressed with 20at.% Pt. These results may collectively suggest that Pt decreases Hf activity which could result in the faster formation of more protective Al-rich oxide scale.

The results presented above indicate that Hf accelerates NiO growth on Pt-free γ'-Ni_3Al alloys. This effect intensifies with increasing Hf content from 0.2 to 0.5at.% in this study. Early-stage Al_2O_3 formation was facilitated by Pt additions and NiO development assisted by Hf additions are competing scale-growth processes, which are influenced by the relative contents of Pt and Hf. Higher Pt certainly promoted more rapid establishment of more-protective Al-rich oxide and suppressed unwanted HfO_2 formation. Higher Hf is detrimental in terms of exhibiting its optimal reactive element effects by forming HfO_2. Alloys with optimum high-temperature oxidation resistance could be expected when the best combination of Pt and Hf were cautiously selected.

4.1.2 4-Day Isothermal Oxidation Results

Macro-images of the coupons at the completion of isothermal oxidation testing for four days at 1150°C in air are shown in Figure 38. The γ-Ni alloys showed uniform scale formation without noticeable oxide spallation. The scale formed on the binary Ni-12.5Al alloy was bluish in color, which is contrasted with the scales formed on the Pt-modified γ-Ni

alloys, which were grayish in color. As verified by the XRD, this difference in scale color is attributable to platinum additions to γ-Ni assisting in the formation of protective Al_2O_3 scales, which is generally grey in color. The binary γ′-Ni_3Al alloy experienced catastrophic scale spallation, as indicated in Figure 38. Extensive scale spallation from this alloy in the form of large oxide flakes during air-cooling from the oxidation temperature of 1150°C occurred. As confirmed by SEM image analysis, oxide scale spallation from the γ′-Ni_3Al alloys took place with decreasing extent in the sequence: Ni-25Al > Ni-25Al-0.2Hf > Ni-25Al-0.5Hf > Ni-25Al-10Pt > Ni-25Al-10Pt-0.2Hf. Thus, the combination of Pt and Hf was the most beneficial. In fact, and as indicated in Figure 38, no spallation could be observed on Ni-25Al-10Pt-0.5Hf, Ni-25Al-20Pt, Ni-25Al-20Pt-0.2Hf and Ni-25Al-20Pt-0.5Hf. The central radial cracks in some of coupons suggest that Pt addition increases the brittleness of γ′-Ni_3Al alloys.

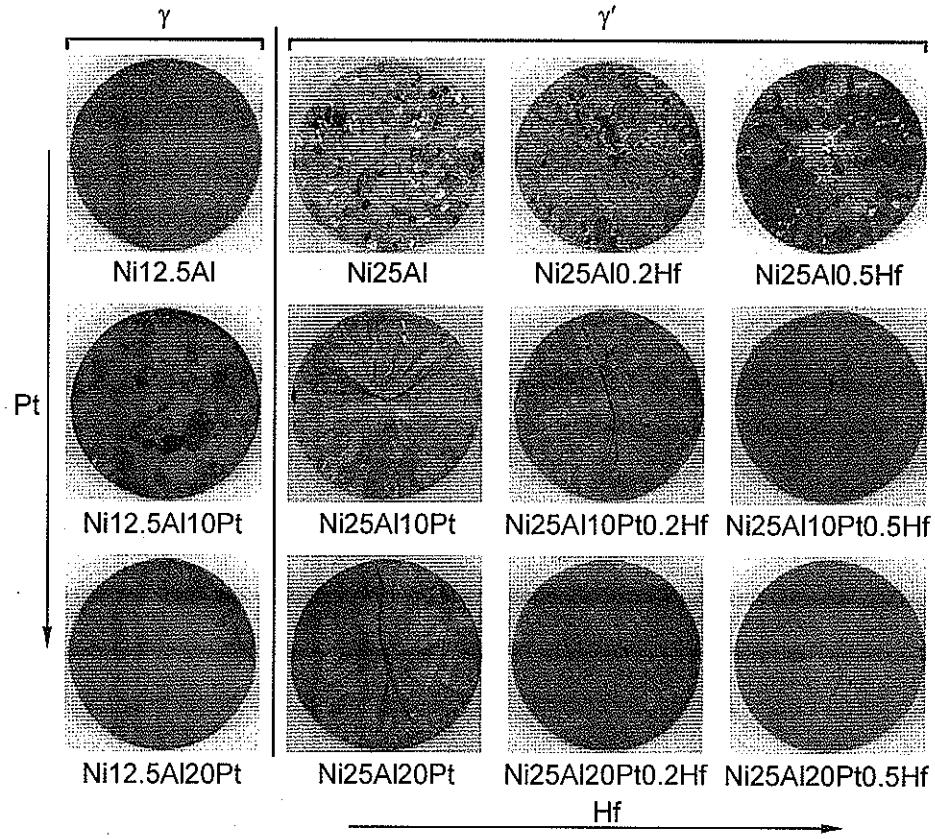

Figure 38. Digital optical micrographs showing the surface morphologies of disk-shaped oxidized coupons.

4.1.2.1 Effects of Platinum in γ-Ni Allloys

Figure 39 shows cross sections of the oxide scales formed on single-phase γ-Ni alloys after 4 days oxidation in air at 1150°C. All coupons were Cu-plated prior to metallographic preparation of the cross sections in order to avoid electronic charging during SEM examination. As shown in Figure 39a and verified with XRD and EDS results as well, the Ni-12.5Al alloy formed a 3-layered scale structure comprised of an outermost NiO layer, an intermediate layer of $NiAl_2O_4$, and an innermost layer rich in Al_2O_3. The alloy/scale interface is seen to be non-planar. Addition of Pt to the γ-Ni alloy apparently facilitated the primary formation of a more protective Al_2O_3 scale. The outward diffusion of Ni^{2+} was apparently hindered to the extent that no NiO was observed and only localized $NiAl_2O_4$ spinel was at the scale surface. The extent of $NiAl_2O_4$ formation decreased with increasing Pt content from 10 to 20at.%. Figure 40 summarizes the measured thickness of each constituent layer in the oxide scale formed on each single-phase γ-Ni alloy. The thickness of the Al_2O_3 layers is seen to decrease with increasing Pt content from 10 to 20at.%.

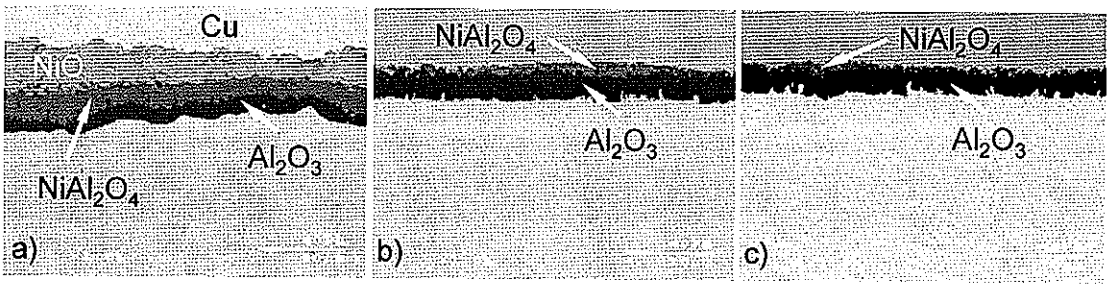

Figure 39. Cross-sectional SEM images showing alloys oxidized at 1150°C for 4 days: a) Ni-12.5Al; b) Ni-12.5Al-10Pt and c) Ni-12.5Al-20Pt.

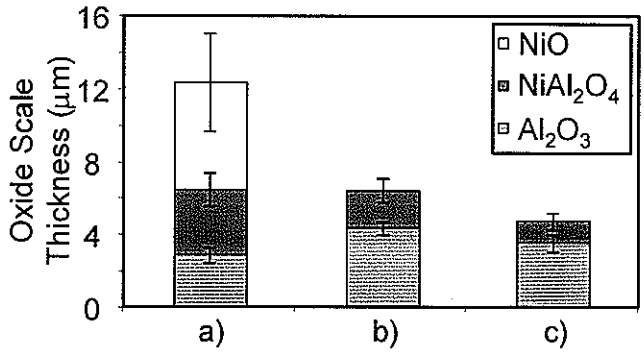

Figure 40. Measured scale thickness of each oxide-scale layer formed on γ-Ni alloys at 1150°C for 4 days: a) Ni-12.5Al; b) Ni-12.5Al-10Pt and c) Ni-12.5Al-20Pt.

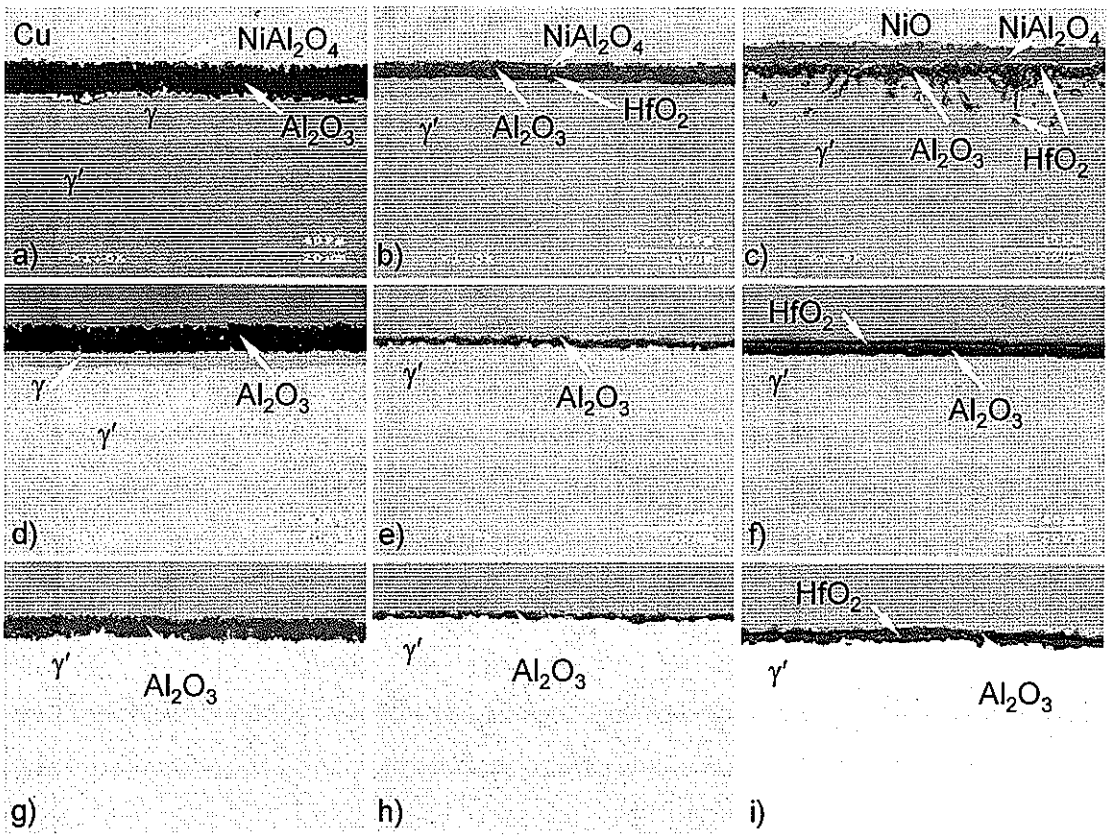

Figure 41. Cross-sectional SEM images showing alloys oxidized at 1150°C for 4 days: a) Ni-25Al; b) Ni-25Al-0.2Hf; c) Ni-25Al-0.5Hf; d) Ni-25Al-10Pt; e) Ni-25Al-10Pt-0.2Hf; f) Ni-25Al-10Pt-0.5Hf; g) Ni-25Al-20Pt; h) Ni-25Al-20Pt-0.2Hf and i) Ni-25Al-20Pt-0.5Hf.

Cross sections of the oxide scales formed on single-phase γ'-Ni_3Al alloys at 1150°C after 4 days are shown in Figure 41. All images were taken at x1500 magnification. It is recalled that a number of the alloys exhibited extensive scale spallation. In general, it appears that a combined positive effect of Pt+Hf on the isothermal oxidation behavior of γ'-Ni_3Al alloys primarily involves an improvement in the adherence of a slow-growing Al_2O_3 scale. Yet to explore their unique beneficial effects objectively, it is prudent to analyze Pt and Hf individually, as will be presented in the following.

4.1.2.2 Effects of Platinum in γ'-Ni_3Al Allloys

The γ' Ni-25Al alloy formed a planar ~5μm Al_2O_3 scale with a discontinuous layer of $NiAl_2O_4$ at the scale surface after 4 days isothermal oxidation at 1150°C (Figure 41a). This alloy also developed a subsurface layer (~8μm) of γ-Ni owing to a greater amount of selective oxidation of Al relative to Ni. As shown in Figure 41d, 10at.% Pt addition, as in alloy Ni-25Al-10Pt, resulted in the exclusive formation of an Al_2O_3 scale, with a reduced thickness of ~4.5μm. The depth of the aluminum-depleted γ-Ni zone diminished to ~3μm, which is about two times lower than in the Pt-free Ni-25Al alloy. With even higher Pt content, as in the Ni-25Al-20Pt alloy (Figure 41g), a slightly thinner (~3.8μm) exclusive Al_2O_3 scale formed. This scale also showed no evidence of spallation. Additionally, no γ-Ni subsurface layer was observed. As seen in Figures 41a, d and g, Pt-containing γ'-Ni_3Al alloys have a potential to develop a planar, adherent and slow-growing Al_2O_3 oxide scale.

Figure 41b shows that Ni-25Al-0.2Hf formed a mixed scale layer of Al_2O_3 and HfO_2 at 1150°C. This scale exhibited considerable scale spallation at the completion of oxidation. With 10at.% Pt in the alloy, as in the Ni-25Al-10Pt-0.2Hf alloy (Figure 41e), formation of spinel was totally suppressed and the thickness of Al_2O_3 scale was decreased. Moreover, this scale showed no apparent spallation. 20at.% of Pt addition effectively resulted in the formation of a homogeneous and continuous Al_2O_3 scale with the lowest scale thickness and without any indication of spallation, as shown in Figures 41h and 42f.

As seen in Figure 41c, the Pt-free Ni-25Al-0.5Hf alloy formed a complex and non-uniform oxide scale structure at 1150°C, consisting of a continuous layer of $NiAl_2O_4$ spinel on the top of a mixture of Al_2O_3 and HfO_2. In addition, there was a discontinuous distribution

of NiO at the scale surface as well as internal HfO_2 surrounded by Al_2O_3. However, addition of 10at.% Pt to the Ni-25Al-0.5Hf alloy resulted in the development of a more planar Al_2O_3 oxide scale with an outer band of the scale containing HfO_2 precipitates, as shown in Figure 41f. There was no observable trace of $NiAl_2O_4$. With 20at.% Pt addition to the Ni-25Al-0.5Hf alloy, an even thinner Al_2O_3 scale formed and there were much less HfO_2 precipitates, Figures 41i and 42i.

Comparison between the high-temperature isothermal oxidation behavior of Pt-free and Pt-containing single-phase γ'-Ni_3Al alloys shows that the main effect of platinum addition is to promote the exclusive formation of an adherent Al_2O_3 scale. Additionally, Pt contributes to reduce the undesired internal oxidation of Hf. However, it seems likely that the addition of Pt at least above 10at.% increases the brittleness of Ni-25Al-based γ'-Ni_3Al alloys.

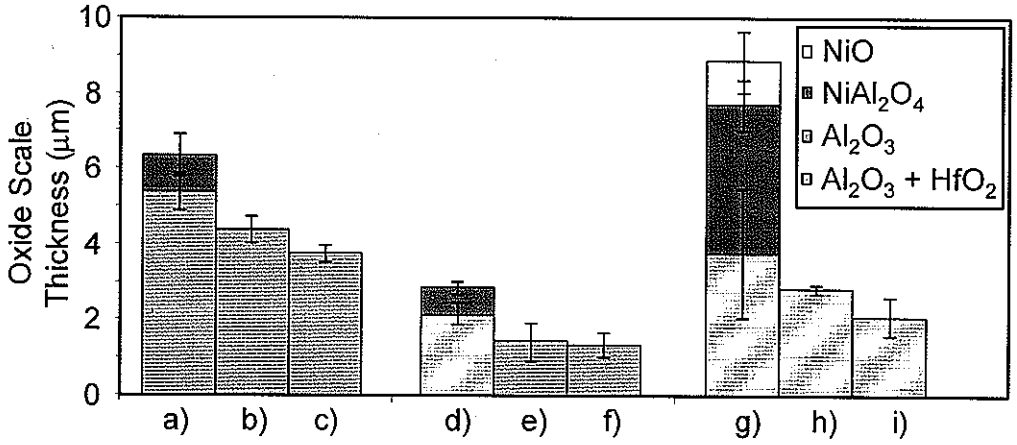

Figure 42. Measured thickness of constituent layers in the oxide scales formed on γ'-Ni_3Al alloys at 1150°C for 4 days: a) Ni-25Al; b) Ni-25Al-10Pt; c) Ni-25Al-20Pt; d) Ni-25Al-0.2Hf; e) Ni-25Al-10Pt-0.2Hf; f) Ni-25Al-20Pt-0.2Hf; g) Ni-25Al-0.5Hf; h) Ni-25Al-10Pt-0.5Hf and i) Ni-25Al-20Pt-0.5Hf.

4.1.2.3 Effects of Hafnium in γ'-Ni_3Al Alloys

Examination of the effects of Hf addition on the oxidation behavior of the single-phase γ' alloys can be approached by comparing the relevant results shown in Figures 38 and

41. Addition of 0.2at.% Hf to the Ni-25Al alloy resulted in the formation of a thinner Al_2O_3 oxide and $NiAl_2O_4$ spinel with less scale spallation and the absence of a γ-Ni subsurface layer, as seen in Figure 41b. The thinner spinel at the scale surface is more continuous than what formed on the Ni-25Al alloy. Increasing Hf content to 0.5at.% in the Ni-25Al alloy increased the extent of spinel formation and led to a small amount of NiO formation at the scale surface, as seen in Figure 41c. It is also seen in this figure that the inner Al_2O_3 contained a rather large amount of HfO_2, with some of the HfO_2/Al_2O_3 product protruding into the alloy.

Hafnium exhibits a more pronounced effect in the case of the Pt-containing alloys. As seen in Figure 41e, the thickness of Al_2O_3 scale formed on Ni-25Al-10Pt-0.2Hf is one third of that formed on the Hf-free Ni-25Al-10Pt alloy (Figure 41d). Additionally, a subsurface γ-Ni layer did not form in 0.2at.% Hf-doped Ni-25Al-10Pt, due presumably to the slow growth of Al_2O_3 on this alloy. However, 0.5at.% Hf additions exhibited detrimental effects, as a much thicker Al_2O_3 scale containing HfO_2 inclusions formed, as seen in Figure 41f for the Ni-25Al-10Pt-0.5Hf alloy.

As seen in Figure 41h and summarized in Figure 43, 0.2at.% Hf addition to the Ni-25Al-20Pt γ' alloy showed the best isothermal oxidation resistance at 1150°C by forming a ~1.5μm Al_2O_3 oxide, with no evidence of scale spallation or subsurface development of a γ-Ni layer. Increasing Hf content in Ni-25Al-20Pt to 0.5at.% promoted the Hf oxidation with enhanced Al_2O_3 growth (Figures 41i and 43i).

Figure 43 illustrates that Hf tends to increase the extent of formation of less-protective nickel oxide and spinel as NiO and $NiAl_2O_4$ when added to Pt-free Ni-25Al. However, 0.2at.% Hf addition was increasingly beneficial to the scaling behavior of the γ' alloy with increasing Pt from 10at.% up to 20at.%. A mixed scale of Al_2O_3 and HfO_2 formed on alloys overdoped with 0.5at.% Hf, suggesting there is an optimum Hf level for a given alloy.

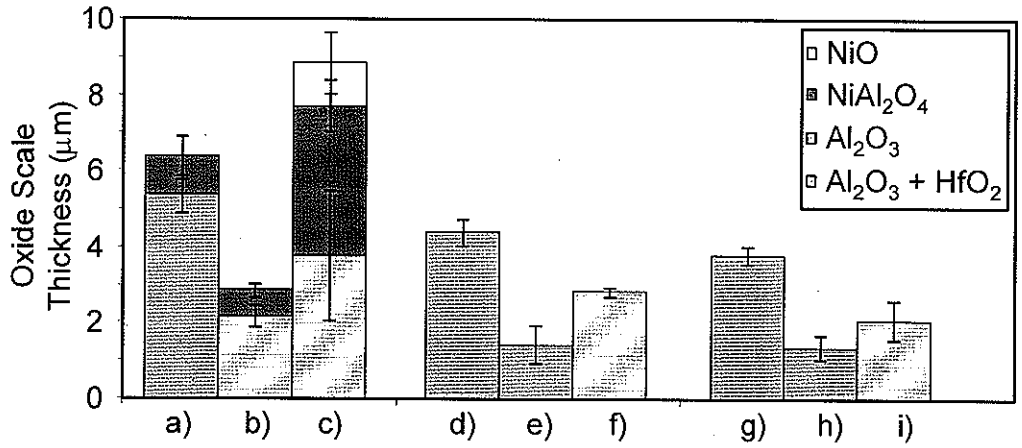

Figure 43. Measured thickness of constituent layers in the oxide scales formed on γ'-Ni_3Al alloys at 1150°C for 4 days: a) Ni-25Al; b) Ni-25Al-0.2Hf; c) Ni-25Al-0.5Hf; d) Ni-25Al-10Pt; e) Ni-25Al-10Pt-0.2Hf; f) Ni-25Al-10Pt-0.5Hf; g) Ni-25Al-20Pt; h) Ni-25Al-20Pt-0.2Hf and i) Ni-25Al-20Pt-0.5Hf.

4.2 Two-Phase γ-Ni+γ'-Ni_3Al Alloys

In practice, high-temperature materials such as superalloys and metallic coatings contain two or more phases [96, 97]. After the preliminary investigation of high-temperature oxidation behavior of single-phase γ-Ni and γ'-Ni_3Al alloys affected by Pt and Hf additions, their effects on two-phase γ-Ni+γ'-Ni_3Al alloys will be examined in this section. Since the most common way to improve high-temperature oxidation resistance is by adding a small amount reactive element (RE) or reactive element oxide to the alloy or coating, the main focus of the current study is the effect of Hf on thermally grown oxide (TGO) scaling kinetics and resulting morphologies.

Seven alloys were prepared with nominal compositions, as shown in Table 4. The base alloy used in this study is Ni-20Al-20Pt as the model composition for high temperature resistant coatings. Increasing content of reactive element Hf, ranges from 0 to 0.91at.%, was added as alloy additions. Thermal gravimetric analyses (TGA) were performed at 1150°C on these alloys to examine the mass-gain kinetics during the high temperature dwell times. To form oxides characteristic of the actual oxidizing temperature rather than those formed upon

furnace heating period, all samples hung by the sapphire on the balance were rapidly immersed into the furnace which is already preheated at the desired temperature. The heating rate of the sample was about 150°C/min. After a 100-hour exposure in laboratory-scale breathing air with the velocity of 70cm^3/minute at 1150°C, all samples were then furnace cooled to room temperature. Long-term (500 cycles) cyclic oxidation was performed on all alloy samples at 1150°C as well to examine their high-temperature thermal cycling resistance. The weight change of each sample was measured by the electronic analytical balance at intermittent cycles. To examine the phase composition presented in alloys at 1150°C, all samples were heated to 1150°C for 1 hour followed with water quenching to withhold high-temperature phases, then cross-sectioned and etched with chromic acid to enhance the phase contrast for SEM examination.

Table 4. Nominal composition (in at.%) of bulk Ni-20Al-20Pt-xHf alloys.

	Ni	Al	Pt	Hf	Phase
Ni-20Al-20Pt	bal.	20	20	0	
Ni-20Al-20Pt-0.05Hf	bal.	20	20	0.05	
Ni-20Al-20Pt-0.13Hf	bal.	20	20	0.13	
Ni-20Al-20Pt-0.23Hf	bal.	20	20	0.23	$\gamma + \gamma'$
Ni-20Al-20Pt-0.31Hf	bal.	20	20	0.31	
Ni-20Al-20Pt-0.48Hf	bal.	20	20	0.48	
Ni-20Al-20Pt-0.91Hf	bal.	20	20	0.91	

4.2.1 TGA Results

Isothermal oxidation kinetics of Ni-20Al-20Pt -xHf alloys at 1150°C for 100 hours are shown in Figure 44. Based on the SEM observations and inherent ideal performance of protective Al_2O_3 scale, it is assumed that there was no spallation occurred during the high-temperature exposure on all samples. Thus, the measured mass gain is considered to be a net mass change totally from oxygen uptake. The weight change of the base alloy Ni-20Al-20Pt-0Hf was artificially trimmed off to present the lower weight change of Hf-doped alloys and

the final weight change of the base alloy after 100 hours is 1.27mg/cm^2. It is clearly seen that the addition of Hf markedly decreases the weight change. The overall effect was to reduce the weight change by factors of between 3 for 0.05Hf and 6 for 0.48Hf from the base alloy after 100 hours. It is observed that the weight change decreases regularly with increasing Hf content from 0.05 to 0.48at.%. However, 0.91at.% Hf addition to the base alloy shows similar weight change as Ni-20Al-20Pt-0.05Hf alloy. This will be discussed later as the observation of the scale formed on the alloy with 0.91Hf is comprised of both Al_2O_3 and internally oxidized HfO_2, which indicate that over-doped alloy exhibits detrimental RE effects.

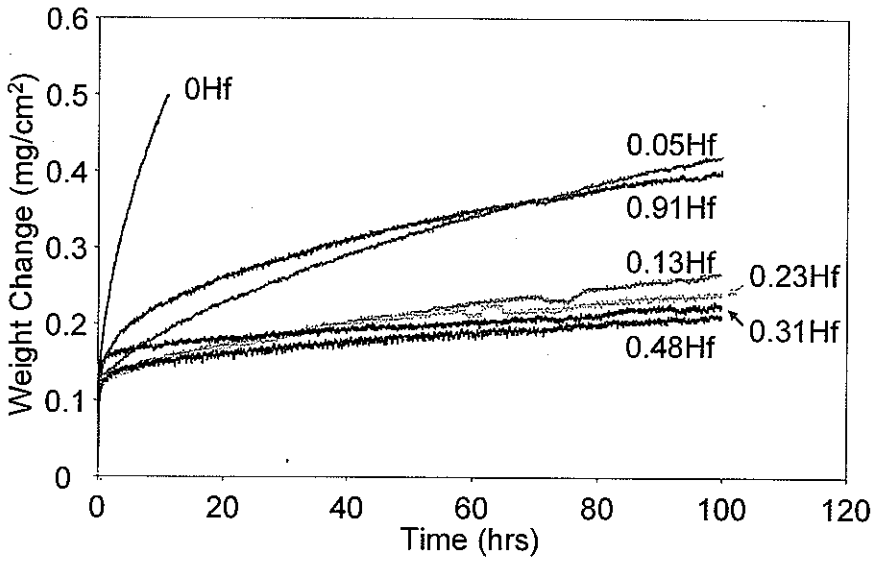

Figure 44. Isothermal mass change of Ni-20Al-20Pt-xHf at 1150°C for 100 hours.

The instantaneous rate constant kp' (apparent rate constant) for each alloy was plotted as a function of time as seen in Figure 45. It is seen that the Hf additions decreases the k_p' value by more than one order of magnitude at the steady-stage oxidation. The most noticeable effect of Hf additions is the fast transition from transient-stage to steady-stage. All Hf-doped alloys exhibit a lower initial reaction rate than that of the base alloy, which implies that the Hf addition accelerates the initial scale nucleation and improves the development of

the protective scale. Therefore, less time is required in transition to the following steady-stage oxidation.

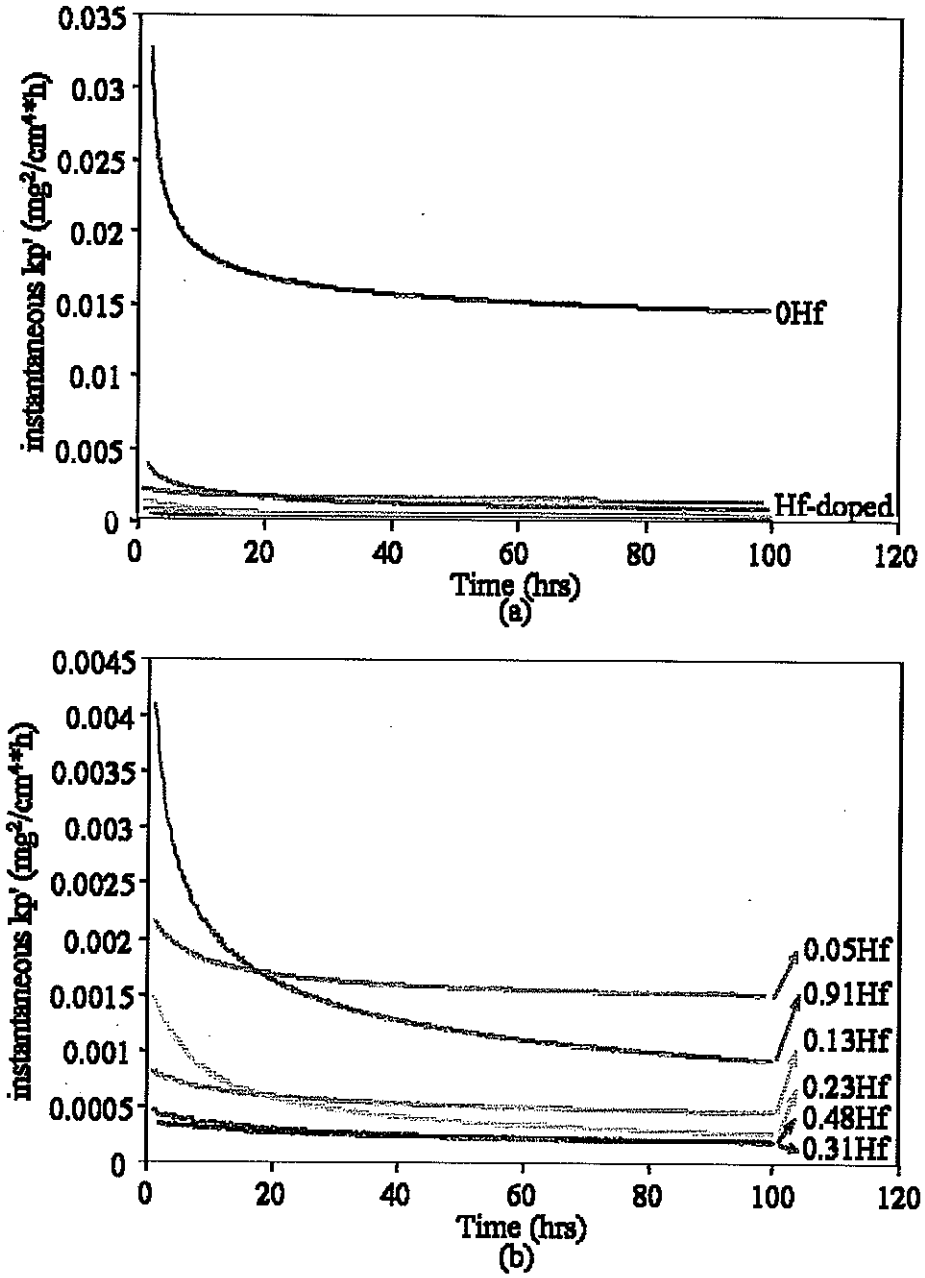

Figure 45. Instantaneous rate constant k_p' as a function of time for Ni-20Al-20Pt-xHf alloys at 1150°C after 100 hours.

Figure 45b presented the k_p' value for only Hf-doped alloys. In a similar way as shown in Figure 44, the reaction rate decreases with increasing Hf content from 0.05at.% to 0.48at.%. Despite that the 0.31Hf shows the slowest rate rather than higher than 0.48Hf, the difference is very minimal. This exception could arise from many factors such as samples crystallographic orientation, phase distribution and Hf segregation. However, a much higher scaling kinetics exhibited by the alloy with 0.91at.% Hf addition could result from the overdoped-Hf as the formation of excessive HfO_2.

In order to verify the Hf effects on the scale growth rate at 1150°C, the isothermal oxidation kinetics were measured and steady-stage reaction rates are listed in Table 5 for each alloy. The parabolic rate constant of Ni-20Al-20Pt-0.05Hf is an order of magnitude lower than that of the base alloy, and even further reduced by two orders of magnitude in the alloy with 0.31at.% Hf. These significant reductions in the parabolic scaling rate suggest that the transport mechanism of Al cation in the scale is altered at the presence of Hf, which tends to segregate into the oxide grain boundaries.

Table 5. Parabolic rate constants at steady state from TGA for Ni-20Al-20Pt-xHf at 1150°C after 100 hours.

Alloy with Hf Content	k_p ($g^2/cm^4 \cdot sec$)
0Hf	3.74×10^{-12}
0.05Hf	3.34×10^{-13}
0.13Hf	0.75×10^{-13}
0.23Hf	0.48×10^{-13}
0.31Hf	0.16×10^{-13}
0.48Hf	0.22×10^{-13}
0.91Hf	1.83×10^{-13}

Figure 46 shows the surface morphology of scales formed on Ni-20Al-20Pt-xHf alloys at 1150°C after 100 hours. The smooth fine-grain patches were observed on the base alloy, as seen in Figure 46a. By adding 0.05at.% Hf addition, oxide ridges were developed as close-packed networks with few depression zones, as shown in Figure 46b. More pronounced

lace-like network was formed with enlarged ridge spacings as the Hf addition increases from 0.13 to 0.91at.%, as seen in Figure 46c to g. The white particle clusters appeared on the top of ridges are likely to be HfO_2 particles as a result of outward diffusion of Hf along the scale grain boundaries [98, 99].

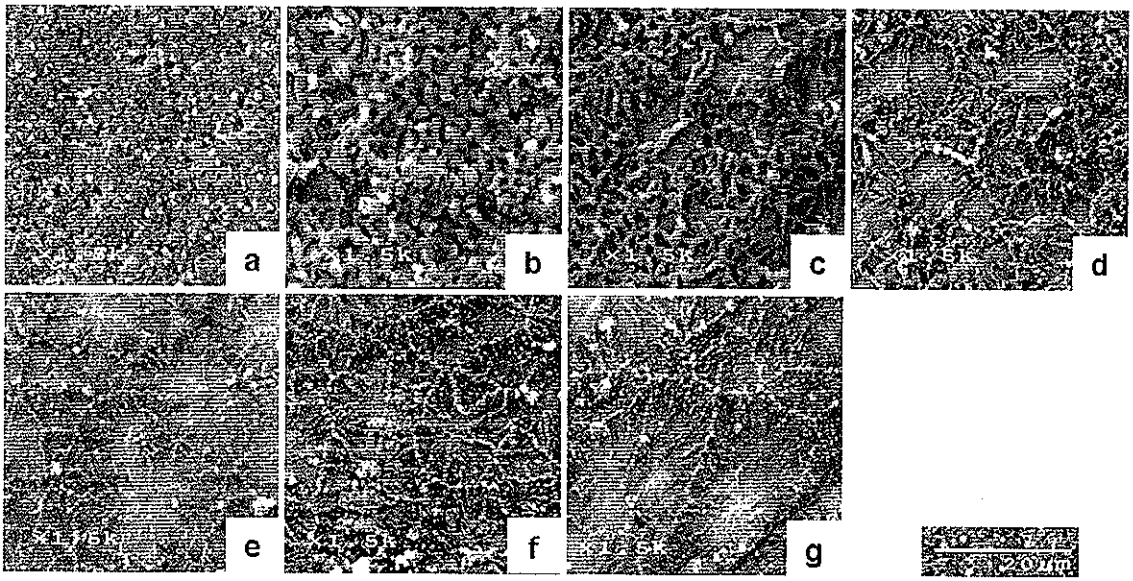

Figure 46. SEM images showing the surface morphology of scales formed on Ni-20Al-20Pt-xHf alloys at 1150C after 100 hours: a) 0Hf; b) 0.05Hf; c) 0.13Hf; d) 0.23Hf; e) 0.31Hf; f) 0.48Hf and g) 0.91Hf.

In order to examine the scale thickness and scale-alloy interface, cross sections of each sample were prepared, as shown in Figure 47. The dark phase and light phase in the substrate presented in each alloy correspond to γ-Ni and γ′-Ni_3Al phase, respectively. The base alloy (Figure 47a) formed a continuous planar Al_2O_3 scale with average 6.5μm in thickness, which is much thicker than scales formed on the rest Hf-doped alloys. A uniform γ-Ni(Al) denuded subsurface layer developed due to the fast outward Al diffusion to form the Al_2O_3 scale. Cusps along the scale-alloy interface from the alloy to oxide were observed and few small alloy islets were found elsewhere encroached by the scale. Figure 47b shows that the Al_2O_3 scale formed on the alloy with 0.05at.% Hf is non-uniform in thickness, although much thinner than the scale formed on the base alloy. The thickness of the denuded γ-Ni

subsurface layer is markedly reduced as well. These results correspond well with those found in scaling kinetics as shown in Figure 44, which indicates that 0.05at.%Hf effectively decreases the oxide growth rate which in turn results in less aluminum depletion within the alloy. With increasing Hf content, the cross sections of alloys from 0.13Hf to 0.48Hf exhibit a more uniform scale in thickness and a smoother scale-gas interface than the scale-alloy interface, as seen in Figure 47c to f. As shown in Figure 47g, the scale formed on the alloy with 0.91at.% Hf exhibits a smooth scale-gas interface, as opposed to the rough scale-alloy interface with oxide intrusions and internally oxidized HfO_2 precipitates indicated by arrows.

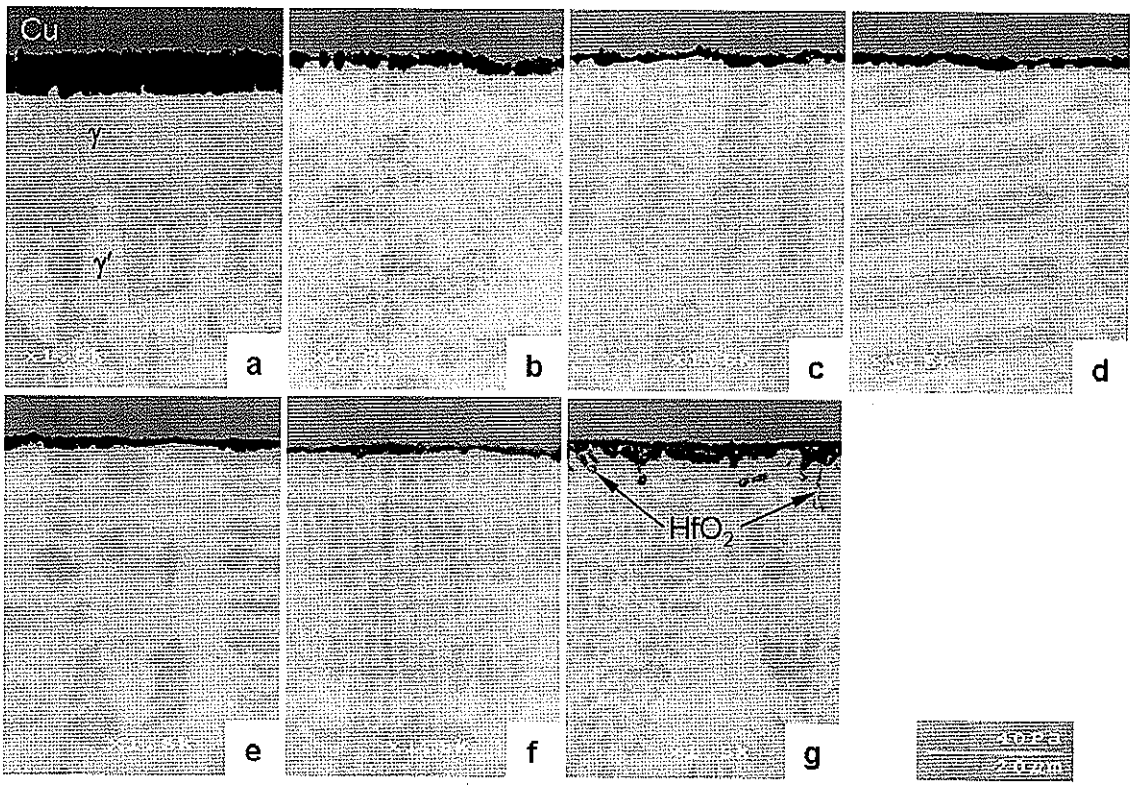

Figure 47. Cross-sectional SEM images showing the scale formed on Ni-20Al-20Pt-xHf alloys at 1150C after 100 hours: a) 0Hf; b) 0.05Hf; c) 0.13Hf; d) 0.23Hf; e) 0.31Hf; f) 0.48Hf and g) 0.91Hf.

4.2.2 Cyclic Oxidation Results

Figure 48a shows the cyclic oxidation weight change of Ni-20Al-20Pt-xHf alloys at 1150°C after 500 cycles. For the purpose of comparison, Pt-modified β alloy Ni-50Al-15Pt was added into the test because of its comparable composition as currently being most-widely used metallic coatings. The weight change curves of both Ni-20Al-20Pt and Ni-50Al-50Pt were artificially trimmed off again to better present the lower weight change of Hf-doped alloys and the final weight change was 1.70mg/cm^2 for Ni-20Al-20Pt and 1.53mg/cm^2 for Ni-50Al-15Pt after 500 cycles. All other Hf-doped alloys performed in a similar way in decreasing the weight change as they did in isothermal TGA test summarized in Section 4.2.1. Compared to the rest Hf-doped alloys, 0.91at.% Hf addition to the alloy shows a high weight change as 1.16mg/cm^2 after 500 cycles which could be attributed to the formation of unwanted HfO_2. 0.05at.% Hf addition was not sufficient to perform an uniform grain boundary blocking effects so that the final weight change of it after 500 cycles was 0.72mg/cm^2 which is still higher than other alloys with Hf additions ranging from 0.13 to 0.48at.%. A remarkable finding was unveiled by enlarging the time scale and focusing on the initial oxidation stage as seen in Figure 48b. It is seen that Hf-free base alloy Ni-20Al-20Pt exhibited a gradually increased weight change with increasing oxidation time without the abrupt slope change. However, all Hf-doped alloys oxidized at a faster rate than the base alloy Ni-20Al-20Pt during the first two hours oxidation and after which the kinetics rapidly slows down to a value much slower than that of the base alloy. Besides, the weight change of Hf-doped alloys increased proportionally with the Hf content during the first 5 hours. This phenomenal difference caused by Hf additions could be attributed to the growth and development of different oxidation products which need to be further investigated with advanced analytical techniques.

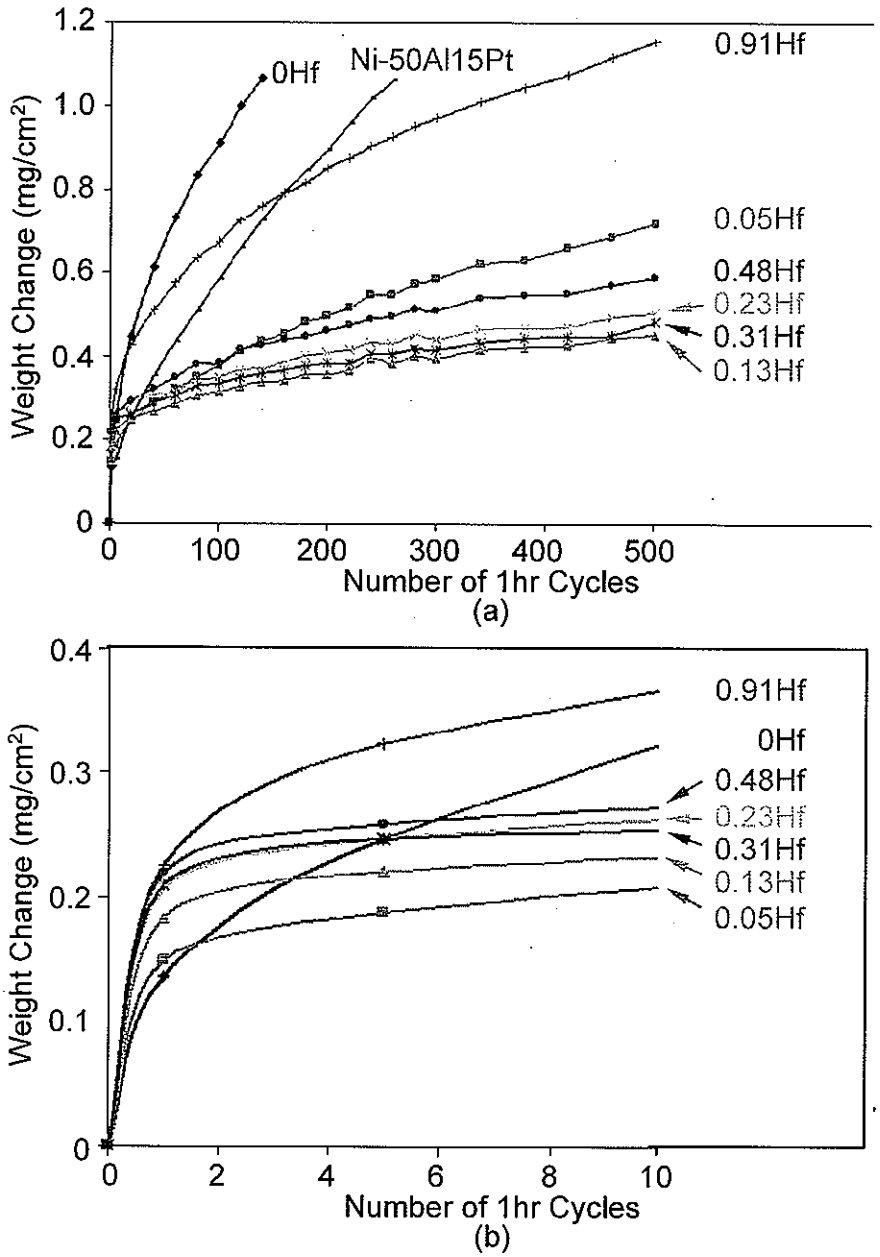

Figure 48. The weight change of Ni-20Al-20Pt-xHf alloys at 1150C after a) 500 cycles and b) 10 cycles.

The surface morphology of scales formed on Ni-20Al-20Pt-xHf alloys at 1150C after 500 cycles are shown in Figure 49. The surface of base alloy Ni-20Al-20Pt was featured by randomly spread whiskers decorating on the smooth subscale as seen in Figure 49a. 0.05at.%

Hf addition to the base alloy changed the scale to close-packed network ridges similar as seen in Figure 46b. Less ridges with larger network spacings were seen in Figure 49c and d as increasing Hf content in the base alloy from 0.13 to 0.23at.%. The oxide surface became smooth patches with further increasing Hf content from 0.31 to 0.91at.% without noticeable network ridges as seen in Figure 49e to g.

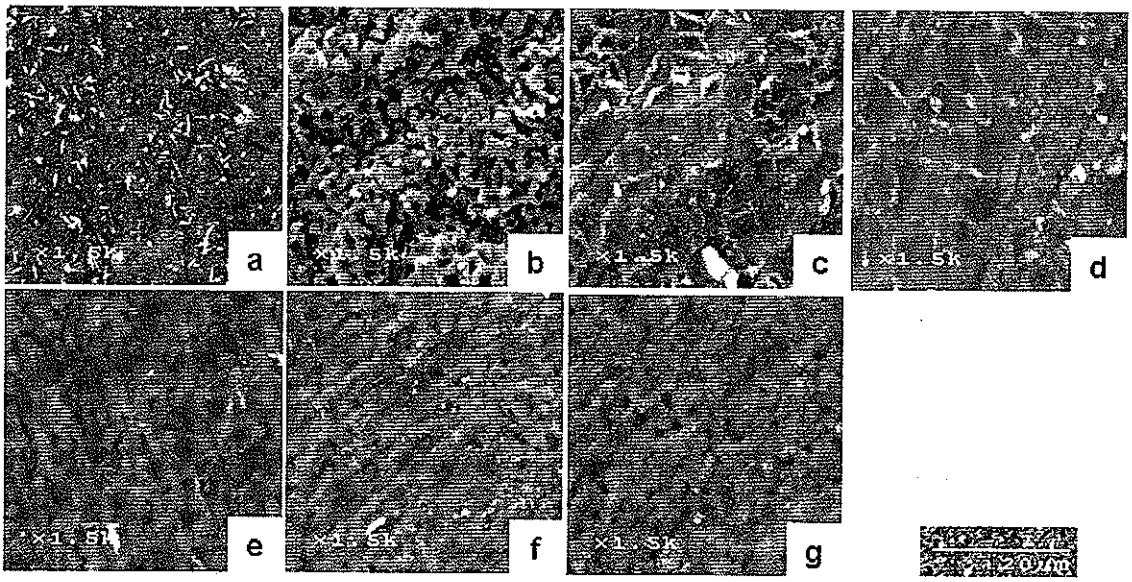

Figure 49. SEM images showing the surface morphology of scales formed on Ni-20Al-20Pt-xHf alloys at 1150°C after 500 cycles: a) 0Hf; b) 0.05Hf; c) 0.13Hf; d) 0.23Hf; e) 0.31Hf; f) 0.48Hf and g) 0.91Hf.

Cross sections of each sample were then prepared to examine the scale thickness and subsurface evolution affected by Hf addtions as showin in Figure 50. The darker and lighter phase in each figure corresponds to γ-Ni and γ'-Ni_3Al phase, respectively, as marked in Figure 50b. Al_2O_3 scale formed on the base alloy Ni-20Al-20Pt was planar and uniform in thickness about 10.3μm with the develpment of a 35μm γ-Ni subsurface layer. The scale thickness was remarkably reduced when 0.05at.% Hf was added, although the oxide was nonplanar and rumpled. It is seen from Figure 50c to f that the scale became more planar with increasing Hf content from 0.13 to 0.48at.%. And the gas/scale interface is relatively smoother than the scale/alloy interface. However, 0.91at.% Hf was over-doped into Ni-20Al-

20Pt so that extensive HfO_2 was formed as a continuous layer within the Al_2O_3 scale and internal islands in alloy subsurface as well. Results obtained from the cyclic oxidation study indicate that Hf could exhibit beneficial RE effects as adding within optimum amount range into γ+γ' alloys. It could also perform negative effects when over-doped beyond its optimal content as the formation of HfO_2 with accelerated Al_2O_3.

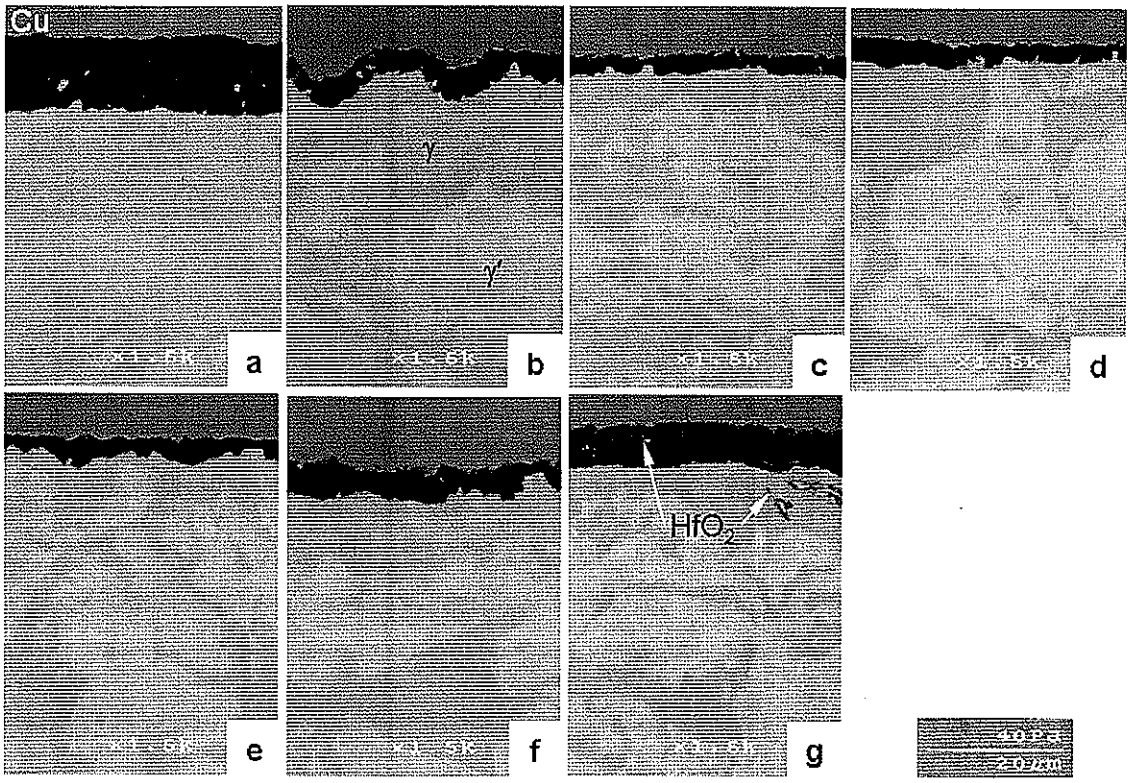

Figure 50. Cross-sectional SEM images showing the scale formed on Ni-20Al-20Pt-xHf alloys at 1150°C after 500 cycles: a) 0Hf; b) 0.05Hf; c) 0.13Hf; d) 0.23Hf; e) 0.31Hf; f) 0.48Hf and g) 0.91Hf.

4.2.3 Partitioning Behavior of Hf

Figure 51 shows the high temperature phases retained by water quenching of 1-hour pre-heated Ni-20Al-20Pt-xHf alloys at 1150°C. The dark phase and light phase presented in each alloy correspond to γ-Ni and γ'-Ni_3Al phase, respectively. The large dendritic γ-Ni

islands change to smaller size and finer shape within the γ′-Ni_3Al matrix as increasing Hf content from 0.05at.% to 0.91at.%.

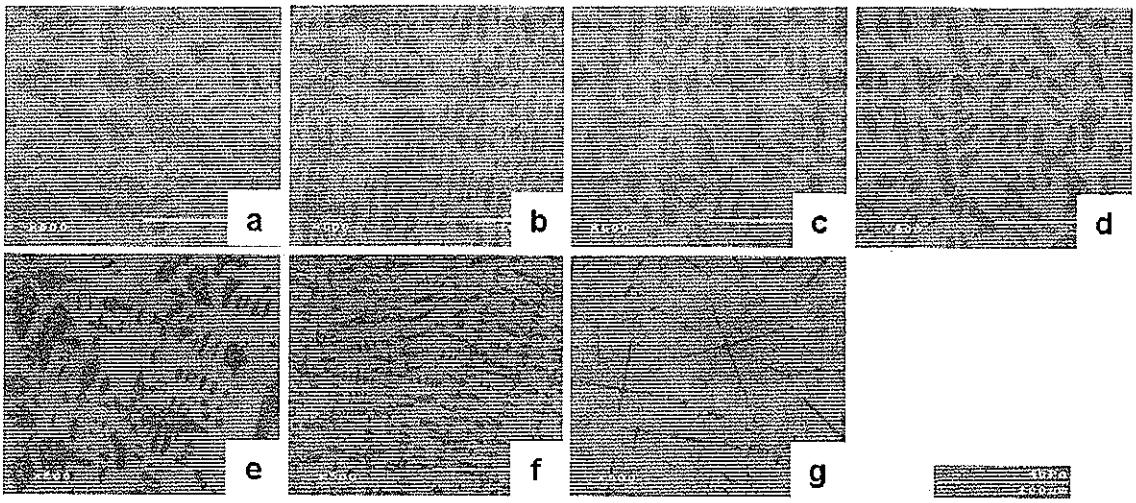

Figure 51. SEM images showing the high temperature phases presented in Ni-20Al-20Pt-xHf alloys at 1150°C: a) 0Hf; b) 0.05Hf; c) 0.13Hf; d) 0.23Hf; e) 0.31Hf; f) 0.48Hf and g) 0.91Hf.

Image analysis was then attempted to examine the Hf content effect on high-temperature phase compositions. As shown in Figure 52, the amount of both γ′-Ni_3Al and γ-Ni phases slightly varied with increasing Hf content since the major determining factors affecting the phase composition would still be the main alloying element concentrations of Ni, Al and Pt. Accordingly, Hf additions barely contribute to extend the configuration of more Al_2O_3-forming helpful γ′-Ni_3Al phases.

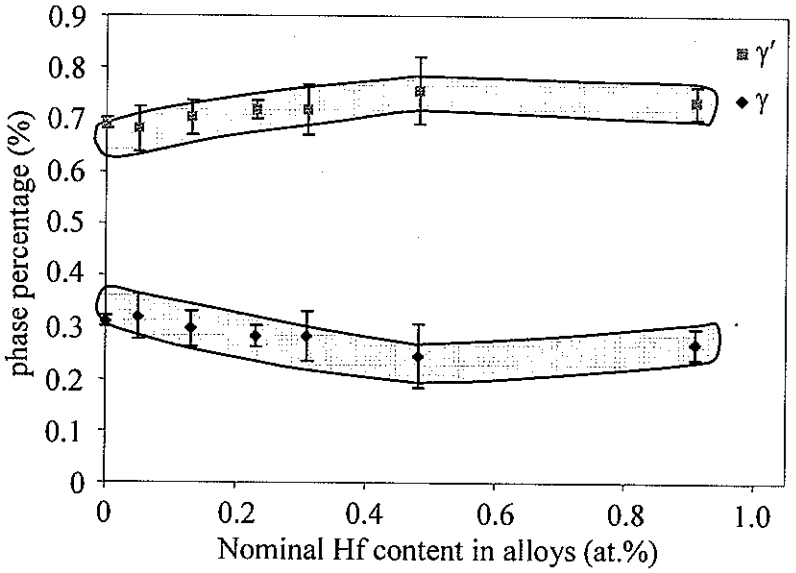

Figure 52. Alloys phase percentage as a function of Hf content.

To study the partitioning behavior of Hf into the γ-Ni and γ′-Ni_3Al phases of Ni-20Al-20Pt-xHf alloys, the partitioning parameter K_i was plotted as a function of Hf content in each phase measured by EPMA as shown in Figure 53. K_i is defined as the ratio of $X_{i\gamma}$ / $Xi_{\gamma'}$, where $X_{i\gamma}$ and $X_{i\gamma'}$ are the compositions of the reactive element *i* in the γ-Ni and γ′-Ni_3Al phase respectively. The element *i* has a tendency to partition into the γ phase when $K_i > 1$, while it prefers to γ′ phase when $K_i < 1$. It can be seen that Hf invariably partitions into the γ′-Ni_3Al phase in which the concentration of Hf is about 10 times of it in the γ-Ni phase except for the alloy with 0.05at.% Hf. This variation results from the limited EPMA resolution since the trace concentration of Hf in the γ-Ni phase of alloy Ni-20Al-20Pt-0.05Hf is beyond the equipments detectability. Not only is Hf much more soluble in the γ′-Ni_3Al phase than in the γ-Ni phase, it is also important to note that 500ppm Hf level was optimized at near the solubility limit in stoichiometric NiAl as reported by Pint [82].

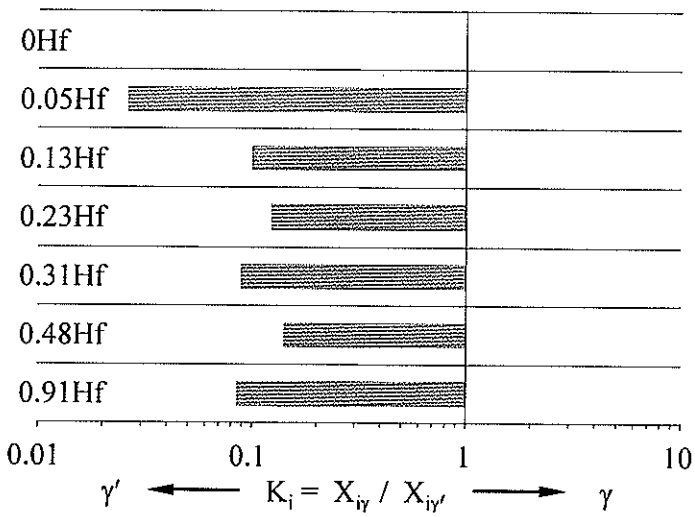

Figure 53. Partitioning behavior of Hf in Ni-20Al-20Pt-xHf alloys.

4.2.4 Thermally Grown Oxide Characterizations

To further understand Hf effects related with the growth and development of the thermally grown oxide, advanced analytical techniques were applied to examine scales formed on selected Ni-20Al-20Pt-xHf alloys. Confocal photo-stimulated microspectroscopy (CPSM) was utilized to measure the room-temperature residual stress and evaluate the phase transformation evolved with Hf-modified oxide scales. Focused ion beam (FIB) prepared samples were given to TEM examination for scale microstructural analysis and Hf segregation measurements. Additionally, field emission gun (FEG) scanning electron microscope (SEM) equipped with the in-lens detector was employed to inspect grain sizes of the scale affected by Hf additions. Results will be summarized and reviewed in the following sections.

4.2.4.1 Confocal Photo-Stimulated Microspectroscopy Results

Ni-20Al-20Pt and Ni-20Al-20Pt-0.48Hf were oxidized at 1100°C for various times ranging from 2, 4, 6 to 50 hours. The residual stress in oxide scales, measured at the room temperature, was calculated by the R1 and R2 doublet fluorescent peak shift [90, 100]. The average stress was obtained from a 30μm × 60μm rectangular area containing 1800 pixels of 1μm × 1μm in resolution. The calculated average stress after each oxidation time was plotted

and reported in Figure 54 and Table 6, respectively. It is seen that the compressive residual stress in oxide formed on Ni-20Al-20Pt decreased slowly from 5.05 to 4.16GPa with increasing oxidation time up to 50 hours. Although with some variations, measured stress on Ni-20Al-20Pt-0.48Hf exhibited similar decreasing trend with increasing oxidation time. The difference is that the room-temperature compressive residual stress in oxide formed on 0.48at.% Hf-doped Ni-20Al-20Pt was consistently lower than on Hf-free Ni-20Al-20Pt alloy.

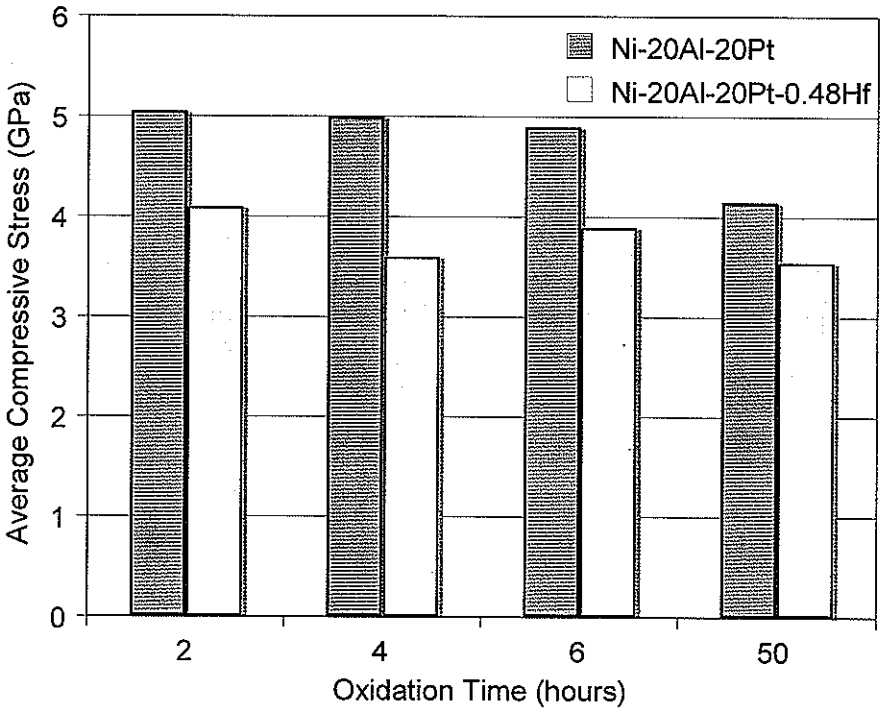

Figure 54. Evolution of compressive residual stress on Ni-20Al-20Pt and Ni-20Al-20Pt-0.48Hf as a function of oxidation time at 1100°C.

Table 6. Calculated average compressive stresses on Ni-20Al-20Pt and Ni-20Al-20Pt-0.48Hf.

Oxidation Time (hrs)	Compressive Stresses (GPa)	
	Ni-20Al-20Pt	Ni-20Al-20Pt-0.48Hf
2	5.05	4.10
4	5.00	3.60
6	4.87	3.90
50	4.16	3.50

CPSM could also examine the alumina phase by mapping the selected oxide surface with confined fluorescence wavelength (frequency). Accordingly, the wavelength of the fluorescence with α-Al_2O_3 ranges from 692 to 697nm and θ-Al_2O_3 ranges from 683 to 692nm. Resulted fluorescence intensities from both equilibrium and metastable alumina phases could be overlapped to illustrate alumina phase distribution within the same area. As the red color represents the equilibrium α-Al_2O_3 and green color represents the metastable θ-Al_2O_3, the alumina phase map from scales formed on both Ni-20Al-20Pt and Ni-20Al-20Pt-0.48Hf after each corresponding oxidation time within a 30μm × 60μm area was plotted, shown in Figure 55. It is seen that the oxide formed on Hf-free Ni-20Al-20Pt was comprised of 18% θ-Al_2O_3 and 82% α-Al_2O_3 after 30 minutes heating at 1100°C. Metastable alumina phases completed the transformation into equilibrium α-Al_2O_3 with further heating from 30 minutes to 2 hours. However, Hf-doped Ni-20Al-20Pt required longer time for this metastable-to-equilibrium phase transformation. The oxide formed on Ni-20Al-20Pt-0.48Hf was predominantly comprised of θ-Al_2O_3 after 30 minutes heating at 1100°C. And this metastable alumina continued growing with further oxidation to 2 hours, at which only about 10% of the scale transformed into equilibrium α-Al_2O_3. The transformation progressed further with increasing oxidation time as only 6% θ-Al_2O_3 was left after 4 hours exposure. It is seen that the oxide was completely comprised of equilibrium α-Al_2O_3 after 6 hours at 1100°C. These results indicate that Hf additions may postpone the phase transformation from metastable to equilibrium alumina.

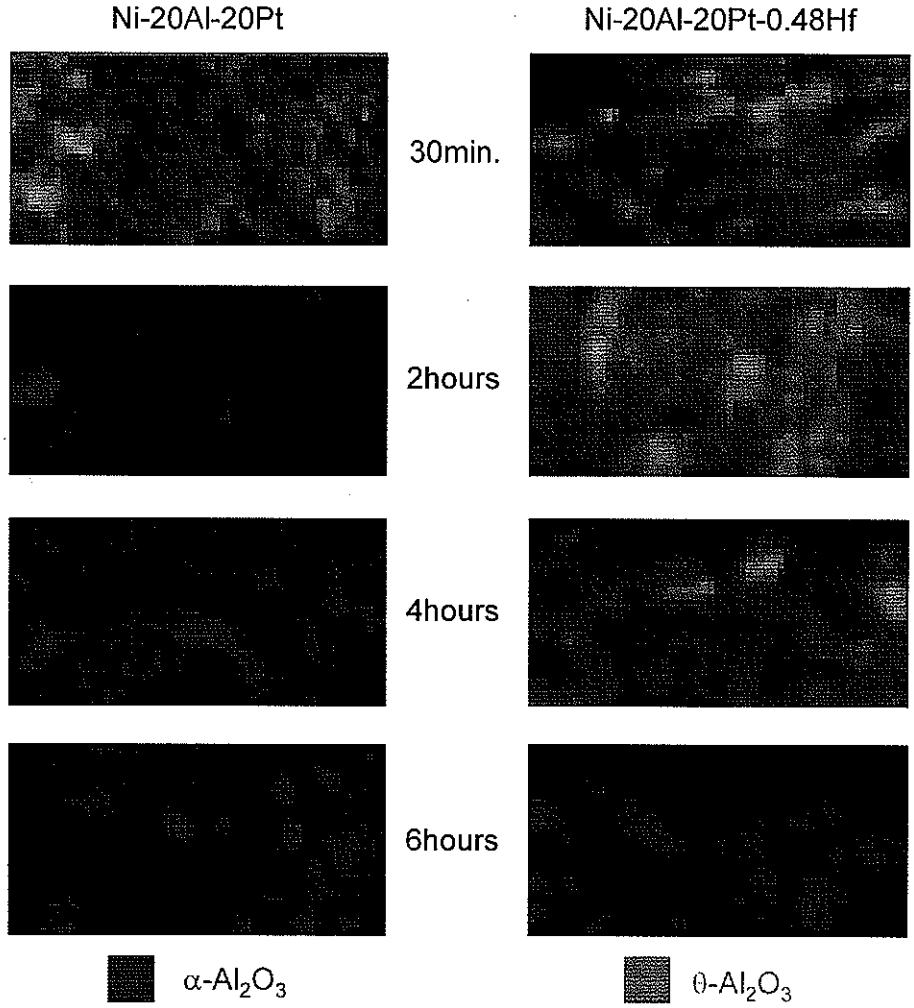

Figure 55. Alumina phase map showing the evolution of oxide phases with increasing oxidation time on both Ni-20Al-20Pt and Ni-20Al-20Pt-0.48Hf at 1100°C.

Since the measurement of the $\theta \rightarrow \alpha$ transformation was conducted on the intermittently cooled samples with similar thermal history as the cyclic oxidation test, results gained may be utilized to explain the higher weight change of Hf-doped alloys presented in Figure 48b. Rybicki and Smialek [101] found that the transformation from $\theta \rightarrow \alpha$-$Al_2O_3$ resulted in the drastic decrease in the growth rate of two orders of magnitude on an NiAl+Zr alloy at 1000°C. This transformation process was accomplished within the first two hours on the Hf-free base alloy Ni-20Al-20Pt. However, it took more than four hours for the completion on the Hf-doped Ni-20Al-20Pt alloy. The faster scale growth rate on Hf-doped

Ni-20Al-20Pt alloys thus could be attributed to the formation of rapid growing metastable θ-Al_2O_3 accompanied with the delayed transformation to equilibrium α-Al_2O_3. Hf-modified scales were growing at a much slower kinetics once the transformation completed after six hours and their following growth may be controlled by the modified grain boundary diffusion process. To further explore this, therefore, microstructural analysis focusing on the Al_2O_3 grain boundary configuration was conducted by in-lens SEM and TEM.

4.2.4.2 In-Lens SEM Examination of Al_2O_3 Scale

To inspect the oxide grain structure evolved with Hf additions, in-lens SEM images were taken on scales formed on both Ni-20Al-20Pt and Ni-20Al-20Pt-0.48Hf alloys isothermally oxidized at 1150°C in air after 100 hours. Al_2O_3 scale grain structure is clearly manifested in Figure 56 despite the presence of a number of voids, which could be introduced from the sample preparation process. It is seen in Figure 56a that more equiaxed grains located on top of columnar grains formed on Hf-free Ni-20Al-20Pt. The average scale thickness was about 5.9μm, which is about two times of that formed on 0.48at.% Hf-modified Ni-20Al-20Pt (2.8μm), shown in Figure 56b. The scale formed on Ni-20Al-20Pt-0.48Hf alloy was featured by two layers as large grains above columnar grains towards to the scale/alloy interface. Besides the thickness, however, the most remarkable difference between these two oxide scales is the width of columnar grains, which is much larger on Ni-20Al-20Pt (~1.1μm) than on Ni-20Al-20Pt-0.48Hf (~0.5μm). In other words, the scale formed on the Hf-doped Ni-20Al-20Pt has more grains (i.e., more grain boundaries) within the unit area than on the Hf-free Ni-20Al-20Pt. Since grain boundaries are major paths for the outward diffusion of Al cations, it is self-explanatory that more gain boundaries will lead to the faster growth of the Al_2O_3 scale. Contrary to this interpretation, however, Hf-doped alloys exhibited a much reduced scaling kinetics with thinner scale thickness. This behavior could be ascribed to that the solutionized Hf blocks the diffusing paths of Al cations by segregating into the Al_2O_3 grain boundaries. Therefore, Hf-doped scale was able to grow at a slower rate even with more grain boundaries.

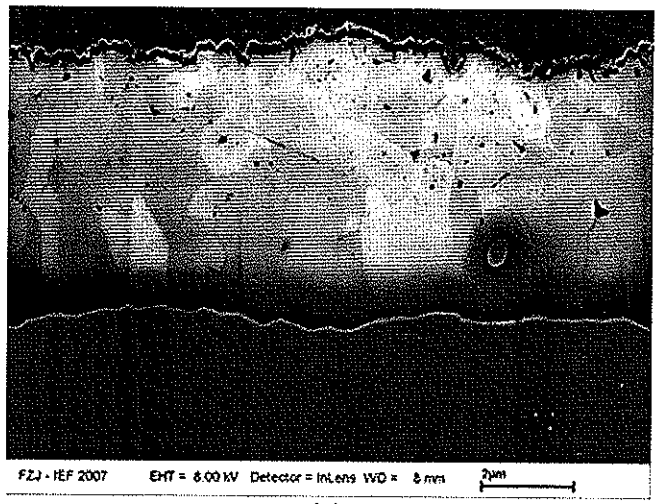

(a)

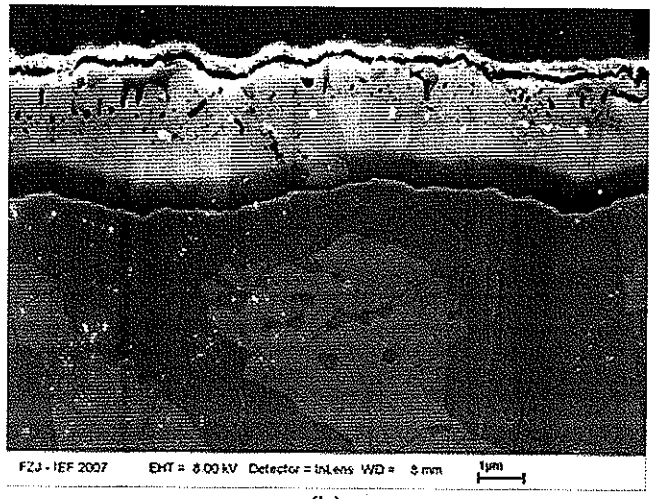

(b)

Figure 56. SEM in-lens images showing the grain structure of oxide formed on a) Ni-20Al-20Pt and b) Ni-20Al-20Pt-0.48Hf at 1150°C after 100 hours.

4.2.4.3 TEM Examination of Al_2O_3 Grain Boundaries

TEM examination on the Hf distribution within the Al_2O_3 scale was performed on isothermally oxidized Ni-20Al-20Pt-0.48Hf alloy at 1150°C for 50 hours. A bright-field TEM micrograph shows that the scale thickness was about 1.6µm, as seen in Figure 57. Large grains were observed near the gas/scale interface, while the grains became columnar

structure towards the scale/alloy interface. Dark particles were Hf-rich oxide confirmed by the elemental spectroscopy imaging (ESI), as marked by arrows shown in Figure 58.

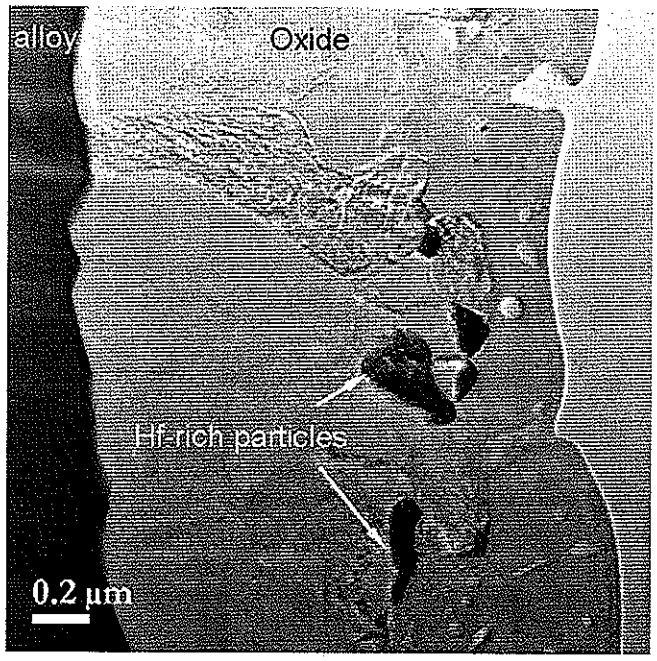

Figure 57. A bright field TEM micrograph showing the scale formed on Ni-20Al-20Pt-0.48Hf at 1150C after 50 hours.

It is seen in Figure 58 that the scale was primarily composed of aluminum oxide with few Hf-rich particles near the scale outer surface. Scarcely distributed Pt particles close to the scale outer surface were also detected. The formation of Hf-rich oxide particles was assumed to take place during the initial oxidation stage accompanied with the formation of Al_2O_3-rich scale.

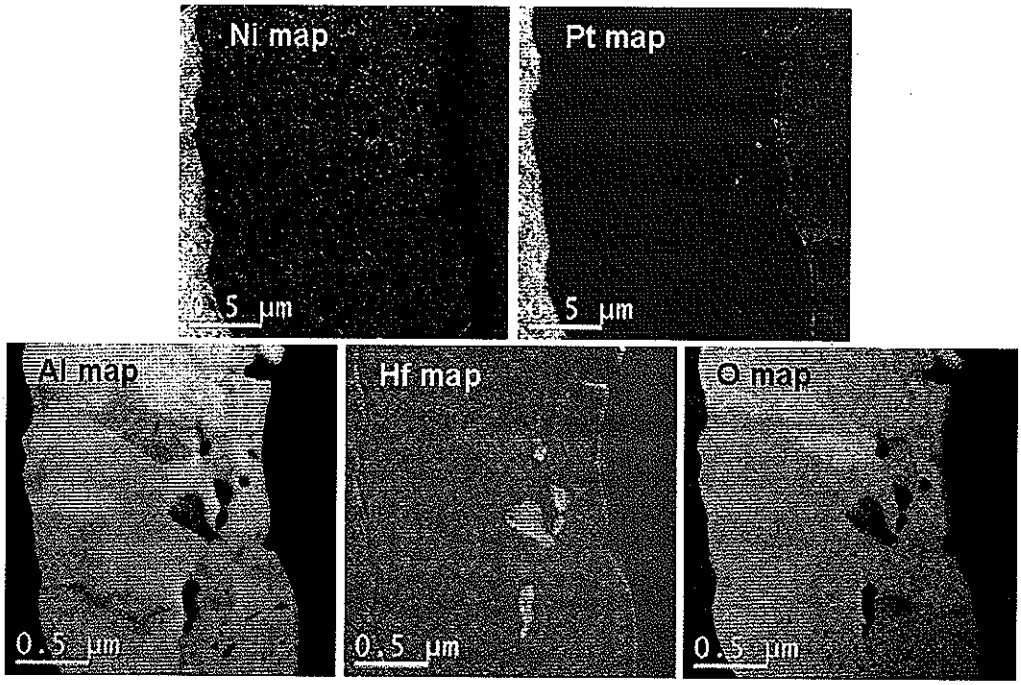

Figure 58. Elemental spectroscopy imaging (ESI) showing the elemental composition of the scale formed on the isothermally oxidized Ni-20Al-20Pt-0.48Hf at 1150°C after 50 hours.

X-ray energy dispersive spectroscopy (XEDS) was performed with line scanning across an Al_2O_3 scale grain boundary, shown in Figure 59. The bright line in Figure 59a delineated a grain boundary between two adjacent Al_2O_3 grains. Damage in the shape of a cavity was introduced during the focus ion beam (FIB) sample preparation. The blue line embedded straight across the grain boundary marked the position of where the XEDS line scanning performed. The concentration profile of Hf was plotted as a function of distance along the Al_2O_3 grain boundary, shown in Figure 59b. It is clearly seen that Hf tends to segregate into the grain boundaries, which acts as the paths for diffusing species that controlling the scale growth kinetics. This is a direct proof of the reactive element grain boundary blocking effect.

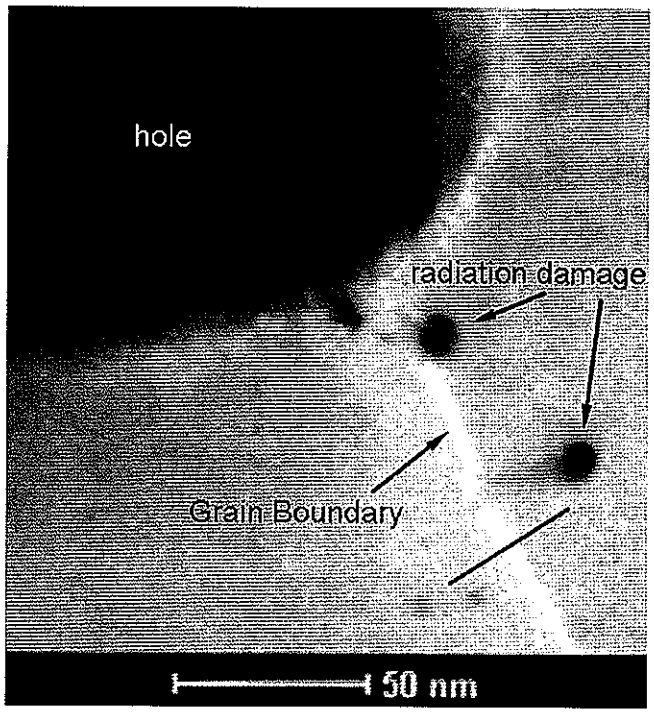

(a)

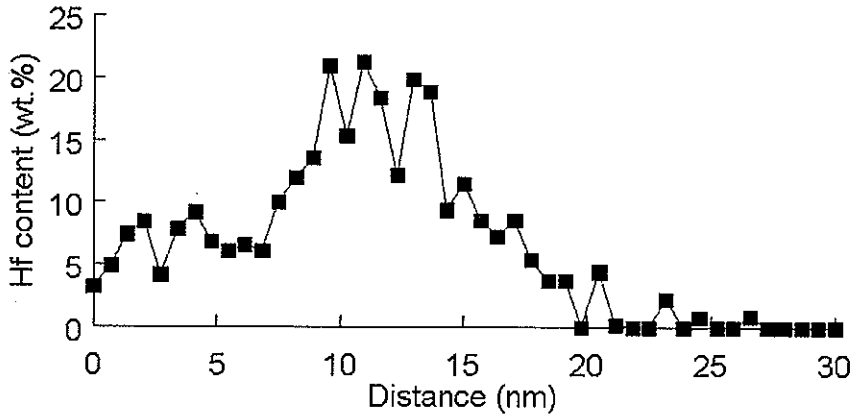

(b)

Figure 59. Hf segregation into Al_2O_3 grain boundaries: a) a bright field image showing the Al_2O_3 grain boundary with marked position for b) XEDS line scanning.

Surface morphology of the oxide scale formed on isothermally oxidized Ni-20Al-20Pt-0.48Hf alloy at 1150°C after 100 hours was examined, shown in Figure 60a, to further study the microstructure of Al_2O_3 scale affected by Hf additions evolved with increasing

oxidation time. The scale surface was marked by the deposited Pt matrix within a 100μm × 100μm square area for the need of positioning. Black spots could be attributed to the electron charging effects. A CPSM determined compressive residual stress map from the same area is shown in Figure 60b. It is seen that there was a large stress variation as localized region with higher stresses up to 6GPa, while the rest part averaged in about 3 to 4GPa. Enlarging Figure 60a, which is a high-quality image, would reveal that the scale surface was featured with localized microcracks matching the area in Figure 60b where higher compressive residual stresses detected. The reason for this stress variation and resulted microcracks needs to be resolved by investigating the scale site-specific cross sections. Therefore, such a region with both high and low stresses was selected and marked by the yellow dotted line, shown in Figure 60b.

Figure 61a shows the magnified surface image of the selected area in Figure 60b. It is seen that the yellow dotted line traversed through oxide ridges and adjacent cracks. Three typical spots were designated for site-specific cross section TEM analysis, marked as number 1, 2 and 3, respectively. The cross section of the corresponding area was then prepared by FIB milling and shown in Figure 61b. It is clearly seen that the scale thickness at region 1 (1.3μm) and 3 (2.7μm) is about 2 to 4 times of region 2 (0.7μm). Correlating the CPSM determined residual stress from the same area shown in Figure 61c, it is further confirmed that the scale thickness is inversely proportional to the measured residual compressive stress. The region with thinner scale thickness invariably corresponds to higher compressive residual stress, which could impart the scale more susceptible to the initiation of cracks. This may rationalize the observation that the position of those microcracks always coincides with higher compressive residual stresses, as seen in Figures 60 and 61.

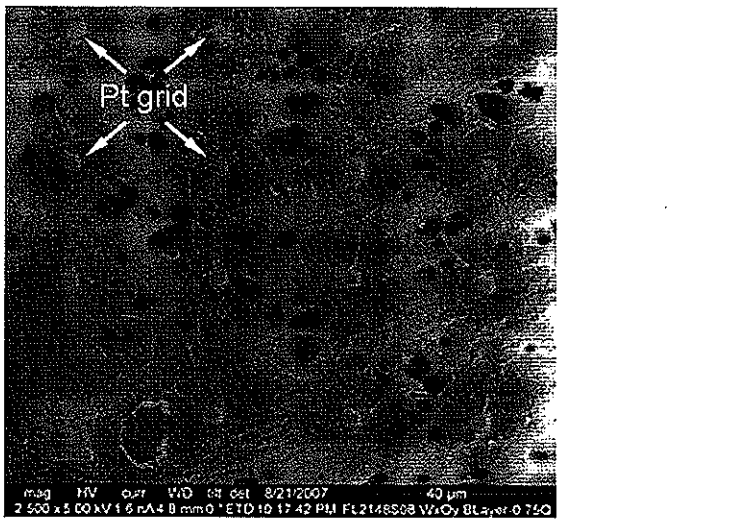

(a)

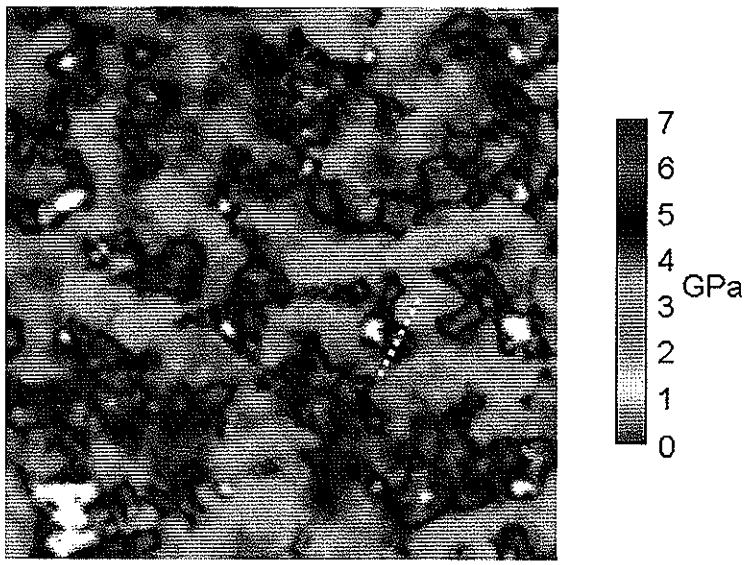

(b)

Figure 60. Isothermally oxidized Ni-20Al-20Pt-0.48Hf at 1150°C after 100 hours a) SEM image showing the surface morphology; b) CPSM determined room temperature residual stress.

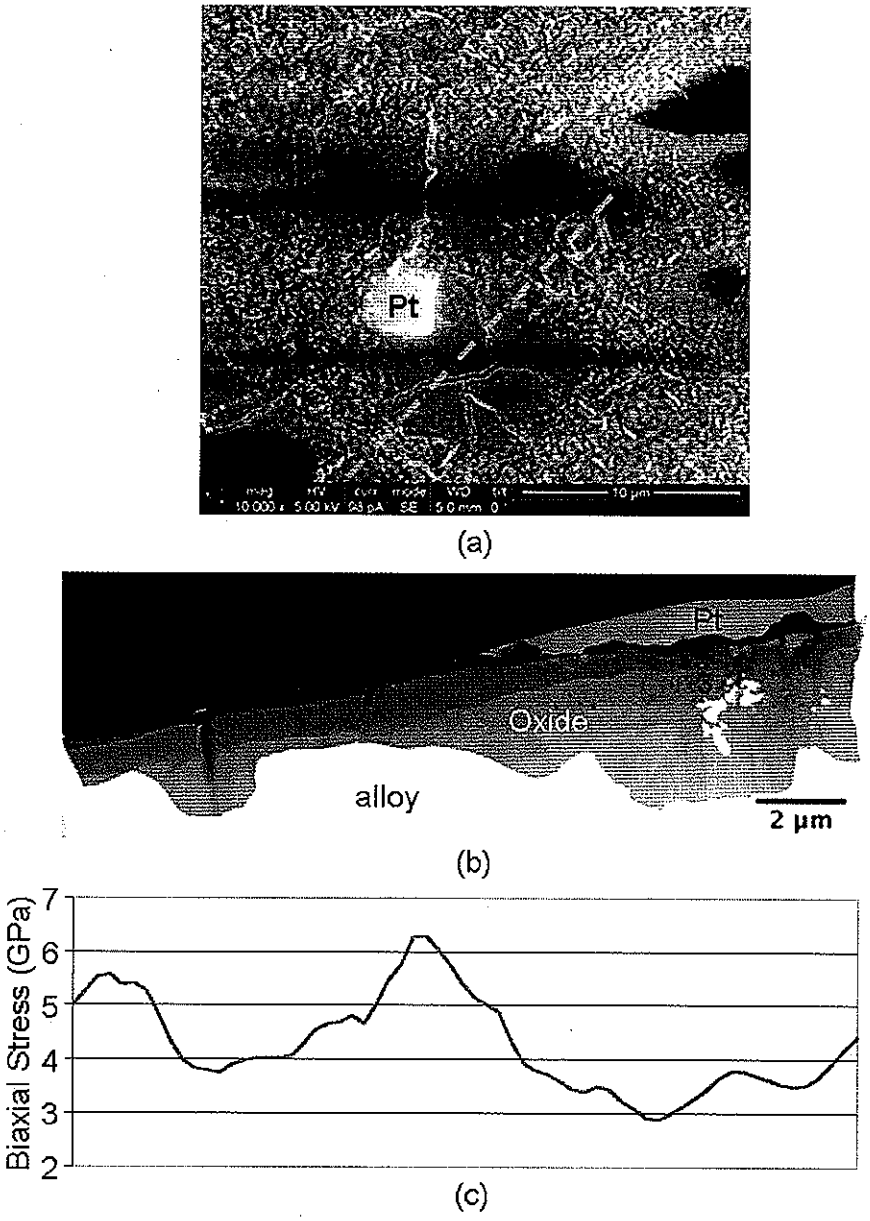

Figure 61: Site-specific examination of the scale formed on isothermally oxidized Ni-20Al-20Pt-0.48Hf at 1150°C after 100 hours a) SEM surface image; b) bright field TEM cross sections; c) CPSM resolved residual stress.

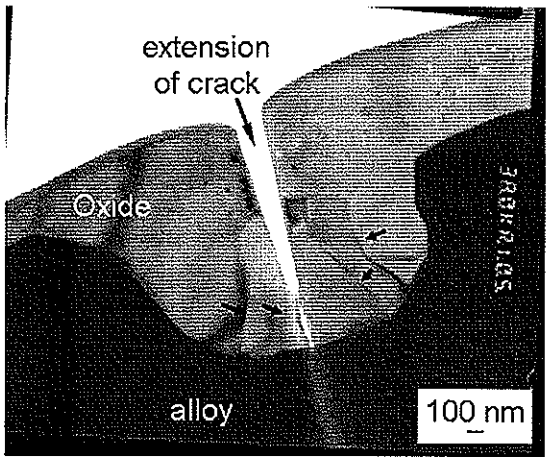

(a)

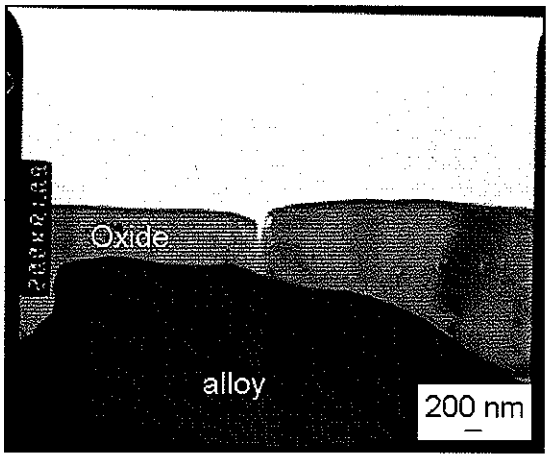

(b)

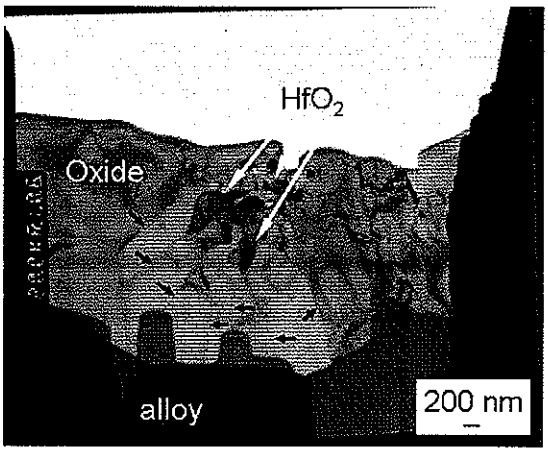

(c)

Figure 62. Microstructural analysis on selected oxide scale at a) region 1; b) region 2 and c) region 3.

Further examination on the scale microstructure from selected areas was conducted by TEM, as shown in Figure 62. It is seen in Figure 62a (region 1) that there was a crack penetrating completely through the scale thickness ending up at the scale/alloy interface. The formation of this crack could be originated as an artificial defect during the FIB milling process. Despite of that, columnar Al_2O_3 grain structure was observed near the scale/alloy interface, indicated by black arrows. The oxide close to the gas/scale interface was featured by large grains without apparent grain boundaries. Figure 62b shows the thin oxide scale at region 2 with large grain size. A microcrack near the gas/scale surface corresponds well with those cracks found on the surface image shown in Figure 61a. It is seen in Figure 62c (region 3) that the scale was featured by large grains near the outer surface and more distinct columnar structure towards the scale/alloy interface. The grain boundaries between each column were marked by black arrows. HfO_2 particles were detected by XEDS within the Al_2O_3 scale.

4.3 Development of Pt+Hf-Modified γ-Ni+γ'-Ni_3Al Coatings

Deposition of the Pt+Hf-modified γ-Ni+γ'-Ni_3Al coatings by a pack cementation process was developed by Gleeson *et al.* [85] in recent years. This study will mainly focus on evaluating coating high-temperature performances and understanding the coating composition dependence on the temperature and time in both pack cementation and post heat treatment processes.

4.3.1 Advantages of Pt+Hf-modified γ-Ni+γ'-Ni_3Al Coatings

The high-temperature cyclic oxidation behavior of a Pt+Hf-modified γ-γ'-based coating and a commercial Pt-modified β-NiAl coating was compared at 1150C after 1000 cycles, shown in Figure 63. The most noticeable advantage of the γ-γ'-based coating is the capability to form a much planar protective Al_2O_3 scale, which is crucial in the development of a more reliable TBCs system. The γ-γ'-based coating did not undergo the phase transformation from β→γ' and/or γ during the long-term high-temperature exposure. Moreover, there was the absence of TCP phases at the interdiffusion zone due to the higher solubilities of alloying elements in both γ-Ni and γ'-Ni_3Al phases. On the contrary, the scale

formed on the Pt-modified β-NiAl coating was subjected to the extensive rumpling after the same exposure. In addition, the formation of TCP phases, as white precipitates seen in Figure 63b, could potentially decrease the mechanical properties of the whole coating system. The disturbance from rumpled TGO scale could lead to the accelerated failure of thermal barrier coating systems with demolished integrity.

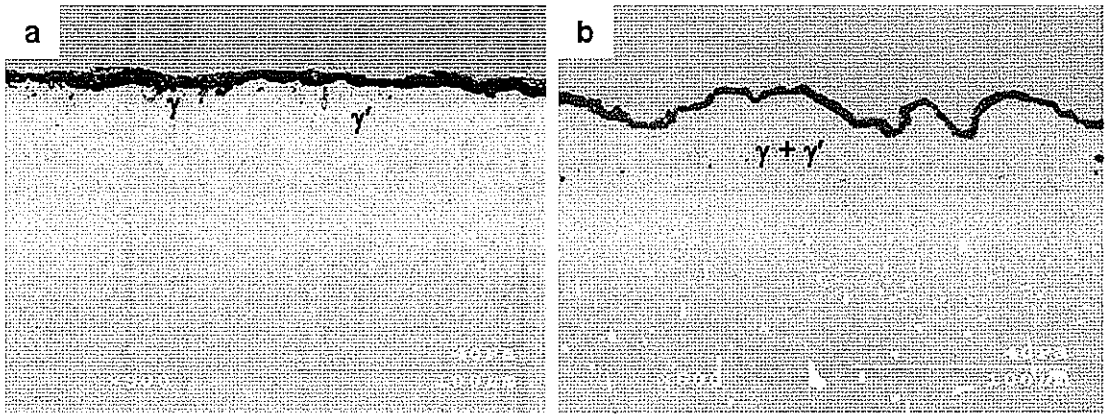

Figure 63. Cross-sectional SEM images showing the comparison between a) γ-Ni + γ'-Ni_3Al coating and b) commercial Pt-modified β-NiAl coating on René-N5 superalloy at 1150°C for 1000 cycles.

Figure 64 shows the composition profiles of major components measured by EPMA in both as-coated and cyclic oxidized γ-Ni + γ'-Ni_3Al coatings (1150°C after 1000 cycles). Measurements started from the coating surface on the as-coated sample (Figure 64a), and the scale/coating interface on the oxidized sample (Figure 64b), respectively. The vertical dotted line inserted in each figure marked the coating/substrate interface.

The thickness of the coating layer increased from ~18μm in the as-coated condition to ~43μm after 1000 cycle exposure due to the interdiffusion between the coating and the substrate. The concentration of Pt in the coating decreased markedly from 28at.% to 4at.% because of the absence of Pt in the superalloy substrate. However, the content of Al maintained at ~17at.% in the γ'-Ni_3Al phase, which still was the major phase present in the coating layer after 1000 cycles exposure at 1150°C. Both Cr and Co tended to segregate into the γ-Ni phase. The significant improvement from the traditional β-NiAl coatings is the

successful deposition of Hf into the γ+γ'-based coatings with 1~2at.% by the patented pack cementation process. However, better controlling the concentration of Hf near the coating surface is crucial in growing a protective Hf-modified Al_2O_3 scale instead of the unwanted HfO_2 + Al_2O_3, as seen in localized region in Figure 63a. Feasible coating surface treatments include grit blasting, polishing and heat treatment.

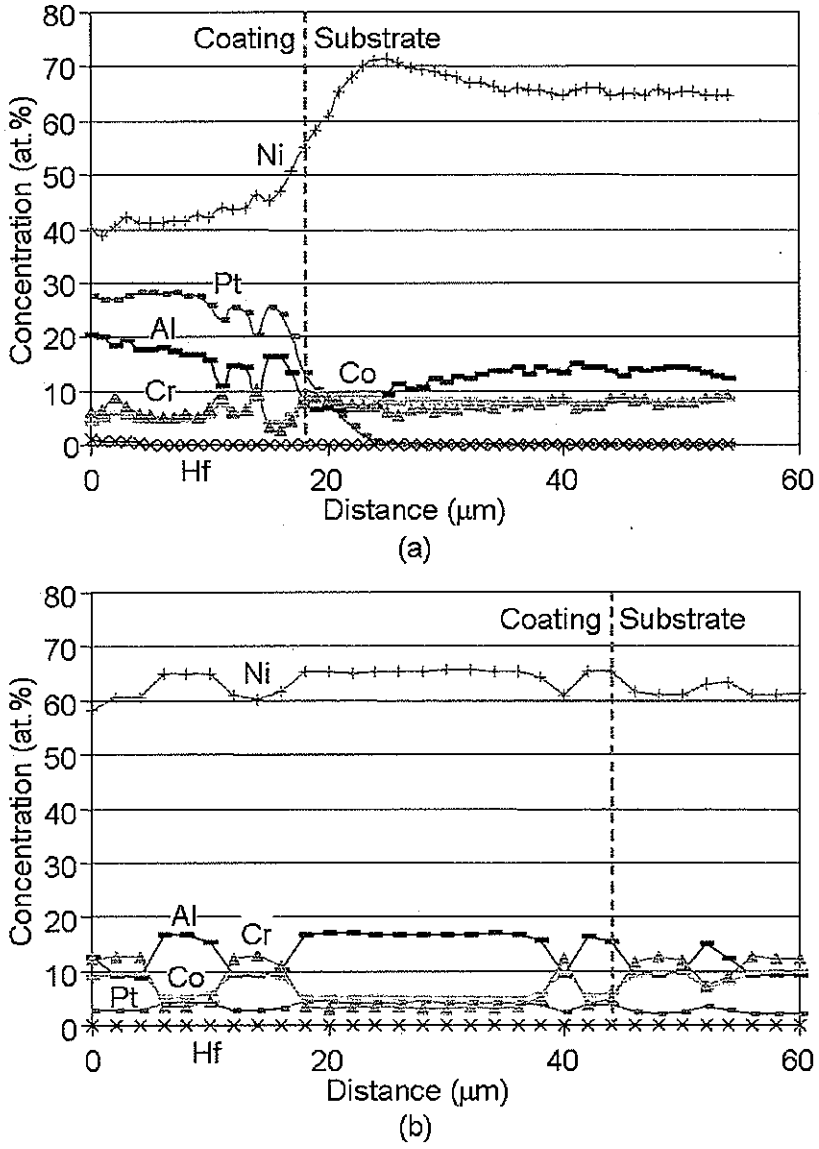

Figure 64. EPMA results showing composition profiles of a) as-coated and b) 1000 cycles at 1150°C oxidized γ-Ni + γ'-Ni_3Al coating.

4.3.2 Coating Composition Dependence on Temperature and Time

The coating composition dependence on temperature and time in both coatings pack cementation and post heat treatment processes were examined. Twelve Pt+Hf-modified γ-Ni+γ'-Ni_3Al coatings were deposited on airfoil spans with CMSX-4 substrate. All coating samples were prepared with different temperature and dwell time as designed and coded in Table 7, in which HT and PC denote the heat treatment and pack cementation, respectively. Since the results are highly proprietary, exact values of each temperature and time were replaced by virtual letters as T for temperature and t for time.

Table 7. Coating samples coding scheme.

HT temp. & time / PC temp. & time	T1 t1	T1 t2	T1 t3	T2 t1	T2 t2	T3 t1
T4/t1	A1	B1	C1	D1	E1	F1
T5/t2	A2	B2	C2	D2	E2	F2

A typical as-coated airfoil span with the terminological definition of each side is shown in Figure 65. Each span was then cut into two pieces through the dotted line. The part near the leading edge side was isothermally oxidized at 1080°C for 30 minutes and the other part near the trailing edge side was oxidized at 1150°C for 100 cycles. As-deposited coating compositions were measured by EDS analysis.

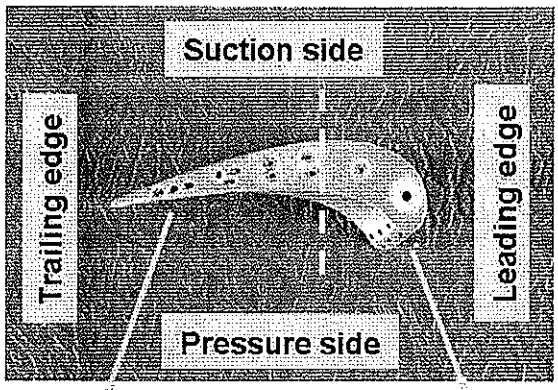

Figure 65. Optical image illustrating the as-coated airfoil span with test schemes.

As the most important elements affecting the formation of protective Al_2O_3 scales, compositions of aluminum, hafnium and platinum were selected to report in Figure 66. The composition of Al on both suction and pressure sides are 1~2at.% higher by the pack cementation at temperature T5 after t2 hours than at temperature T4 after t1 hours, shown in Figure 66a. Although with few deviations, it was found that the compositions of Hf and Pt on the suction side are higher than on the pressure side, shown in Figures 66b and c. However, the concentration dependence of Hf and Pt on the pack cementation temperature and time are not as significant as of aluminum. Meanwhile, Figure 66c also shows that content of Pt tends to decrease with increasing heat treatment time at a fixed heat treatment temperature, as the decreasing in the sequence of A1>B1>C1 and A2>B2>C2 at temperature T1; D1>E1 and D2>E2 at temperature T2. These results indicate that the contents of Al and Hf rely highly upon the temperature and time in the pack cementation process. Higher pack cementation temperature and longer time will lead to higher amounts of both Al and Hf. Meanwhile, the content of Pt in the coating is strongly affected by the heat treatment time. Longer heat treatment process could reduce the Pt content as it diffusing inward to the superalloy substrate, which is a very dynamic process. Therefore, appropriate combination of the temperature and time in both pack cementation and post heat treatment processes is of essence in obtaining the key elemental concentration in Pt+Hf-modified γ-Ni+γ'-Ni_3Al coatings.

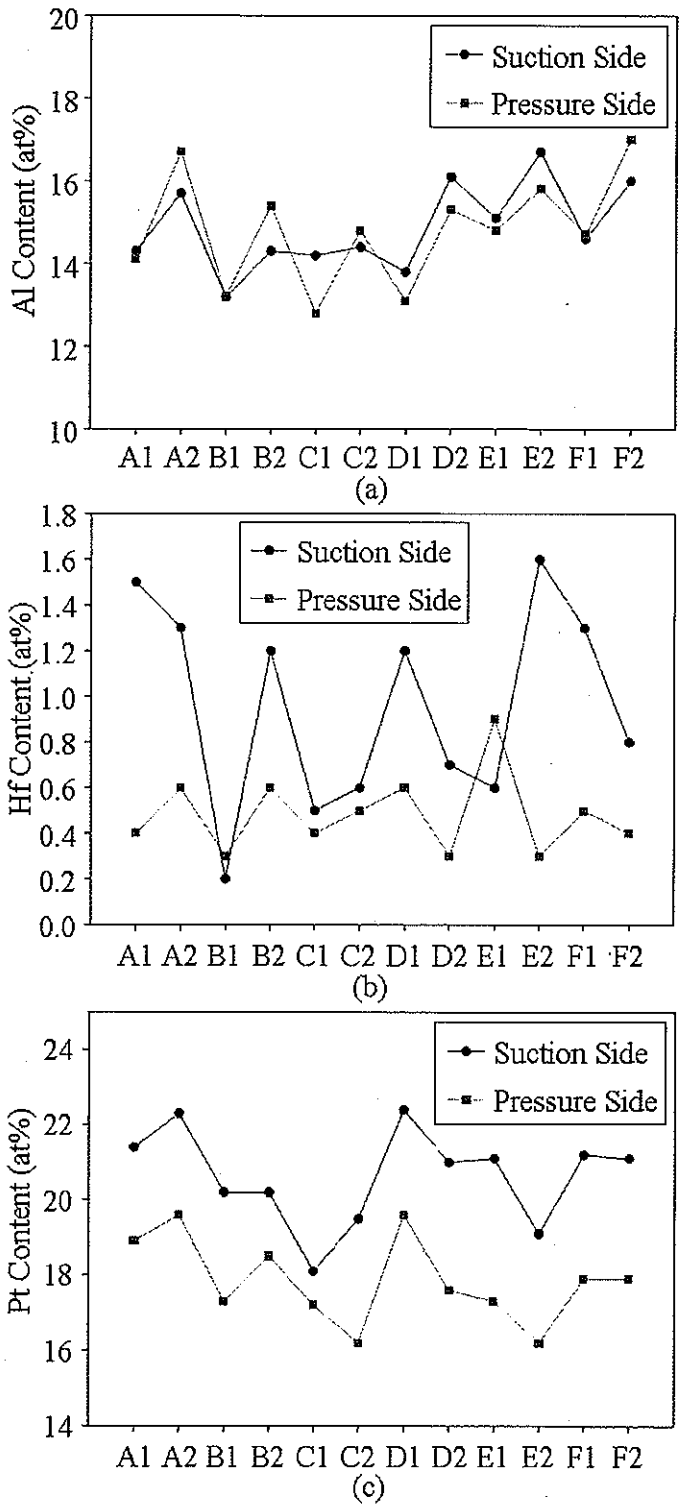

Figure 66. Selected coatings composition of a) Al, b) Hf and c) Pt.

4.3.3 Coating Short-Term Oxidation Performance

A short-term isothermal oxidation test was performed at 1080°C for 30 minutes to qualitatively examine the configuration of the thermally grown oxide formed on each coating. The oxidation temperature was selected as 1080°C as the benchmark to match the industrial manufacturing criterion. Surface morphologies of the oxide formed on each coating are shown in Figure 67. The surface of scales formed on coatings A1, B1 and C1 was featured by large oxide clusters as seen in Figure 67a. With increasing heat treatment temperature from T1 to T2 and T3, scales became finer with smaller grain size. Due to the higher Al content obtained from higher pack cementation temperature and longer time, the surface morphology of scales formed on coatings prepared at temperature T5 after t2 hours (Figure 67b) was invariably finer and smoother than on coatings fabricated at temperature T4 after t1 hours. Therefore, it is seen that the scale formed on coating F2 became the finest. EDS results indicate that scales were comprised of less Hf and more Al_2O_3 on coatings fabricated with higher temperature and longer time in the pack cementation process.

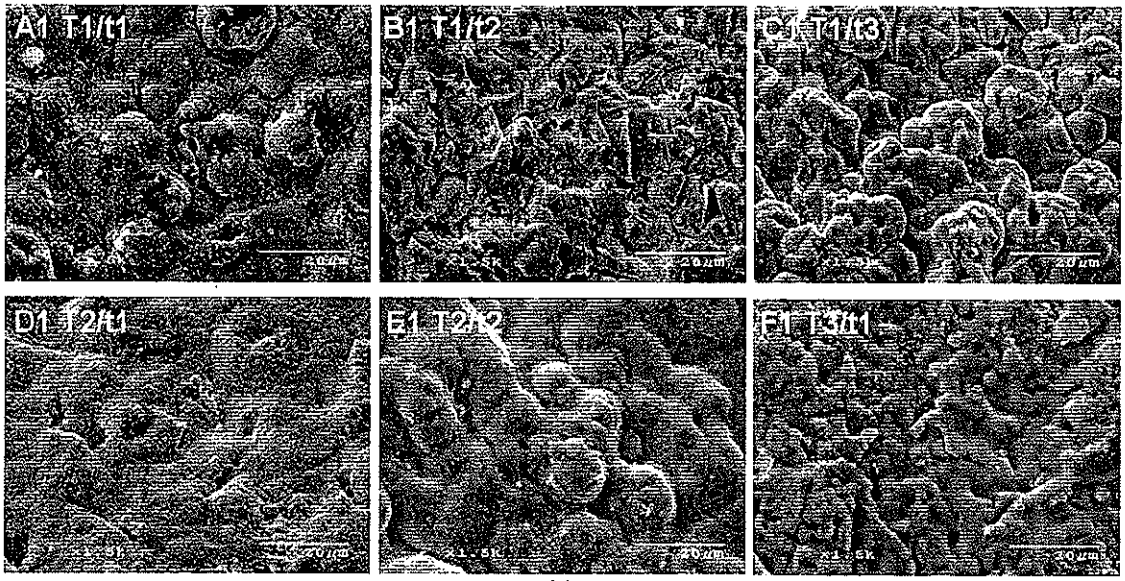

(a)

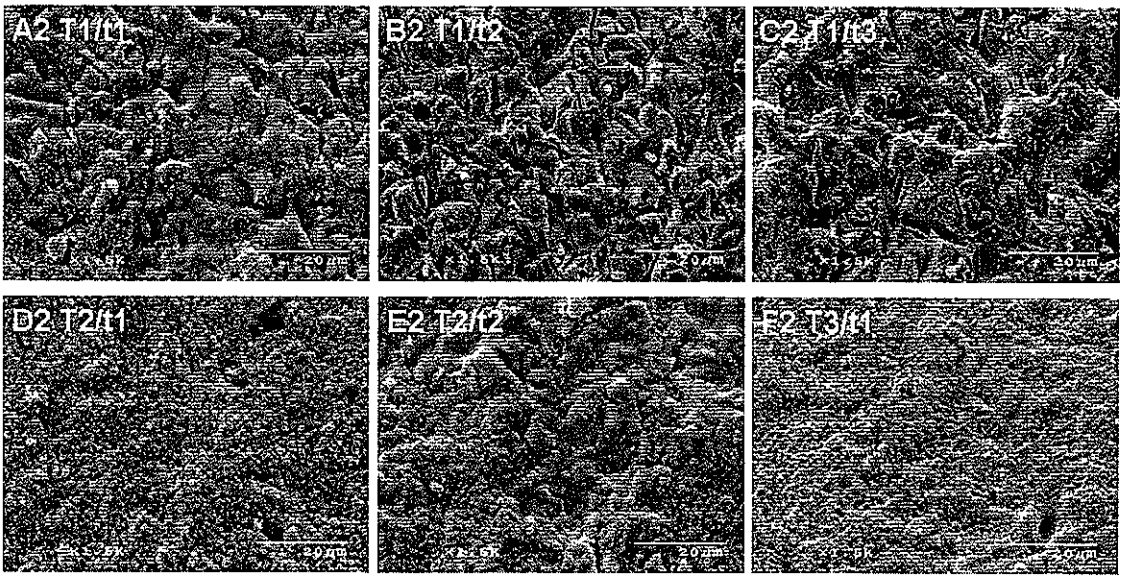

(b)

Figure 67. SEM images showing the oxide scale formed at 1080°C fro 30 minutes on the suction side of coatings prepared by pack cementation process a) at temperature T4 after t1 hours; b) at temperature T5 after t2 hours.

4.3.4 Coating Cyclic Oxidation Performance

A relative long-term cyclic oxidation test was performed on each coating sample at 1150°C for 100 cycles. The cross section of the scale on the suction side of each oxidized sample was prepared and shown in Figure 68. Results were divided by the pack cementation temperature and time, and marked with the post heat treatment temperature and time. The oxide products were complex with multi-layered structure as HfO_2 with the brightest contrast, Al_2O_3 with the darkest contrast, and spinel with contrast in between as marked in Figure 68a, respectively. The darker phase present in the coating layer was identified by EDS as γ-Ni and the lighter phase was γ'-Ni_3Al. The oxide products formed on each sample, subjected to coating as-deposited composition and structure, are summarized and listed in Table 8. It is seen in both Figure 68 and Table 8 that coating F2 outperformed others by forming a planar and slow-growing Al_2O_3 scale. Other samples were over-doped with Hf as the formation of HfO_2 and spinel, which led to the development of less-protective oxides. Therefore, it is verified that higher temperature in the pack cementation process could assure the deposition of Al and Hf with desired content. Meanwhile, Pt depletion due to its inward diffusion to the superalloy substrate could be greatly reduced with shorter heat treatment time.

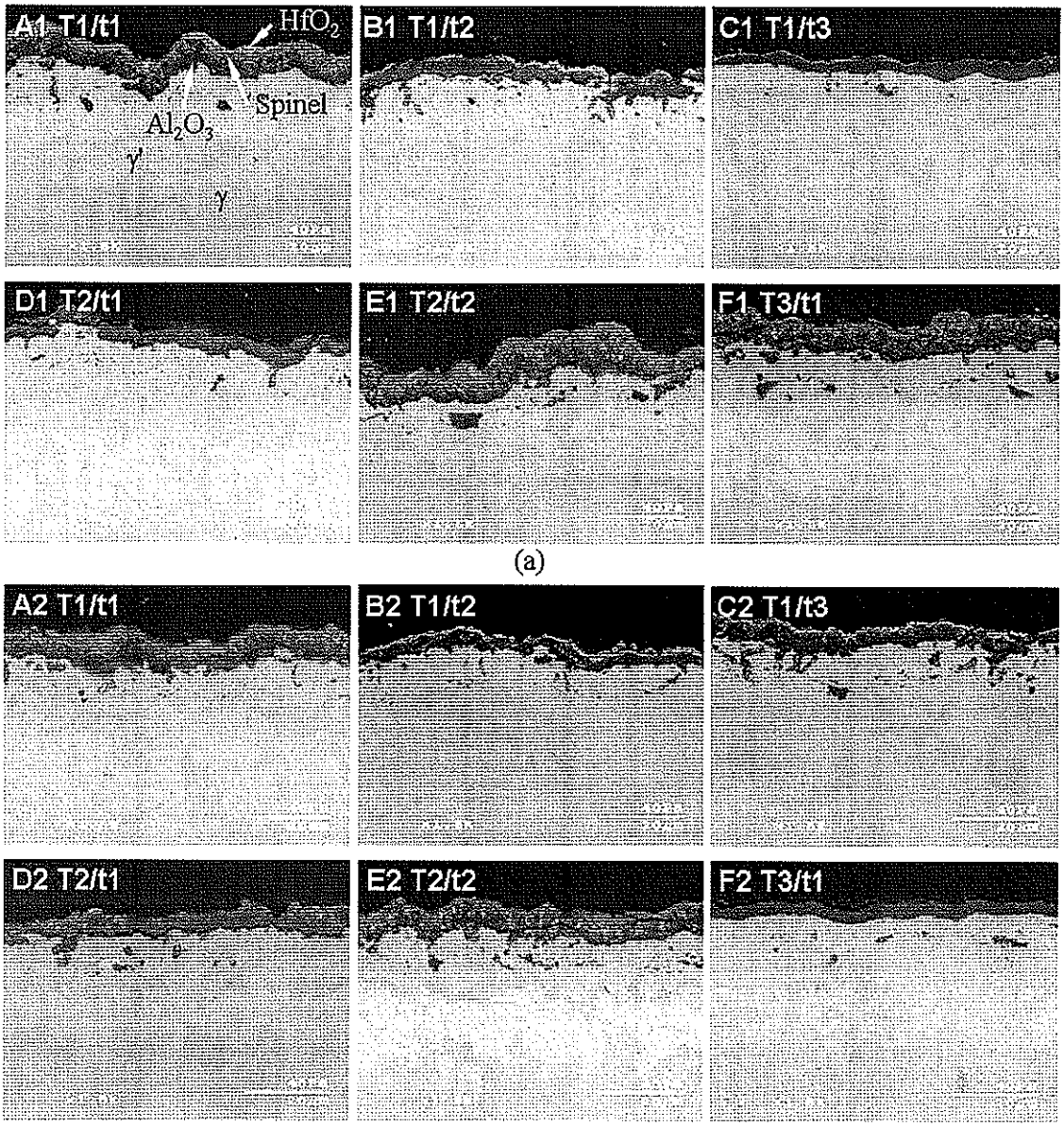

Figure 68. Cross-sectional SEM images showing the oxide scale formed at 1150°C for 100 cycles on the suction side of coatings prepared by pack cementation process a) at temperature T4 after t1 hours; b) at temperature T5 after t2 hours.

Table 8. Oxide products formed on the suction side of airfoil spans at 1150°C after 100 cycles.

Coatings	Surface Products
A1	$NiAl_2O_4$, HfO_2, Al_2O_3
A2	$NiAl_2O_4$, HfO_2, Al_2O_3
B1	$NiAl_2O_4$, HfO_2, Al_2O_3
B2	$NiAl_2O_4$, HfO_2, Al_2O_3
C1	HfO_2, Al_2O_3
C2	$NiAl_2O_4$, HfO_2, Al_2O_3
D1	$NiAl_2O_4$, HfO_2, Al_2O_3
D2	$NiAl_2O_4$, HfO_2, Al_2O_3
E1	$NiAl_2O_4$, HfO_2, Al_2O_3
E2	$NiAl_2O_4$, HfO_2, Al_2O_3
F1	$NiAl_2O_4$, HfO_2, Al_2O_3
F2	Al_2O_3

4.3.5 Comparison between Coatings and Alloys

Selected γ-Ni+γ'-Ni_3Al-based alloys and coatings were oxidized at 1150°C for 100 cycles to further evaluate their high-temperature oxidation resistance. Figure 69 shows the weight change of each alloy and coating sample measured at intermittently selected cycles. It is seen that Ni-20Al-20Pt alloy oxidized at a faster rate than Ni-50Al-15Pt alloy. However, the weight change of Ni-20Al-20Pt-0.3Hf alloy was about half of Ni-50Al-15Pt alloy. This phenomenon was observed and explained repeatedly in previous sections. Remarkably, Pt+Hf-modified γ+γ' coatings on a selected second generation superalloy substrate even oxidized at a slower rate than Ni-20Al-20Pt-0.3Hf alloy. And the final weight change of this coating after 100 cycles was only about 0.23mg/cm^2. Contrary to this, the second generation superalloy alone achieved an initial weight gain up to 60 cycles following with the weight loss afterwards. Being the poorest candidate among all samples, Pt-only coating on the second generation superalloy substrate experienced the weight loss from the early-stage oxidation.

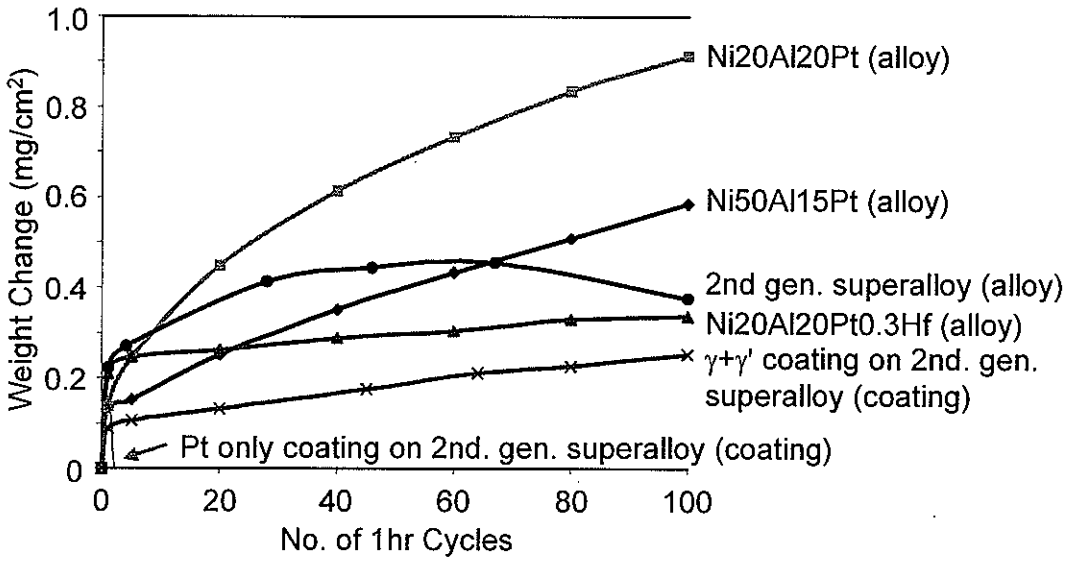

Figure 69. Weight change of selected alloys and coatings at 1150°C for 100 cycles.

Cross sections of each oxidized sample were prepared and shown in Figure 70. It is seen that alloy Ni-20Al-20Pt formed a ~11μm Al_2O_3 scale with the development of a ~33μm denuded γ-Ni layer. A 9μm planar Al_2O_3 scale formed on Ni-50Al-15Pt alloy without the indication of the phase change near the subsurface area. Ni-20Al-20Pt-0.3Hf alloy formed a much thinner Al_2O_3 scale, although not fairly uniform in the thickness. There was not a continuous γ-Ni depletion zone formed owing to the slow growth rate of the protective Al_2O_3 scale. The second generation bare superalloy formed a duplex scale as the spinel on top of the Al_2O_3 scale accompanied with a 9μm subsurface Al-depletion zone. Pt only coating formed a similar scale structure regardless of the higher thickness of the spinel layer. Pt+Hf-modified γ+γ′ coating formed the thinnest Al_2O_3 scale, which is also indicated by its lowest weight change shown in Figure 69. It is worth noting that there was no surface treatment prior to the cyclic oxidation test. The resulted scale roughness, therefore, was originated from the as-deposited coating structure. Separate experiment shows that the coating with proper surface treatment could form quite planar Al_2O_3 scale with similar thickness.

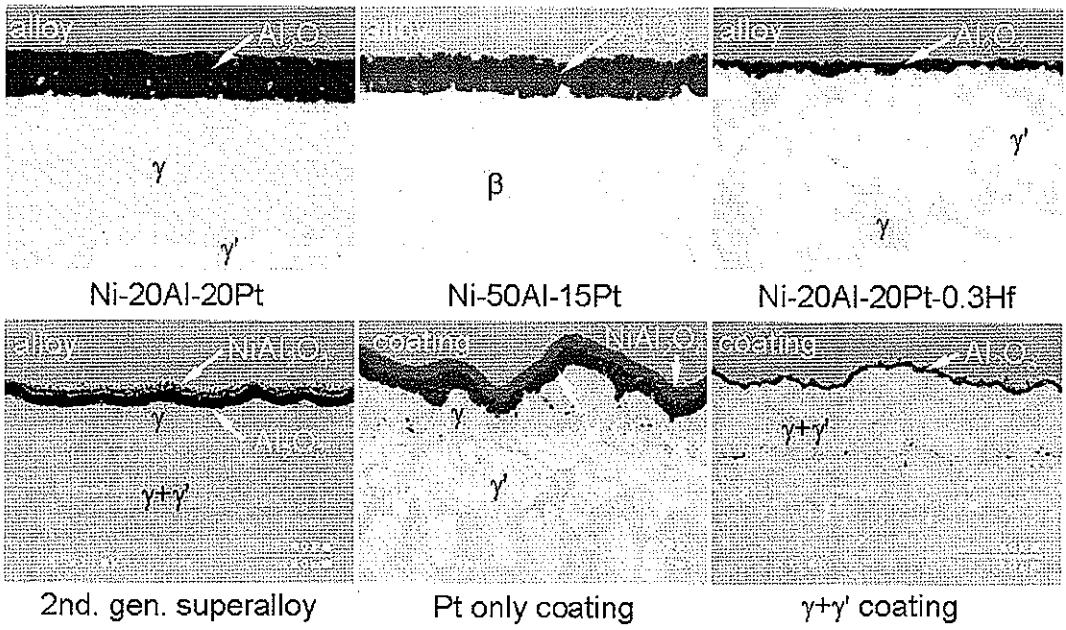

Figure 70. Cross-sectional SEM images showing the scale formed on selected alloys and coatings at 1150°C after 100 cycles.

CHAPTER 5 DISCUSSION

5.1 Pt Effects on Al_2O_3 Formation

It has been shown that Pt can promote Al_2O_3 formation on both single-phase γ'-Ni_3Al and γ-Ni alloys. Because the intermetallic γ'-Ni_3Al phase and solid solution γ-Ni phase have the similar face center cubic (FCC) crystal structures, the mechanism by which Pt affected oxidation behavior should be similarly applicable to both of them; although, the ordered arrangement of the γ' structure does bring differences. The Ni-Al-Pt isotherm at 1150°C (Figure 8) shows that both γ' and γ have large phase regions, extending from the Ni-rich side to the Pt-rich side. The nature of these phase regions implies that Pt can be added into each phase solely at the expense of Ni while keeping a fixed Al content. This is particularly important for the γ'-Ni_3Al phase, as it has a narrow Al composition range varying from 22 to 27at.%. This phenomenological interpretation is by the results of a first-principles study by Chao *et al.* [102]. Their calculations showed that Pt has a predominant preference for the Ni sublattice (face centers) in the ordered $L1_2$ structure (Figure 7) at temperatures ranging from -273 to 1727°C and compositions varying from Ni-rich, stoichiometric to Al-rich Ni_3Al. Consequently, Pt additions to Ni_3Al essentially enhance the effective Al content available for oxidation in a given crystallographic plane. Increasing Pt content from 10 to 20at.% in the studied single-phase alloys decreases the effective Ni content while simultaneously increasing the effective Al content. Because of its virtually non-oxidizing nature [49], the presence of Pt can even affect the early-stage competitive oxidation of Al and Ni to the extent that Al_2O_3 formation is favored.

The addition of 10at.% Pt to a Ni-12.5Al alloy caused the scale structure to change from triple-layered (NiO, $NiAl_2O_4$, Al_2O_3 as a sequence from gas/scale interface to scale/alloy interface) to two-layered ($NiAl_2O_4$ on top of Al_2O_3), as shown in Figure 39. Further increasing the Pt content to 20at.% resulted in a decrease in the Al_2O_3 thickness under a discontinuous layer of $NiAl_2O_4$. In a similar manner, 10at.% Pt addition suppressed the formation of $NiAl_2O_4$ above Al_2O_3 on a Ni-25Al-base alloy, as shown in Figure 41a. Additionally, the thickness of the Al_2O_3 scale was reduced, leading to the formation of a thinner γ-Ni subsurface denuded zone, which is caused by the selective oxidation of Al

leading to its removal from the near-surface region of the alloy. The addition of 20at.% Pt to Ni-25Al facilitated the formation of a thinner Al_2O_3 scale and the virtual absence of a γ-Ni subsurface denuded zone. It is worth noting that the spinel results from a solid-state reaction of NiO and Al_2O_3 by the following equation:

$$NiO + Al_2O_3 \rightarrow NiAl_2O_4 \tag{26}$$

and higher temperature accelerates the consumption of NiO to from spinel [103, 104].

Qin *et al.* [105] examined the surface segregation behavior on a clean $(Pt,Ni)_3Al$ (111) surface and confirmed from experimental measurements and density functional calculations that Pt does segregate to the γ' surface. It was postulated by these authors that the atom size differences are mainly responsible for the Pt segregation, as the atomic volume of Pt is over 35% larger than Ni and would serve to reduce the strain. This study may serve to explain the surface enrichment of Pt during the early-stage oxidation of Ni-12.5Al-10Pt, Ni-12.5Al-20Pt, Ni-25Al-10Pt and Ni-25Al-20Pt, as seen in Figures 21, 22, 29 and 30, respectively. In addition, the surface-segregated Pt would further increase the effective Al/Ni content ratio at the alloy surface to further facilitate Al_2O_3 formation during the early-stage oxidation.

Another important factor is that Pt has a negative chemical interaction with Al such that the Al activity (a_{Al}) decreases with increasing Pt content. Hayashi *et al.* [38, 106] reported this effect by observing the uphill diffusion of aluminum from the low-Al side to the high-Al side in a series of diffusion couples. Copland [107] directly measured Al activity in a series of γ'-$(Ni,Pt)_3Al$ alloys with varying Al (24 and 27at.%) and Pt (2 to 25at.%) contents, and his results validated Hayashi *et al.*'s conclusions. Therefore, the Pt surface segregation would cause a decrease in a_{Al} at the scale/alloy interface, which would result in an increased a_{Al} gradient from the alloy to scale/alloy interface. This increase in a_{Al} gradient would lead to an increase in the outward diffusive flux of Al at the scale/alloy interface according to the relation:

$$J_{Al}^{i} = -C_{Al}^{i} D_{Al} \frac{\partial \ln a_{Al}}{\partial x} \tag{27}$$

where C_{Al}^{i} is the interfacial Al content at the scale/alloy interface, D_{Al} is the diffusion coefficient of Al. This increased Al flux would assist in the fast and continuous development

of an Al_2O_3-rich scale. This significant effect is very instrumental in directing the development of Pt-modified γ-Ni+γ'-Ni_3Al-based coatings. One could intuitively imagine the uphill diffusion of Al from a superalloy substrate into a Pt-modified γ+γ' coating, which would make such coatings a long-term Al source for Al_2O_3 scale growth.

It was also reported by Gleeson *et al.* [38] that Pt may decrease the oxygen permeability in both γ-Ni and γ'-Ni_3Al alloys. This inference was arrived at by comparing the thickness of the internal oxidation zones formed in a Pt-free and Pt-modified γ-Ni alloys containing 3at.% Al. Such a decrease in oxygen permeability would decrease the critical Al content within the alloy necessary for Al_2O_3 scale formation.

So far, the following four effects of Pt have been identified as: 1) Pt has a predominant site preference for the Ni sublattice in the ordered $L1_2$ structure so that the effective Al/Ni ratio is enhanced in certain crystallographic planes; 2) Pt tends to segregate to the alloy surface due to its larger atomic size compared to Ni, which leads to the Pt surface enrichment; 3) Pt has a negative chemical interaction with Al, which results in an increased Al diffusive flux at the scale/alloy interface when there is the subsurface enrichment of Pt; and 4) Pt decreases the oxygen permeability into the alloy and, in turn, decreases the critical Al concentration for Al_2O_3 formation. Effect (1) is specific to the γ' phase, while the other effects are relevant to both γ' and γ. All four effects are synergistic and favor the formation of Al_2O_3 over NiO on both γ'-$(Ni,Pt)_3Al$ and γ-Ni alloys.

5.2 Hf Effects on NiO Growth

To form a more protective Al_2O_3 scale, Hf was added to alloys in this study. Hafnium has been shown to be a very beneficial reactive element [32, 33, 73]. Incorporation of Hf into Pt-free γ'-Ni_3Al alloys, however, resulted in a further investigation of its effects on the NiO growth. The first-principles calculation by Chao *et al.* [102] confirmed that Hf has a predominant preference for the Al sites in $L1_2$ Ni_3Al at all compositions and temperatures studied. Nevertheless, it is incorrect to explain the accelerated NiO formation on Ni-25Al-0.2Hf and Ni-25Al-0.5Hf (Figures 26a to c, Figures 27a to c, Figures 31 and 34, Figure 37a, Figures 41b and c) as a result of increased effective Ni/Al ratio, i.e., the opposite to what was

elucidated for the Pt effect in Chapter 5.1. It is unlikely that less than 1at.% Hf could have such a profound effect in modifying surface configuration of Ni and Al.

Many studies [108, 109, 110] have examined the reactive element effect on the growth of NiO scales at temperatures above 1000°C. It is well established that the predominant defects in NiO, which has the rock salt cubic crystal structure, are charged Ni and metal vacancies, thus giving the NiO p-type semiconducting behavior. In order to maintain electroneutrality, the addition of higher valence foreign cations by substitution causes a decrease in the concentration of holes and increase in the concentration of cation vacancies. Thus, when added at dopant levels, the tetravalent Hf^{4+} would raise the diffusivity of divalent Ni^{2+} by increasing the Ni vacancy concentration according to the defect reaction:

$$HfO_2 = Hf_{Ni}^{\cdot\cdot} + V_{Ni}^{''} + 2O_O \qquad (28)$$

Furthermore, Hf was found to form the highly stable oxide HfO_2 when increasing Hf content from 0.2 to 0.5at.% in a Ni-25Al alloy. The formation of HfO_2, a reactive-element oxide and oxygen getterer, may further inhibit the formation of a continuous and protective Al_2O_3 scale.

Evolution of grain structure in NiO scales has been carefully studied [111, 112, 113]. Two main types of scale were observed on pure Ni: single-layered and duplex. The latter has two layers comprised of an inner oxide next to the metal consisting of fine, equiaxed grains with relatively high porosity, and an outer, larger-grained, columnar oxide layer. Moosa and Rothman [109] reported that the addition of yttrium increases the NiO scale grain size with increasing oxidation temperatures from 700 to 900°C. Similar results were found in Hf-doped γ'-Ni_3Al alloys in this study. It was observed that the lateral mitigation of grain boundaries was exacerbated with increasing Hf content, as shown in Figures 25a to c, Figures 26a to c and Figures 27a to c. The exact mechanism by which Hf affects the NiO grain growth is not fully understood and is beyond the scope of this research.

5.3 Cooperation of Pt and Hf

Previous discussion confirmed that Pt addition (up to 20at.%) promotes the formation of a continuous Al_2O_3 scale on γ'-Ni_3Al alloys, while Hf addition (up to 0.5at.%) may enhance NiO growth on Pt-free γ'-Ni_3Al alloys. Based on previous studies on the RE effect,

Hf can be expected to perform beneficially when present at a dopant level (i.e., as a cation in solution) in the Al_2O_3 scale, and therefore one could conceive that the γ' alloy containing both Pt and Hf at appropriate amounts could exhibit outstanding high-temperature oxidation resistance. It was shown in Figure 41h that the formation of a slow-growing continuous Al_2O_3 scale was observed on the Pt and Hf co-doped Ni-25Al-20Pt-0.2Hf alloy, which is superior to the behavior of either Pt or Hf as individual additions to γ'. However, increasing the Hf content from 0.2 to 0.5at.% in Ni-25Al-20Pt did not reduce the Al_2O_3 scale growth kinetics. Moreover, a mixed scale containing both Al_2O_3 and HfO_2 was observed with increasing Hf content to 0.5at.%. This same effect was seen on a Ni-20Al-20Pt two-phase γ+γ' alloy containing 0.91at.% Hf, as shown in Figure 47g. These results suggest that Hf can impart the beneficial RE effect (i.e., reduced Al_2O_3 scale growth due to a "grain boundary blocking" effect), but only when it is added within a definite concentration window, above which a negative effect will arise. That negative effect is the oxidation of Hf to form HfO_2, which is non-protective.

Thus, an important factor that must be taken into account is that Pt can reduce or even preclude HfO_2 formation. It is seen in Figures 41c, f and i that increasing the Pt content from 0 to 20at.% in Ni-25Al-0.5Hf resulted in not only a thinner Al_2O_3 scale, but also a reduced amount of HfO_2 formation. As will be discussed in the following, this result indicates that Pt may have a negative chemical effect on Hf, thereby reducing its tendency to oxidize. As would be expected, this is even borne out during the early stages of oxidation. It was observed in Figures 32 and 35 that Hf starts to enrich at both the scale surface and the scale/alloy interface during the heating period on alloys with 10at.% Pt. However, when 20at.% Pt was added, this surface enrichment was not seen, as shown in Figures 33 and 36.

Thermodynamic considerations can help to elucidate the observed impact of Pt on the oxidation of Hf. Figure 71 shows a simplified Ellingham diagram that was generated using data compiled by Sigler [114]. The formation energies of Al_2O_3 and HfO_2 are in their standard state (i.e., activities of both Al and Hf are unity) to straightforwardly compare the relative thermal stability between Al_2O_3 and HfO_2.

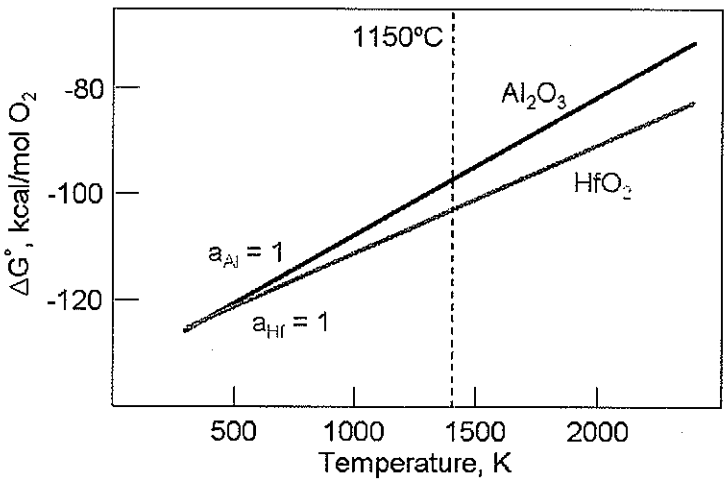

Figure 71. A schematic Ellingham diagram showing the standard free energy of formation vs. temperature for Al_2O_3 and HfO_2.

At the testing temperature of 1150°C the HfO_2 is thermodynamically more stable than Al_2O_3 under standard state conditions (Figure 71). Thus, Hf should always be oxidized below the Al_2O_3 scale as long as the Hf activity and content are above critical values. At dilute levels, the activity of Hf is directly proportional to the Hf content in accordance with Henry's law, i.e.,

$$a_{Hf} \approx \gamma \times X_{Hf} \tag{29}$$

where γ is the activity coefficient and X_{Hf} is the Hf content.

The internal oxidation of Hf may be accomplished by the following displacement reaction:

$$3\underline{Hf} + 2Al_2O_3 \rightarrow 3HfO_2 + 4\underline{Al} \tag{30}$$

in which the state of the underlining metal elements are in solution within the alloy and have chemical activities less than unity. The above reaction proceeds to the right in the Ni-25Al-0.5Hf alloy, as indicated in Figure 41c. The stability of this reaction proceeding to the right can be expressed mathematically using the Gibbs free energy change ΔG and the law of mass action, giving $RT\ln(K/K_{eq})$, <0. However, no internal HfO_2 formation was observed in the Pt-modified Ni-25Al-0.5Hf alloys as seen in Figures 41f and i. In order for the above reaction to proceed to the left the reaction constant K, defined by the activity quotient $(a_{Al})^4/(a_{Hf})^3$, must be larger than the equilibrium constant K_{eq} and therefore $\Delta G>0$. This could be achieved by a

significant decrease in the value of a_{Hf}. Since the Hf content in the alloys studied was relatively high (0.2 to 0.5at.%) from the common standpoint of reactive element additions (few hundreds ppm level), the above argument leads to the inference that the Hf activity in the alloys was decreased by the Pt additions. Furthermore, the extent of the Hf activity decrease is directly proportional to the Pt content as was also reported elsewhere [115].

5.4 Pt and Hf effects on Scale Spallation Behavior

The oxidation resistance of high-temperature alloys and metallic coatings is dependent on the formation of an adherent oxide scale. While the formation of an Al_2O_3 scale is desirable because of its excellent thermodynamic stability and slow growth rate, it is equally important to maintain good adhesion between the scale and the substrate. The development of voids at the scale/alloy interface during the oxidation process is an important factor when considering scale adhesion. These voids are a common feature of oxidized systems, and may be important in initiating scale spallation. [22, 28, 116].

It was seen in Figure 38 that the oxide formed on Ni-25Al spalled readily in large flakes during cooling from a 4-day isothermal oxidation test at 1150°C. A marked improvement in the scale adherence was observed with Ni_3Al alloys containing either increasing Pt, Hf or both Pt and Hf. Therefore, examinations of the scale/alloy interface may provide valuable information about the mechanisms of spallation and scale adherence. Figure 72a shows the intact oxide surface formed on Ni-25Al at 1150°C after 4 days. The scale surface was comprised of fine Al_2O_3 grains with localized oxide blisters. A triple grain junction area at the scale/alloy interface with complete oxide spallation is illustrated in Figure 72b. Partially separated islands with a rough surface were observed with interspaced smooth regions. The difference in the density of islands divided by the alloy grain boundaries may suggest that the void growth depends on the alloy crystallographic orientation. A higher magnification SEM image of a spalled region is shown in Figure 72c and indicates that the rough islands have small dimpled surfaces features, which are believed to be the oxide imprints at the scale/alloy interface before scale spallation occurred, as reported previously by other researchers [117, 118]. It was also seen that the oxide imprints were surrounded by large smooth craters with substrate alloy grain boundaries. These concave craters were

referred to as typical features resulting from a thermal etching process [119]. Its smoothness suggests that evaporation of aluminum from the alloy enabled the continued growth of the scale, even though out of contact with the scale inner surface [120]. The size and shape of these craters may thus be well correlated with the oxide blisters seen in Figure 72a. Meanwhile, alloy grain boundaries were considered as the principal cavity nucleation sites [121].

Figure 72d shows the intact oxide surface on a 4-day isothermally oxidized Ni-25Al-10Pt alloy at 1150°C. Besides the fine Al_2O_3 grains, the oxide blisters observed were smaller in size than those formed on Pt-free Ni-25Al. Their configuration and distribution are well in line with the scale/alloy interface shown in Figure 72e. The density of islands with oxide imprints on Ni-25Al-10Pt alloy was observably larger than on Ni-25Al. The islands in the Pt-containing alloy were mostly inter-connected with each other, which would certainly contribute to the improved scale adhesion. A higher magnification SEM image of the spalled region shown in Figure 72f indicates that the smooth area was not completely featureless but contains steps, characteristic of thermal etching [117].

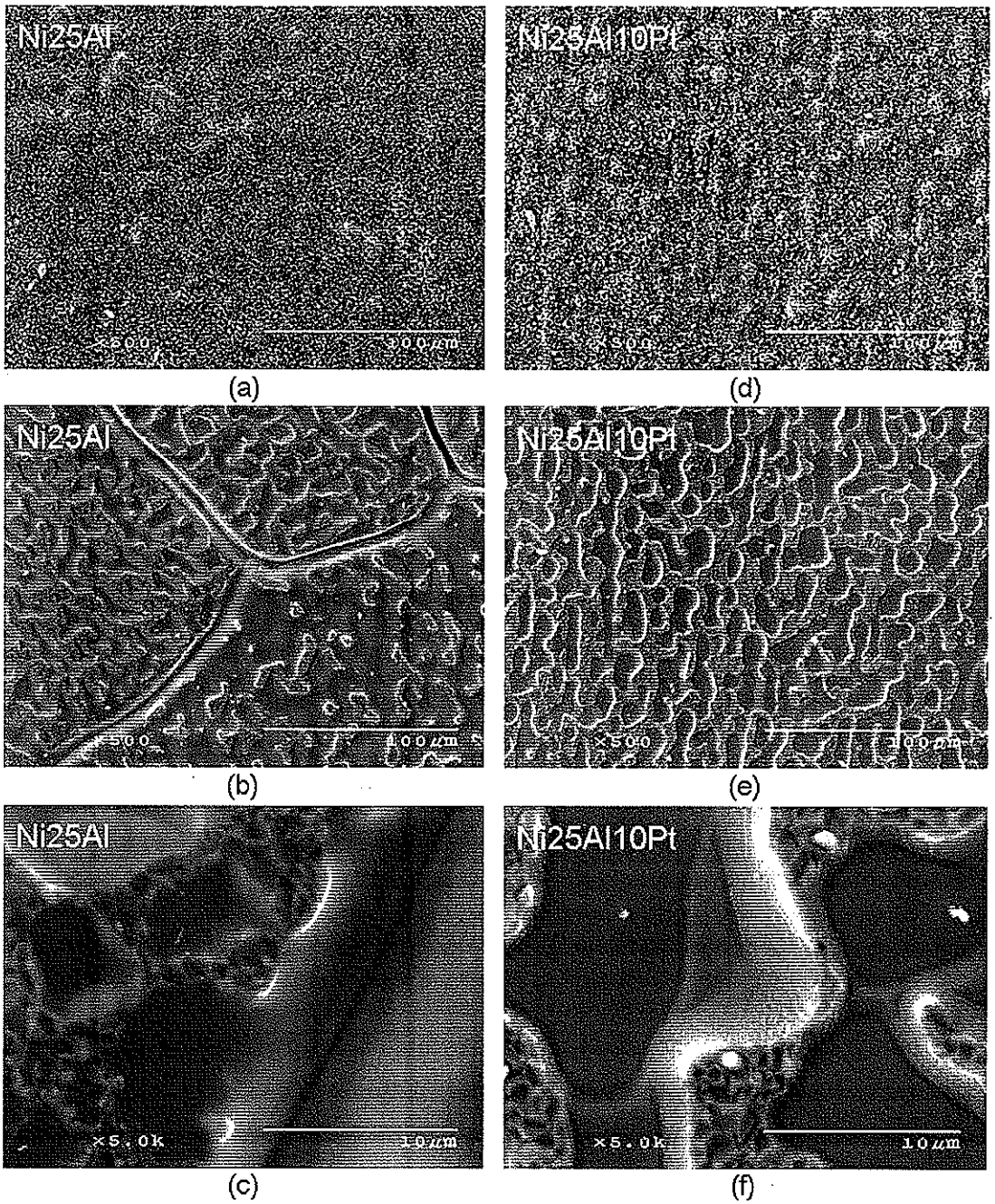

Figure 72. SEM images showing the surface of 4-day isothermally oxidized Ni-25Al: a) intact oxide; b) spalled area; c) higher mag. of spalled area; and Ni-25Al-10Pt: d) intact oxide; e) spalled area; f) higher mag. of spalled area; at 1150°C.

Interfacial void formation was further investigated by confocal photo-stimulated microspectroscopy (CPSM) using a polarized light source, the results are shown in Figure 73. Alloys Ni-25Al, Ni-25Al-10Pt and Ni-25Al-20Pt were oxidized at 1100°C for 50 hours to illustrate the formation of interfacial voids. Figure 73 indicates that increasing the Pt content up to 20at.% in Ni-25Al effectively reduced the interfacial void quantity, which could be responsible for the greatly reduced scale spallation illustrated in Figure 38.

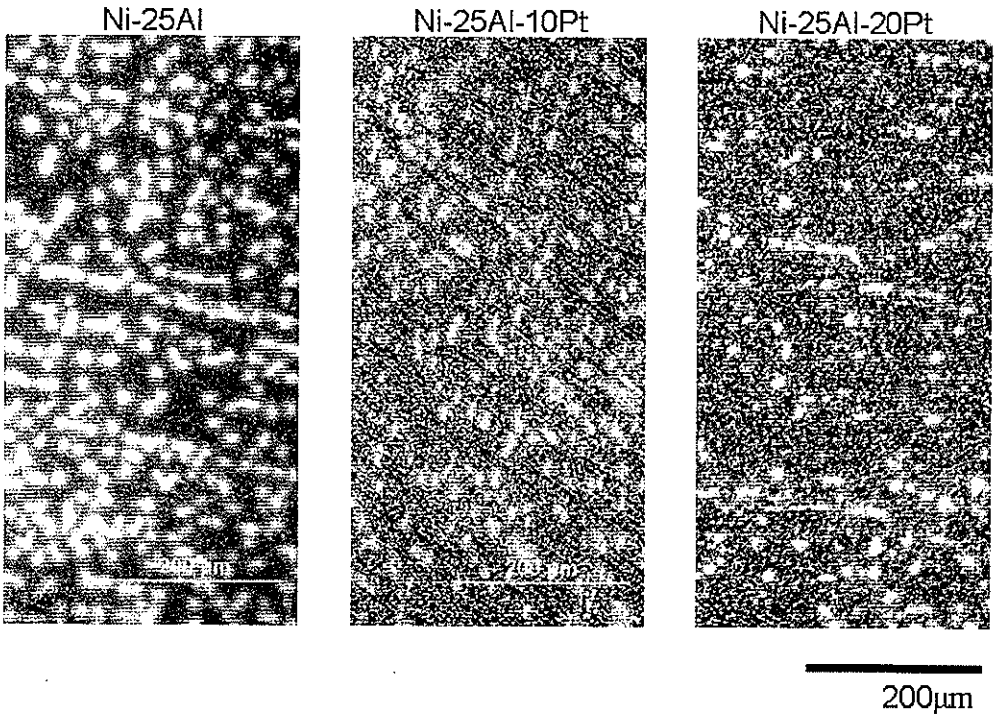

Figure 73. Interfacial voids formation detected by CPSM on alloys Ni-25Al, Ni-25Al-10Pt and Ni-25Al-20Pt isothermally oxidized at 1100°C for 50 hours.

A CPSM 3D construction showing the void depths on both Ni-25Al and Ni-25Al-10Pt after 50 hours isothermal oxidation at 1100°C is shown in Figure 74. Both images were plotted within a virtual cube using identical edge lengths of 10μm. The depth of voids formed on Ni-25Al was measured to be approximately 2 to 3μm, while on Ni-25Al-10Pt the measured depth was was less than 1μm. Thus, Pt not only decreased the interfacial void

quantity, but it also reduced the void depth and size, both of which could enhance scale adhesion.

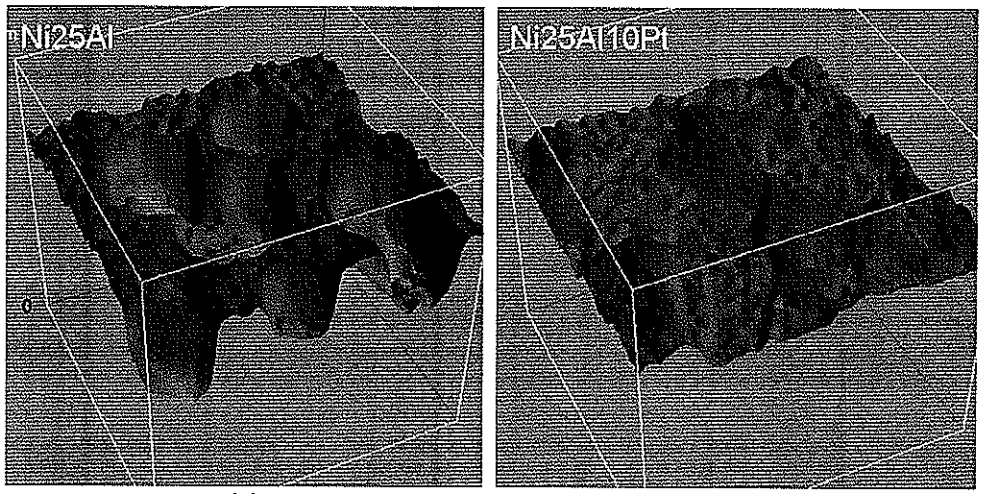

Figure 74. CPSM resolved 3D projections showing the voids formed at scale/alloy interface on isothermally oxidized a) Ni-25Al and b) Ni-25Al-10Pt at 1100°C for 50 hours.

Many investigations have revealed large interfacial voids associated with a convoluted scale configuration [118, 120]. It was suggested by Stott and Wood [13, 16] that the development of the convoluted morphology resulted in extensive detachment of the oxide from the alloy. The coarsening of the convoluted oxide morphology as blisters was the result of a progressive increase in the length of the oxide comprising individual oxide blisters. This may occurred as an outcome of lateral growth of both the intact and separated oxide. However, they did not clarify the origin responsible for the nucleation and development of interfacial voids, which in turn, dictates the scale spallation.

A further examination on γ'-Ni_3Al alloys revealed that the interfacial voids formed during the early-stage oxidation. Figure 75 shows the scale surface of Ni-25Al-xPt (x=0, 10, and 20) alloys evolved with increasing oxidation time from 90 to 1800 seconds under the 15keV SEM beam accelerating voltage. This figure is the same as Figure 25 except for only the increased beam energy from 5keV to 15keV. This higher beam voltage facilitates electrons penetrating deeper into surface and yielding more information from scale/alloy

interface [94]. Despite the loss of scale surface morphology, it is seen that there were a number of voids formed, presumably in the alloy at the scale/alloy interface on both Ni-25Al-10Pt and Ni-25Al-20Pt right after 90 seconds heating at 970°C. These voids tended to coalesce and expand with increasing oxidation time and temperature. Although a thicker oxide made them more indistinct, the shape and distribution of these interfacial voids were still discernible after 1800 seconds. Faster growing NiO made it not possible to clearly observe void growth on Ni-25Al alloy. However, there was extensive scale spallation from this alloy after 4 days isothermal oxidation at 1150°C, as seen in Figure 38, so it is plausible that interfacial voids had also formed on Ni-25Al during early-stage oxidation.

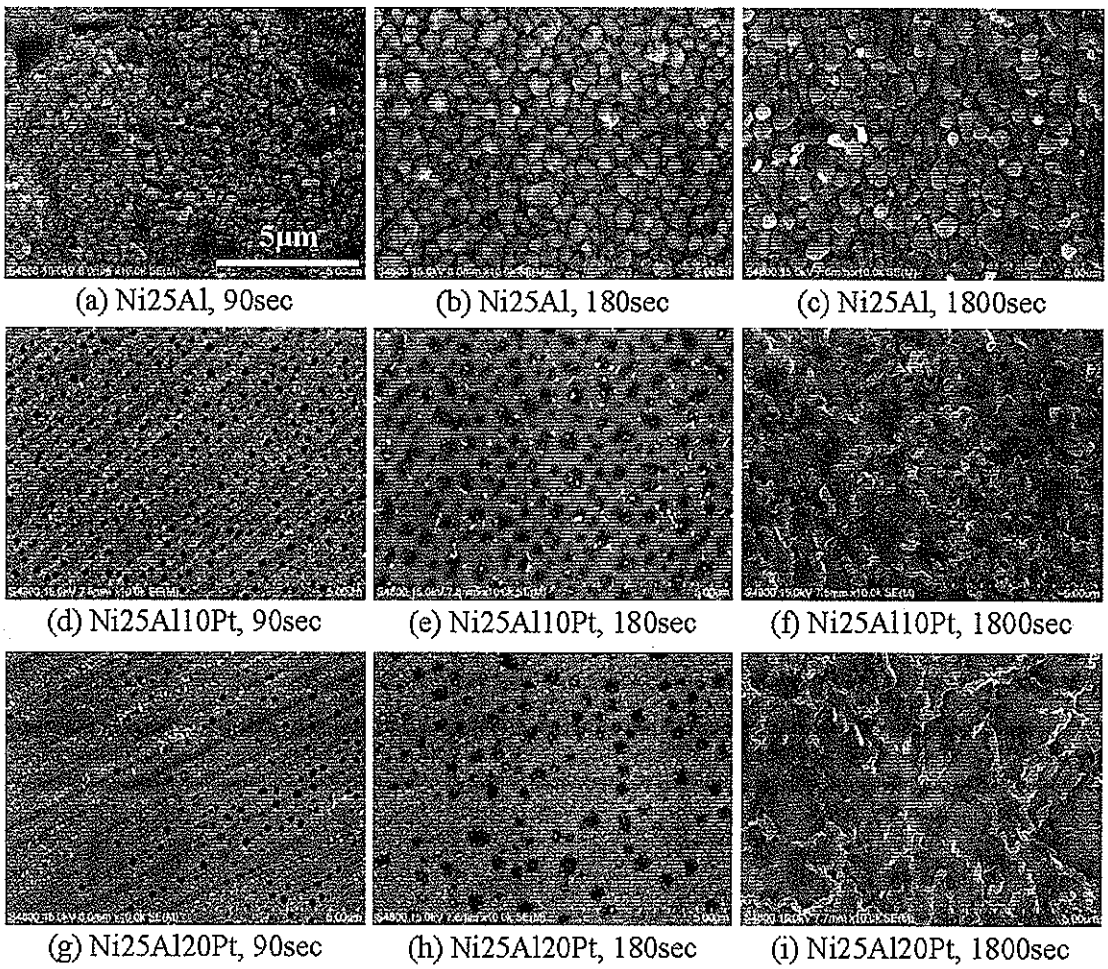

Figure 75. SEM images showing the surface morphology of scales formed on Ni-25Al-xPt (x=0, 10 and 20) alloys with 15keV beam accelerating voltage.

Kuenzly and Douglass [104] carefully studied the oxidation behavior of Ni_3Al containing yttrium. The alloys they investigated were Ni-13.2wt.%Al (Ni-24.9at.%Al) and Ni-13.2wt.%Al-0.5wt.%Y (Ni-24.9at.%Al-0.3at.%Y) which are quite similar to the γ'-Ni_3Al alloys used in this study as Ni-25at.%Al and Ni-25at.%Al-0.2at.%Hf. They concluded that the presence of voids at the scale/alloy interface played an important role in scale spallation and poor scale adherence on Ni_3Al.

A model was then proposed by Kuenzly and Douglass to account for the creation of interfacial voids. The specific case considered the initial formation of NiO followed by the development of an Al_2O_3 layer. At the beginning, NiO nuclei tend to overgrow and undercut the Al_2O_3 because NiO is the faster growing oxide. The formation of NiO results in nickel depletion and aluminum enrichment, as was confirmed by GDOES results shown in Figure 28. As soon as the Al content reaches the critical value, Al_2O_3 would establish itself as a complete layer to shut down further Ni outward diffusion. The subsequent selective oxidation process results in aluminum depletion and nickel enrichment at the scale/alloy interface.

Many studies confirmed that the backward diffusion of nickel occurs at a greater rate than the migration of aluminum to the surface [122, 123]. This behavior could be attributed to the crystal structure of γ'-Ni_3Al, in which a Ni atom is surrounded with its nearest eight Ni sites without producing disorder to the $L1_2$ crystal structure, while an Al atom has to exchange its position with the neighboring Ni atom. In other words, the number of possible vacancy jumps for Ni must be much higher than Al due to the three times more common Ni sites.

The vacancies are formed by unequal diffusion of Al towards the Al_2O_3 scale and backward diffusion of Ni in the opposite direction by the following flux balance reaction:

$$J_V = J_{Ni} - J_{Al} \tag{31}$$

where J is the flux and the subscripts V, Ni and Al denote vacancy, nickel and aluminum, respectively. These vacancies may coalesce and condense as small voids, which further grow to a larger size. It is postulated that the condensed voids observed in the scale/alloy interface acted to promote extensive scale spallation.

As Pt promotes the fast build-up of a protective Al_2O_3 scale, much improved scale adherence was observed on Ni-25Al-10Pt and Ni-25Al-20Pt, as seen in Figure 38. This

improvement should also be related with the reduced interfacial voids both in number (Figure 73) and size (Figure 74). It is known that Pt increases the diffusive flux of Al in γ'-Ni_3Al from Equation (27). Meanwhile, the backward diffusive flux of Ni could be reduced as well since the Pt was added at the expense of Ni. Both the decrease of J_{Ni} and increase of J_{Al} could reduce the diffusive flux of outward vacancies as predicted in Equation (31).

From the standpoint of oxide mechanical properties, it is desirable to have a thinner oxide scale that has higher critical strain energy for scale spallation. The approach of the critical strain ε_c for scale spallation can be calculated by [124, 125, 126]:

$$\varepsilon_c = \sqrt{\frac{2\gamma_0}{dE_{ox}(1-\nu)}} \tag{32}$$

where $2\gamma_0$ being the fracture energy of the scale/alloy interface, d the oxide thickness, E_{ox} the Young's modulus of the oxide and ν the Poisson ratio. The important point to make is that the critical strain energy for oxide scale spallation has an inverse relationship to the scale thickness. The thinner oxide formed on Pt-modified Ni-25Al would have a higher ε_c, which may translate to better scale adherence.

Hf additions completely changed the scale growth mechanism on Ni-25Al. Fast growing NiO significantly restrained the vacancy condensation at scale/alloy interface by Kirkendall effect. What resulted was limited scale spallation with increasing Hf content, as seen in Figure 38. SEM examinations on the scale/alloy interface confirmed that the interfacial voids were much reduced on γ'-Ni_3Al alloy with Hf additions. Besides, 0.5at.% Hf led to overdoping of the Ni-25Al, as indicated by the formation of Hf-rich oxide intrusions at the scale/alloy interface. This may be categorized as the mechanical keying effect by the formation of macropegs to improve scale adhesion [32].

5.5 Al_2O_3 Microstructures Affected by Hf Additions

The experimental results presented in this study clearly indicated that the Hf additions altered the Al_2O_3 scale morphology, presumably by modifying the transport processes of diffusing species such as oxygen and aluminum ions. And macroscopically, the Hf-doped alloys exhibited a slower Al_2O_3 scale growth rate, as seen in Figures 44, 45 and 48. Thus, fundamentals regarding the parameters affecting the modes and mechanisms of Al_2O_3 scale

development are necessary in understanding the influence of RE effects in the diffusion processes. Kingery *et al.* [127, 128] showed that oxygen diffusivity in polycrystalline Al_2O_3 was two-orders of magnitude higher than in single-crystal alumina between 1300°C and 1900°C due to the enhanced short-circuit diffusion along the alumina grain boundaries (GB); whereas, aluminum diffusivity was reported to be not strongly dependent upon the presence of GB. However, extrapolation of these high temperature data to 1150°C will result in erroneous results since the oxygen diffusivity is sensitive to impurities and structures at lower temperatures. Kuenzly and Douglass [104] concluded that the enhanced grain boundary diffusion of oxygen controls the oxidation rate of alloys forming Al_2O_3 scales between the temperatures of 900°C and 1300°C. Although the exact growth mechanism may vary in different alloy systems, it has been widely accepted that short circuits such as grain boundaries are major ionic diffusing paths that control the rate of Al_2O_3-scale growth. The Al_2O_3 scale seen in Figure 46a shows no indication of ridges growing above alumina grain boundaries — referred as intrinsic ridges [129] — due to outward aluminum transport. Meanwhile, the metal extrusion at the scale-alloy interface to result in metal inclusions within the scale, as shown in Figure 47a, suggests that the rate-controlling transport process was the enhanced diffusion of oxygen down grain boundaries.

However, the popularly accepted belief that α-Al_2O_3 scale grows by inward diffusion of oxygen seems to be an oversimplification [58]. Many studies on Al_2O_3 growth mechanism by oxygen isotope indicated that the contribution from Al outward diffusion along grain boundaries could not be excluded [16, 130]. Figure 56a exhibited the typical cross-section of an Al_2O_3 scale with considerable variations in the grain size [120, 131 , 132]. The morphology gradually changes from fine equiaxed grains, submicron in size at the outer interface, to large columnar grains a few microns in diameter extending toward the inner interface parallel to the growth direction. In agreement with the previous studies [133, 134], this Al_2O_3 microstructure is a typical morphology resulted from the preferential grain boundary diffusion of both aluminum and oxygen.

The remarkable difference of Hf-doped Al_2O_3 scale was shown in Figure 56b. Comparing with the scale formed on Ni-20Al-20Pt, it is seen that there are more columnar grains (i.e., more grain boundaries) near the scale inner surface on alloy Ni-20Al-20Pt-0.5Hf

after 100 hours isothermal oxidation at 1150°C. Serving as the diffusing paths responsible for the Al_2O_3 growth as discussed above, more grain boundaries should result in faster scaling kinetics and larger scale thickness. However, it is unequivocally seen that the thickness of Hf-doped Al_2O_3 was only about half of the Hf-free scale. This result can only be explained by the grain boundary blocking effect exerted by Hf additions [135]. Assuming the oxygen inward diffusion was unaltered by the presence of Hf at grain boundaries, the effective diffusion coefficient of aluminum can be expressed as [136]:

$$D_{eff}^{Al} = (1-f)D_l^{Al} + fD_{gb}^{Al} \tag{33}$$

where D_l^{Al} is the Al lattice diffusivity, D_{gb}^{Al} is Al grain boundary diffusivity, and f is the volume fraction of grain boundaries. Since the value of f was increased with the Hf additions, the only feasible way by which D_{eff}^{Al} could be reduced is a significant decrease in the value of D_{gb}^{Al}. Confirmed by the TEM analysis as shown in Figure 59, it is rationalized that the routinely observed Hf grain-boundary segregation is indeed responsible for the reduction in Al_2O_3 growth rate. Detailed TEM analysis on localized scale would further substantiate the grain boundary blocking effect. It was seen in Figures 61 and 62 that Al_2O_3 grains evolve to a columnar structure deeper within the scale. Moreover, the scale was much thinner away from the scale grain boundaries, reflecting that the growth of the scale was primarily by diffusion along these short circuits paths. This observation is exactly the same as the result reported by Pint *et al.* [99] that the scale formed on a Hf-doped NiAl possessed similar columnar grain structure.

It is suggested that the oxide ridges formed on the scale surface were caused by the outward diffusion of Al and following lateral growth of new oxide within grain boundaries. Therefore, Hf blocking effect should reduce the formation of these ridges. This is supported by the observation that less oxide ridges formed on the scale outer surface with increasing Hf content in Ni-20Al-20Pt, as seen in Figure 46.

However, achieving an adequate Hf dopant level is of primary importance in acquiring the excellent oxidation performance. Despite the thinner Al_2O_3 scale formed on 0.05Hf than the undoped base alloy in Figure 47b, localized scale thickening indicates that the Hf content was too low so that the RE benefit was observed in only confined areas,

whereas higher than optimum Hf levels as 0.91at.% promoted the formation of HfO_2, as seen in Figure 47g with accelerated scaling kinetics shown in Figure 44. Moreover, methods of uniformly incorporating optimal amount of Hf in coatings are of considerable importance since excessive Hf-rich oxides will detrimentally form as scale inclusions and internal oxides (Figure 68).

5.6 Hf Effects of θ-α-Al_2O_3 Transformation

It has been widely reported that the metastable forms of alumina, γ-, δ- and θ-Al_2O_3, develop on all alumina-forming alloys at relatively low oxidation temperatures <1000°C [101, 137, 138, 139]. There are many debates on the formation sequence of these metastable alumina phases. However, it is widely accepted that the transformation from θ-Al_2O_3 to α-Al_2O_3 involves a change in the oxygen sublattice from cubic to hexagonal close packing (ccp → hcp) and generally occurs above 1000°C. The metastable alumina phases contain a high concentration of cation vacancies so that the diffusivity of Al^{3+} is rather high and the resulting oxides grow relatively fast. Brumm and Grake [140] carefully studied the oxidation behavior of NiAl and plotted the parabolic growth rate constant (k_p) of each alumina phase present within the temperature range 700 to 1400°C, as shown in Figure 76. It is seen that the θ→α transformation leads to a considerable decrease of k_p, i.e., over two orders of magnitude. Needless to say, α-Al_2O_3 is the most desirable phase for high-temperature protection due to its slowest scaling kinetics. However, a 13% volume reduction in the scale was reported [141, 142] to accompany the θ→α transformation and the resulting tensile stress tends to lead to scale cracking.

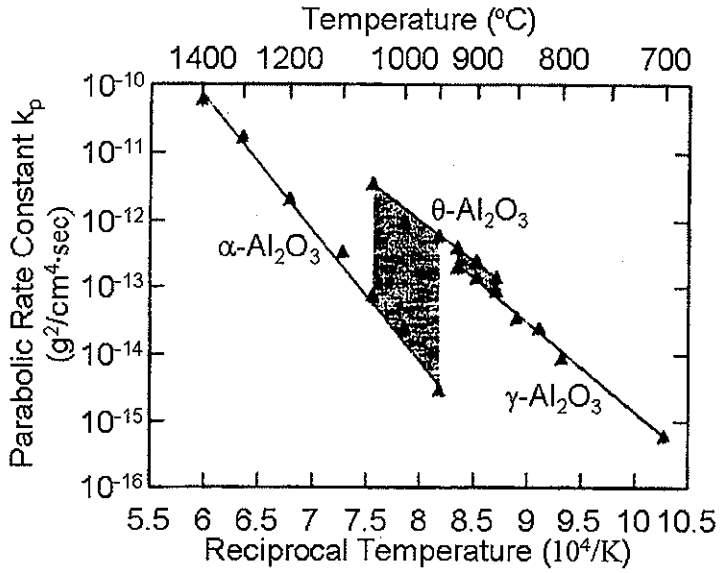

Figure 76. Arrhenius plot of the parabolic rate constants k_p of NiAl oxidation [140].

Burtin *et al.* [137] reported that certain additives such as Zr, Ca, and La etc. tend to inhibit the $\theta \rightarrow \alpha$ transformation. Pint *et al.* [142] found that ions with a relatively large ionic size acted as inhibitors to the phase transformation. However, Grabke [138] argued that the possible retardation of transformation does not play a role since large cations do not enter the oxide or only to a negligible amount. Therefore, according to Grabke, large ions do not participate in the phase transformation by affecting the crystal structure.

It was clearly shown in this study that Hf additions delayed the $\theta \rightarrow \alpha$ transformation, as seen in Figure 55. Due to the fast growth rate of θ-Al_2O_3, the weight change of Hf-doped Ni-20Al-20Pt alloys was always higher than the Hf-free alloy Ni-20Al-20Pt, as shown in Figure 48. This effect was directly proportional to the Hf content. The exact mechanism by which large ion additions inhibit the $\theta \rightarrow \alpha$ phase transformation is not well understood. It was suggested that large ions in the relatively open cubic lattice inhibit the diffusionless, martensitic- or shear-type transformation from cubic to hexagonal Al_2O_3 [143]. By distorting the surrounding cubic Al_2O_3 lattice, large dopant ions may stall a diffusionless transformation by requiring more energy to overcome the distortion.

TEM studies [144, 145] have shown the α-Al_2O_3 nucleation takes place at the scale/alloy interface on RE-free alloys. In this way, α-Al_2O_3 can easily undercut the

metastable oxides growth and initiate their transformation. It is suggested that the scale/alloy interface could provide preferential α-Al_2O_3 nucleation sites, such as defects, which are preferred over the gas/scale interface. Recent unpublished results on Hf-free $\gamma+\gamma'$ alloys obtained from Hayashi at Hokkaido University are in agreement with this. Moreover, Hayashi found that the $\theta \rightarrow \alpha$ transformation occurred on the outer surface of the scale formed on Hf-doped $\gamma+\gamma'$ alloys. A schematic showing this difference in $\theta \rightarrow \alpha$ transformation location is presented in Figure 77.

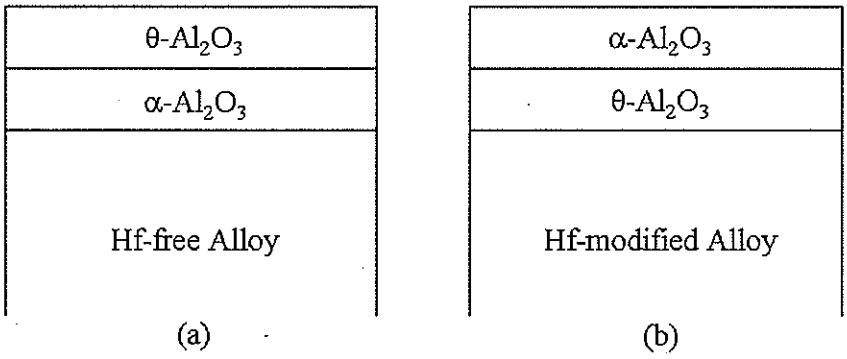

Figure 77. A schematic showing the $\theta \rightarrow \alpha$-$Al_2O_3$ transformation area in a) Hf-free alloy and b) Hf-modified alloy.

The transformation preference near the scale outer surface on Hf-modified alloy may be due to the higher Hf concentration near the scale inner surface retarding the transformation. Doychak and Rühle [146] studied the alumina scale microstructure on Zr-doped β-NiAl and observed that the solubility of impurities was less in α-Al_2O_3 than in θ-Al_2O_3, resulting in a sweeping effect of the Zr-rich precipitates out of α-Al_2O_3 as the transformation front progressed. They further concluded that the transformation from θ-Al_2O_3 to α-Al_2O_3 begins at the free surface of the gas/scale interface. It was proposed by Pint [72] that the reactive element tends to diffuse out from the scale/alloy interface toward gas/scale interface as a result of the oxygen potential gradient across the scale. Therefore, a Hf concentration gradient down to the gas/scale interface could cause the $\theta \rightarrow \alpha$ transformation to occur easier near the scale outer surface.

5.7 Hf Effects on Scale Stress Evolution

It has been recognized for years that the growth of an oxide on a metal surface may result in the generation of stresses [50]. Other stresses, such as those mechanically imposed, geometrical constraints, temperature change and temperature gradient, cannot be avoided for components in service at high temperatures [124]. From the point of view of oxidation protection, the scale adhesion is highly dependent on the mechanisms of stress generation, of stress relief, and of scale failure. Because of the complexity of the problems involved with stresses, this discussion will only focus on the scale growth stress and thermal stresses induced by temperature change.

Since Hf delays the $\theta \rightarrow \alpha$ transformation, less stress could be expected during the metastable Al_2O_3 growth by outward cationic diffusion. This is because the new oxide has enough free space to grow at the gas/scale interface. Due to the volume contraction from $\theta \rightarrow \alpha$ transformation, tensile stress will be generated in α-Al_2O_3 while compressive stress in θ-Al_2O_3.

It was mentioned above that Hf-modified Al_2O_3 scale microstructure transitioned from large grains near the gas/scale interface to finer columnar morphologies towards scale/alloy interface on an isothermally oxidized Ni-20Al-20Pt-0.48Hf alloy at 1150°C for 100 hours, as shown in Figure 56b. It is widely accepted that reactive elements can reduce compressive growth stress in alumina scales by segregating into their grain boundaries. In this way, segregated RE dopants suppress lateral scale growth by restraining the formation of new oxide following the reaction between inward diffusing oxygen ions and outward diffusing aluminum ions. Ramanarayanan *et al.* [125, 147] suggested that such modified grain structures may permit scales to deform more easily by diffusional plastic flow or grain boundary sliding enabling growth stresses to be accommodated. However, Kumar and Douglass [148] argued that the doping of α-Al_2O_3 with reactive elements would increase the strength of alumina and thus reduce its plasticity. Veal *et al.* [149] recently found that the relaxation rates for alumina grown on the Hf-doped γ'-Ni_3Al alloy are about an order of magnitude slower than the relaxation rates for alumina grown on Hf-free γ'-Ni_3Al alloy. This is in agreement with Kumar and Douglass's conclusion. Nonetheless, Veal *et al.* assumed

that the oxide grain size on Hf-doped sample is larger than the grain size formed on undoped samples, contributing to the reduction in creep rate. This is obviously counter to the results obtained by in-lens SEM in this study, which showed that smaller grain size develops in the Al_2O_3 scales formed on the Hf-doped alloys. Results obtained in the current study are insufficient to clarify these conflicting findings.

It is worth noting that Veal *et al.* [149] also observed that the oxides formed on the Ni-25Al-20Pt γ'-Ni_3Al alloy showed steady state compressive stress during isothermal oxidation at 1100°C, while the oxides formed on Hf-doped Ni-25Al-20Pt-0.2Hf γ'-Ni_3Al alloy exhibited a significant steady state tensile stress. The exact growth mechanism responsible for this persistent tensile behavior on Hf-doped alloys was not rationalized.

5.8 Determination of Al_2O_3 Scale Growth Rate

The most common way to evaluate the high-temperature oxidation behavior of a material is to determine its oxidation kinetics. Since the growth of alumina scales is governed by the diffusion of aluminum and/or oxygen through the scale via lattice or short-circuits diffusion, the oxidation kinetics of Al_2O_3-forming metals and alloys is usually described through the so-called parabolic law [150] given by Equation (16), with k_p being the parabolic rate constant. For practical purposes, the parabolic law is normally expressed in terms of sample weight change Δm, instead of the scale thickness. This is because the sample weight change is typically obtained more easily by using an analytical balance. Accompanied with the increasing storage and calculation capability of modern computers, TGA allows the continuous and accurate recording of the sample weight change over the long oxidation periods, which makes accurate determination of oxidation kinetics more feasible. Providing there is no loss of oxide during the oxidation and so the weight change is the same as the weight gain, Equation (16) changes to its simplest form as:

$$\Delta m^2 = k_p t \tag{34}$$

where Δm is the weight gain per unit area (mg/cm^2) at time t and k_p is the parabolic rate constant (g^2/cm^4·sec). However, it is often found [151] that the early-stage oxidation mass-gain curve cannot be simulated by this classical parabolic law. Discrepancies may arise from many factors, such as heating rate, sample surface preparation, scale composition and oxide

grain size, etc. Monceau and Pieraggi [151] meticulously examined different initial oxidation conditions and concluded that a more accurate parabolic rate constant should be obtained by fitting the mass change curve with a complete quadratic expression:

$$t = A + B\Delta m + C\Delta m^2 \tag{35}$$

here C is the reciprocal of the parabolic rate constant, $1/k_p$.

Moreover, there are frequent observations of sub-parabolic oxidation kinetics of Al_2O_3-forming alloys and coatings [152, 153, 154]. Quadakkers [152] examined the oxidation of the Y_2O_3-strengthened alloy MA956 at 1000-1100°C and reported that the oxide grain size increases progressively when moving from the gas/scale interface to the scale/metal interface (i.e., grain size increases in the scale growth direction), and that this leads to a sub-parabolic scale growth rate. This behavior could be accurately approximated by power-law relationship between the weight gain Δm and time t as:

$$\Delta m = kt^n \tag{36}$$

in which n ranges from 0.3 to 0.4. This deviation from the classic parabolic law (n = 0.5) will result in thinner protective oxides at long times, a reduced extent of aluminum depletion, and a longer lifetime before chemical failure or oxide spallation [154]. The exact value of n can be determined from a double logarithmic plot of Equation (36), i.e., $\log \Delta m$ vs. $\log t$.

Therefore, accurate evaluation of thermogravimetric data to determine the oxide scaling kinetics becomes an issue of choosing the correct process for better mathematical approximation of weight change data as a function of time. For that reason, it was discussed by Peraldi *et al.* [155] that it is more accurate to simulate the thermogravimetric data by the following cubic equation:

$$t = A + B\Delta m + C\Delta m^2 + D\Delta m^3 \tag{37}$$

which is a full polynomial expression with n ranging from 0 through to 3. Whether a curve fits parabolic or cubic kinetics could then be resolved by comparing the relative weight of the constant term A, linear term $B\Delta m$, parabolic term $C\Delta m^2$, and cubic term $D\Delta m^3$ in Equation (37). In this way, Peraldi *et al.* [155] concluded that the oxidation of pure Ni at 800°C follows the cubic rate law.

Assessment of the thermogravimetric data shown in Figure 44 by using Equation (37) indicates that the oxidation kinetics of the Hf-doped Ni-20Al-20Pt alloys are indeed sub-

parabolic. A more accurate estimation of the oxidation rate would require quantification of alumina scale microstructure. More recently, Naumenko *et al.* [156] successfully simulated a sub-parabolic near-cubic oxidation rate of a FeCrAlY alloy by determining the columnar grain size evolution of the alumina scale aided by in-lens SEM. It is reasonable that the oxidation rate has a strong dependence on the scale microstructure evolution rather than possessing a fixed value during the overall oxidation period.

5.9 Surface Segregation of Indigenous Sulfur

The effect of impurity sulfur on the adhesion of oxide scales formed on alloys and metals has been a topic of considerable discussion and research since the 1980s [157, 158, 159, 160, 161]. Many researchers found that the scale adherence is inherently strong on "S-free" alloys. Sigler [160] observed excellent scale adherence on a vacuum annealed metal surface. Smialek [158] found that highly adherent Al_2O_3 eventually formed on undoped NiCrAl alloys by an initial repeated oxidation and surface removal (i.e., sulfur purging), presumably due to the successive removal of interfacial segregated sulfur. Indeed, without surface treatments, indigenous sulfur at tramp levels (less than 100ppm) within alloys tends to segregate to the interface, weakening the scale-alloy bonding and accounting for the massive spallation of thermally grown oxide. Grabke *et al.* [162] examined FeCr and β-NiAl alloys and concluded that the sulfur effect on the scale adherence is most probably due to the very high tendency for sulfur segregation on free-metal surfaces, which leads to a remarkable decrease in the interface energy. Once void formation and/or scale detachment started at the scale/alloy interface, sulfur would segregate to there and stabilize these defects.

Efforts have been conducted to overcome this deleterious sulfur effect, including vacuum annealing, H_2 annealing and surface removal. Nonetheless, the most practical way is by adding reactive elements [27, 33, 163, 164]. It is suggested by Funkenbusch *et al.* [165] that most commonly used reactive elements, Ce, Y, Hf, Zr, etc., are strong sulfide formers and their presence may prevent the sulfur segregation since the effective amount of free sulfur available for segregation is reduced. Another possibility is that reactive element additions may segregate preferentially to the scale/alloy interface and thus restrict the interface impurity content by site competition. Other researchers [24, 28, 29, 166] have

proposed that Pt additions, when added into coatings, may inhibit the formation of interfacial voids and therefore indirectly hinder the sulfur segregation as well. Although exact mechanism by which Pt and RE additions affect the sulfur segregation remains unclear, this effect is frequently observed and discussed.

A series of alloys as listed in Table 9 were examined through the collaboration with Dr. Peggy Hou at Lawrence Berkeley National Laboratory. These alloys were made by the MPC in the Ames Laboratory using the same sample preparation procedures as described in Chapter 3.1. Isothermal oxidation testing was then performed at 1150°C for 100 hours. Interfacial sulfur content and interface strength were then examined by Hou using an *in situ* scratch technique in an ultrahigh vacuum chamber equipped with a scanning Auger microscope (SAM). Interface strength was taken in arbitrary unit as the ratio between the width of the scratch and of the spalled area caused by the scratch. More detailed experimental procedures have been presented elsewhere [164]. Both interfacial sulfur content and interface strength results are summarized in Table 9 and plotted in Figure 78. The sulfur content was about 1.1at.% at the scale/alloy interface on the Ni-25Al base alloy. Interfacial sulfur was not detected when the base alloy was doped with Pt or co-doped with Pt and Hf. Not only was the sulfur prevented, interface strength was also enhanced with Pt and Hf additions. Quite interestingly, interfacial sulfur content was markedly increased with lowered interface strength when Cr, known as an active sulfur carrier [99], was added into Ni-22Al-0.3Hf and Ni-22Al-5Pt-0.3Hf.

Careful examination of interfacial sulfur content was further taken on alloy Ni-25Al-10Pt. Although sulfur was not present on any interfaces (oxide imprinted area), it is worth noting that various amounts of sulfur (1.4~4.7at.%) were found on pores and voids formed at scale/alloy interfaces. This result appears to be in good agreement with the conclusions drawn by Grabke *et al.* [162], who suggested that sulfur would segregate to the free-metal surface upon separation of scale and metal (pores and voids) rather than to the adherent scale/metal interface.

Table 9. Sulfur segregation vs. interface strength.

Alloy	Sulfur Content at Interface (at.%)	Interface Strength (arbitrary unit)
Ni-25Al	1.1 ± 0.4	1.9
Ni-25Al-10Pt	0	6
Ni-22Al-5Pt-0.3Hf	0	12
Ni-22Al-5Cr-0.3Hf	8.5 ± 1.1	2
Ni-22Al-5Cr-5Pt-0.3Hf	8.2 ± 1.3	5

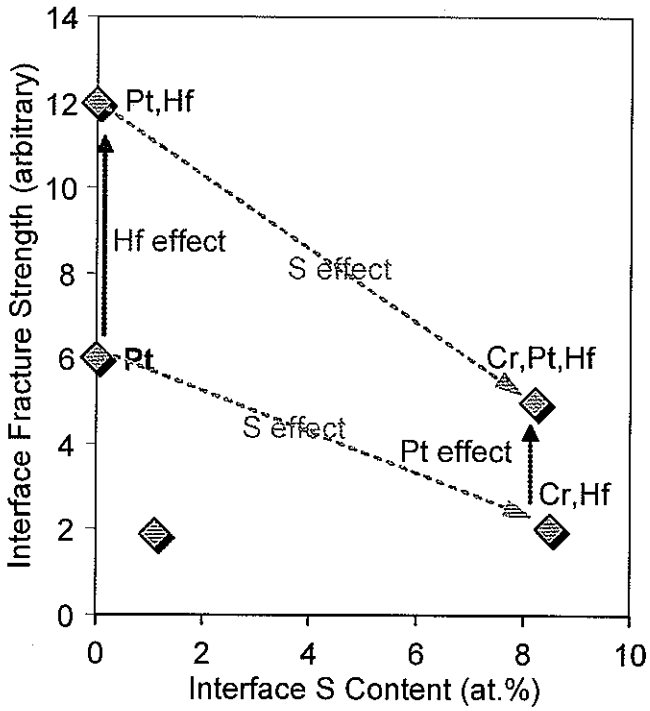

Figure 78. A schematic showing the relationship between interface fracture strength and interfacial sulfur content affected by Pt, Hf and Cr.

5.10 Pt+Hf-Modified γ-Ni+γ'-Ni_3Al Coatings

The high-temperature oxidation behavior of coating is more complicated than that of pure metals and single-phase alloys. These complications mainly originated from the dynamic compositional changes that results from coating/substrate interdiffusion. Due to the

complexity of this topic, attention will be limited primarily to the overall performance of the coatings.

The ability to form an equally or even more protective oxide scale is a key prerequisite for the replacement of currently being-used β-NiAl coatings with the Pt+Hf-modified γ-Ni+γ'-Ni_3Al coatings. It was shown that γ+γ'-based alloys and coatings are indeed protective alumina formers with improved high-temperature oxidation resistance compared to the Pt-modified β-NiAl. Although Pt diffused into the superalloy substrate during extended thermal exposure, its presence within the coating layer at relatively high concentration level contributed to the coating maintaining Al_2O_3-scale growth. On the other hand, Hf could effectively reduce the scaling kinetics when it is doped at appropriate amounts. Therefore, the synergistic effect of co-doping with Pt and Hf underwrites the applicability of Pt+Hf-modified γ-Ni+γ'-Ni_3Al coatings.

The key improvement of the application of Pt+Hf-modified γ-Ni+γ'-Ni_3Al coatings is the relief of TCP phases generated from the interdiffusion between the widely used β-NiAl coatings and superalloy substrate. Accompanied with the development of higher generation superalloys, further additions of Re have been employed due to its ability in improving the superalloy's mechanical properties, particularly creep resistance [167]. Together with other alloying elements, however, Re also increases the formation of TCP phases because of its lower solubility in the interdiffusion zone of β-NiAl and the superalloy substrate. By the same token, a new type of phase instability called secondary reaction zone (SRZ) was observed having a strong dependence on the Re content [83] as well. Thus, the inherited phase compatibility between γ+γ' coatings with Ni-based superalloys could effectively suppress the formation of both TCPs and SRZs.

Another advantage of γ+γ' coatings is the exclusion of stresses induced by any phase transformations. Tolpygo and Clarke [168] reported the large Al depletion-driven volume contraction from β to γ' is a major cause for surface rumpling. Zhang *et al.* [36] examined the transformation from β phase (B2) to a martensitic phase ($L1_0$) and concluded that the volume change associated with the martensitic transformation likely to contribute to the early-stage surface roughening. Stresses related with these phase transformations directly promote the failure of thermally grown oxide and can dictate the lifetime of entire TBCs. Therefore, the

utilization of γ+γ' coatings could preclude the transformation induced stresses so as to efficiently stabilize the overall TBCs system.

The successful deposition of Pt+Hf-modified γ-Ni+γ'-Ni_3Al coatings depends on many factors including the temperature and time in both pack cementation and post heat treatment processes. Due to the influence from numerous other alloying elements, it is seen that coating performance is highly sensitive to the Hf content and distribution compared to what was found with alloys. Therefore, a correct combination of temperature and time is necessary to ensure the penetration of Hf into coatings so as to avoid any surface enrichment. In addition, proper surface treatment such as polishing and grit-blasting could also facilitate the formation of protective alumina scale.

Up to date, research on the Pt+Hf-modified γ-Ni+γ'-Ni_3Al coatings has been focused on the preparation and assessment of stand-alone metallic coatings upon various superalloy substrates. It is worth examining the performance of such coatings with top ceramic thermal barrier layers as well for future applications. Preliminary results done in Gleeson's group indicate that the Pt+Hf-modified γ-Ni+γ'-Ni_3Al coatings perform well with YSZ top coatings. Moreover, it does appear that the performance of such coatings is directly affected by the substrate superalloy compositions as well.

CHAPTER 6 SUMMARY

6.1 Single-Phase γ-Ni and γ'-Ni_3Al Alloys

Both early-stage and 4-day isothermal oxidation behavior of single-phase γ-Ni and γ'-Ni_3Al alloys were investigated by examining weight-change kinetics, oxide scale microstructures, and GD-OES resolved elemental concentration profiles.

Pt promotes Al_2O_3 formation by quenching the NiO growth on both γ-Ni and γ'-Ni_3Al single-phase alloys. This effect increases with increasing Pt content and, in the case of γ', can be partly attributed to the preference of Pt on the Ni sublattice sites in the $L1_2$ crystal structure. Moreover, Pt exhibits this effect even at lower temperatures (~970°C) in the very early stage of oxidation. The present findings also suggest that Pt enhances Al diffusive flux from the substrate to the scale/alloy interface, particularly during the very early stages of oxidation. This latter "Pt effect" is applicable to both the γ and γ' systems.

Contrary to the beneficial Pt effects, Hf could profoundly promote the NiO formation when added as reactive elements with trace amount into Pt-free γ'-Ni_3Al Ni-25Al alloy. This effect intensified with increasing Hf content from 0.2 to 0.5at.%. It could be inferred as the semiconducting doping effect as Hf additions increasing cation vacancies of Ni in NiO.

The synergistic effect of co-doping of Pt and Hf was studied by examining Pt+Hf-modified γ'-Ni_3Al alloys. It was deduced that Pt acts to reduce the Hf activity so that the formation of HfO_2 was more effectively suppressed with higher Pt content. Therefore, the formation of Al_2O_3 facilitated by Pt additions and the development of NiO assisted by Hf additions are a competing scale growth process, which is influenced by the relative content of both Pt and Hf. Higher Pt certainly promoted the growth of more-protective Al-rich oxide and suppress the growth of unwanted HfO_2. Hf was detrimental beyond its optimal reactive element amounts by forming unnecessary HfO_2. Thus, alloys with optimum high-temperature oxidation resistance require a judicious combination of Pt and Hf. For instance, based on the present results, optimum alloys were Ni-25Al-10Pt-0.2Hf and Ni-25Al-20Pt-0.2Hf.

Large interfacial voids were observed on Ni-25Al alloy after a 4-day isothermal oxidation at 1150°C. The formation of interfacial voids is attributed to the Kirkendall effect.

Pt promotes the scale adherence effectively by minimizing the flux of vacancies so as to suppress the formation of interfacial voids.

Pt can act to prevent the segregation of indigenous S to the scale/alloy interface so as to strengthen it. Hf strengthens the scale/alloy interface as well. Sulfur was only detected on free surfaces while there was no sulfur presented on the interfaces.

6.2 Two-Phase γ-Ni+γ'-Ni_3Al Alloys

Pt and Hf effects on the two-phase γ-Ni+γ'-Ni_3Al Ni-20Al-20Pt-xHf (x ranges from 0 to 0.91) alloys were examined by both thermal gravimetric analyses and cyclic oxidation tests. The microstructure of the thermally grown oxide was characterized by confocal photo-stimulated microspectroscopy (CPSM), in-lens SEM, and FIB-TEM.

Hf additions markedly decrease the weight change of isothermally oxidized Hf-doped alloys by forming thinner oxide scales than on Hf-free base alloy Ni-20Al-20Pt. The overall effect was to reduce the weight change by factors of between 3 for 0.05Hf and 6 for 0.48Hf from the base alloy after 100 hours. It is observed that the weight change decreases regularly with increasing Hf content from 0.05 to 0.48at.%. Accordingly, the parabolic rate constant of Ni-20Al-20Pt-0.05Hf was an order of magnitude lower than that of the base alloy, and even further reduced by two orders of magnitude in the alloy with 0.48at.% Hf. This could be attributed to a grain boundary blocking effect in the α-Al_2O_3 scale brought about by the segregated Hf additions. However, an over-doped alloy with 0.91at.% Hf exhibited a detrimental RE effect by forming both Al_2O_3 and internally oxidized HfO_2, which implies that Hf only exhibits beneficial RE effect when added within the optimum level.

An additional effect of Hf additions is the fast transition from transient-stage to steady-stage oxidation, which could be referred to that Hf additions accelerate the nucleation of more-protective Al_2O_3 scale.

It was shown that Hf additions do not change the alloy phase configurations significantly. However, it was measured that Hf invariably partitions into the γ'-Ni_3Al phase in which the concentration of Hf is about 10 times that in the γ-Ni phase. As a consequence, an optimum oxidation benefit brought about by the Hf addition can only be fully realized if the γ' is uniformly distributed within the alloy. Stated more specifically, γ' must be the

principal phase in order for a given Pt+Hf-modified γ+γ' alloy to be of optimum composition and structure for oxidation resistance.

It was observed that Hf additions altered the microstructure of Al_2O_3 scale with modified scale growth mechanism. More equiaxed grains above columnar grains formed on isothermally oxidized Hf-free Ni-20Al-20Pt. The scale formed on Ni-20Al-20Pt-0.48Hf had a two-layered structure, with large grains near the outer surface and columnar grains near the scale/alloy interface. The most remarkable difference between these two samples was that the column width of grains on Ni-20Al-20Pt (~1.1μm) was much larger than on Ni-20Al-20Pt-0.48Hf (~0.5μm). Even so, the Hf-doped alloys exhibited much slower scaling kinetics, with a resulting thinner scale thickness. This behavior was ascribed to Hf blocking diffusing paths by segregating into Al_2O_3 grain boundaries. Therefore, Hf-doped scale was growing at a lower rate even with more grain boundaries.

Accompanied with the scale microstructure modification, Hf additions led to a further two effects: 1) Hf delayed the $\theta \rightarrow \alpha$-$Al_2O_3$ transformation; 2) compressive residual stress in the scale formed on Hf-doped alloys was lower than on Hf-free Ni-20Al-20Pt alloy.

6.3 Development of Pt+Hf-Modified γ-Ni+γ'-Ni_3Al Coatings

Pt+Hf-modified γ-Ni+γ'-Ni_3Al-based coatings were successfully developed with improved high-temperature oxidation resistance compared to the most widely used Pt-modified β-NiAl coatings.

The key improvement of the application of Pt+Hf-modified γ-Ni+γ'-Ni_3Al coatings was the absence of TCP phases, as are generated from the interdiffusion between the β-NiAl coatings and superalloy substrate. This could be simply attributed to the inherited phase compatibility between γ+γ' coatings and Ni-based superalloy substrates. This effect is more favorable with the higher generation superalloys, which have higher amounts of refractory elements susceptible to the formation of TCPs and SRZs.

Traditional β-NiAl coatings experience phase transformations from $\beta \rightarrow \gamma'$ and/or β→martensite. Large stresses are generated from these phase transformations. On the contrary, a major advantage of γ+γ' coatings is the exclusion of phase transformation induced

stresses. The exclusion of such stresses is believed to be a primary reason for the $\gamma+\gamma'$ coatings to not undergo unwanted surface rumpling during extended thermal cycling from 1150°C.

Pt+Hf-modified γ-Ni+γ'-Ni_3Al coating composition has a strong dependence on the temperature and time in both pack cementation and post heat treatment processes. Meanwhile, the coating performance is more sensitive to the Hf content than alloys. Moreover, the coating performance is also strongly affected by the surface finish and substrate superalloy compositions.

REFERENCES

1 J.R. Nicholls, Advances in Coating Design for High-Performance Gas Turbines, MRS Bulletin, p. 659-670, September, 2003.

2 National Research Council, Coatings for High-Temperature Structural Materials: Trends and Opportunities, ISBN: 0-309-05381-1, National Academy Press, Washington, D.C., 1996.

3 R.W. Cahn, A. G. Evans and M. McLean, High-Temperature Structural Materials, ISBN: 0-412-75010-4, Chapman & Hall for the Royal Society, 1996.

4 J.L. Smialek, Advances in the Oxidation Resistance of High-Temperature Turbine Materials, Surface and Interface Analysis, vol. 31, p. 582-592, 2001.

5 R.C. Reed, the Superalloys: Fundamentals and Applications, ISBN-10: 0-521-85904-2, Cambridge University Press, 2006.

6 T.M. Pollock et al., Superalloys 2000, ISBN: 0-87339-477-1, TMS, 2000.

7 A.G. Evans, D.R. Mumm, J.W. Hutchinson, G.H. Meier, F.S, Pettit, Mechanisms Controlling the Durability of Thermal Barrier Coatings, Progress in Materials Science, vol. 46, p. 505-553, 2001.

8 C.G. Levi, Emerging Materials and Processes for Thermal Barrier Systems, Current Opinion in Solid State and Materials Science, vol. 8, p. 77-91, 2004.

9 N.P. Padture, M. Gell, E.H. Jordan, Thermal Barrier Coatings for Gas-Turbine Engine Applications, Science, vol. 296, p. 280-284, 2002.

10 B. Gleeson, Thermal Barrier Coatings for Aeroengine Applications, Journal of Propulsion and Power, vol. 22, no. 2, p. 375-383, 2006.

11 R.L. Jones, Thermal Barrier Coatings, Metallurgical and Ceramic Protective coatings, edited by K.H. Stern, ISBN: 0-412-54440-7, Chapman & Hall, 1996.

12 N.B. Dahotre, J.M. Hampikian, J.E. Morral, Elevated Temperature Coatings: Science and Technology IV, ISBN: 0-87339-489-5, TMS, 2001.

13 F.H. Stott, G.C. Wood, Growth and Adhesion of Oxide Scales on Al_2O_3-Forming Alloys and Coatings, materials Science and Engineering, vol. 87, p. 267-274, 1987.

14 G.C. Wood, High-Temperature Oxidation of Alloys, Oxidation of Metals, vol. 2, no. 1, p. 11-57, 1970.

15 H. Hindam and D.P. Whittle, Microstructure, Adhesion and Growth Kinetics of Protective Scales on Metals and Alloys, Oxidation of Metals, vol. 18, nos. 5/6, p. 245-284, 1982.

16 G.C. Wood and F.H. Stott, The Development and Growth of Protective α-Al_2O_3 Scales on Alloys, High Temperature Corrosion, NACE6, p. 227-250, 1983.

17 J.L. Smialek and R. Gibala, Diffusion Processes in Al_2O_3 Scales: Void Growth, Grain Growth, and Scale Growth, NASA Technical Reports Server, p. 274-283, Jan. 1, 1983.

18 F.H. Stott, The Oxidation of Alumina-Forming Alloys, Materials Science Forum, vol. 251-251, p. 19-32, 1997.

19 B. Gleeson, High-Temperature Corrosion of Metallic Alloys and Coatings, Corrosion and Environmental Degradation, edited by M. Schütze, ISBN: 3-527-29505-4, 2000.

20 A.M. Karlsson, J.W. Hutchinson, A.G. Evans, The Displacement of the Thermally Grown Oxide in Thermal Barrier Systems Upon Temperature Cycling, Materials Science and Engineering, A351, p. 244-257, 2003.

21 G. Lehnert and H. Meinhardt, Present State and Trend of Development of Surface Coating Methods Against Oxidation and Corrosion at High Temperature, Electrodeposition and Surface Treatment, vol. 1, p. 71-76, 1972.

22 E.J. Felten, Use of Platinum and Rhodium to Improve Oxide Adherence on Ni-8Cr-6Al Alloys, Oxidation of Metals, vol. 10, no. 1, p. 23-28, 1976.

23 J.H. Chen, J.A. Little, Degradation of the Platinum Aluminide Coating on CMSX-4 at 1100°C, Surface and Coatings Technology, vol. 92, p. 69-77, 1997.

24 Y. Cadoret, M.P. Bacos, P. Josso, V. Maurice, P. Marcus and S. Zanna, Effect of Pt Additions on the Sulfur Segregation, Void Formation and Oxide Scale Growth of Cast Nickel Aluminides, Materials Science Forum, vols. 461-464, p. 247-254, 2004.

25 P.Y. Hou, K.F. McCarty, Surface and Interface Segregation in β-NiAl with and without Pt Addition, Scripta Materialia, vol. 54, p. 937-941, 2006.

26 Y. Zhang, J.A. Haynes, W.Y. Lee, I.G. Wright, B.A. Pint, K.M. Cooley and P.K. Liaw, Effects of Pt Incorporation on the Isothermal Oxidation Behavior of Chemical Vapor Deposition Aluminide Coatings, Metallurgical and Materials Transactions A, vol. 32A, p. 1727-1741, 2001.

27 H.J. Grabke, D. Wiemer and H. Viefhaus, Segregation of Sulfur During Growth of Oxide Scales, Applied Surface Science, vol. 47, issue 3, p. 243-250, 1991.

28 B.A. Pint, On the Formation of Interfacial and Internal Voids in α-Al_2O_3 Scales, Oxidation of Metals, vol. 48, nos. 3/4, p. 303-328, 1997.

29 B.A. Pint, I.G. Wright, W.Y. Lee, Y. Zhang, K. Prüßner, K.B. Alexander, Substrate and Bond Coat Compositions: Factors Affecting Alumina Scale Adhesion, Materials Science and Engineering A, vol. 245, p. 201-211, 1998.

30 L.B. Pfeil, U. K. Patent no. 459848, 1937.

31 P. Kofstad, Appraisal Keynote: Future Trends and Developments, The Role of Active Elements in the Oxidation Behaviour of High Temperature Metals and Alloys, edited by E. Lang, ISBN: 1-85166-420-3, Elsevier Applied Science, 1989.

32 D.P Whittle and J. Stringer, Improvements in High Temperature Oxidation Resistance by Additions of Reactive Elements or Oxide Dispersions, Philosophical Transactions of the Royal Society of London, Series A, vol. 295, p. 309-329, 1980.

33 D.P. Moon, Role of Reactive Elements in Alloy Protection, Materials Science and Technology, vol. 5, p. 754-764, 1989.

34 D.B. Miracle, The Physical and Mechanical Properties of NiAl, Acta Metallurgica et Materialia, vol. 41, no. 3, p. 649-684, 1993.

35 D.R. Clarke, C.G. Levi, Materials Design for the Next Generation Thermal Barrier Coatings, Annual Review of Materials Research, vol. 33, p. 383-417, 2003.

36 Y. Zhang, J.A. Haynes, B.A. Pint, I.G. Wright, W.Y. Lee, Martensitic Transformation in CVD NiAl and (Ni, Pt)Al Bond Coatings, Surface and Coatings Technology, vol. 163-164, p. 19-24, 2003.

37 W.S. Waltson, J.C. Schaeffer and W.H. Murphy, A New Type of Microstructural Instability in Superalloys – SRZ, Superalloys, edited by R.D. Kissinger, et al., The Minerals, Metals & materials Society, p. 9-18, 1996.

38 B. Gleeson, W. Wang, S. Hayashi, D. Sordelet, Effects of Platinum on the Interdiffusion and Oxidation Behavior of Ni-Al-Based Alloys, Materials Science Forum, vol. 461-464, p. 213-222, 2004.

39 B. Gleeson et al., US Patent no. 7,273,662, 2007.

40 D.R. Gaskell, Introduction to the Thermodynamics of Materials, Third Edition, ISBN: 1-56032-432-5, Taylor & Francis, 1995.

41 N. Birks, G.H. Meier, and F.S. Pettit, Introduction to the High-Temperature Oxidation of Metals, Second Edition, ISBN-10: 0-521-48042-6, Cambridge University Press, 2006.

42 A.S. Khanna, Introduction to High Temperature Oxidation and Corrosion, ISBN-10: 0-871-70762-4, ASM International, 2002.

43 P. Kofstad, High-Temperature Oxidation of Metals, John Wiley & Sons Inc., 1966.

44 C. Wagner, Theoretical Analysis of the Diffusion Processes Determining the Oxidation Rate of Alloys, Journal of the Electrochemical Society, vol. 99, no. 10, p. 369-380, 1952.

45 C. Wagner, Atom Movements, American Society for Metals, Cleveland, Ohio, p. 153, 1951.

46 F.A. Kröger, The Chemistry of Imperfect Crystals, Second Edition, ISBN-10: 0-444-10561-1, American Elsevier, 1964.

47 F.H. Stott, Methods of Improving Adherence, Materials Science and Technology, vol. 4, p. 431-438, 1988.

48 N.B. Pilling and R.E. Bedworth, The Oxidation of metals at High Temperatures, The Journal of the Institute of Metals, vol. 29, p. 529-591, 1923.

49 O. Kubaschewski and B.E. Hopkins, Oxidation of Metals and Alloys, Second Edition, Butterworth and Co. Ltd., 1962.

50 J. Stringer, Stress Generation and Relief in Growing Oxide Films, Corrosion Science, vol. 10, p. 513-543, 1970.

51 E. Schumann, C. Sarioglu, J.R. Blachere, F.S. Pettit, and G.H. Meier, High-Temperature Stress measurements During the Oxidation of NiAl, Oxidation of Metals, vol. 53, nos. 3/4, p. 259-272, 2000.

52 D.M. Lipkin, and D.R. Clarke, Measurement of the Stress in Oxide Scales Formed by Oxidation of Alumina-Forming Alloys, Oxidation of Metals, vol. 45, nos. 3/4, p. 267-280, 1996.

53 C. Wagner, Formation of Composite Scales Consisting of Oxides of Different Metals, Journal of the Electrochemical Society, vol. 103, no. 11, p. 627-633, 1956.

54 C.E. Birchenall, Oxidation of Metals and Alloys, American Society for Metals, Metals Park, Ohio, p. 177-200, 1970.

55 E.J. Felten and F.S. Pettit, Development, Growth, and Adhesion of Al_2O_3 on Platinum-Aluminum Alloys, Oxidation of Metals, vol. 10, no. 3, p. 189-222, 1976.

56 K.P.R. Reddy, J.L Smialek, and A.R. Cooper, ^{18}O Tracer Studies of Al_2O_3 Scale Formation on NiCrAl Alloys, Oxidation of Metals, vol. 17, nos. 5/6, p.429-449, 1982.

57 J.K. Doychak, T.E. Mitchell, J.L. Smialek, High Temperature Oxidation of β-NiAl, Materials Research Society Symposia Proceedings, vol. 39, p. 475-484, 1985.

58 R. Prescott and M.J. Graham, The Formation of Aluminum Oxide Scales on High-Temperature Alloys, Oxidation of Metals, vol. 38, nos. 3/4, p. 233-254, 1992.

59 F.S. Pettit, Oxidation Mechanisms for Nickel-Aluminum Alloys at Temperatures Between 900° and 1300°C, Transactions of the Metallurgical Society of AIME, vol. 239, p. 1296-1305, September, 1967.

60 J. Doychak, A TEM Study of Transient Oxide Scales on β-NiAl, Proceedings of the 42nd Annual Meeting of the Electron Microscopy Society of America, Edited by G.W. Bailey, p. 598-599, 1984.

61 H.J. Grabke, M.W. Brumm and B. Wagemann, The Oxidation of NiAl, Materials and Corrosion, vol. 47, p. 675-677, 1996.

62 R. Streiff, O. Cerclier and D.H. Boone, Structure and Hot Corrosion Behavior of Platinum-Modified Aluminide Coatings, vol. 32, p. 111-126, 1987.

63 J. Schaeffer, G.M. Kim, G.H. Meier and F.S. Pettit, The Effects of Precious Metals on the Oxidation and Hot Corrosion of Coatings, The Role of Active Elements in the Oxidation Behaviour of High Temperature Metals and Alloys, edited by E. Lang, ISBN: 1-85166-420-3, Elsevier Applied Science, 1989.

64 M.R. Jackson, J.R. Raiden, The Aluminization of Platinum and Platinum-Coated IN-738, Metallurgical Transactions A, vol. 8A, p. 1697-1707, 1977.

65 T. Xu, M.Y. He, and A.G. Evans, A Numerical Assessment of the Durability of Thermal Barrier Systems that Fail by Ratcheting of the Thermally Grown Oxide, Acta Materialia, vol. 51, issue 13, p. 3807-3820, 2003.

66 L.B. Pfeil, U. K. Patent, no. 574088, 1945.

67 G. Beranger, F. Armanet and M. Lambertim, Active Elements in Oxidation and Their Properties, The Role of Active Elements in the Oxidation Behaviour of High Temperature Metals and Alloys, edited by E. Lang, ISBN: 1-85166-420-3, Elsevier Applied Science, 1989.

68 M.W. Chase, JANAF Thermochemical Tables, Journal of Physical and Chemical Reference Data, vol. 4, 1985, Supplement no. 1, third edition, American Institute of Physics for the National Bureau of Standards.

69 W.D. Kingery, Property Measurements at High Temperatures, John Wiley & Sons Inc., 1959.

70 D.P. Moon and M.J. Bennett, The Effects of Reactive Element Oxide Coatings on the Oxidation Behaviour of Metals and Alloys at High Temperatures, Materials Science Forum, vol. 43, p. 269-298, 1989.

71 B.A. Pint, Limitations on the Use of Surface Doping for Improving High-Temperature Oxidation Resistance, MRS Bulletin, October, p. 26-30, 1994.

72 B.A. Pint, Experimental Observations in Support of the Dynamic-Segregation Theory to Explain the Reactive-Element Effect, Oxidation of Metals, vol. 45, nos. 1/2, p. 1-37, 1996.

73 A.M. Huntz, Effect of Active Elements on the Oxidation Behaviour of Al_2O_3-Formers, The Role of Active Elements in the Oxidation Behaviour of High Temperature Metals and Alloys, edited by E. Lang, ISBN: 1-85166-420-3, Elsevier Applied Science, 1989.

74 J.C. Schaeffer, W.H. Murphy, and J.L. Smialek, The Effect of Surface Condition and Sulfur on the Environmental Resistance of Airfoils, Oxidation of Metals, vol. 43, nos. 1/2, p. 1-23, 1995.

75 C.T. Sims, W.C. Hagel, The Superalloys, ISBN: 0-471-79207-1, John Wiley & Sons Inc., 1972.

76 G.H. Meier and F.S. Pettit, High-Temperature Corrosion of Alumina-Forming Coatings for Superalloys, Surface and Coatings Technology, vol. 39-40, p. 1-17, 1989.

77 M.W. Chen, R.T. Ott, T.C. Hufnagel, P.K. Wright, K.J. Hemker, Microstructural Evolution of Platinum Modified Nickel Aluminide Bond Coat During Thermal Cycling, Surface and Coatings Technology, vol. 163-164, p. 25-30, 2003.

78 J.A. Nesbitt, E.J. Vinarcik, C.A. Barrett and J. Doychak, DiffusionTransport and Predicting Oxidative Failure During Cyclic Oxidation of β-NiAl Alloys, Materials Science and Engineering A, vol. 153, p. 561-566, 1992.

79 J.G. Foutain, F.A. Golightly, F.H. Stott, and G.C. Wood, The Influence of Platinum on the Maintenance of α-Al_2O_3 as a Protective Scale, Oxidation of Metals, vol. 10, no. 5, 1976, p. 341-345.

80 G. Hultquist, B. Tveten, E. Hörnlund, M. Limbäck, and R. Haugsrud, Self-Repairing Metal Oxides, Oxidation of Metals, vol. 56, no. 3/4, p. 313-346, 2001.

81 J. Angenete, K. Stiller, and V. Langer, Oxidation of Simple and Pt-Modified Aluminide Diffusion Coatings on Ni-Base Superalloys — I. Oxide Scale Microstructure, Oxidation of Metals, vol. 60, no. 1/2, p. 47-82, 2003.

82 B.A. Pint, The Role of Chemical Composition on the Oxidation Performance of Aluminide Coatings, Surface and Coatings Technology, vol. 188-189, p. 71-78, 2004.

83 I.E. Locci, R.A. MacKay, A. Garg, F. Ritzert, Successful Surface Treatments for Reducing Instabilities in Advanced Nickel-Base Superalloys for Turbine Blades, NASA/TM — 2004-212920, March, 2004.

84 R. Bianco, M.A. Harper, and R.A. Rapp, Codepositing Elements by Halide-Activated Pack Cementation, JOM, p. 68-73, November, 1991.

85 B. Gleeson et al., US Patent, application: 20060127695, 2006.

86 J. Pisonero, B. Fernández, R. Pereiro, N. Bordel, A. Sanz-Medel, Glow-Discharge Spectrometry for Direct Analysis of Thin and Ultra-Thin Solid Films, Trends in Analytical Chemistry, vol. 25, no. 1, p. 11-18, 2006.

87 S. Hayashi, T. Narita, and B. Gleeson, Early-Stage Oxidation Behavior of γ'-Ni_3Al-Based Alloys with and without Pt Addition, Materials Science Forum, vols. 522-523, p. 229-238, 2006.

88 D.M. Lipkin and D.R. Clarke, Measurement of the Stress in Oxide Scales Formed by Oxidation of alumina-Forming Alloys, Oxidation of Metals, vol. 45, nos. 3/4, p. 267-280, 1996.

89 D.M. Lipkin, H. Schaffer, F. Adar, and D.R. Clarke, Lateral Growth Kinetics of α-Alumina Accompanying the Formation of a Protective Scale on (111) NiAl During Oxidation at 1100°C, Applied Physics Letters, vol. 70, no. 19, p. 2550-2552, 1997.

90 D.B. Hovis, A.H. Heuer, Confocal Photo-Stimulated Microspectroscopy (CPSM) — Residual Stress Measurements in Al_2O_3 Using Confocal Microscopy, Scripta Materialia, vol 53, p. 347-349, 2005.

91 G.M. Raynaud and R.A. Rapp, In Situ Observation of Whiskers, Pyramids and Pits During the High-Temperature Oxidation of Metals, Oxidation of Metals, vol. 21, nos. 1/2, p. 89-102, 1984.

92 R. Peraldi, D. Monceau, and B. Pieraggi, Correlations Between Growth Kinetics and Microstructure for Scales formed by High-Temperature Oxidation of Pure Nickel. I. Morphologies and Microstructures, Oxidation of Metals, vol. 58, nos. 3/4, p. 249-273, 2002.

93 T.F. An, H.R. Guan, X.F. Sun and Z.Q. Hu, Effect of the θ-α-Al_2O_3 Transformation in Scales on the Oxidation Behavior of a Nickel-Base Superalloy with an Aluminide Diffusion Coating, Oxidation of Metals, vol. 54, nos. 3/4, p. 301-316, 2002.

94 S. Hayashi and B. Gleeson, Effects of Pt on the Short-Term Oxidation Behavior of γ-Ni+γ'-Ni_3Al Alloys, Materials at High Temperatures, vol. 22, no. 3/4, p. 321-328, 2005.

95 M.P. Brady, B. Gleeson, and I.G. Wright, Alloy Design Strategies for Promoting Protective Oxide-Scale Formation, JOM, p.16-21, January, 2000.

96 P. Kofstad, High Temperature Corrosion, ISBN-10: 1-851-66154-9, Elsevier Applied Science, 1988.

97 F. Gesmundo and B. Gleeson, Oxidation of Multicomponent Two-Phase Alloys, Oxidation of Metals, vol. 44, nos. 1/2, p. 211-237, 1995.

98 B.A. Pint, A.J. Garratt-Reed, and L.W. Hobbs, Possible Role of the Oxygen Potential Gradient in Enhancing Diffusion of Foreign Ions on α-Al_2O_3 Grain Boundaries, Journal of the American Ceramic Society, vol. 81, p. 305-314, 1998.

99 B.A. Pint, K.L. More, and I.G. Wright, Effect of Quaternary Additions on the Oxidation Behavior of Hf-Doped NiAl, Oxidation of Metals, vol. 59, nos. 3/4, p. 257-283, 2003.

100 A.H. Heuer, A. Reddy, D.B. Hovis, B. Veal, A. Paulikas, A. Vlad, M. Rühle, The Effect of Surface Orientation on Oxidation-Induced Growth Strains in Single Crystal NiAl: An In Situ Synchrotron Study, Scripta Materialia, vol. 54, p. 1907-1912, 2006.

101 G.C. Rybicki and J.L. Smialek, Effect of the θ-α-Al_2O_3 Transformation on the Oxidation Behavior of β-NiAl+Zr, Oxidation of Metals, vol. 31, nos. 3/4, p. 275-304, 1989.

102 C. Jiang, D.J. Sordelet, B. Gleeson, Site Preference of Ternary Alloying Elements in Ni_3Al: A First-Principles Study, Acta Materialia, vol. 54, p. 1147-1154, 2006.

103 P.G. Kotula and C.B. Carter, Interfacial Control of Reaction Kinetics in Oxides, Physical Review Letters, vol. 77, no. 16, p. 3367-3370, 1996.

104 J. D. Kuenzly and D.L. Douglass, The Oxidation Mechanism of Ni_3Al Containing Yttrium, Oxidation of Metals, vol. 8, no. 3, p. 139-171, 1974.

105 F. Qin, C. Jiang, J.W. Anderegg, C.J. Jenks, B. Gleeson, D.J. Sordelet, P.A. Thiel, Segregation of Pt at Clean Surfaces of $(Pt,Ni)_3Al$, Surface Science, vol. 601, p. 376-380, 2007.

106 S. Hayashi, W. Wang, D.J. Sordelet and B. Gleeson, Interdiffusion Behavior of Pt-Modified γ-Ni + γ'-Ni_3Al Alloys Coupled to Ni-Al-Based Alloys, Metallurgical and Materials Transactions A, vol. 36A, p. 1769-1775, 2005.

107 E. Copland, Partial Thermodynamic Properties of γ'-$(Ni,Pt)_3Al$ in the Ni-Al-Pt System, Journal of Phase Equilibria and Diffusion, vol. 28, no. 1, p. 38-48, 2007.

108 A.A. Moosa, S.J. Rothman and L.J. Nowicki, Effect of Yttrium Additions to Nickel on the Volume and Grain Boundary Diffusion of Ni in the Scale Formed on the Alloy, Oxidation of Metals, vol. 24, nos. 3/4, p. 115-132, 1985.

109 A.A. Mossa and S.J. Rothman, Effect of Yttrium Additions on the Oxidation of Nickel, Oxidation of Metals, vol. 24, nos. 3/4, p. 133-148, 1985.

110 D.P. Moon, The Reactive Element Effect on the Growth Rate of Nickel Oxide Scales at High Temperature, Oxidation of Metals, vol. 32, nos. 1/2, p. 47-66, 1989.

111 H.V. Atkinson, A Review of the Role of Short-Circuit Diffusion in the Oxidation of Nickel, Chromium, and Nickel-Chromium Alloys, Oxidation of Metals, vol. 24, nos. 3/4, p. 177-197, 1985.

112 H.V. Atkinson, Evolution of Grain Structure in Nickel Oxide Scales, Oxidation of Metals, vol. 28, nos. 5/6, p. 353-389, 1987.

113 L.C. Dufour and F. Morin, The Growth of Oxide Platelets on Nickel in Pure Oxygen. II. Surface Analyses and Growth Mechanism, Oxidation of Metals, vol. 39, nos. 1/2, p. 137-154, 1993.

114 D.R. Sigler, Aluminum Oxide Adherence on Fe-Cr-Al Alloys Modified with Group IIIB, IVB, VB, and VIB Elements, Oxidation of Metals, vol. 32, nos. 5/6, p. 337-355, 1989.

115 T. Izumi and B. Gleeson, Oxidation Behavior of Pt+Hf-Modified γ-Ni+γ'-Ni_3Al Alloys. Materials Science Forum, vols. 522-523, p. 221-228, 2006.

116 J. Stringer and G.C. Wood, The Adhesion of Growing Oxides to Metallic Substrates, Materials Research Society Symposia Proceedings, Materials Research Society, vol. 119, p. 185-203, 1988.

117 J.K. Tien and F.S. Pettit, Mechanism of Oxide Adherence on Fe-25Cr-4Al (Y or Sc) Alloys, Metallurgical Transactions, vol. 3, p. 1587-1599, 1972.

118 F.A. Golightly, F.H. Stott, and G.C. Wood, The Influence of Yttrium Additions on the Oxide-Scale Adhesion to an Iron-Chromium-Aluminum Alloy, Oxidation of Metals, vol. 10, no. 3, p. 163-187, 1976.

119 H.M. Hindam and W.W. Smeltzer, Application of Auger Electron Spectroscopy and Inert Metal Marker Techniques to Determine Metal and Oxygen Transport in Oxide Films on Metals, Oxidation of Metals, vol. 14, no. 4, p. 337-349, 1980.

120 F.H. Stott, G.C. Wood, and J. Stringer, The Influence of Alloying Elements on the Development and Maintenance of Protective Scales, Oxidation of Metals, vol. 44, nos. 1/2, p. 113-145, 1995.

121 L.D. Romeu and J. Reyes, Cavity Nucleation on Special Boundaries, Proceedings of the 42nd Annual Meeting of the Electron Microscopy Society of America, edited by G.W. Bailey, San Francisco Press, Inc., p. 592-593, 1984.

122 M.M. Janssen and G.D. Rieck, Reaction Diffusion and Kirkendall-Effect in the Nickel-Aluminum System, Transactions of Metallurgical Society of the American Institute of Mechanical Engineers, vol. 239, p. 1372-1385, 1967.

123 J. Angenete and K. Stiller, Oxidation of Simple and Pt-Modified Aluminide Diffusion Coatings on Ni-Base Superalloys — II. Oxide Scale Failure, Oxidation of Metals, vol. 60, nos. 1/2, p. 83-101, 2003.

124 M. Schütze, Mechanical Properties of Oxide Scales, Oxidation of Metals, vol. 44, nos. 1/2, p. 29-61 1995.

125 T.A. Ramanarayanan, R. Ayer, R. Petkovic-Luton, and D.P. Leta, The Influence of Yttrium on Oxide Scale Growth and Adherence, Oxidation of Metals, vol. 29, nos. 5/6, p. 445-472, 1988.

126 A. Rahmel and M. Schütze, Mechanical Aspects of the Rare-Earth Effect, Oxidation of Metals, vol. 38, nos. 3/4, p. 255-266, 1992.

127 Y. Oishi and W.D. Kingery, Self-Diffusion of Oxygen in Single Crystal and Polycrystalline Aluminum Oxide, The Journal of Chemical Physics, vol. 33, no. 2, p. 480-486, 1960.

128 A.E. Paladino and W.D. Kingery, Aluminum Ion Diffusion in Aluminum Oxide, The Journal of Chemical Physics, vol. 37, no. 5, p. 957-962, 1962.

129 B.A. Pint, J.A. Haynes, K.L. More, I.G. Wright and C. Leyens, Compositional Effects on Aluminide Oxidation Performance: Objective for Improved Bond Coats, Superalloys 2000, Edited by T.M. Pollock et al., TMS 2000, p.629-638, 2000.

130 E.W.A. Young and J.H.W. de Wit, An ^{18}O Tracer Study on the Growth Mechanism of Alumina Scales on NiAl and NiAlY Alloys, Oxidation of Metals, vol. 26, nos. 5/6, p. 351-361, 1986.

131 I.M. Allam, D.P. Whittle and J. Stringer, Improvements in Oxidation Resistance by Dispersed Oxide Additions: Al_2O_3-Forming Alloys, Oxidation of Metals, vol. 13, no. 4, p. 381-401, 1979.

132 H.M. Hindam and W.W. Smeltzer, Growth and Microstructure of α-Al_2O_3 on β-NiAl, Journal of the Electrochemical Society, vol. 127, no. 7, p. 1630-1635, 1980.

133 B.A. Pint, A.J. Garratt-Reed, L.W. Hobbs, The Reactive Element Effect in Commercial ODS FeCrAl Alloys, Materials at High Temperatures, vol. 13, p. 3-16, 1995.

134 V.K. Tolpygo and D.R. Clarke, Microstructural Evidence for Counter-Diffusion of Aluminum and Oxygen During The Growth of Alumina Scales, Materials at High Temperatures, vol. 20, p. 261-271, 2003.

135 W.D. Kingery, Segregation Phenomena at Surfaces and at Grain Boundaries in Oxides and Carbides, Solid State Ionics, vol. 12, p. 299-307, 1984.

136 E.W. Hart, On the Role of Dislocations in Bulk Diffusion, Acta Metallurgica, vol. 5, 1957, p. 597.

137 P. Burtin, J.P. Brunelle, M. Pijolat and M. Soustelle, Influence of Surface Ara and Additives on the Thermal Stability of Transition Alumina Catalyst Supports. I: Kinetic Data, Applied Catalysis, vol. 34, p. 225-238, 1987.

138 H.J. Grabke, Oxidation of NiAl and FeAl, Intermetallics vol. 7, p. 1153-1158, 1999.

139 S. Rossignol, C. Kappenstein, Effect of Doping Elements on the Thermal Stability of Transition Alumina, International Journal of Inorganic Materials, vol. 3, p. 51-58, 2001.

140 M.W. Brumm and H.J. Grabke, The Oxidation Behaviour of NiAl — I. Phase Transformations in the Alumina Scale During Oxidation of NiAl and NiAl-Cr Alloys, Corrosion Science, vol. 33, no. 11, p. 1677-1690, 1992.

141 J. Jedlinski and G. Borchardt, On the Oxidation Mechanism of Alumina Formers, Oxidation of Metals, vol. 36, nos. 3/4, p. 317-337, 1991.

142 B.A. Pint, M. Treska, and L.W. Hobbs, The Effect of Various Oxide Dispersions on the Phase Composition and Morphology of Al_2O_3 Scales Grown on β-NiAl, Oxidation of Metals, vol. 47, nos. 1/2, p.1-20, 1997.

143 J.R. Wynnyckyj and C.G. Morris, A Shear-Type Allotropic Transformation in Alumina, Metallurgical Transactions B, vol. 16B, p. 345-353, 1985.

144 E. Schumann, Y.C. Yang, M.J. Graham, M. Rühle, The Effect of Y and Zr on the Oxidation of NiAl, Materials and Corrosion, vol. 47, p. 631-632, 1996.

145 J.C. Yang, E. Schumann, I. Levin and M. Rühle, Transient Oxidation of NiAl, Acta Materialia, vol. 46, no. 6, p. 2195-2201, 1998.

146 J. Doychak and M. Rühle, TEM Studies of Oxidized NiAl and Ni_3Al Cross Sections, Oxidation of Metals, vol. 31, nos. 5/6, p. 431-452, 1989.

147 T.A. Ramanarayanan, M. Raghavan, and R. Petkovic-Luton, The Characteristics of Alumina Scales Formed on Fe-Based Yttria-Dispersed Alloys, Journal of the Electrochemical Society, vol. 131, no. 4, p. 923-931, 1984.

148 A. Kumar, M. Nasrallah, and D.L. Douglass, The Effect of Yttrium and Thorium on the Oxidation Behavior of Ni-Cr-Al Alloys, Oxidation of Metals, vol. 8, no. 4, p. 227-263, 1974.

149 B.W. Veal, A.P. Paulikas, B. Gleeson, P.Y. Hou, Creep in α-Al_2O_3 Thermally Grown on β-NiAl and NiAlPt Alloys, Surface & Coatings Technology, in press, corrected proof, 2007.

150 B. Pieraggi, Calculations of Parabolic Reaction Rate Constants, Oxidation of Metals, vol. 27, nos. 3/4, p. 177-185, 1987.

151 D. Monceau and B. Pieraggi, Determination of Parabolic Rate Constants From a Local Analysis of Mass-Gain Curves, Oxidation of Metals, vol. 50, nos. 5/6, p. 477-493, 1998.

152 W.J. Quadakkers, Growth Mechanisms of Oxide Scales on ODS Alloys in the Temperature Range 1000-1100°C, Materials and Corrosion, vol. 41, p. 659-668, 1990.

153 W.J. Quadakkers and M.J. Bennett, Oxidation Induced Lifetime Limits of Thin Walled, Iron Based, Alumina Forming, Oxide Dispersion Strengthened Alloy Components, Materials Science and Technology, vol. 10, p. 126-131, 1994.

154 H.E. Evans and M.P. Taylor, Oxidation of High-Temperature Coatings, Proceedings of the Institute of Mechanical Engineers, vol. 220, Part G: Journal of Aerospace Engineering, p. 1-10, 2006.

155 R. Peraldi, D. Monceau, and B. Pieraggi, Correlations Between Growth Kinetics and Microstructure for Scales Formed by High-Temperature Oxidation of Pure Nickel. II. Growth Kinetics, Oxidation of Metals, vol. 58, nos. 3/4, p. 275-295, 2002.

156 D. Naumenko, B. Gleeson, E. Wessel, L. Singheiser and W.J. Quadakkers, Correlation Between the Microstructure, Growth Mechanism and Growth Kinetics of Alumina Scales on an FeCrAlY-Alloy, Metallurgical and Materials Transactions A, *in press*, 2007.

157 D.G. Lees, On the Reasons for the Effects of Dispersions of Stable Oxides and Additions of Reactive Elements on the Adhesion and Growth-Mechanisms of Chromia and Alumina Scales — The "Sulfur Effect", Oxidation of Metals, vol. 27, nos. 1/2, p. 75-81, 1987.

158 J.G. Smeggil, Some Comments on the Role of Yttrium in Protective Oxide Scale Adherence, Materials Science and Engineering, vol. 87, p. 261-265, 1987.

159 J.L. Smialek, Adherent Al_2O_3 Scales Formed on Undoped NiCrAl Alloys, Metallurgical Transactions A, vol. 18A, p. 164-167, 1987.

160 D.R. Sigler, The Influence of Sulfur on Adherence of Al_2O_3 Grown on Fe-Cr-Al Alloys, Oxidation of Metals, vol. 29, nos. 1/2, p. 23-43, 1988.

161 J.G. Smeggil, and G.G. Peterson, Nature of Indigenous Sulfur Segregated to the Free Metal Surface and to the Scale-Metal Interface, Oxidation of Metals, vol. 29, nos. 1/2, p. 103-119, 1988.

162 H.J. Grabke, G. Kurbatov, and H.J. Schmutzler, Segregation Beneath Oxide Scales, Oxidation of Metals, vol. 43, nos.1/2, p. 97-114, 1995.

163 A. Strawbridge and P.Y. Hou, The Role of Reactive Elements in Oxide Scale Adhesion, Materials at High Temperatures, vol. 12, nos. 2/3, p. 177-181, 1994.

164 P.Y. Hou, Beyond the Sulfur Effect, Oxidation of Metals, vol. 52, nos. 3/4, p. 337-351, 1999.

165 A.W. Funkenbusch, J.G. Smeggil, and N.S. Bornstein, Reactive Element-Sulfur Interaction and Oxide Scale Adherence, Metallurgical Transactions A, vol. 16A, 1985, p. 1164-1166.

166 Y. Zhang, W.Y. Lee, J.A. Haynes, I.G. Wright, B.A. Pint, K.M Cooley, and P.K. Liaw, Synthesis and Cyclic Oxidation Behavior of a (Ni,Pt)Al Coating on a Desulfurized Ni-Base Superalloy, Metallurgical and Materials Transactions A, vol. 30A, p. 2679-2687, 1999.

167 T. Yokokawa, M. Osawa, K. Nishida, T. Kobayashi, Y. Koizumi, H. Harada, Partitioning Behavior of Platinum Group Metals on the γ and γ' Phases of Ni-Base Superalloys at High Temperatures, Scripta Materialia, vol. 49, p. 1041-1046, 2003.

168 V.K. Tolpygo and D.R. Clarke, Surface Rumpling of a (Ni, Pt)Al Bond Coat Induced by Cyclic Oxidation, Acta Materialia, vol. 48, p. 3283-3293, 2000.